PROCEEDINGS

9TH INTERNATIONAL CONFERENCE ON COMMUNICATIONS, ELECTROMAGNETICS AND MEDICAL APPLICATIONS (CEMA'14)

Organized by:

FACULTY OF TELECOMMUNICATIONS
TECHNICAL UNIVERSITY OF SOFIA, BULGARIA

NATIONAL TECHNICAL UNIVERSITY OF ATHENS, GREECE,
SCHOOL OF ELECTRICAL AND COMPUTER ENGINEERING

NATIONAL TECHNICAL UNIVERSITY OF ATHENS, GREECE

SCHOOL OF ELECTRICAL AND COMPUTER ENGINEERING

Sofia, Bulgaria
16th – 18th October, 2014

KING

Edited by Prof. Dr. Eng. **Dimiter Tz. Dimitrov**

ISSN: 1314-2100

Printed in Bulgaria
KING 2001, Sofia

D. Dimitrov

Dear Colleagues,

It's my privilege to thanks to all of you for your contributions submitted at 8th regular International Conference on 'Communication, Electromagnetic and Medical Applications' CEMA'14. This is one conference which should help future collaboration between engineering, especially communication technologies and medicine. This is an important scientific event not only in Balkan region, but in Europe, also. The International Conference on Communication, Electromagnetism and Medical Application CEMA'14 is dedicated to all essential aspects of the development of global information and communication technologies and their impact for medicine. The objective of Conference is to bring together lecturers, researchers and practitioners from different countries, working on the field of communication, electromagnetism and medical applications, computer simulation of electromagnetic field, in order to exchange information and bring new contribution to this important field of engineering design and application in medicine. The Conference will bring you the latest ideas and development of the tools for the above mentioned scientific areas directly from their inventors. The objective of the Conference is also to bring together the academic community, researchers and practitioners working in the field of Communication, Electromagnetic and Medical Applications, not only from all over Europe, but also from America and Asia, in order to exchange information and present new scientific and technical contributions. Many well known scientists took part in conference preparation as members of International Scientific Committee or/and as reviewers of submitted paper. I would like to thanks to all of them for their efforts, for their suggestions and advices.

On behalf of the International Scientific Committee, I would like to wish you successful presentations of your papers, successful discussions and new collaborations for your future scientific investigations. Engineering and medicine should provide high level of live for all people.

Dimiter Tz. Dimitrov
Conference Chairman

INTERNATIONAL SCIENTIFIC COMMITTEE

Chairman:
Prof. D. TZ. DIMITROV, Technical University of Sofia, Bulgaria

Vice Chairman:
Prof. P. FRANGOS, National Technical University of Athens, Greece

Members:

N. AMPILOVA,	University of Perersburg, Russia
A. BEKJARSKY,	Technical University of Sofia, Bulgaria
V. GEORGIEVA,	Technical University of Sofia, Bulgaria
B. DEKERIS,	Kaunas University of Technology, Litvania
V. DEMIREV,	Technical University of Sofia, Bulgaria
N. DIB,	Jordan University of Science and Technology, Jordan
K. DIMITROV,	Technical University of Sofia, Bulgaria
M. DONTSCHEWA,	University of Applied Sciences, Dorbirn, Austria
V. DUMBRAVA,	Kaunas University of Technology, Litvania
D. EIDUKAS,	Kaunas University of Technology, Litvania
N. ESCUDEIRO,	ISEP, Porto, Portugal
E. GAGO-RIBAS,	University of Oviedo, Spain
G. GOUSSETIS,	Heriot - Watt University, United Kingdom
A. GRIGORIEV,	St. Petersburg University, Russia
S. Ver HOEYE,	University of Oviedo, Spain
M. HOFMANN,	University of Ulm, Germany
I. ILIEV,	Technical University of Sofia, Bulgaria
R. KRIVICKAS,	Kaunas University of Technology, Litvania
V. KUKENSKA,	Technical University of Gabrovo, Bulgaria
G. MALLET,	University "Sophia Antipolis", Nice, France
G. MATSOPOULOS,	National Technical University of Athens, Greece
V. MARINKEV,	Medical University of Plovdiv, Bulgaria
M. MARTINS,	Instituto Superior Tйcnico, Lisboa, Portugal
M. MORALES-GONZALES,	University of Valladolid, Spain
K. NIKITA,	National Technical University of Athens, Greece
M. NIKOLOVA,	High Naval School, Varna, Bulgaria
J. PETROVSKA,	Medical University of Sofia, Bulgaria
F. PRATO,	University of Western Ontario, Canada
H. ROTH,	University of Siegen, Germany
S. SAUTBEKOV,	Euroasian University, Astana, Kazakhstan
A. SAVOV,	Medical University of Sofia, Bulgaria
S. SAVOV,	Technical University of Varna, Bulgaria
H-P. SCHADE,	Technical University of Ilmenau, Germany
L. SONG,	Technical University of Harbin, China
A. USHEVA,	University of Boston, USA

REVIEWERS

Q. BALZANO,	University of Maryland, USA
H. BERG,	Technical University of Jena, Germany
E. BOEMO,	Technical University of Madrid, Spain
M. DONTSCHEWA,	University of Applied Sciences, Dorbirn, Austria
D.DIMITROV,	Technical University of Sofia, Bulgaria
M. HOFMANN,	University of Ulm, Germany
F. KLETT,	Franhofer Institute, Ilmenau, Germany
G. MALLET,	University "Sophia Antipolis", Nice, France
M. MARINKEV,	Medical University of Plovdiv, Bulgaria
M. MARTINS,	Instituto Superior Técnico, Lisboa, Portugal
M. MORALES-GONZALES,	University of Valladolid, Spain
J. PETROVSKA,	Medical University of Sofia, Bulgaria
A. SAVOV,	Medical University of Sofia, Bulgaria
H-P. SCHADE,	Technical University of Ilmenau, Germany
L. SONG,	Technical University of Harbin, China
A. USHEVA,	University of Boston, USA

Sponsor: **INTRACOM – Bulgaria**

REGISTRATION

October, 17th, 09h – 16h

Conference registration desk:

International Meeting Centre of Technical University – Sofia

CONFERENCE PROGRAM

16th October

Technical University of Sofia
International Meetings Center "Helmut Boehme"

OPENING CEREMONY

09h 30 – 10h

FIRST SESSION

10h – 12h

Chairman: Prof. L. Narbutaite, Kaunas University of Technology, Lithuania

1. **A DESED ENHANCED SLANT RANGE ROTATIONAL MOTION COMPENSATION ALGORITHM FOR A NOVEL FINE RANGE PROFILE ALIGNMENT IN AIR – TARGET ISAR IMAGING**
   E. Kallitsis, A. Karakasiliotis, A. Kotopoulis and P. Frangos

2. **SAR IMAGE TERRAIN CLASSIFICATION USING THE MODIFIED FRACTAL SIGNATURE (MFS) METHOD**
   Malamou, C. Pandis, P. Frangos and P. Stefaneas

3. **THE RADIATION PROBLEM FROM A VERTICAL SHORT DIPOLE ANTENNA ABOVE FLAT AND LOSSY GROUND: NOVEL FORMULATION IN THE SPECTRAL DOMAIN WITH NUMERICAL SOLUTION AND CLOSED – FORM ANALYTICAL SOLUTION IN THE HIGH FREQUENCY REGIME**
   S. Bourgiotis, K. Ioannidi, Ch. Christakis, S. Sautbekov and P. Frangos

4. **FSO AVAILABILITY DEPENDING ON THE METEOROLOGICAL CONDITIONS**
   Yordan Kovachev, Tsvetan Mitsev

5. **RANDOM PHASED ANTENNA ARRAYS – THE NEW CHALLENGE FOR THE FUTURE MICROWAVE RETRO DIRECTIVE SYSTEMS**
   Veselin Demirev

6. **LOW NOISE MICROWAVE AMPLIFIERS WITH IMPROVED INPUT MATCHING APPLICABLE IN ACTIVE ARRAY ANTENNAS**
   Mihail Plamenov Tonev

LUNCH
12h – 13h

SECOND SESSION

13h – 14h30

Chairman: Prof. P. Frangos, NTUA, Athens, Greece

1. **ALGORITHM FOR DETECTION OF MUSCLE CONTRACTIONS IN THE EMG SIGNAL, FOR USE IN ACTIVE PROSTHESIS,** *Viktor A. Nedialkov*
2. **FRACTAL CHARACTERISTICS OF DIGITAL IMAGES AND THEIR WAVELET TRANSFORMS,** *I. P. Soloviev, M. V. Videneeva*
3. **IMAGE SEGMENTATION ALGORITHM BASED OF MULTIFRACTAL SPECTRUM COMPUTING,** *N. B. Ampilova, Y. V. Shupletsov*
4. **ALGORITHMS OF INTERPOLATION AND VISUALIZATION OF LOW FREQUENCY MAGNETIC FIELD BY USING EXPERIMENTAL DATA,** *B. Kudrin, V. Nikolov*
5. **ON MODELING OF DIFFUSION LIMITED AGGREGATION PROCESSES ON TRIANGULATION NET,** *N. B. Ampilova, A. M. Batyukov*
6. **VISUALIZATION OF THE STUDY FOR SPACE-TIME CONFIGURATION OF THE ELECTROMAGNETIC FIELD EMITTED BY EQUIPMENT FOR MICROWAVE THERAPY** *Antoniya P. Petrova*

BREAK

14h 30 – 15h

THIRD SESSION

15h – 16h 30

Chairman: Prof. Kalin Dimitrov, Technical University of Sofia, Bulgaria

1. **DESIGN OF RADIO CHANNEL FOR DVB-T SYSTEM,** *Lidia Jordanova, Georgi Karpov, Dobri Dobrev*
2. **ISOTROPIC MULTI-HOP MODEL FOR WIRELESS SENSOR NETWORKS** *Zlatan Ganev, Sava Savov*
3. **LOG-NORMAL SHADOWINGMODEL FOR WIRELESS SENSOR NETWORKS** *Zlatan Ganev, Sava Savov*
4. **ON THE LIMITATIONS OF GAIN CALIBRATION IN HARMONIC REJECTION MIXERS,** *Ludwig Lubich*
5. **THE BENEFITS OF IEEE 802.11AC STANDARD: COMPARISON WITH 802.11N WIRELESS NETWORK AND EXPERIMENTAL INVESTIGATIONS FOR REAL-TIME SERVICE TRANSMISSION,** *Arnoldas Matusevičius, Tomas Adomkus, Lina Narbutaitė, Rasa Brūzgienė*
6. **USING EMBEDDED SOFTWARE FOR ACHIEVING HIGHER PRECISION IN POWER DETECTORS,** *Boyan Ivanov Ivanov*

17th October

Technical University of Sofia

International Meetings Center "Helmut Boehme"

FOURTH SESSION

10h – 12h

Chairman: Prof. Dimitar Dimitrov, Technical University of Sofia, Bulgaria

1. **ON THE MATHEMATICAL MODEL OF INTERPOLATION OF LOW FREQUENCY MAGNETIC FIELD USING EXPERIMENTAL DATA,** *B. Kudrin, V. Nikolov*

2. **PZT AND MEMS APPLICATIONS FOR THE VESTIBULAR SYSTEMS,** *Tsvetan Kachamachkov*

3. **ALGORITHM TO CALCULATE THE MAXIMUM VALUE OF THE LOW-FREQUENCY MAGNETIC FIELD USING MICROPROCESSOR AND MAGNETIC SENSORS,** *Vladimir Nikolov*

4. **SYSTEM FOR MEASUREMENT OF MAGNETIC INDUCTION OF LOW FREQUENCY MAGNETIC FIELD,** *Vladimir Nikolov*

5. **EVALUATION OF A MAGNETIC 3D MEASUREMENT SYSTEM FOR APPLICATION IN COMPUTER ASSISTED SURGERY COMPARED TO ESTABLISHED OPTICAL TRACKING SYSTEMS,** *Matthias Mende, Erwin Gerz, Hubert Roth*

6. **EVALUATION STUDY OF UNDERWATER LASER COMMUNICATION SYSTEM IN SHATT AL –HILLA – IRAQ,** *Jassim Mohammed Jassim*

LUNCH

12h – 13h

FIFTH SESSION

13h – 14h30

Chairman: Prof. V. Demirev, Technical University of Sofia, Bulgaria

1. **ACTIVE SHAPE MODELS WITH 2D PROFILES FOR STRESS/ANXIETY RECOGNITION FROM FACE IMAGES,** *Martin Penev, Agata Manolova, Ognian Boumbarov*

2. **SYSTEM FOR TOUCHLESS INTERACTION WITH MEDICAL IMAGES IN SURGERY USING LEAP MOTION,** *Agata Manolova*

3. **THE IMPACT OF THE ELECTROMAGNETIC FIELD RADIATIONS FROM THE GADGETS TO THE USERS,** *Darko Brodić, Čedomir A. Maluckov, Agata Manolova, Ivo Draganov*

4. **DETECTION OF RENAL CYSTS BASED ON COMPLEX SEGMENTATION OF CT IMAGES,** *Veska M. Georgieva, Ant. Nankova*

5. **GUI FOR COMPLEX SEGMENTATION OF MEDICAL IMAGES,** *Veska M. Georgieva, Ant. Nankova*

6. **INFRARED TEMPERATURE CONTROL DURING MAGNET THERAPY,** *Kalin Dimitrov, Atanas Dimitrov, Tsvetan Mitsev*

BREAK
14h 30 – 15h

SIX SESSION

15h – 16h

Chairman: Prof. N. Ampilova, St. Petersburg University, St. Petersburg, Russia

1. **STUDIES OF SOUNDPROOFING CHARACTERISTICS OF SANDWICH PANEL WITH HONEYCOMB CORE AND ELASTIC POROUS ABSORBER,** *Tsvetan Nedkov*

2. **DEVELOPMENT OF SOUND SOURCE LOCALIZATION MODULE BASED ON MEMS TECHNOLOGY,** *V. Hristov*

3. **KEY CHALLENGES FOR BIOMEDICAL ENGINEERING CONCERNING LIFELONG LEARNING PROGRAMES ON APPLICATION OF INFORMATION TECHNOLOGIES IN MEDICINE**, *Dimitar Dimitrov*

4. **SOME BASIC CHALLENGES FOR COURSES ON MEDICAL SYSTEMS FOR THERAPY IN BIOMEDICAL ENGINEERING CURRICULUM IN THE PROCESS OF LIFELONG LEARNING**, *Atanas Dimitrov*

5. **ON INTERPOLATION METHODS OF LOW FREQUENCY MAGNETIC FIELD IN SYSTEMS FOR MAGNETOTHERAPY,** *B. Kudrin, I. P. Soloviev*

CLOSING SESSIONS

16h– 16h30

SOCIAL PROGRAM

Banquet
October, 16th, 19h 30

Trip
October 18th

CONTACT US:

GENERAL INFORMATION AND SUBMISSION OF CONTRIBUTIONS

Prof. Dr. D. Dimitrov

Faculty of Telecommunications
Technical University of Sofia
8, Kliment Ohridsky str.
1756 Sofia, Bulgaria
Phone / Fax: ++359 2 9652278
E-mail: dcd@tu-sofia.bg

Prof. Dr. P. Frangos

National Technical University of Athens
School of Electrical and Computer Engineering
9, Iroon Polytechniou Str.,
157 73 Zografou, Athens, Greece
Phone: 00 30 210 772 3694
Fax: 00 30 210 772 2281
E-mail: pfrangos@central.ntua.gr

TABLE OF CONTENTS

AUTHOR INDEX

A DESED ENHANCED SLANT RANGE ROTATIONAL MOTION COMPENSATION ALGORITHM FOR A NOVEL FINE RANGE PROFILE ALIGNMENT IN AIR – TARGET ISAR IMAGING

E. Kallitsis, A. Karakasiliotis, A. Kotopoulis and P. Frangos

National Technical University of Athens
9, Iroon Polytechniou Str., GR 157 73, Zografou, Athens, Greece
Tel: +30 210 772 3694, Fax: +30 210 772 2281, E-Mail: ekalorama@gmail.com, anastasiskarak@yahoo.gr, emalkotopoulis@gmail.com, pfrangos@central.ntua.gr

Abstract

In this paper we propose the use of a super-resolution decimative spectrum estimation (DESED) method for highly accurate estimation of the slant-range positions of the target scattering centers. Based on these position estimates, we develop a novel slant-range rotational compensation (SRRC) method. The proposed decimative spectrum estimation based SRRC technique achieves fine range alignment, in terms of fractional range bin correction, and constitutes the first step towards significant de-blurring of the final ISAR image. The proposed method is validated with synthetic ISAR data under realistic simulation scenarios, for both uniform and non-uniform rotational motion.

1. INTRODUCTION

Inverse synthetic aperture radar (ISAR) is a radar technique to obtain a high resolution image of a moving target. Usually, a wideband transmitted waveform is used to obtain high slant-range resolution, whereas cross-range resolution depends on target aspect angle variation during the coherent processing interval (CPI) [1]. The conventional assumption of relatively small aspect angle variation during CPI is vitiated for small, rapidly maneuvering targets (i.e. fighter aircrafts) [2]. In the current scenario of high-range resolution radar and non-cooperative target, the rotational motion parameters of the target are unknown and migration through resolution cells (MTRC) is apparent in the obtained ISAR images, in both slant-range and cross-range direction [1]-[4].

Target motion may be divided into a translational component and a rotational component [2]. The first one is further decomposed into a radial and a tangential component, whereas the second one has three attitude components: yaw, pitch and roll. On the one hand, the radial component of the translational motion [that is, the component along the line-of-sight (LOS)] is undesired, because it does not induce variation of the target aspect angle, i.e. it does not generate Doppler gradient among target scatterers situated in the same range bin. Furthermore, this component causes significant blurring in ISAR images.

On the other hand, the rest of motion components may produce the desired Doppler gradient among scatterers, hence obtaining two - dimensional information. It is true that the rotational motion (and the tangential component of the translational motion), may also generate blurring effects on the image (MTRC), but they are of minor importance compared to the blurring caused by the radial component of the translational motion, which must always be compensated [3]. Conventional methods for translational motion compensation [1], [2] mostly follow two steps: (i) range tracking (coarse range bin alignment) and Doppler tracking (fine phase correction with respect to a prominent scatterer). Range tracking can keep scatterers in their range cells, while Doppler tracking keeps Doppler frequency shift of each scatterer constant during CPI.

Range tracking can be performed by a cross-correlation method that finds misaligned range cells with respect to a reference range profile and then performs range alignment for all other range profiles. Cross-correlation allows for integer range bin correction, thus it has no capability of compensating misalignments less than slant-range resolution. Even if zero padding is performed before Fast Fourier transform (FFT) is applied to derive range profiles, cross-correlation based range alignment method can only estimate more accurately the average slant-range migration of the target as a whole and not the migration of each scatterer individually.

In this paper, we develop a novel fine range alignment method that can very accurately compensate for different slant-range migrations of individual scatterers of a rotating target. The proposed range alignment method that is based on range position estimates derived by applying a super-resolution decimative spectrum estimation method, namely DESED [5], on raw ISAR data. These range estimates are applied to raw data as compensating phase terms, separately for each scatterer, and the obtained per scatterer range profiles are combined together to produce finely aligned overall range profiles. Simulation results verify the novelty and validity of the proposed method.

2. MATHEMATICAL DESCRIPTION

Figure 1 shows the position of a rotating scatterer at the initial instant (p_0) and at slow-time instant τ. Translational motion compensation is assumed to be completed and ISAR image artifacts induced by rotational motion have to be compensated. Consequently, the rotation center does not change its position during the CPI. R_0 is the distance from the radar to the rotation center. The following calculations divide the MTRC into migration in slant-range and cross range [6].

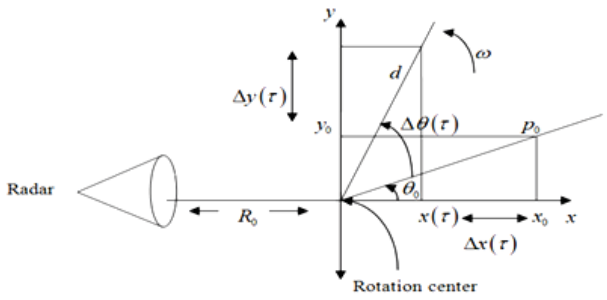

Fig. 1. ISAR scenario with a rotating scatterer

$\Delta x(\tau)$ is the rotation-induced slant-range migration of the scatterer and has the expression $\Delta x(\tau) = x(\tau) - x_0$, where $x(\tau) = d\cos(\theta_0 + \Delta\theta(\tau))$ and $x_0 = d\cos(\theta_0)$

Thus

$$\Delta x(\tau) = d\left[\cos(\theta_0)\cos(\Delta\theta(\tau)) - \sin(\theta_0)\sin(\Delta\theta(\tau)) - \cos(\theta_0)\right] \quad (1)$$

Assuming that $\Delta\theta(r)$ is not very large, the following Taylor series approximations are applicable:

$$\begin{aligned} \sin(\Delta\theta(\tau)) &\approx \Delta\theta(\tau) \\ \cos(\Delta\theta(\tau)) &\approx 1 - \frac{(\Delta\theta(\tau))^2}{2} \end{aligned} \quad (2)$$

Taking second order term into account, the following equation describes slant-range migration

$$\begin{aligned} \Delta x(\tau) &= -d\cos(\theta_0)\frac{(\Delta\theta(\tau))^2}{2} - d\sin(\theta_0)\Delta\theta(\tau) \\ &= -y_0\Delta\theta(\tau) - x_0\frac{(\Delta\theta(\tau))^2}{2} \end{aligned} \quad (3)$$

With respect to cross-range, the received signal phase for the rotating scatterer at instant τ is $\varphi(\tau) = \frac{4\pi}{\lambda}R(\tau)$, where λ is the wavelength and $R(\tau)$ is the range from the radar to the scatterer. Since $R(\tau)$ can be approximated as

$$R(\tau) = R_0 + x(\tau)$$

where

$$\begin{aligned} x(\tau) &= d\cos(\theta_0 + \Delta\theta(\tau)) \\ &= d\left[\cos(\theta_0)\cos(\Delta\theta(r)) - \sin(\theta_0)\sin(\Delta\theta(r))\right] \\ &= x_0\cos(\Delta\theta(r)) - y_0\sin(\Delta\theta(r)) \end{aligned} \quad (4)$$

Using the approximations of Eq. (2), without ignoring the term $x_0\frac{(\Delta\theta(\tau))^2}{2}$ we derive the phase expression related to cross-range migration

$$\varphi(\tau) = \frac{4\pi}{\lambda}\left[R_0 + x_0 - y_0\Delta\theta(\tau) - x_0\frac{(\Delta\theta(\tau))^2}{2}\right] \quad (5)$$

SRRC (slant-range rotational compensation) corrects the slant-range migration induced by rotational motion, as expressed in Eq. (3). The contribution of both slant-range and cross-range to the range misalignment of the obtained ISAR images becomes obvious through the following figure. Simple target geometry of five scatterers is examined in this paper as a proof of concept for the proposed range alignment method. Taking a closer look to the ISAR images of Fig. 2, the significant slant-range migration of the "wing" scatterers $(|y| > 0)$ is apparent, while the "fuselage" scatterers $(y = 0)$ exhibit quite small range shift, not to mention zero shift for the center of rotation. Equation (3) provides valua-

ble insight into the expected range migration of each scatterer.

On the other hand, CRRC (cross-range rotational compensation) compensates for the last phase term of equation (5) which is associated with the ISAR image blurring. In this paper, it is pre-assumed that the constant distance related phase terms of equation (5) are removed through a translational motion compensation technique [1], [3]. Future research effort is oriented towards a novel CRRC method in view of a combination with the proposed SRRC method [7], [8].

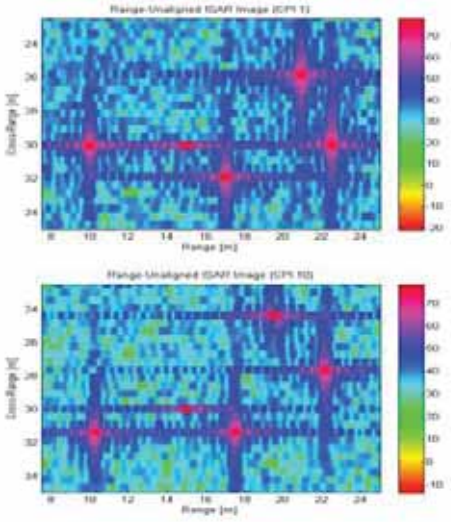

Fig. 2. Slant-range migration induced by uniform rotational motion.

3. PROPOSED RANGE ALIGNMENT METHOD

Super-resolution spectrum or frequency estimation techniques have been studied extensively over the past 3 decades from the signal processing community. Amongst their applications radar imaging has been a very important one [9]-[11]. Decimative spectrum estimation methods have also attracted research interest because of their inherent frequency resolution improvement, achieved via decimation of the data sequence under spectral analysis.

In [5], the use of a decimative frequency estimation technique, namely DESED, is proposed for estimating the range positions of target scatterers. Belonging to the wide class of parametric spectrum estimation methods, DESED is applied for a specific order, equal to the number of prominent scatterers, and for a specific decimation factor D, determined empirically with respect to the available data length.

In this paper, we apply DESED to two-dimensional raw synthetic data, which are generated by a MATLAB program simulating the classical ISAR geometry with a rotating target consisting of a specific number of point scatterers. In order to derive consistent range estimates from DESED, we need to provide the method with a correct model order (signal model is considered to be a sum of damped exponentials).

Order selection is non-trivial task in parametric spectral analysis [12]. For a radar imaging application, a scattering center extraction method [13], [14] can be employed to estimate accurately the model order.

For simulation purposes in the present study, a trivial peak search algorithm finds the initial range positions, based on the first few range profiles. Alternatively, we use the DESED range estimates averaged over the first few bursts. By taking into account that the rotation center of the target will always be present at the center of the unambiguous range window, we can compute the initial range positions by utilizing DESED estimates.

Analytical mathematical description of DESED method is provided in [5]. The DESED based frequency estimates are translated to range estimates by relating the ISAR signal model to the conventional damped exponentials model. In the proposed approach, we exploit DESED's accuracy and robustness to noise and use the obtained range estimates to calculate the misalignment between range profiles. Each raw data burst is analyzed through DESED. The range estimates for the first burst serve as reference estimates to compute the range migration of each scatterer from burst to burst (slow time). Averaging the range estimates for the first few bursts is an alternative effective way to derive reference estimates in case of low signal-to-noise ratio (SNR).

As shown in Fig. 2 and explained through Eq. (3), each scatterer behaves differently with respect to slant-range and cross-range migration during the imaging integration time (one or more CPIs). For the simple target examined in this paper, we observe in Fig. 2 that the two "wing" scatterers move towards each other in slant-range as the target rotates counter-clockwise. This very important detail is missed by conventional range alignment techniques referring to slant-range migration induced by translational motion.

Throughout this paper we name the amount of range misalignment with respect to the reference range estimates as normalized range migration. This amount differs for each scatterer and is expressed as an integer number of fine range bins. One fine range bin unit is a fraction of range resolution ΔR_s (range cell or bin). Fractional range bin correction [15] is achieved via zero-padding each raw data burst by a factor M_{zpd} before performing FFT based range compression. Thus, one fine range bin unit equals to $\frac{\Delta R_s}{M_{zpd}}$ and the obtained fine range profile data length is $M \cdot M_{zpd}$, where M is the raw data burst length.

Once DESED is applied to the current burst and the estimated range misalignments of all scatterers are derived, an aligned range profile has to be formed. The proposed SRRC algorithm consists of four steps with DESED based range estimation being the fundamental one. The block diagram of Fig. 3 presents the basic steps towards fine range alignment. Blocks enclosed by the red dashed box are associated with per scatterer processing, in contrast to per burst processing.

The second step of the proposed SRRC methodology is the individual range shift application, referring to the estimated range migration of each scatterer. Symbolizing DESED order as p and the range estimate of $i-th$ scatterer for the $k-th$ burst as $\hat{r}_i(k)$, the corresponding normalized range migration is computed by

$$\Delta\hat{r}_i(k) = round\left(\frac{\hat{r}_i(k) - \hat{r}_i(0)}{\left[\frac{\Delta r_s}{M_{zpd}} \right]} \right), \quad i = \overline{1,p} \tag{6}$$

where p is DESED order, equal to the number of prominent scatterers $(p=5)$ and i is an index for scatterers (the bar above the symbols shows the values which index i takes).

Utilizing the inherent FFT property of frequency shift, p phase shifted versions of the $k-th$ burst are generated by multiplying it with the term

$$\exp\left[-j \frac{2\pi}{M \cdot M_{zpd}} (m-1) \Delta\hat{r}_i(k) \right]$$

where $m = \overline{1,M}$. In this way, we compensate for the individual range misalignment of each scatterer.

The phase shifted versions of each raw data burst are then transformed through FFT (with zero-padding) into properly range shifted versions of the corresponding range profile. This is the third step of the proposed SRRC algorithm, named individual fine range profile computation.

The final step is the overall fine range profile synthesis, where the individual fine range profiles are combined into an overall one. First, we construct a mask around the estimated initial range position of the $i-th$ scatterer and we retain the corresponding samples from the $i-th$ fine range profile. The mask length is proportional to the zero-padding factor M_{zpd} and, from a signal processing perspective, it is useful to employ a window function with variable roll-off factor, especially for closely spaced scatterers. The masking procedure is repeated for all *p* scatterers. Secondly, we detect the "shared regions" between scatterers, again based on their initial positions. The corresponding samples from the f_0 *p* individual range profiles are averaged in order to compute the contribution of "shared regions" to the overall fine range profile. Azimuth compression through FFT is performed after the fine range alignment procedure to obtain the range-aligned ISAR image.

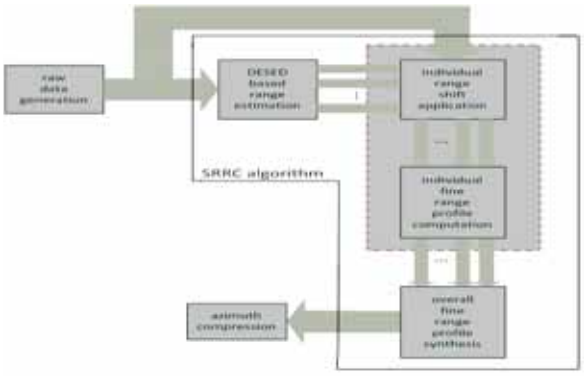

Fig. 3. SRRC algorithm

4. SIMULATION RESULTS

Raw ISAR data for the target of Fig. 4 are generated through MATLAB simulation, based on the signal model presented in [7]. The math formulas for raw data and rotational motion simulation are the following

$$x(m,n)=\sum_{k=1}^{d} s_k \exp\left[-j\frac{4\pi}{c} f_m\left(x_k\cos(\theta_n)-y_k\sin(\theta n)\right)\right]+u(m,n)$$

$$\theta_n=\theta_0+\omega t_n+\frac{1}{2}\gamma\left(t_n-t_{start}\right)^2 \qquad (7)$$

where d the number of scatterers; s_k the scattering intensity of $k-th$ point scatterer, (x_k, y_k) the Cartesian coordinates of $k-th$ point scatterer, with respect to the radar position; m the stepped frequency index $\left(m=\overline{1,M}\right)$ and n the burst index $n=\left(\overline{1, N\cdot N_{CPI}}\right)$ for a number of simulated CPIs (N_{CPI}); N the number of bursts during one CPI; $u(m,n)$ the two-dimensional additive white Gaussian noise component, with simulated SNR equal to 10db; θ_0 the initial aspect angle of the target, assumed to be at a distance of 10 Km; ω the constant angular velocity; γ the angular acceleration, which is zero for uniform rotation; t_{start} the time instant (as an integer multiple of burst duration) at which an angular acceleration period begins.

Table 1 presents the aforementioned simulation parameters, as following:

Table 1. Isar simulation parameters

Parameter	Value [units]
initial carrier frequency, f_0	10 [GH_z]
range resolution, Δr_s	0.46875 [m]
cross-range resolution, Δr_c	0.47244 [m]
radar bandwidth, B	320 [GH_z]
number of frequencies, M	64
frequency step, Δf	5 [MH_z]
pulse repetition frequency, PRF	15 [KH_z]
burst duration, T_b	4.266 [$msec$]
coherent processing interval, CPI	0.546 [sec]
number of bursts, N	128
number of CPI'S, N_{CPI}	10
angular velocity, ω	0.0586[rad/sec]
angular acceleration, γ	0.64 [rad/sec^2]
model order, p	5
decimation factor, D	2
zero – padding factor, M_{zpd}	32

The rotational motion evolution over 10 CPIs simulated in case of uniform and non-uniform rotation is depicted in the next two figures respectively. The latter profile includes angular acceleration within the 4th and the 8th CPI, with smoothed transition from uniform to non-uniform rotation periods.

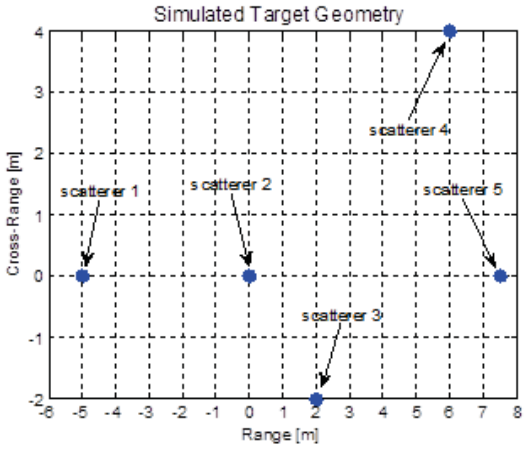

Fig. 4. Simple target geometry with five scatterers

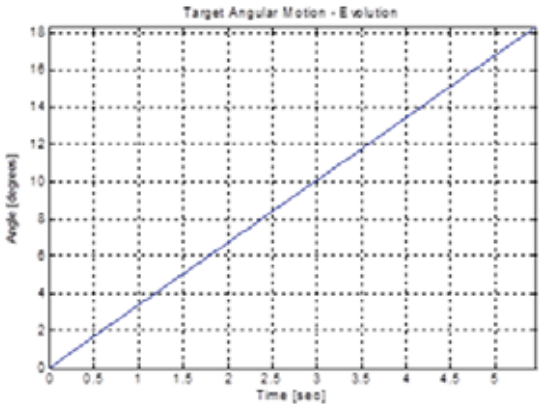

Fig. 5. Uniform rotational motion profile

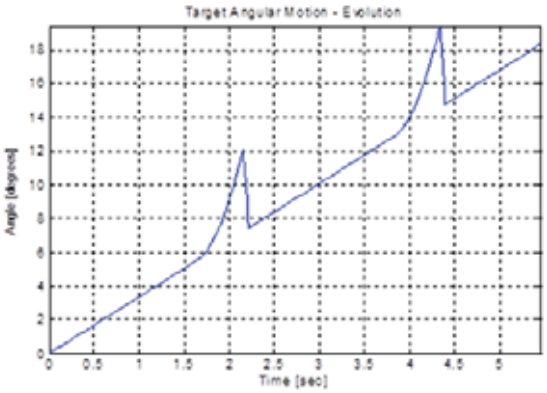

Fig. 6. Non-uniform rotational motion profile

The DESED based range estimates for each scatterer (as noted in Fig. 4) are presented in Figs. 7 and 8 for both simulation scenarios. The variation in terms of fine range bin units is attributed to noise and can be smoothed out by a moving average filter of small length (i.e. 10-20 bursts). As expected, the "wing" scatterers (scatterers 3 and 4) exhibit significant slant-range migration compared to other scatterers, with scatterer 4 migrating by more than 3 range bins during the simulated time. In Fig. 8, the effect of non-uniform rotation is obvious in the range estimate of each scatterer. The similarity of the profile of Fig. 6 with the range estimate of scat-

terer 4 (at the wing edge) is evident and can be easily explained through Eq. (3).

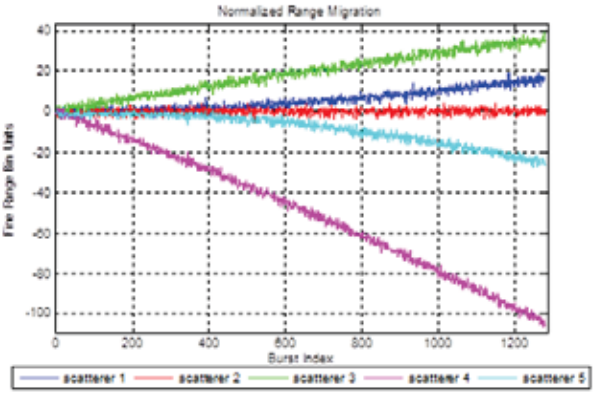

Fig. 7. Normalized range migration of each scatterer for uniform rotation

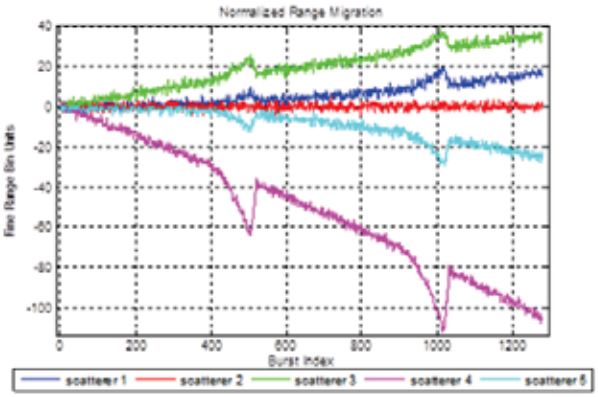

Fig. 8. Normalized range migration of each scatterer for non Uniform rotation

Since DESED provides very accurate and robust to noise range estimates, the proposed range alignment method is expected to produce very well aligned range profiles. In Figs. 9(b) and 10(b), the range alignment is noticeable, as well as the considerable sidelobe reduction within "shared regions" between scatterers.

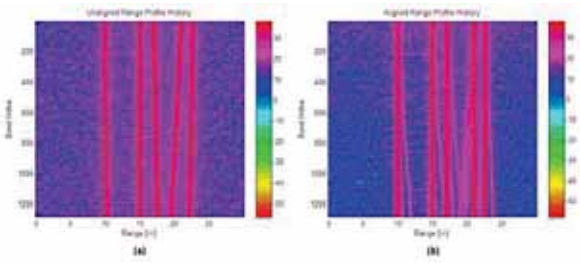

Fig. 9. Range profile history before (a) and after (b) the proposed range alignment method for uniform rotation

The focusing effect of the proposed range alignment method can also be verified by examining carefully the obtained ISAR images before and after its application. Figs. 11 and 12 show this effect clearly in range direction for uniform and non-uniform rotation respectively.

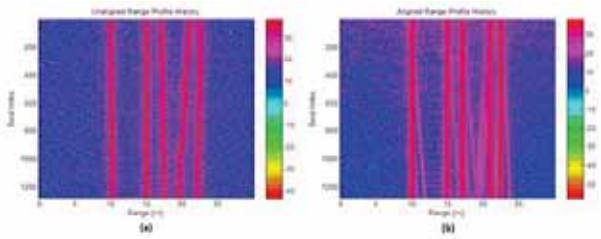

Fig. 10. Range profile history before (a) and after (b) the proposed range alignment method for non-uniform rotation

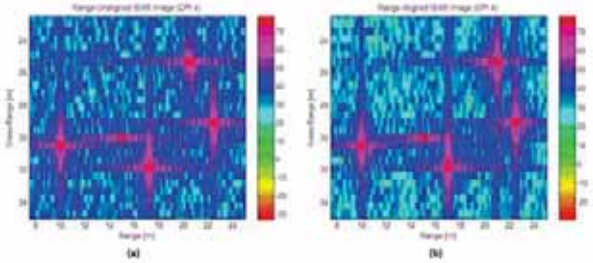

Fig. 11. ISAR images before (a) and after (b) the proposed range alignment method for uniform rotation

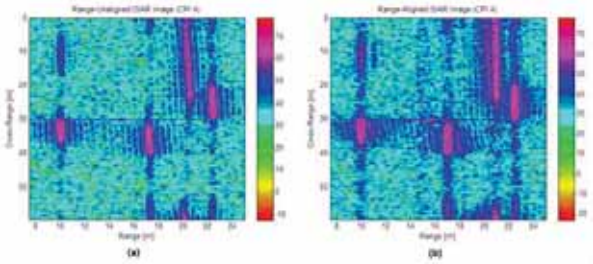

Fig. 12. ISAR images before (a) and after (b) the proposed range alignment method for uniform rotation

Furthermore, the entropy values of the power normalized ISAR images [16], shown in Figs. 13 and 14, strongly indicate the focusing improvement after fine range alignment.

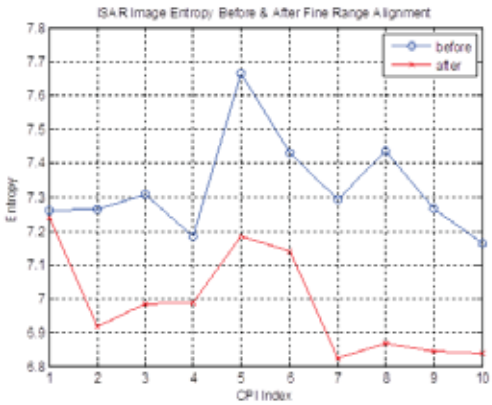

Fig. 13. ISAR image entropy before and after the proposed range alignment method for uniform rotation

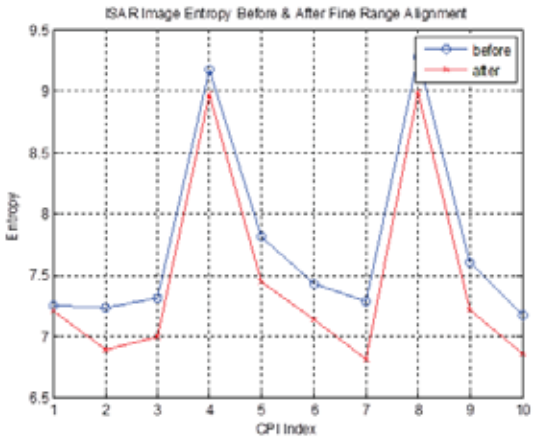

Fig. 14. ISAR image entropy before and after the proposed range alignment method for non-uniform rotation

5. CONCLUSIONS

In this paper we presented a novel slant-range rotational compensation method with application to ISAR imaging. This method is based on super-resolution decimative spectrum estimation for accurate range position estimates. Compared to conventional range alignment methods, our method is capable of fractional range bin correction and takes into account the different slant-range migration of each scatterer. The effectiveness of the proposed range alignment method is proven through extensive ISAR simulations for both uniform and non-uniform air – target rotation, looking into the range profile history, the obtained ISAR images and the corresponding entropy values before and after the application of the proposed methodology.

References

[1] D. Wehner, High-Resolution Radar, London, Artech House, 2nd edition, 1995.

[2] V. Chen, and H. Ling, Time-Frequency Transforms for Radar Imaging and Signal Analysis, London, Artech House, 2002.

[3] J. Son, G. Thomas, and B. Flores, Range-Doppler Radar Imaging and Motion Compensation, Artech House, 2001.

[4] G. Lu, and Z. Bao, "Compensation of scatterer migration through resolution cell in inverse synthetic aperture radar imaging", IEE Proc. Radar, Sonar and Navigation, Vol. 147 (2), pp. 80-85, Apr. 2000.

[5] A. Karakasiliotis, and P. Frangos, "Decimative Spectrum Estimation Method for High-Resolution Radar Parameter Estimates," Proc. 5th International Symposium on Communications, Networks and Digital Signal Processing (CSNDSP 2006), Patras, Greece, July 2006.

[6] J. Munoz-Ferreras and F. Perez-Martinez, "Uniform rotational motion compensation for inverse synthetic aperture radar with non-cooperative targets", IET Radar, Sonar and Navigation, Vol. 2 (1), pp. 25-34, Feb. 2008.

[7] E. Kallitsis, A. Karakasiliotis, G. Boultadakis, and P. Frangos, "A Fully Automatic Autofocusing Algorithm for Post-processing ISAR Imaging based on Image Entropy Minimization", Electronics and Electrical Engineering Journal, T121 Signal Technology, No. 4 (110), pp.125-130, Apr. 2011.

[8] E. Kallitsis, A. Karakasiliotis, and P. Frangos, "Combination of range alignment technique with autofocusing post-processing algorithm for ISAR image optimization", International Conference on 'Communications, Electromagnetics and Medical Applications' (CEMA'11), Sofia, Bulgaria, Oct. 2011.

[9] A. Karakasiliotis, and P. Frangos, "Comparison of Several Spectral Estimation Methods for Application to ISAR Imaging," Proc. RTO SET 080 International Symposium on 'Target Identification and Recognition using RF Systems', Oslo, Norway, 11-13 October 2004.

[10] S. DeGraaf, "SAR imaging via modern 2-D spectral estimation methods", IEEE Transactions on Image Processing, Vol. 7 (5), pp.729-761, May 1998.

[11] E. Corral, G. Thomas, and B. Flores, "Effects of using superresolution techniques in ISAR imagery", Proc. CCECE 2002, Vol. 1, pp. 353-357, 2002.

[12] P. Stoica, and Y. Selen, "Model-order selection: a review of information criterion rules", IEEE Signal Processing Magazine, Vol. 21 (4), pp. 36-47, July 2004.

[13] K.-T. Kim, and H.-T. Kim, "Two-dimensional scattering center extraction based on multiple elastic modules network", IEEE Transactions on Antennas and Propagation, Vol.51 (4), pp. 848-861, Apr. 2003.

[14] Y. Wang, J. Chen, and Z. Liu, "Two-dimensional scattering center extraction using super-resolution techniques [Inverse SAR applications]", International Symposium of IEEE Antennas and Propagation Society, Vol. 2, pp. 2091- 2094, June 2004.

[15] J. Munoz-Ferreras, and F. Perez-Martinez, "Sub-integer Range-Bin Alignment Method for ISAR Imaging of Noncooperative Targets", EURASIP Journal on Advances in Signal Processing-Special Issue on Advanced Image Processing for Defense and Security Applications, Vol. 2010, pp. 1-16, Feb. 2010.

[16] A. Karakasiliotis, A. Lazarov, G. Boultadakis, G. Kalognomos and P. Frangos, "Two-dimensional ISAR Model and Image Reconstruction with Stepped Frequency Modulated Signal", IET Signal Processing, Vol. 2 (3), pp. 277-290, Sept. 2008.

SAR IMAGE TERRAIN CLASSIFICATION USING THE MODIFIED FRACTAL SIGNATURE (MFS) METHOD

A. Malamou, C. Pandis, P. Frangos and P. Stefaneas

National Technical University of Athens
9, Iroon Polytechniou Str., GR 157 73, Zografou, Athens, Greece
Tel. +30 210 772 3694, Fax. +30 210 772 2281, E-mail : pfrangos@central.ntua.gr

Abstract

The Modified Fractal Signature (MFS) method is applied to real Synthetic Aperture Radar (SAR) images containing different terrain types. Useful information for SAR image classification is obtained using this method, and the SAR image can be classified as an urban, suburban, rural, mountain or sea site. Moreover, the corresponding Fractal Area curve and Fractal Dimension curve of the image are calculated through the MFS method. The classification of different types of terrain is possible due to the fact that the terrain types encountered in SAR images, yield different values of Fractal Area curves and Fractal Dimension curves.

1. INTRODUCTION

Fractals are characterised by a high degree of geometrical complexity in several groups of data as well as in images. Images, and in particular Synthetic Aperture Radar (SAR) images, can be considered as fractals for a certain range of magnifications. Moreover, fractal objects have unique properties that can be related to their geometric structure [1] – [3]. The fractal properties of images, provide interesting classification and characterization results for different terrain types encountered in real SAR images [4], [5]. For example, a SAR image of an urban area in comparison with a SAR image of a rural area, is expected to exhibit different properties, when they are both treated as fractal objects.

In this paper the Modified Fractal Signature (MFS) method is applied to real spaceborne SAR images, provided to us by an International Working Group on SAR techniques (SET 163 Working Group). The main idea concerning this technique is the fact that different terrain types encountered in SAR images yield different characteristic values of 'Fractal Area' curves (A_δ) and 'Fractal Dimension' (or 'Fractal Signature') curves (F_D) [5] in particular, through which classification of different types of terrain is possible.

2. MATHEMATICAL FORMULATION OF THE MFS METHOD

In this section the mathematical formulation of the modified Fractal Signature (MFS) method [2] - [5] is described. This 'multi – resolution' method is applied at images and it computes the values of 'Fractal Area' (A_δ) and 'Fractal Dimension' (or 'Fractal Signature') (F_D) at different scales δ of the original image. The corresponding algorithm incorporates the so called 'blanket' technique [2] – [5] and the images are initially converted to a gray – level function $g(x,y)$. In the 'blanket' approach all points of the three - dimensional space at distance δ or less from the gray level function $g(x,y)$ are considered. These points construct a 'blanket' of thickness 2δ covering the initial gray level function. The covering blanket is defined by its upper surface $u_\delta(x,y)$ and its lower surface $b_\delta(x,y)$, as it is shown in Fig. 1 [5].

The upper and lower surface can be computed using an iterative algorithm (δ iterations). Initially, the iteration number δ equals to zero ($\delta = 0$) and the gray-level function equals to the upper and lower surfaces, namely: $u_0(x,y) = b_0(x,y) = g(x,y)$. For iteration $\delta = 1,2,\ldots$ the blanket surfaces are calculated through the following iterative formulae:

$$u_\delta(x,y) = \max\{u_{\delta-1}(x,y)+1,\ \max_{|(m,n)-(x,y)|\le 1} u_{\delta-1}(m,n)\}$$
$$b_\delta(x,y) = \min\{b_{\delta-1}(x,y)-1,\ \min_{|(m,n)-(x,y)|\le 1} b_{\delta-1}(m,n)\} \quad (1)$$

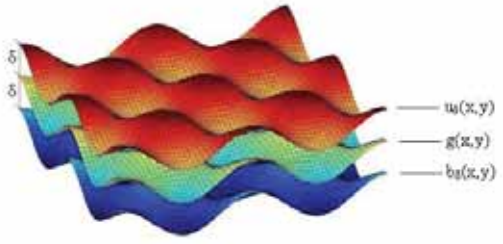

Fig. 1. 'Blanket' of thickness 2δ defined by its upper $u_\delta(x,y)$ and lower $b_\delta(x,y)$ surface

The image pixels *(m, n)* with distance less than one from pixel *(x,y)* are chosen in this paper as the four immediate neighbors of pixel *(x,y)* [3]. Equation (1) ensures that the new upper surface u_δ is higher than $u_{\delta-1}$ by at least one. Likewise, the new lower surface b_δ is lower than $b_{\delta-1}$ by at least one [3].

Subsequently, the volume of the 'blanket' is calculated from $u_\delta(x,y)$ and $b_\delta(x,y)$ by:

$$Vol_\delta = \sum_{(x,y)} (u_\delta(x,y) - b_\delta(x,y)) \qquad (2)$$

Furthermore, the 'Fractal Area' (A_δ) can be calculated as following [3]-[5] :

$$A_\delta = \frac{Vol_\delta}{2\delta} \quad \text{or} \quad \mathrm{A}_\delta = \frac{\mathrm{Vol}_\delta - \mathrm{Vol}_{\delta-1}}{2} \qquad (3)$$

The 'Fractal Dimension' [or 'Fractal Signature' [3]] (F_D) can be calculated by the fractal area (A_δ) using the following formula:

$$A_\delta \approx \beta \delta^{2-F_D} \qquad (4)$$

where β is a constant. In other words the 'Fractal Dimension' (F_D) corresponds to the rate of decreasing of the 'Fractal Area' (A_δ) with increasing iteration δ. Subsequently, from (4) it can be easily derived [4] that the 'Fractal Dimension' (F_D) can be obtained as a slope of the function A_δ in log-log scale, according to the formula:

$$F_D \approx 2 - \frac{\log_2 A_{\delta_1} - \log_2 A_{\delta_2}}{\log_2 \delta_1 - \log_2 \delta_2} \qquad (5)$$

In the present application of the algorithm, we selected for convenience $\delta_1=1$ and $\delta_2=2,3,4\ldots$[3]-[5].

3. NUMERICAL RESULTS – TRAINING DATA

In this paper, the Modified Fractal Signature (MFS) method is applied in real field spaceborne SAR images which depict different types of terrain. The images were provided to us by an International Working Group on SAR techniques, named 'SET 163 Working and are related to 4 different geographic regions in the United States of America (USA), namely in the city of New York, the city of Washington D.C., the city of Las Vegas and the state of Colorado.

From the provided real SAR images mentioned above, twenty sub- images of the same size were extracted in order to construct the proposed terrain classifier. These twenty sub-images were organized in five groups, each one of them corresponding to the five different terrain types selected for this terrain classifier. The terrain types that are examined in this paper are the following: urban site, suburban site, rural site, mountain site and sea site. In other words, four sub-images per terrain type were selected. All twenty sub-images represent the so – called 'training data' of our proposed classifier.

The 'Fractal Area' curves (A_δ) for all twenty sub-images of terrain mentioned above were calculated, and the average 'Fractal Area' curve for each type of terrain (out of 5) was calculated. The corresponding 'multiresolution' curves for these five types of terrain are shown in Fig. 2, in log – log scale (all the logarithms mentioned in this paper have as base the number two and each curve is the average of four curves). Subsequently, through the use of (5), the corresponding 'Fractal Dimension' [or 'Fractal Signature' [3]] (F_D) curves were calculated, as shown in Fig. 3.

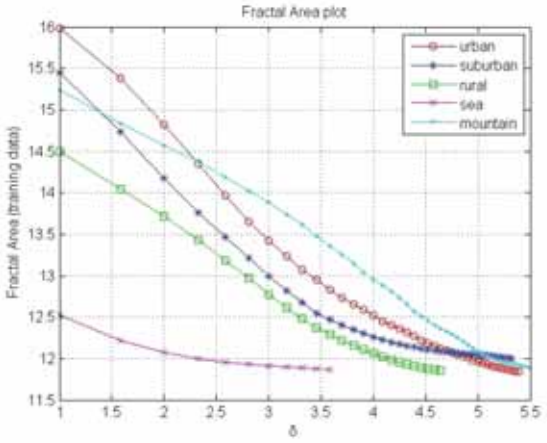

Fig. 2. 'Fractal Area' versus iteration δ for each type of terrain (training data) in a log-log scale.

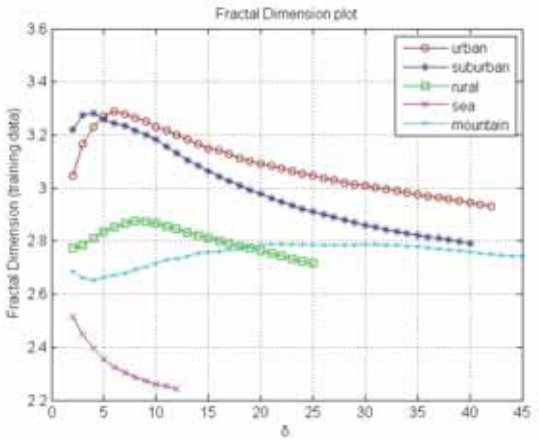

Fig. 3. 'Fractal Dimension' versus iteration δ for each type of terrain (training data) in a log-log scale.

It appears that the value of 'Fractal Dimension' [or 'Fractal Signature'] (F_D) contains more information about the fractal properties of each terrain type than the value of 'Fractal Area' (A_δ) [2] regarding the classification of different types of terrain in SAR images, and this is exactly the quantity which is used for image classification purposes [2] – [5].

The curves in Fig. 3 show a clearly different pattern (with respect to 'Fractal Dimension' values and form of the corresponding curve) for each of the five selected terrain types. These different patterns will provide to us the basis for the construction of our terrain classifier.

4. CLASSIFICATION RESULTS

For classification purposes, two sub-images of each terrain type [of the same size with the 'training data'] were obtained from the same SAR images. These ten sub – images construct two sets of 'testing data', namely each terrain type (urban, suburban, rural, mountain and sea site) is represented by two images, one in test data set 1 and another in test data set 2.

Each set of 'testing data' sub - images was compared to the 'training data' sub - images based on their 'distance *D*' in the corresponding 'Fractal Dimension' curves (F_D). Namely, for two sub - images *i* and *j* with 'Fractal Dimension' curves $F_{Di}(\delta)$ and $F_{Dj}(\delta)$ respectively, the 'distance *D*' between them was computed using the following formula [2]:

$$D(i,j) = \sum_{\delta} \left[\left(F_{Di}(\delta) - F_{Dj}(\delta) \right)^2 \cdot \log \left(\frac{\delta + \frac{1}{2}}{\delta - \frac{1}{2}} \right) \right] \quad (6)$$

where δ represents the number of iteration.

The above formula was applied to all possible pairs of sub images between the 'training data', Fig. 3, and the newly selected 'testing data'. The calculated 'distances *D*' for all possible pairs are shown in Table 1. A terrain type is identified by choosing the smallest 'distance *D*' from the corresponding 'training data'.

From Table 1 we conclude that the same terrain types between 'training' and 'test' data (for each test set) exhibit the smallest 'distance *D*' in 'Fractal Dimension' curves (F_D), thus providing correct classification results in the classification experiment performed here. In other words, minimum value of 'distance *D*' were found between the same terrain types among the training and test sub-images in the 'classification matrix' of Table 1.

Table 1. Classification Matrix

Training data	Test data 1				
	Urban	Sub-urban	Rural	Mountain	Sea
Urban	0,0254	0,0623	0,3765	1,0909	2,2352
Sub-urban	0,0316	0,0075	0,4034	1,2081	2,2353
Rural	0,4674	0,6774	0,0334	0,1092	0,501
Mountain	0,8321	1,1013	0,1915	0,0221	0,4432
Sea	1,8113	2,2272	0,8342	0,2046	0,0291
Training data	Test data 2				
	Urban	Sub-urban	Rural	Mountain	Sea
Urban	0,0077	0,0273	0,6846	1,1483	2,8118
Sub-urban	0,1038	0,0449	0,718	1,2535	2,839
Rural	0,4227	0,3634	0,0378	0,1194	0,8183
Mountain	0,793	0,6953	0,0531	0,0263	0,6564
Sea	1,7218	1,6739	0,4451	0,1818	0,0004

5. CONCLUSION

In this paper a novel approach for the classification of different terrain types which appear in SAR radar images is described. This classification scheme is based on the calculation of 'Fractal Dimension' 'multi – resolution' curves (F_D) for corresponding sub – images, and comparison of 'training' and 'testing' data sets through calculation of the corresponding 'distance *D*' between them. Correct classification results were obtained for the classification experiment performed in this paper, based on real – life spaceborne SAR radar images.

As a future research in this area, more terrain data based on SAR radar images could be obtained for both 'training' and 'test' datasets, in order to build a more robust and more reliable terrain type classifier.

6. ACKNOWLEDGMENTS

The authors (AM, PF) would like to acknowledge SET 163 Working Group, and its Chairman Dr. Luc Vignaud (ONERA, France) in particular, for providing to us the real field Synthetic Aperture Radar (SAR) images. The SAR images were provided to SET 163 Working Group by the 'German Airospace Center, DLR' (spaceborne images). To the above institutes and involved scientists we express our sincere.

Furthermore, the authors would like to express their sincere thanks to Prof. N. Ampilova and Prof. I. Soloviev, Faculty of Mathematics and Mechanics, St. Petersburg State University, Russia, for the very interesting discussions and helpful suggestions of them.

References

[1] D. Jaggard, A. Jaggard and P. Frangos, "*Fractal electrodynamics: surfaces and superlattices*", 'Frontiers in Electromagnetics', IEEE Press, Edited by D. Werner and R. Mittra, 2000.

[2] S. Peleg, J. Naor, R. Hartley, D. Avnir, "Multiple Resolution Texture Analysis and Classification", *IEEE Transactions on Pattern Analysis and Machine Intelligence*, Vol. PAMI-6, NO. 4, pp. 518-523, July 1984.

[3] Y. Tang, H. Ma, D. Xi, X. Mao, C. Suen, "Modified Fractal Signature (MFS): A New Approach to Document Analysis for Automatic Knowledge Acquisition", *IEEE Transactions on Knowledge and Data Engineering*, Vol. 9, No. 5, pp. 747-762, Sept. – Oct. 1997.

[4] N.B. Ampilova, E.Y. Gurevich, I.P. Soloviev, "Application of modified fractal signature and Regny spectrum methods to the analysis of biomedical preparation images", *CEMA'11 International Conference*, Sofia, Bulgaria, October 2011, pp. 96 - 100.

[5] A. Malamou, C. Pandis, P. Frangos, A. Karakasiliotis, P. Stefaneas and D. Kodokostas, "Application of the Modified Fractal Signature Method for Terrain Classification from Synthetic Aperture Radar Images", *Electronics and Electrical Engineering Journal*, Vol. 20, No. 6, pp. 747-762, June 2014.

THE RADIATION PROBLEM FROM A VERTICAL SHORT DIPOLE ANTENNA ABOVE FLAT AND LOSSY GROUND: NOVEL FORMULATION IN THE SPECTRAL DOMAIN WITH NUMERICAL SOLUTION AND CLOSED – FORM ANALYTICAL SOLUTION IN THE HIGH FREQUENCY REGIME

S. Bourgiotis[1], K. Ioannidi[1], Ch. Christakis[1], S.Sautbekov[2] and P. Frangos[1]

[1]School of Electrical and Computer Engineering,
National Technical University of Athens,
9, Iroon Polytechniou Str., 157 73 Zografou, Athens, Greece
Tel. +30 210 772 3694, Fax. +30 210 772 2281, E-mail: pfrangos@central.ntua.gr

[2]Eurasian National University, 5, Munaitpassov Str., Astana, Kazakhstan, E-mail: sautbek@mail.ru

Abstract

In this paper we consider the problem of radiation from a vertical short (Hertzian) dipole above flat lossy ground, which represents the well–known in the literature 'Sommerfeld radiation problem'. The problem is formulated in a novel spectral domain approach, and by inverse three-dimensional Fourier transformation the expressions for the received electric and magnetic (EM) field in the physical space are derived as one–dimensional integrals over the radial component of wavevector, in cylindrical coordinates. This formulation appears to have inherent advantages over the classical formulation by Sommerfeld, performed in the spatial domain, since it avoids the use of the so – called Hertzian vector and its subsequent differentiation for the calculation of the received EM field. It also gives new insights regarding the propagation mechanism. Subsequent use of the Stationary Phase Method (SPM) in the high frequency regime yields closed–form analytical solutions for the received EM field vectors, which coincide with the corresponding reflected EM field originating from the image point. In this way, we conclude that the so–called in the literature 'space wave' (line of sight plus reflected EM field) represents the total solution of the Sommerfeld problem in the high frequency regime, in which case the surface wave can be ignored. Furthermore, numerical results in the high frequency regime are presented in this paper, in comparison with corresponding numerical results based on Norton's solution of the problem (space and surface waves). Finally, numerical results based on the numerical integration of the spectral integral are also presented for comparison purposes. These results essentially provide a means of estimating the frequency limits of applicability of the SPM method for the problem in question. Subsequent suggestions on the preferred method (SPM vs Numerical) for calculating received signal level for various frequency ranges are made.

1. INTRODUCTION

The so-called 'Sommerfeld radiation problem' is a well – known problem in the area of propagation of electromagnetic (EM) waves above flat lossy ground for obvious applications in the area of wireless telecommunications [1-5]. The classical Sommerfeld solution to this problem is provided in the physical space by using the so- called 'Hertz potentials' and it does not end – up with closed form analytical solutions. K. A. Norton [6] concentrated in subsequent years more in the engineering application of the above problem with obvious application to wireless telecommunications, and provided approximate solutions to the above problem, which are represented by rather long algebraic expressions for engineering use, in which the so – called 'attenuation coefficient' for the propagating surface wave plays an important role.

In this paper the authors take advantage of previous research work of them for the EM radiation problem in free space [7] by using the spectral domain approach. Furthermore, in Ref. [8] the authors provided the fundamental formulation for the problem considered here, that is the solution in spectral domain for the radiation from a dipole moment at a specific angular frequency (ω) in isotropic media with a flat infinite interface. At that paper, the authors end – up with integral representations for the received electric and magnetic fields above or below the interface [Line of Sight (LOS) plus reflected field – transmitted fields, respectively], where the integration takes place over the radial spectral coordinate k_ρ. Then, in the present paper the authors concentrate to the solution of the classical 'Sommerfeld radiation problem' described above, where the radiation of a vertical dipole moment at angular frequency ω takes place above flat lossy ground [this is equivalent to the radiation of a vertical small

(Hertzian) dipole above flat lossy ground]. The proposed spectral – domain approach and particularly the derived integral representations for the EM field is not just a more effective means of reaching the same results compared to the classical spatial domain Sommerfeld's method. It also helps deducing new inferences regarding the propagation mechanism, as explained in Section 3.

Next, by using the Stationary Phase Method, (SPM method, [9]-[11]) integration over the radial spectral coordinate k_ρ is performed and the high frequency solution to the problem ['space wave', which represents the interference of the Line – of – Sight (LOS) and the wave scattered from the ground] is derived in a novel, to our knowledge, closed – form analytic solution, as exhibited in Section 4, below. In addition, numerical results which show both the 'space wave' mentioned above, as well as the Norton's 'surface wave' [6] are presented in Section 5. Finally, numerical results based on the numerical integration of the spectral integral are also presented for comparison purposes, as well as for obtaining an indication of the frequency limits of the SPM method, which is an inherently 'high frequency approximation' technique ([9]).

2. PROBLEM GEOMETRY

The geometry of the problem is given in Fig. 1. Here a Hertzian (small) dipole with dipole moment p directed to positive x – axis, at altitude x_0 above the infinite, flat and lossy ground, radiates time – harmonic electromagnetic (EM) waves at angular frequency $\omega=2\pi f$ [exp(-iωt) time dependence is assumed in this paper]. Here the relative complex permittivity of the ground is $\varepsilon_r'=\varepsilon'/\varepsilon_0= =\varepsilon_r+ix$, where $x=\sigma/\omega\varepsilon_0=18\times10^9\ \sigma/f$, σ being the ground conductivity, f the frequency of radiation and $\varepsilon_0=8.854\times10^{-12}$ F/m is the absolute permittivity in vacuum or air. Then the wavenumbers of propagation of EM waves in air and lossy ground, respectively, are given by the following equations:

$$k_{01}=\omega/c_1=\omega\sqrt{\varepsilon_1\mu_1}=\omega\sqrt{\varepsilon_0\mu_0} \tag{1}$$

$$k_{02}=\omega/c_2=\omega\sqrt{\varepsilon_2\mu_2}=k_{01}\sqrt{\varepsilon_r+ix} \tag{2}$$

The Maxwell equations for the time – harmonic EM fields considered above are given by:

$$\begin{cases}\mathrm{rot}\,\underline{E}-i\omega\mu_0\mu_r\underline{H}=0\\ \mathrm{rot}\,\underline{H}+i\omega\varepsilon_0\varepsilon_r\underline{\mathrm{H}}=\underline{\mathrm{j}}\end{cases} \tag{3}$$

where $\underline{\mathrm{j}}$ is current density (source of EM fields considered here).

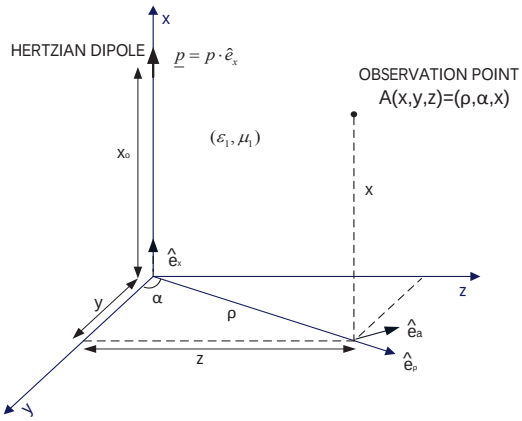

Fig. 1. Geometry of the problem

3. INTEGRAL FORMS FOR THE RECEIVED ELECTRIC AND MAGNETIC FIELDS IN THE SPECTRAL DOMAIN

Following [7]-[8], the EM field in physical space is derived from current density in spectral domain and Green's function, also in the spectral domain, through inverse three – dimensional (3D) Fourier transformation as following :

$$\underline{H}=-i\,\mathrm{F}^{-1}\left[\tilde{\psi}\cdot(\underline{k}\times\tilde{\underline{\mathrm{J}}})\right] \tag{4}$$

$$\underline{E}=-\frac{i}{\omega\varepsilon_r\varepsilon_0}\mathrm{F}^{-1}\left\{\tilde{\psi}\left[\varepsilon_r\mu_r k_0^2\tilde{\underline{\mathrm{J}}}-<\underline{k},\tilde{\underline{\mathrm{J}}}>\underline{k}\right]\right\} \tag{5}$$

where the symbol < > denotes the inner product and F^{-1} is the inverse 3D Fourier Transform (FT) operator and

$$\tilde{\psi}=\left(k_{01}^2-k^2\right)^{-1}=\left(k_{01}^2-k_\rho^2-k_x^2\right)^{-1} \tag{6}$$

is the 3D Green's function in spectral domain and cylindrical coordinates.

Application of the problem specifics (i.e. current density vector in spectral domain has only x – component, the wavevector $k=(k_\rho,k_\alpha=0,k_x)$ does not possess azimuthal α component, see Fig. 1) and the corresponding boundary value problem ([8], [12]) yields the following integral representations for the space wave (LOS field plus reflected field) above the ground level (x > 0)

$$\underline{H}(\underline{r})=\underline{H}^{LOS}-\frac{i\omega p\,\hat{e}_\alpha}{8\pi}\int_{-\infty}^{\infty}\frac{\varepsilon_{r2}\kappa_1-\varepsilon_{r1}\kappa_2}{\kappa_1(\varepsilon_{r2}\kappa_1+\varepsilon_{r1}\kappa_2)}k_\rho^2\cdot\mathrm{H}_0^{(1)}(k_\rho\rho)e^{i\kappa_1(x_0+x)}dk_\rho \tag{7}$$

$$\underline{E}(\underline{r}) = \underline{E}^{LOS}(\underline{r}) - \frac{ip}{8\pi\varepsilon_{r1}\varepsilon_0}\hat{e}_\rho \int_{-\infty}^{\infty} k_\rho^2 \frac{\varepsilon_{r2}\kappa_1 - \varepsilon_{r1}\kappa_2}{(\varepsilon_{r2}\kappa_1 + \varepsilon_{r1}\kappa_2)} e^{i\kappa_1(x+x_0)} \mathrm{H}_0^{(1)}(k_\rho\rho)dk_\rho +$$

$$+ \frac{ip}{8\pi\varepsilon_{r1}\varepsilon_0}\hat{e}_x \int_{-\infty}^{\infty} k_\rho^3 \frac{\varepsilon_{r2}\kappa_1 - \varepsilon_{r1}\kappa_2}{\kappa_1(\varepsilon_{r2}\kappa_1 + \varepsilon_{r1}\kappa_2)} e^{i\kappa_1(x+x_0)} \cdot \mathrm{H}_0^{(1)}(k_\rho\rho)dk_\rho \quad (8)$$

where

$$\kappa_1 = \sqrt{k_{01}^2 - k_\rho^2} \quad (9)$$

$$\kappa_2 = \sqrt{k_{02}^2 - k_\rho^2} \quad (10)$$

and $H_0^{(1)}$ is the Hankel function of first kind and zero order.

The line-of-sight (LOS) EM field of the Hertzian dipole in the far field is given in spherical coordinates by [9,13]:

$$H_\alpha^{LOS}(r,\theta) = \frac{\omega^2 p}{4\pi}\sqrt{\varepsilon_0\mu_0}\frac{\exp(ikr)}{r}\sin\theta = \frac{\omega k_{01} p}{4\pi}\frac{\exp(ikr)}{r}\sin\theta \quad (11)$$

$$\underline{E}^{LOS}(r,\theta) = \zeta H_\alpha^{LOS}\cos\theta\,\hat{e}_\rho - \zeta H_\alpha^{LOS}\sin\theta\,\hat{e}_x \quad (12)$$

Conversion to cylindrical coordinates is made by means of the following expressions (see Fig 1 above):

$$r \approx \rho + \frac{(x - x_0)^2}{2\rho} \quad (13)$$

$$\theta = \pi - \tan^{-1}\left[\frac{\rho}{(x_0 - x)}\right], \quad \text{for } x_0 > x \quad (14a)$$

$$\theta = \tan^{-1}\left[\frac{\rho}{(x - x_0)}\right], \quad \text{for } x > x_0 \quad (14b)$$

The physical interpretation of eqns. (7) and (8) is that the scattered EM field at the observation point consists of a complex summation of the EM waves scattered from the different points of the flat and lossy ground, each one with its own local reflection coefficient (here the term 'complex summation' means that both the amplitude and phase of these individual scattered waves must be taken into account).

Similar expressions are derived for the transmitted fields below the ground interface (x < 0):

$$\underline{\mathrm{H}}^{\mathrm{T}}(\underline{r}) = -\frac{i\omega p}{4\pi}\hat{e}_\alpha \int_{-\infty}^{\infty} k_\rho^2 \frac{\varepsilon_{r2}}{\varepsilon_{r2}\kappa_1 + \varepsilon_{r1}\kappa_2} e^{i(\kappa_1 x_0 - \kappa_2 x)} \cdot \mathrm{H}_0^{(1)}(k_\rho\rho)dk_\rho \quad (15)$$

$$\underline{\mathrm{E}}^{\mathrm{T}}(\underline{r}) = -\frac{ip}{4\pi\varepsilon_0}\int_{-\infty}^{\infty}(k_\rho\hat{e}_x - \kappa_2\hat{e}_\rho)\frac{k_\rho^2}{\varepsilon_{r2}\kappa_1 + \varepsilon_{r1}\kappa_2} \cdot e^{i(\kappa_1 x_0 - \kappa_2 x)}\mathrm{H}_0^{(1)}(k_\rho\rho)dk_\rho \quad (16)$$

4. ANALYTICAL CLOSED – FORM EXPRESSIONS FOR THE SCATTERED EM FIELDS OBTAINED THROUGH THE APPLICATION OF THE STATIONARY PHASE METHOD (SPM)

Following [8], [12], [14], [16] and [17] and by using the Stationary Phase Method (SPM) [9]), we finally end – up with the following closed - form expressions for the space wave (in the higher – half space, x>0), as given below:

$$\underline{E}_{x>0} = \underline{E}^{LOS} - \frac{ip}{8\pi\varepsilon_o\varepsilon_{r1}}\mathrm{I}_1\cdot\hat{e}_\rho - \frac{ip}{8\pi\varepsilon_o\varepsilon_{r1}}\mathrm{I}_2\cdot\hat{e}_x \quad (17)$$

$$\underline{\mathrm{H}}_{x>0} = \underline{\mathrm{H}}^{LOS} - \frac{i\omega p}{8\pi}\mathrm{I}_3\cdot\hat{e}_\alpha \quad (18)$$

where

$$I_1 = \frac{i2}{k_{01}\rho^{1/2}}\frac{1}{(x+x_0)^{1/2}}\kappa_{1s}^{3/2}k_{\rho s}^{3/2}\cdot \cdot\frac{\varepsilon_2\kappa_{1s} - \varepsilon_1\kappa_{2s}}{\varepsilon_2\kappa_{1s} + \varepsilon_1\kappa_{2s}}e^{ik_{\rho s}\rho}e^{i\kappa_{1s}(x+x_0)} \quad (19)$$

$$I_2 = \frac{i2}{k_{01}\rho^{1/2}}\frac{1}{(x+x_0)^{1/2}}\kappa_{1s}^{1/2}k_{\rho s}^{5/2}\cdot \cdot\frac{\varepsilon_2\kappa_{1s} - \varepsilon_1\kappa_{2s}}{\varepsilon_2\kappa_{1s} + \varepsilon_1\kappa_{2s}}e^{ik_{\rho s}\rho}e^{i\kappa_{1s}(x+x_0)} \quad (20)$$

$$I_3 = \frac{i2}{k_{01}\rho^{1/2}}\frac{1}{(x+x_0)^{1/2}}\kappa_{1s}^{1/2}k_{\rho s}^{3/2}\cdot \cdot\frac{\varepsilon_2\kappa_{1s} - \varepsilon_1\kappa_{2s}}{\varepsilon_2\kappa_{1s} + \varepsilon_1\kappa_{2s}}e^{ik_{\rho s}\rho}e^{i\kappa_{1s}(x+x_0)} \quad (21)$$

and

$$k_{\rho s} = \frac{k_{01}\rho}{\left[(x+x_0)^2 + \rho^2\right]^{1/2}} = \\ = k_{01}\frac{1}{\left[1 + \left(\frac{x+x_0}{\rho}\right)^2\right]^{1/2}} = k_{01}\cos\phi \quad (22)$$

is the (unique) stationary point [9, 12, 16, 17]. Moreover the following expressions hold:

$$\kappa_{1s} = \sqrt{k_{01}^2 - k_{\rho s}^2} = k_{01}\sin\phi \quad (23)$$

$$\kappa_{2s} = \sqrt{k_{02}^2 - k_{\rho s}^2} \tag{24}$$

Note that in the above expressions the angle φ is the well – known in the literature 'grazing angle' [13], as shown in Fig. 2 below.

Then our final closed-form analytical solution for the reflected fields can also be written in the compact form of the following expressions:

$$\underline{E}_{x>0}^{sc} = \frac{p}{4\pi\varepsilon_o\varepsilon_{r1}} \frac{1}{\rho^{1/2}} \frac{1}{(x+x_0)^{1/2}} \frac{\kappa_{1s}^{1/2} k_{\rho s}^{3/2}}{k_{01}} \cdot \frac{\varepsilon_2\kappa_{1s} - \varepsilon_1\kappa_{2s}}{\varepsilon_2\kappa_{1s} + \varepsilon_1\kappa_{2s}} e^{ik_{\rho s}\rho} e^{i\kappa_{1s}(x+x_0)} \cdot (\kappa_{1s}\hat{e}_\rho + k_{\rho s}\hat{e}_x) =$$

$$= \frac{pk_{01}}{4\pi\varepsilon_o\varepsilon_{r1}} \frac{(\sin\phi)^{1/2}(\cos\phi)^{3/2}}{\rho^{1/2}(x+x_0)^{1/2}} \cdot \frac{\varepsilon_2\kappa_{1s} - \varepsilon_1\kappa_{2s}}{\varepsilon_2\kappa_{1s} + \varepsilon_1\kappa_{2s}} e^{ik_{\rho s}\rho} e^{i\kappa_{1s}(x+x_0)} \cdot (\kappa_{1s}\hat{e}_\rho + k_{\rho s}\hat{e}_x) =$$

$$= \frac{pk_{01}\cos\phi}{4\pi\varepsilon_o\varepsilon_{r1}(\mathrm{A'A})} \cdot \frac{\varepsilon_2\kappa_{1s} - \varepsilon_1\kappa_{2s}}{\varepsilon_2\kappa_{1s} + \varepsilon_1\kappa_{2s}} e^{ik_{\rho s}\rho} e^{i\kappa_{1s}(x+x_0)} \cdot (\kappa_{1s}\hat{e}_\rho + k_{\rho s}\hat{e}_x) \tag{25}$$

$$\underline{H}_{x>0}^{sc} = \frac{\omega p}{4\pi} \frac{1}{\rho^{1/2}} \frac{1}{(x+x_0)^{1/2}} \frac{\kappa_{1s}^{1/2} k_{\rho s}^{3/2}}{k_{01}} \cdot \frac{\varepsilon_2\kappa_{1s} - \varepsilon_1\kappa_{2s}}{\varepsilon_2\kappa_{1s} + \varepsilon_1\kappa_{2s}} e^{ik_{\rho s}\rho} e^{i\kappa_{1s}(x+x_0)} \hat{e}_\alpha =$$

$$= \frac{\omega k_{01} p}{4\pi} \frac{(\sin\phi)^{1/2}(\cos\phi)^{3/2}}{\rho^{1/2}(x+x_0)^{1/2}} \frac{\varepsilon_2\kappa_{1s} - \varepsilon_1\kappa_{2s}}{\varepsilon_2\kappa_{1s} + \varepsilon_1\kappa_{2s}} e^{ik_{\rho s}\rho} e^{i\kappa_{1s}(x+x_0)} \hat{e}_\alpha =$$

$$= \frac{\omega k_{01} p \cdot \cos\phi}{4\pi(\mathrm{A'A})} \frac{\varepsilon_2\kappa_{1s} - \varepsilon_1\kappa_{2s}}{\varepsilon_2\kappa_{1s} + \varepsilon_1\kappa_{2s}} e^{ik_{\rho s}\rho} e^{i\kappa_{1s}(x+x_0)} \hat{e}_\alpha \tag{26}$$

where (A'A) is the distance between the image point and the observation point (Fig. 2).

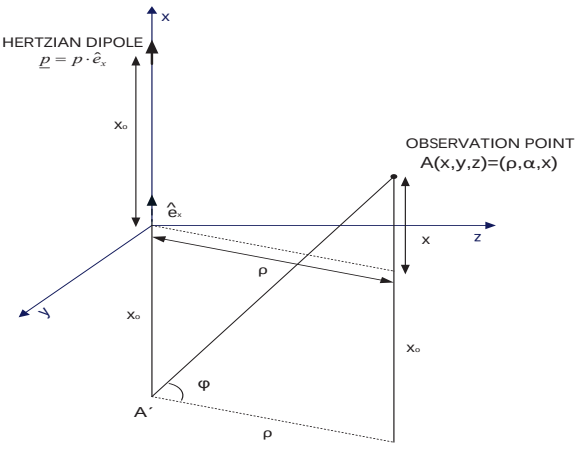

Fig. 2. Geometry of the radiation where the image A' of the radiating Hertzian dipole is also shown.

5. NUMERICAL RESULTS – COMPARISON OF SPM WITH (i) NORTON'S APPROXIMATE SOLUTION (ii) NUMERICAL INTEGRATION TECHNIQUES

In this Section two types of indicative numerical results are provided for comparison purposes. Firstly, the magnitudes for the following fields:

- Scattered Electric field, eq. (25) above,
- Line – of – Sight (LOS) field,
- 'Space Wave', i.e. the complex summation of the previously mentioned fields,

are presented for various distance points (ρ) between the transmitting dipole and the receiving point and compared with Norton's results [6, 13]. Two demonstration frequency sets were selected for the radiating dipole, namely f=80 MHz (Fig. 3) and f=30 MHz (Fig. 4).

Fig. 3: Electric fields a oint as a function of horizontal distance (ρ) for frequency f=80 MHz. Here the various components of received electric field are shown as following: Line – of – Sight (LOS) field (circle), field scattered from ground (asterisk), 'space wave' (square) and 'surface wave' (diamond).

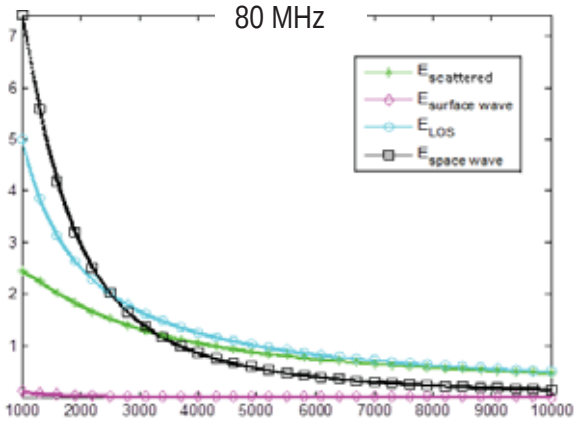

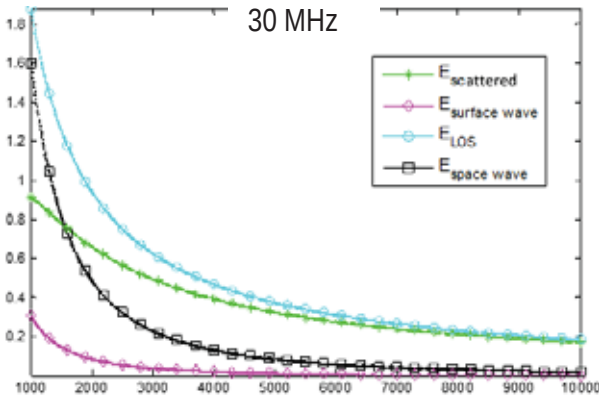

Fig. 4. Same as Figure 3, except that here frequency f = 30 MHz.

The rest of the problem parameters are the following: height of transmitting dipole x_0=60m, height of observation point (receiver position) x=15m, current of the radiating Hertzian dipole I=1A, length of the Hertzian dipole 2h=0.1m (much smaller than the wavelength λ=c/f in both cases), relative dielectric constant of ground ε_r=20 and ground conductivity σ=0.01 S/m. Finally, note that the relation between current I and dipole moment p is given by: I(2h) = iωp, where ω=2πf and i is the unit imaginary number.

Comparison of numerical results derived from our formulation, and the Norton's results [6,13] shows very good agreement, as it can be seen in Figs. 3 and 4. The surface wave represented in Figs. 3 and 4 is the so-called 'Norton surface wave' [6, 13]. Note that at the higher frequency of 80 MHz (Fig. 3) the surface wave, according to Norton's formulation [6, 13] is rather negligible, as compared to the 'space wave', while it becomes rather more important at the lower frequency of 30 MHz (Fig. 4). Our proposed SPM method of Sections 4 and 5 (which is inherently a 'high frequency method') ignores this surface wave contribution in the high frequency regime.

The second type of numerical data, shown in this paper, compare the results obtained using the analytical, closed – form formulas of the SPM method, described in section 4 above, i.e. eqns. (17) through (26), with those taken by numerically evaluating the corresponding integral expressions of eqns. (7) through (14), given in section 3. Figure 5, below, provides indicative results for the scattered electric field of, eq. (8) (here the LOS field is not shown).

In order to numerically estimate the integral of eq.(8), the adaptive Simpson's algorithm was used ([18]). The error tolerance was set to 10^{-6}. Moreover to mitigate the 'small scale' oscillating behaviour of the resulting graphs, which is an outcome of the fact that the integrated expression consists of complex numbers of fast – varying phases, a typical three (3) sample smoothing (averaging) was applied, where appropriate.

Careful examination of eq. (8) reveals the fact that there exists a singular point at $\kappa_1=0$, that is at $k_\rho=k_{01}$ (see eq.(9) above) and hence it must be excluded by a sufficient range around k_{01}. Our preliminary tests, showed that this range needs to be no less than10^{-4} times the limiting value of k_{01} (according to eq. (22), $k_{\rho s} < k_{01}$). However, this indicates that a segment around the stationary point will be excluded from the calculation (see respective labels in the diagrams of Fig. 5, below). The inferences for this are described below.

Examining the curves of Fig. 5 below, it is evident that for frequencies of about 100 KHz and above the results taken under the numerical integration approach underestimate the received signal level compared with the SPM method. The reason for this behaviour is related with the properties of the SPM method, which indicate that for large arguments (in our case frequencies) the integral expression can be asymptotically approximated by taking into consideration just the contributions of the areas around the stationary points and their neighbourhoods [9]. However, as mentioned above, when numerically evaluating the integral expression of eq. (8) a sufficiently large range around k_{01} had to be excluded for the algorithm to converge. In most cases this range overlaps with the stationary point, essentially meaning that a significant contributing part is missed.

On the contrary, according to the last curve of Fig. 5 (f = 10 KHz), it is now the SPM method that seems to underestimate the EM field values (we also reach the same findings for f < 30 KHz). Indeed, for such low frequencies, the large argument approximation of the SPM method cannot be invoked, in other words, eqns. (19) through (26) do not hold. It is still necessary to exclude a range around $k_\rho=k_{01,}$ for the numerical integration algorithm to converge, however this time this range is not a major contributor to the overall outcome.

In conclusion, our research group suggests the following 'safe' recommendations (see Fig. 5):

- For frequencies in the MF (300 KHz – 3 MHz, [13]) frequency range and higher, the SPM method significantly provides more accurate results for the received signal level and hence should be the selection of choice for prediction purposes.
- For the VLF frequency range (<30 KHz, [13]) the SPM fails and the estimation ought to be based on numerical integration techniques.
- Finally, in the LF range (30 – 300 KHz [13]), the results, given by the two methods, seem comparable and our research group proposes that a closer examination and potential fine – tunning of the numerical integration algorithm is necessary, before reaching 'safe' inferences (see Section 6 below)

Further clarifications about the above presented numerical results and the related inferences that can be made based on them will be provided during the Conference.

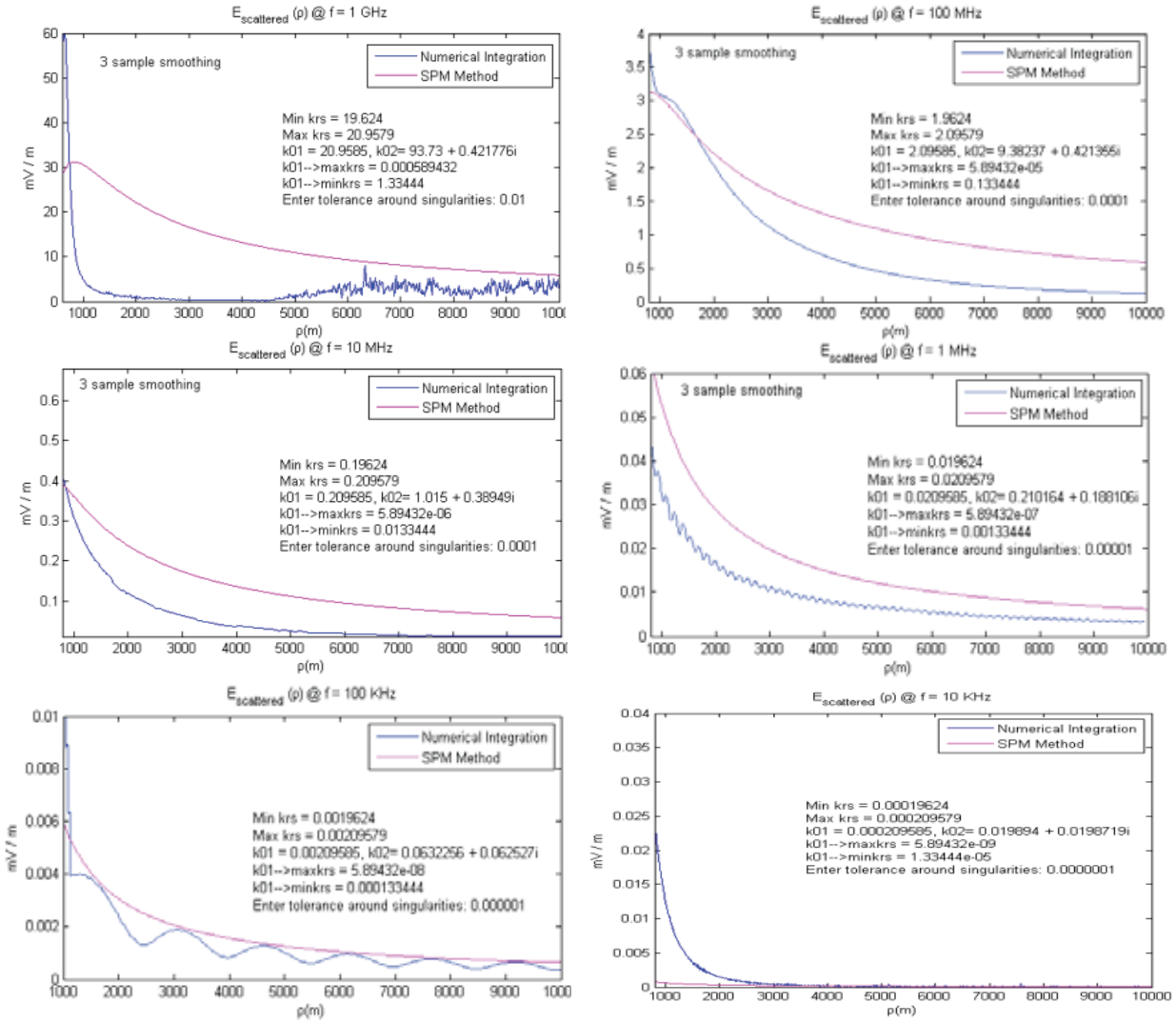

Fig. 5. Value of the scattered electric field as a function of horizontal distance ρ between transmitter and receiver, calculated by (i) the SPM method and (ii) numerical integration techniques.

6. CONCLUSIONS – FUTURE RESEARCH

In this paper we formulated the radiation problem from a vertical short (Hertzian) dipole above flat and lossy ground in the spectral domain, which resulted in an easy to manipulate integral expression for the received EM field above or below the ground. As also explained above, this formulation appears to have inherent advantages over the classical formulation by Sommerfeld [5], since it avoids the use of the so – called Hertz potential and its subsequent differentiation for the calculation of the received EM field. Subsequently, by applying the Stationary Phase Method (SPM) in the high frequency regime, the classical solution for the 'space wave' was re-derived in a new fashion, thus showing that this is the dominant solution in this high frequency regime. Moreover, we explained why the SPM method even appears to provide more accurate results than many common numerical integration techniques for most frequencies of interest in the area of wireless telecommunications and hence can be the basis for an efficient simulation tool for radio signal propagation.

Corresponding research in the near future by our research group will concentrate to the calculation of the received EM field below the ground at the high frequency regime (by using again the SPM method). Furthermore, we intend to calculate the received EM field, above or below the ground, for any frequency of the radiating dipole, in an exact and analytical manner [19]. In this context, the behavior of surface waves will become evident through the use of the residue theorem, when applied to eqns. (7) and (8) above, in a way similar to Ref. [5].

Moreover, we also intend to investigate the formulation of the same radiation problem in spectral domain, but now in the case of a horizontal radiating Hertzian dipole above flat and lossy ground. In ad-

dition, further investigations will be performed in the case of rough (and not flat) ground and in the case of curvature of the earth's surface for large distance communication applications. Finally, in the near future our research group will focus on the design of a software product for accurate prediction of pass loss in different types of environment, like urban, suburban and rural environments. The above software tool will be based on the exact electromagnetic (EM) method proposed in this paper, and therefore it is expected that it will exhibit important advantages over previously developed corresponding software tools. Some of these advantages might include accuracy, speed, efficiency and low complexity, since the various calculations will be based on closed form analytical expressions, instead of resource starving and time consuming numerical methods. We also intend to fine tune the numerical method presented in this paper (e.g. numerical experiment with convergence tolerances), as well as to test alternative algorithms and techniques (e.g. the 'adaptive Lobatto' algorithm will be examined) and to use the most appropriate as the back - up method in situations where the SPM is not sufficient (e.g. at low frequency regime). In this framework, comparisons with existing commercial software tools will also be performed [21].

References

[1] A. N. Sommerfeld, 'Propagation of Waves in Wireless Telegraphy', Ann. Phys., 28, pp. 665 – 736, March 1909; and 81, pp. 1135 – 1153, December 1926.

[2] J. R. Wait, 'The Ancient and Modern History of EM Ground Wave Propagation', IEEE Antennas and Propagation Magazine, Vol. 40, No. 5, pp. 7-24, October 1998.

[3] R. J. King, 'EM Wave Propagation over a Constant Impedance Plane', Radio Science, Vol. 4, pp. 225-268, 1969.

[4] J. Zenneck, 'Propagation of Plane EM Waves along a Plane Conducting Surface', Ann. Phys. (Leipzig), 23, pp. 846-866, 1907.

[5] T. K. Sarkar et. al., 'Electromagnetic Macro Modeling of Propagation in Mobile Wireless Communication: Theory and Experiment', IEEE Antennas and Propagation Magazine, Vol. 54, No. 6, pp. 17 – 43, Dec. 2012.

[6] K.A.Norton, 'The Propagation of Radio Waves Over the Surface of the Earth', Proceedings of the IRE, 24, pp. 1367 – 1387, 1936; and 25, pp. 1203 – 1236, 1937.

[7] S. Sautbekov, 'The Generalized Solutions of a System of Maxwell's Equations for the Uniaxial Anisotropic Media', Chapter 1 in book Electromagnetic Waves Propagation in Complex Matter, edited by A. A. Kishk, Croatia, pp. 3 – 24, June 2011.

[8] S. Sautbekov, R. Kasimkhanova and P. Frangos, 'Modified solution of Sommerfeld's problem', Communications, Electromagnetics and Medical Applications (CEMA'10) International Conference, National Technical University of Athens (NTUA), Athens, Greece, 7-9/10/ 2010, pp. 5 – 8.

[9] C. A. Balanis, 'Antenna Theory : Analysis and Design, Appendix VIII : Method of Stationary Phase', pp. 922 – 927, J. Wiley and Sons Inc., New York, 1997.

[10] H. Moschovitis, 'Asymptotic methods and High Frequency Techniques for the Calculation of Electromagnetic Scattering by Using the Modified Stationary Phase Method', Doctoral Dissertation, in Greek, National Technical University of Athens (NTUA), Athens, Greece, December 2010.

[11] Ch. Moschovitis, K. Karakatselos, E. Papkelis, H. Anastassiu, I. Ouranos, A. Tzoulis and P. Frangos, 'High Frequency Analytical Model for Scattering of Electromagnetic Waves from a Perfect Electric Conductor Plate using an Enhanced Stationary Phase Method Approximation', IEEE Trans. Antennas and Propagation, Vol. 58, No. 1, pp. 233 – 238, January 2010.

[12] http://arxiv.org/abs/1401.1720

[13] J. Fikioris, 'Introduction to Antenna Theory and Propagation of Electromagnetic Waves', Book in Greek, National Technical University of Athens (NTUA), Athens, Greece, 1982.

[14] S. Sautbekov, P. Frangos, Ch. Christakis and K. Ioannidi, 'A closed – form analytical solution to the radiation problem from a short dipole antenna above flat ground using spectral domain approach', ICEAA Conference, Torino, Italy, September 2013.

[15] Ch. G. Moschovitis, H. T. Anastassiu, and P. V. Frangos, 'Scattering of electromagnetic waves from a rectangular plate using an Extended Station Phase Method based on Fresnel functions (SPM-F)', Progress In Electromagnetics Research (PIER), Vol. PIER 107, pp. 63-99, August 2010.

[16] Ch. Christakis, K. Ioannidi, S.Sautbekov, P. Frangos and S.K. Atanov, 'The Radiation Problem from a Vertical Short Dipole Antenna above Flat and Lossy Ground: Novel Formulation in the Spectral Domain with Closed – Form Analytical Solution in the High Frequency Regime', accepted for publication to 'Electronics and Electrical Engineering Journal', April 2014

[17] K. Ioannidi, Ch. Christakis, S. Sautbekov, P. Frangos and S.K. Atanov, 'The radiation problem from a vertical Hertzian dipole antenna above flat and lossy ground: novel formulation in the spectral domain with closed – form analytical solution in the high frequency regime', accepted for publication by 'International Journal Antennas and Propagation' (IJAP), Hindawi Ed. Co., Special Issue 'Propagation of electromagnetic (EM) waves over terrain' (PEWT), July 2014.

[18] George B. Thomas , Maurice D. Weir, Joel R. Hass, Frank Giordano, 'Thomas' Calculus', Pearson, 12th Edition, 2010.

[19]G. Arfken, 'Mathematical Methods for Physists', 3rd Edition, pp. 400 – 414, Academic Press Inc., Orlando, Florida, USA, 1985.

[20] M. Abramowitz and I.A. Stegun, 'Handbook of Mathematical Functions', Dover Publ. Inc., N.Y., 10th Ed., 1972.

[21] A. Hrovat et. al., 'An Open – Source Radio Coverage Prediction Tool', ICCOM'10 Proceedings of the 14th WSEAS International Conference on Communications, pp. 135-140, 2010.

FSO AVAILABILITY DEPENDING ON THE METEOROLOGICAL CONDITIONS

Yordan Kovachev, Tsvetan Mitsev

Faculty of Telecommunications, Technical University of Sofia,
8 Kliment Ohridski Blvd., 1000 Sofia, Bulgaria,
E-mail: mitzev@tu-sofia.bg

Abstract

This paper studies the availability of FSO systems. For the purpose meteorological data from different regions is used to obtain statistical model of the atmospheric visibility S_M. Statistical method, that utilizes the cumulative distribution function (CDF) of S_M and the mechanical vibrations of the transmitting antenna ($\Delta\rho$) for calculating FSO availability, is proposed. Based on the derived analytical expressions numerical results are obtained and FSO availability is analyzed.

1. INTRODUCTION

The commercialization of FSO systems in the past years imposes the need for improving their channel capacity and reliable work (availability). This poses the question for selecting the optimal parameters of the free space laser communication system [1].

One of the main factors for unreliable work of FSO is the atmospheric visibility [3]. Unbearable drawbacks in S_M can cause system outage.

Another cause for the decrease of FSO reliable work is the random mechanical vibrations of the transmitting aperture [2], which result in linear shifts of the laser beam axis from its original direction. These shifts significantly decrease the quality of the transmitted data and FSO availability.

In this paper the FSO availability under different distributions of S_M is studied. The availability of FSO systems working with fixed divergence angle, θ_t, and working with variable (optimal) beam divergence angle, $\theta_{t,opt}$, (FSO employing a device for controlling θ_t) is made. Also a graphical representation of the outage probability, due to unbearable aperture misalignment, is shown.

2. THEORY

2.1. Statistical model of the atmospheric visibility

A real yearly measurements of the atmospheric visibility [3] have been used for creating this generalized version of the statistical model of atmospheric visibility. The steps for generalization of the measured data are:

- Calculating the arithmetic mean value, $\bar{x}$, of each $P(S_M \geq S_{M,min})$
- Calculate the standard deviation σ for the given statistical data
- For each $S_M \geq S_{M,min}$ column we create an interval $[\bar{x} - \sigma;\ \bar{x} + \sigma]$
- Plot the results as a graphic and approximate the resulting curves using the simple trend line tool of Excel software

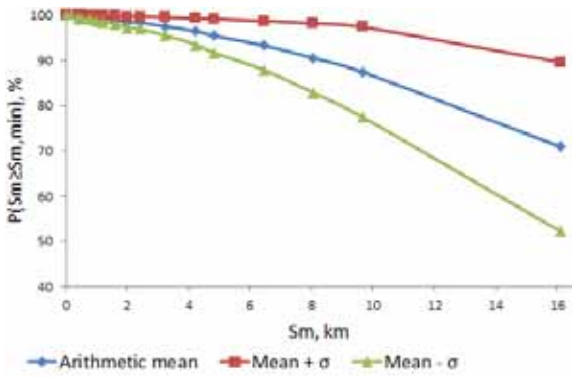

Fig. 1. Generalized model of the atmospheric visibility

The trend lines that approximate the three models of $P(S_M \geq S_{M,min})$ are:

- worst case "Mean - σ":

$$P(S_M \geq S_{M,min}) = \square x^{\square} - \square x^{\square} - \square x + \square \quad (1)$$

- arithmetic mean:

$$P(S_M \geq S_{M,min}) = \square x^{\square} - \square x^{\square} - \square x^{\square} - \square x + \square \quad (2)$$

- best case "Mean + σ":

$$P(S_M \geq S_{M,min}) = -(\ldots)x^{\square} + (\ldots)x + \\ + (\ldots) \quad (3)$$

For complete statistical model, the cumulative distribution function (CDF) and the probability density function (pdf) of S_M are needed. By definition CDF is equal to the probability $P(S_M \leq S_{M,min})$, hence for each of the models in Fig.1:

$$CDF = P(S_M \leq S_{M,min}) = \\ = 1 - P(S_M \geq S_{M,min}) \quad (4)$$

Also

$$P(S_M \leq S_{M,min}) = \int_{\square}^{S_{M,min}} f(S_M)\,dS_M \quad (5)$$

Hence the probability density function $f(S_M)$ for each of the models (Arithmetic mean, Mean + σ and Mean – σ) is equal to

$$f(S_M) = \frac{dP(S_M \leq S_{M,min})}{dS_M} \quad (6)$$

As defined in probability theory the pdf is the probability for the random variable X falling within the infinitesimal interval [x,x+dx], and it is a derivative of CDF.

Having all the functions $P(S_M \geq S_{M,min})$, $CDF(S_M)$ and $f(S_M)$ defined, the statistical model for the atmospheric visibility is complete.

2.2. Statistical model of the mechanical vibrations of the transmitter

In order to define a statistical model for FSO availability, it is also needed to have the model of the mechanical vibrations of the transmitting aperture. Consider the case illustrated on Fig. 2

When the transmitting aperture (TA) is randomly shifted in any direction with a random angle γ, the receiving aperture (RA), with radius R_r is displaced from the axis (z) of the optical beam. This displacement Δρ is also random, because, when z=Z:

$$\Delta\rho = \gamma Z \quad (7)$$

Where γ represents the angular misalignments defined on Fig. 2.

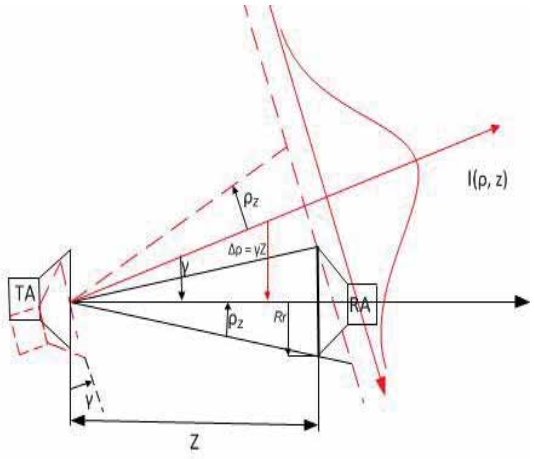

Fig. 2. Misalignment between transmitter and receiver

Having no statistical data in the literature, it is practical to assume a Gaussian distribution of the angular misalignments of the transmitting aperture [2], which considering (7) makes the linear displacements, Δρ, of RA in the plane z=Z, also normally distributed:

$$f(\Delta\rho) = \frac{1}{\sqrt{2\pi}\sigma_{\Delta\rho}} \exp\left(-\frac{\Delta\rho^2}{\sigma_{\Delta\rho}^2}\right) \quad (8)$$

In accordance to (7), it can be concluded that

$$\sigma_{\Delta\rho}^2 = Z^2\sigma_\gamma^2 \quad (9)$$

The cumulative density function is:

$$CDF = F(\rho_{max}) = \int_{-\infty}^{\rho_{max}} f(\Delta\rho)\,d\Delta\rho = \\ = \frac{1}{2}\left[1 + erf\left(1 + erf\frac{\Delta\rho}{\sqrt{2}\sigma_{\Delta\rho}}\right)\right] \quad (10)$$

2.3. Mathematical model of FSO system's availability

To have an FSO system working reliably, it is required that the power of the optical radiation, at the receiver's site (plane z=Z), is greater than or equal to the minimal acceptable power. So it is required that $I(\rho, z) \geq I_{min}$ [1].

When FSO is set according to particular channel parameters (S_M), that is beam divergence angle (θ_t), beam radius (ρ_z) and maximum acceptable misalignments ($\Delta\rho = \rho_{max}$) are calculated according to $S_{M,min}$, the system will be in outage if:

1) S_M falls below critical value $S_{M,min}$, for which system parameters are calculated,

or

2) Linear misalignments Δρ exceed the maximum acceptable value ρ_{max}, defined by $S_{M,min}$.

It is considered that S_M and Δρ are two independent random variables. Therefore $f(S_M)$ and $f(\Delta\rho)$ are also independent.

From condition 1) follows that the probability for reliable work is $P(S_M \geq S_{M,min})$, which was already defined in equations (1) through (3).

From condition 2) FSO will work reliably if mechanical vibrations are less than ρ_{max} in both directions X > 0 and X < 0

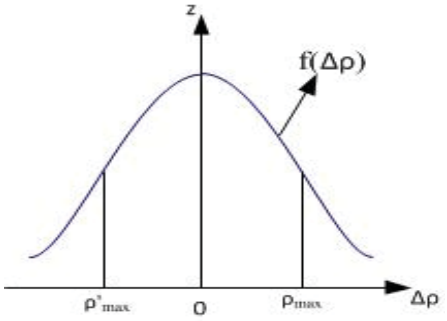

Fig. 3. Interval of maximum acceptable mechanical vibrations Δρ

This means reliable work of FSO, depending on Δρ is equal to:

$$\int_{\rho^*_{max}}^{\rho_{max}} f(\Delta\rho)\,d\Delta\rho = 2\int_{0}^{\rho_{max}} f(\Delta\rho)\,d\Delta\rho = 2F(\rho_{max}) - F(0) \quad (11)$$

Hence availability is equal to the joint distribution of the two random variables (Δρ and S_M):

$$Availability = P(S_M \geq S_{M,min}, \rho^*_{max} \leq \Delta\rho \leq \rho_{max}) \quad (12)$$

Which considering the assumption that $f(S_M)$ and $f(\Delta\rho)$ are independent and (11) is equal to

$$P(S_M \geq S_{M,min}, \rho^*_{max} \leq \Delta\rho \leq \rho_{max}) = \int_{S_{M,min}}^{\infty}\int_{\rho^*_{max}}^{\rho_{max}} f(S_M, \Delta\rho)\,dS_M\,d\Delta\rho = \int_{S_{M,min}}^{\infty} f(S_M)\,dS_M \int_{0}^{\rho_{max}} f(\Delta\rho)\,d\Delta\rho \quad (13)$$

Needed system parameters are calculated as proposed in [1]:

$$\rho_{max} = Z\theta_{max} \quad (14)$$

Where

$$\theta_{max} = \frac{1}{Z}\sqrt{\frac{\tau_{opt}\tau_{atm}\tau_r R_r \Phi_L}{\Phi_{bg}\,\Delta\lambda_F}}\,e = const \quad (15)$$

And

$$\rho_{max} = \frac{1}{\sqrt{2}}\rho_z\sqrt{2\ln\frac{\tau_{opt}\tau_{atm}\Phi_L}{\pi\rho_z^2 I_{bg}(1-e^{-1})}} \quad (16)$$

Hence, considering (11) through (13), FSO availability can be easily calculated with the following analytical expression:

$$Availability = 2F(\rho_{max}) - F(0) = 2P(S_M \geq S_{M,min}) \quad (17)$$

3. SIMULATION RESULTS

To make the calculations for FSO availability simulations, the following system parameters were used:

Channel capacity, C_l = 100 Mbps; quantum efficiency of the photodetector material, η (λ0) = 0,7; SNR = 11,2 (corresponds to BER = 10^{-8});central wavelength λ_0 = 0,85 and 1,55 μm; T = 300 K; A = 5; value of the resistor in the feedback of the preamplifier, R_{Fb} = 1 kΩ; $\tau_r = \tau_t$ = 0,85; R_r = 5,5 cm; transmission wavelength of the interface filter before the photodetector $\Delta\lambda_F$ = 10 nm; background radiation, $L_{\lambda,B}$ = 10^{-2} (corresponds to bright day); angular width of the receiving antenna θ_r = 5 mrad. System parameters are derived using [1] and formulas (14) through (16). Availability is calculated from (17).

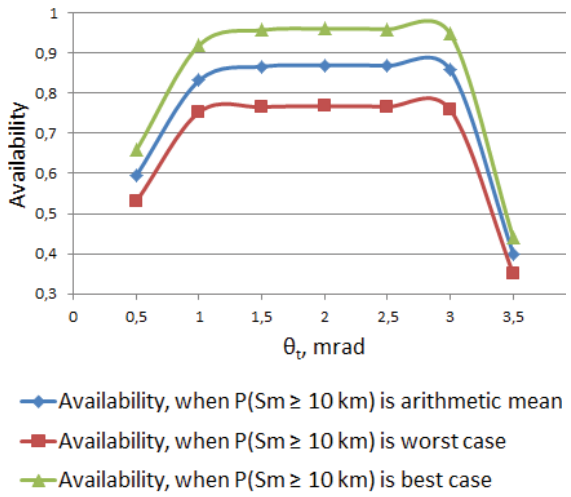

Fig. 4. FSO Availability depending on θ_t, z=2km, Φ_L=10 mW

Figures 4 through 6 represent the change of systems reliable work (FSO availability) when different parameters of FSO are varying.

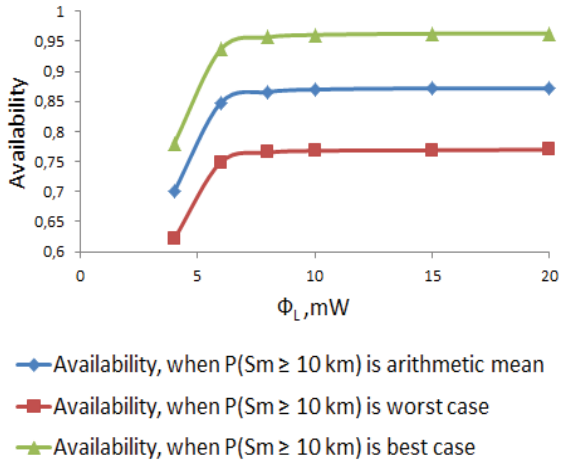

Fig. 5. FSO Availability depending on Φ_L, z=2km, θ_t = 2 mrad

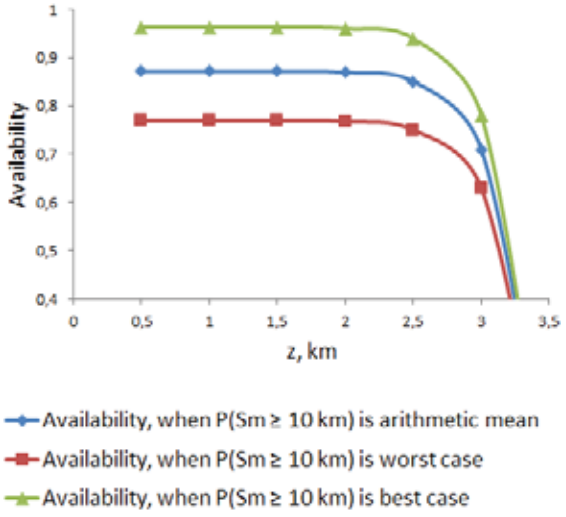

Fig. 6. FSO Availability depending on z, θ_t = 2 mrad, Φ_L=10 mW

Simulations are performed using all three models for P(S_M≥10 km) (Arithmetic mean, Best case- "Mean + σ" and Worst case – "Mean - σ"). For calculation of P(0 ≤ Δρ ≤ ρ_{max}) σ_Y = 0.5mrad, which corresponds to $\sigma_{\Delta\rho}$ = 1 m is used, see (9).

It is observed that in extreme cases, when high or very low values of θ_t (above 3 mrad or below 1 mrad) or low power lasers (bellow 10 mW) are used there is a significant drop in availability. That is because when using low beam divergence or low power lasers, the acceptable mechanical vibrations of the transmitter (ρ_{max}) are lower and can be often exceeded.

Following figures depict the comparison of two FSO systems. One is using fixed value of θ_t; the other one always employs optimal value of θ_t =*var*= $\theta_{t,\,opt}$, as derived from (15), thus allowing for absolute maximal values of Δρ. Simulations are done as follows: $\sigma_{\Delta\rho}$ =1 m, arithmetic mean for P(S_M ≥ $S_{M,min}$) is used. FSOs with λ_0 = 0,85 and 1,55 μm are compared.

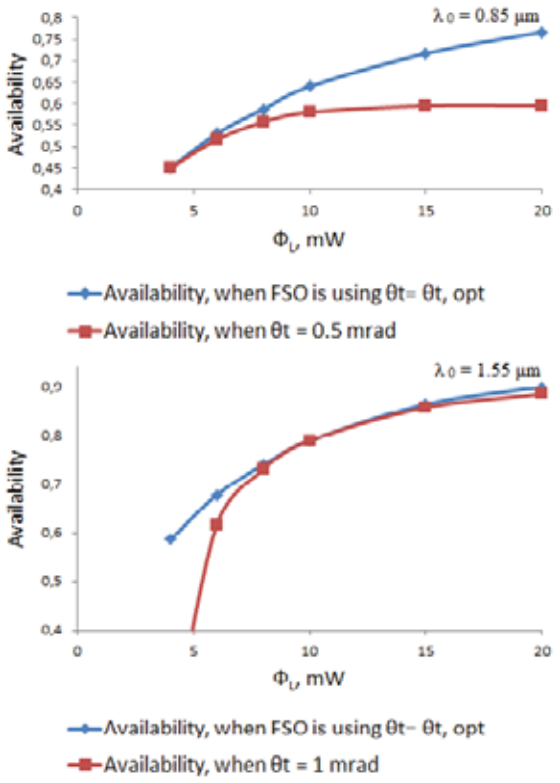

Fig. 7. Comparison between Availability of two FSO systems (Φ_L = var, z = 3km)

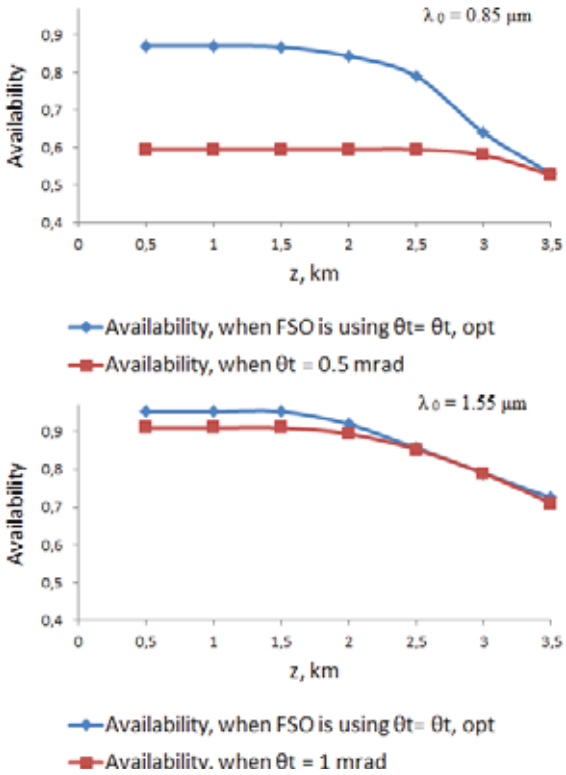

Fig. 8. Comparison between Availability of two FSO systems (z = var, Φ_L = 10 mW)

Calculations of Availability for $\lambda_0 = 0.85$ μm are made with $P(S_M \geq 10\text{km})$ and calculations for $\lambda_0 = 1.55$ μm are done for $P(S_M \geq 5\text{km})$. It is observed that using $\theta_{t,opt}$ increases the system availability. The results are better, when using smaller λ.

4. CONCLUSION

In this paper we've presented a generalised statistical model for atmospheric visibility. A mathematical model for evaluating the FSO systems availability was proposed. Using that model we've analysed the availability of FSOs with different system parameters. Also we've compared the availability of FSO system using fixed θ_t for different conditions and FSO using $\theta_t = \theta_{t,\,opt}$. Comparison is made for two wavelengths $\lambda_0 = 0.85$ and 1.55 μm. The results clearly show that using optimal values of the FSO parameters could result in significant increase of system's availability.

5. ACKNOWLEDGEMENT

The research described in this paper is supported by the Bulgarian National Science Fund under the contract Nb ДДВУ 02/74/2010

References

[1] Tsvetan Mitsev, Kalin Dimitrov, Hristo Ivanov, Nikolai Kolev, "Optimum divergence of laser radiation in FSO systems", CEMA, 2012.

[2] B. Pachedjieva, E. Ferdinandov, B. Bonev, Sl. Saparev, "Influence of the Transmitters Antenna Mechanical Vibrations on Bit-Error Rate in ground-to-ground Free-Space Laser Communication Systems"

[3] Isaak Kim, Eric Korevaar, "Availability of free-space optics (FSO) and hybrid FSO/RF systems", Proc. SPIE 4530, Optical Wireless Communications IV, November 27, 2001

[4] E. Ferdinandov, B. Pachedjieva, Probability and Statistical Methods in Telecommunications (in Bulgarian), Ciela, Sofia, 2005

[5] E. Ferdinandov, B. Pachedjieva, K.Dimitrov, Optical Wireless Communications (in Bulgarian), Sofia, 2007

RANDOM PHASED ANTENNA ARRAYS – THE NEW CHALLENGE FOR THE FUTURE MICROWAVE RETRO DIRECTIVE SYSTEMS

Veselin Demirev

Radiocommunication and Video Technology Department, TU-Sofia
Kl. Ohridski blv. № 8, 1756-Sofia
Tel. 359-887-526-936, e-mail: demirev_v@tu-sofia.bg

Abstract

Retro directive arrays are of growing interest due to their unique functionality and relative simplicity in comparison to phased array and smart antennas approaches. They have the characteristic of reflecting an incident wave toward the source direction without any prior information on the source location. The analog self-phasing function in these arrays makes them good candidates for possible wireless communication scenarios where high link gain and high-speed target tracking is desired. The main disadvantage of the retro directive arrays, used in microwave systems, is the need of high number antenna array elements, followed by complicated for the same reason distribution and signal processing networks.

In this report new and very promising applications of Random Phased Antenna Arrays (RPAA) in Microwave Retro Directive Systems (MRDS,s) are proposed by the author. By means of mathematical model of the proposed systems, based on matrix and vector algebra, it is shown that the combination of RPAA and a phase – conjugate circuits will work as simple and cheap MRDS. RPAA, based on Radial Line Antenna with random distributed and oriented slot radiators, are part of the proposed systems too.

The proposed MRDS,s have shown much potential for use in many applications. The autonomous beam steering feature of the RPAA MRDS,s make them attractive for automatic pointing and tracking systems, microwave tracking beacons, radar transponders, Radio Frequency Identification (RFID), solar power satellites, microwave power transmission, cross links for small satellite networks, as well as for complex communication systems.

1. INTRODUCTION

The retro directive arrays are of growing interest due to their unique functionality and relative simplicity in comparison to phased array and smart antennas approaches [1, 2, 3]. They have the characteristic of reflecting an incident wave toward the source direction without any prior information on the source location. The analog self-phasing function in these arrays makes them good candidates for possible wireless communication scenarios where high link gain and high-speed target tracking is desired. Conventional phased-array antennas are able to steer their beams by exciting elements with phase shifters. In contrast, retro directive arrays steer their beams automatically without any computationally intensive algorithms or hardware based phase shifters in response to an interrogating signal.

Retro directive arrays have shown much potential for use in many applications. The autonomous beam steering feature of the retro directive systems makes them attractive for automatic pointing and tracking systems, microwave-tracking beacons, radar transponders, Radio Frequency IDentification (RFID), solar power satellites, microwave power transmission, cross links for small satellite networks, as well as for complex communication systems.

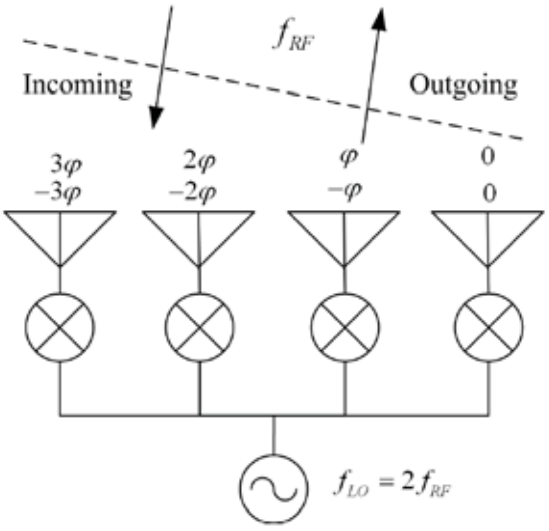

Fig. 1. Block scheme of a linear retro directive array system using HPCC

The main disadvantage of the linear retro directive arrays, used in microwave systems (fig.1), is the fact, that they have retro-directive properties only in

one plane. The practical implementation of these systems needs these properties to be realized in 2D-coordinates system, which means that plane (rectangular or circular shaped arrays) should be used. Another disadvantage in the microwave frequency bands is the need of high number (in order of several thousands) identical Heterodyne Phase – Conjugate Circuits (HPCC), equal to the numbers of the used antenna array elements, as well as the complicated power distribution system for the heterodyne signals.

A Circular Random Phased Antenna Array (CRPAA) for Microwave Retro Directive Systems (MRDS) is proposed in this report. Using mathematical model of the proposed system, based on matrix and vector algebra, it is shown that the combination of a CRPAA and only one HFCC, supplied by heterodyne signal at double frequency, will work as simple and cheap 2D MRDS.

2. CRPAA-MRDS THEORY

2.1. Introduction in CRPAA

The CRPAA is an entirely new approach in the field of microwave antenna theory, used and patented by the author one decade before. The goal was solving of the problems of the tracking microwave antenna systems for mobile satellite communications. The CRPAA were used in receive mode (SCP technology) [4, 5] and in transmit mode (RPSC technology) [6] in order to phase spread in random manner the microwave signals and to communicate with noise like signals. The random phase spreading is followed by correlation signal processing to obtain high antenna gain and spatial directive properties. In this report only the random phased antenna array of the SCP-RPSC technology is used, followed by heterodyne signal processing. The goals here are also quite different – to obtain retro directive properties with high gain.

2.2. Basic matrix expression of the signals in a CRPAA retro directive system using heterodyne phase conjugating circuit

The CRPAA-MRDS system can be represented by a block diagram, shown in fig. 2. It involves interrogators ($I_1, I_2, \ldots, I_m, \ldots, I_M$), random distributed in the space with angular positions, given with their angular coordinates in a coordinate system, centred in the centre of the transponder antenna and shown in fig. 3. To analyze such a system, the most suitable mathematical tools available involve matrix and vector algebra.

The corresponding interrogator signals $c_{1,2,3,\ldots,m,\ldots,M}$ are at frequency f_{RF} .They will travel through space to reach the CRPAA, where they will be picked up by every antenna array element and collected by the antenna array power divider to the input of the HFCC mixer. Here, the collected signals will mix with a heterodyne signal with frequency $f_{LO} = 2f_{RF}$. The interrogating signal sources are located correspondingly at azimuth angles ϕ_c , zenith angles θ_c and distances R_c .

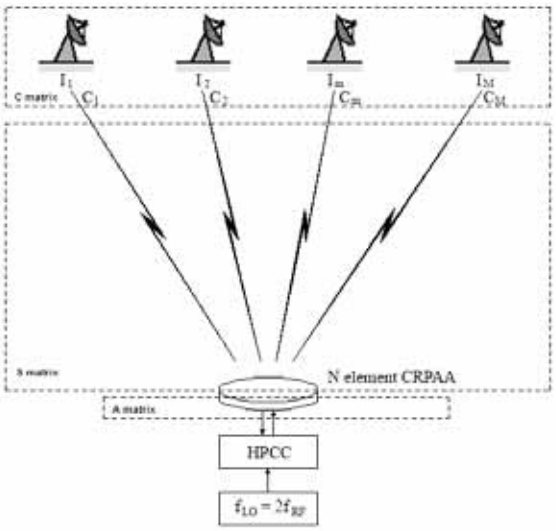

Fig. 2. Block scheme of a CRPAA-MRDS

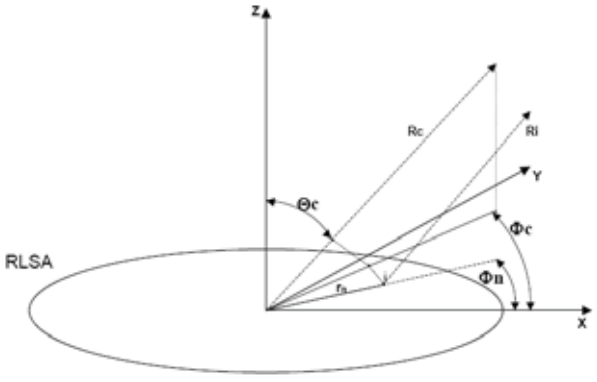

Fig. 3. Coordinate system of a CRPAA-MRDS

Each element of the N-elements CRPAA will pick up signals from all the interrogating signal sources and deliver them to its output. Thus the CRPAA output will carry signals from all the signal sources. Let s_{nm} be the transfer function between m -th in-

terrogating signal source and the n-th element of the CRPAA. Then:

$$s_{nm} = L_{snm} e^{j\psi_{nm}} \quad (1)$$

Where L_{snm} are the free space propagation losses, $\psi_{nm} = k r_n \cos\theta_m \cos\phi_m - \phi_n$ is the phase of the signal received by n-th element of CRPAA relative to its centre, $k = 2\pi/\lambda$ - free space phase constant, r_n, ϕ_n - the coordinates of the n-th element of CRPAA, ϕ_m, θ_m - the angular coordinates of m-th interrogator.

Let $\mathbf{s_m}$ represents the transfer functions between m-th signal source and all elements of the CRPAA, then:

$$\mathbf{s_m} = \begin{vmatrix} s_{1m} \\ s_{2m} \\ \cdots\cdots \\ s_{nm} \\ \cdots\cdots \\ s_{Nm} \end{vmatrix} \quad (2)$$

Where $\mathbf{s_m}$ is called a column matrix or vector. The transfers functions among all interrogators and CRPAA elements could be represented by means of matrix $\mathbf{S}$, given by:

$$S = \left| S_1 \; S_2 \; \ldots\ldots \; S_m \; \ldots\ldots \; S_M \right| =$$

$$= \begin{vmatrix} s_{11} & s_{12} & \ldots\ldots & s_{1m} & \ldots\ldots & s_{1M} \\ s_{21} & s_{22} & \ldots\ldots & s_{2m} & \ldots\ldots & s_{2M} \\ \ldots\ldots & \ldots\ldots & \ldots\ldots & \ldots\ldots & \ldots\ldots & \ldots\ldots \\ s_{n1} & s_{n2} & \ldots\ldots & s_{nm} & \ldots\ldots & s_{nM} \\ \ldots\ldots & \ldots\ldots & \ldots\ldots & \ldots\ldots & \ldots\ldots & \ldots\ldots \\ s_{N1} & s_{N2} & \ldots\ldots & s_{Nm} & \ldots\ldots & s_{NM} \end{vmatrix} \quad (3)$$

If $c_1, c_2, \ldots\ldots, c_m \ldots\ldots c_M$ are the signals transmitted by the interrogating sources $1 \ldots\ldots m \ldots\ldots M$ respectively, then the signals at the n-th CRPAA element due to the signals from the m-th interrogating signal source will be given by:

$$x_{nm} = s_{nm} . c_m \quad (4)$$

Therefore the signal vector, combining the signals from all interrogating signal sources, at the n-th element of the CRPAA is:

$$X_n = \left| x_{n1} \quad x_{n2} \ldots\ldots x_{nm} \ldots\ldots x_{nM} \right| =$$

$$= \left| s_{n1} c_1 \quad s_{n2} c_2 \ldots\ldots s_{nm} c_m \ldots\ldots s_{nM} c_M \right| \quad (5)$$

Considering the interrogating signals, the signal vector at all elements of CRPAA due to interrogating signal sources can be represented by:

$$\begin{vmatrix} \mathbf{x_1} \\ \mathbf{x_2} \\ \cdots\cdots \\ \mathbf{x_n} \\ \cdots\cdots \\ \mathbf{x_N} \end{vmatrix} = \begin{vmatrix} s_{11} & s_{12} & s_{13} \ldots s_{1m} \ldots s_{1M} \\ s_{21} & s_{22} & s_{23} \ldots s_{2m} \ldots s_{2M} \\ \cdots\cdots & \cdots\cdots & \cdots\cdots \\ s_{n1} & s_{n2} & s_{n3} \ldots s_{nm} \ldots s_{nM} \\ \cdots\cdots & \cdots\cdots & \cdots\cdots \\ s_{N1} & s_{N2} \ldots\ldots & s_{Nm} \ldots s_{NM} \end{vmatrix} X \begin{vmatrix} c_1 \\ c_2 \\ c_3 \\ \ldots\ldots \\ c_m \\ \ldots\ldots \\ c_M \end{vmatrix} \quad \text{or}$$

$$\mathbf{x} = \mathbf{S}.\mathbf{c}, \text{ where } \mathbf{x} = \begin{vmatrix} \mathbf{x_1} \\ \mathbf{x_2} \\ \cdots\cdots \\ \mathbf{x_n} \\ \cdots\cdots \\ \mathbf{x_N} \end{vmatrix}$$

and (3) $\mathbf{c} = \begin{vmatrix} c_1 \\ c_2 \\ c_3 \\ \ldots\ldots \\ c_m \\ \ldots\ldots \\ c_M \end{vmatrix}$ (6)

Thus the column vector $\mathbf{x}$ represents all signals from all interrogating signal sources at all elements of the CRPAA, while column vector $\mathbf{c}$ represents all signals transmitted by all interrogating signal sources.

As it was mentioned above, the CRPAA will transport all the signals, received by different antenna elements, to the CRPAA output and to the input of the HPCC. Let the transfer functions between all CRPAA elements and its output be represented by the column vector a:

$$\mathbf{a} = \begin{vmatrix} a_1 \\ a_2 \\ a_3 \\ \ldots\ldots \\ a_n \\ \ldots\ldots \\ a_N \end{vmatrix} \quad (7)$$

Where $a_n = L_{an} e^{j\varphi n}$, L_{an}- gain of a single element, propagation losses of the CRPAA splitter are included, $\varphi_n = 2\pi r_n / \lambda_g + \Delta\varphi_n$,where $2\pi . r_n / \lambda_g$ – phase shift due to antenna array power divider, $\Delta\varphi_n$- phase shift due to the element inclination if Circular Polarization (CP) is used.

Due to the finite transfer function that exists between the input and output ports of a CRPAA, the signals appearing at its output will be those at the antenna elements, modified by the transfer function a. The signal vector I , combining all interrogating signals appearing at the CRPAA output, is:

$$I = \left| \; a_1 e^{j\varphi_1} \quad a_2 e^{j\varphi_2} \quad a_3 e^{j\varphi_3} \ldots\ldots \right. \\ \left. \ldots\ldots a_n e^{j\varphi_n} \ldots\ldots \quad a_N e^{j\varphi_N} \; \right| = 2\pi \quad (8)$$

The received by the CRPAA signals I are mixed in the HPCC with a local oscillated signal S with $f_{LO} = 2f_{RF}$. The mixer output signals contain the following frequency components:

$$f_\Sigma = f_{RF} + 2f_{RF} = 3f_{RF} \text{ and}$$
$$f_\Delta = f_{RF} - 2f_{RF} = -f_{RF}$$

The first component with $3f_{RF}$ is low pass filtered. The second component T with frequency f_{RF} is with negative signs, which means, that it is phase conjugated with the signal vector I .

The output signal of the multiplication process in HPCC will be:

$$I \cdot H = G \begin{vmatrix} i_1 \cdot H \\ i_2 \cdot H \\ \ldots\ldots \\ i_n \cdot H \\ \ldots\ldots \\ i_N \cdot H \end{vmatrix} \quad (10)$$

Where the term n consists of:

$$i_n \cdot H = i_n e^{j[\omega t - kr_n \sin\theta_c \cos(\phi_c - \phi_n) + k_g r_n]} e^{j 2\omega t} \quad (11)$$

Where i_n is the amplitude of the information signal per antenna element (uniform distribution of the amplitudes of the antenna elements is considered), the same for the heterodyne signal ***H*** is chosen to be 1, for simplicity only one interrogator with angular coordinates $\phi_c \cdot \theta_c$ is considered, $\omega = 2\pi f_{RF}$, G is the conversion gain of the HPCC.

By means of eq.
$\cos A . \cos B = 0,5 \cos(A - B) + 0,5 \cos(A + B)$
eq. (11) can be represented in real form as:

$$i_n \cdot H = 0,5 i_n \cos(\omega t - k r_n \sin\theta_c \cos(\phi_c - \varphi_n) + k r_n) + \\ + 0,5 i_n \cos(3\omega t - k r_n \sin\theta_c \cos(\phi_c - \varphi_n) + k r_n) \quad (12)$$

Where the second term of eq. (12) is with triple RF frequency and after Low Pass Filtering (LPF) it cancels. Obviously:

$$T = G \cdot I^H = G \cdot a^H \cdot X^H \quad (13)$$

Where $(I \cdot a \cdot X)^H$ are the Hermitian (transpose and conjugate) matrix of $I \cdot a \cdot X$.

The retransmitted signal vector B by the CRPAA at the antenna array elements is the sum of the diagonal elements (or the trace) of the square matrix $a \cdot T$, as follows:

(9)

$$B = trace \cdot a \cdot T = G \cdot trace \cdot a \cdot a^H X^H = \\ = G \left| a_1 \cdot a_1^H + a_2 \cdot a_2^H \ldots + a_N \cdot a_N^H \right| X^H = G \cdot N \cdot L_a^2 \cdot X^H \quad (14)$$

The non-diagonal terms of the squared matrix $a \cdot T$ are statistical independent zero mean quantities and their sum according Central Limit Theorem (CLT) is zero too. The diagonal terms $a_n \cdot a_n^H = L_{an}^2$ are in phase, which means that the CRPAA, followed by a HPCC, works as phased array antenna with total receive-retransmit gain $G \cdot N \cdot L_a^2$ (consider for simplicity equal gain of the different antenna elements).

Bearing in mind that for simplicity only the $m-th$ interrogator is active, then the retransmitted signal vector towards him is:

$$B_m = G \cdot N \cdot L_a \cdot X_m^H \quad (15)$$

The signal at the output of the interrogator receive antenna with gain G_m^{rec} will be c_m^{rec}, as follows:

$$c_m^{rec} = G_m^{rec} \cdot G \cdot N \cdot L_a \cdot c_m \cdot trace \cdot s_m \cdot s_m^H \quad (16)$$

The non-diagonal terms of the squared matrix (16) are statistical independent zero mean quantities and their sum according CLT is zero too. Equation (16) proves the idea, that the CRPAA, followed by a HPCC, works as retro directive system with maximum of the received signal c_m^{rec} equal to:

$$c_m^{rec} = G_m^{rec} \cdot G \cdot N \cdot L_a \cdot c_m \cdot \left| s_{nm} \right| \quad (17)$$

3. CONCLUSION

In this report new and very promising applications of Random Phased Antenna Arrays in Microwave Retro Directive Systems are proposed by the author. By means of mathematical model of the proposed systems, based on matrix and vector algebra, it is shown that the combination of RPAA and a phase – conjugate circuits will work as simple and cheap MRDS. RPAA, based on Radial Line Antenna with random distributed and oriented slot radiators, are part of the proposed systems too.

Only one interrogator is considered to be active for simplicity in the report. More complicated case of multiple active interrogators will be discussed in future works, as well as the equivalent radar cross section and the parameters of the retransmitted antenna patterns

The proposed MRDS,s have shown much potential for use in many applications. The autonomous beam steering feature of the RPAA MRDS,s make them attractive for automatic pointing and tracking systems, microwave-tracking beacons, radar transponders, Radio Frequency IDentification (RFID), solar power satellites, microwave power transmission, cross links for small satellite networks, as well as for complex communication systems.

References

[1] *Y. Guo, X. Shi, L. Chen, "Retrodirective Array Technology"*, Progress in Electromagnetics Research B, *Vol.5, Internet, 2008, pp. 153-167.*

[2] *M.Kevin, H. Leong, R. Miyamoto, T. Itoh, "Moving Forward in Retrodirective Antenna Arrays",* IEEE Potentials, *Internet, August-September 2003, pp.16-21.*

[3] *D. Jorgensen, C. Loadman, Z. Chen, "Retrodirective Antenna Systems for Wireless Communications",* CNSR 2003 Conference*, Monston, Canada, May 15-16, 2003, pp. 20-23.*

[4] *V. Demirev, "Spatial Correlation Processing - the New Approach in the Broadband Satellite Tracking Systems",* Journal of Electrical and Control Engineering*, V.3, N 5, October, 2013, pp. 55-64.*

[5] *V. Demirev, "Some Important Parameters of the Spatial Correlation Processing Technology",* Journal of Electrical and Control Engineering, *V.3, N 5, October, 2013, pp. 49-54.*

[6] *V. Demirev, "Random Phase Spread Coding - the New Way to Communicate with Noise Signals at Microwaves", Journal of Electrical and Control Engineering, V.4, N 2, April, 2014, pp. 1-9.*

LOW NOISE MICROWAVE AMPLIFIERS WITH IMPROVED INPUT MATCHING APPLICABLE IN ACTIVE ARRAY ANTENNAS

Mihail Plamenov Tonev

Technical University of Sofia, Bulgaria)
Faculty of Telecommunication, TU-Sofia, "Kl. Ohridsky" str. 8, 1000 Sofia, Bulgaria
E-mail: mihail_tonev@abv.bg

Abstract

The difference between the optimal input reflection coefficient for achieving minimal noise figure and those needed for perfect matching is usually a challenge for low noise amplifiers design. Normally amplifiers designed to achieve lowest possible noise figure have very poor input reflection coefficient. This may cause a lot of problems in case of their application as a component in modern active phased array antennas and can be a reason for significant performance degradation. One of the possible solutions is to use balanced amplifier configuration in order to improve input and output matching. The main disadvantages of this solution are degradation of the noise figure due to the losses in the input hybrid and a bigger occupied space.

Another approach for solving the problem is presented in this paper. The non – unilateral properties of the transistors are used in order to obtain minimum noise figure and at the same time conjugate matching. Practical circuits and achieved performance are discussed in details.

INTRODUCTION

As known in general for every radio-communications receiver first stage of input amplifier is matched to achieve minimal noise figure. This often leads to poor input return loss of the receiver and when it is directly connected to the receiving antenna may cause problems. Usually microwave antennas are designed to be matched at their output to 50 ohms. When they see different impedance, for example as those of poorly matched low-noise amplifier, their characteristics might be changed. This is true especially concerning phased antenna arrays. Good example for such mismatch sensitive system is active antenna arrays used in modern mobile satellite communications. Such type of antennas must provide dynamic polarization control while on move. In order to support such functionality antennas must comprise dual port antenna elements receiving signals with two orthogonal linear polarizations and two independent summation feed circuits. In order to achieve good isolation between these summation circuits and to avoid phase and amplitude errors in antenna aperture it is need to ensure good matching between all feed line components inside the antenna. So if low noise amplifiers at the antenna outputs are not well matched to their characteristic impedance it may cause significant degradation of the most important antenna parameters, such as gain and cross-polarization isolation.

Two possible solutions of the mentioned above problem are known in practice. The first possible solution is to connect isolator between antenna and the receiver. This completely solves the problem with poor input matching of the receiver but degrades its nose figure performance because of the insertion loss introduced by the isolator. From another side using isolator with low insertion loss will significantly increase price of the device, which is another factor that restrict using isolators. Another less expensive solution is to use balanced amplifiers. Balancing technique is well known method for improving return loss of low noise amplifiers, but it also degrades noise performance due to the input hybrid device loss. Other disadvantages of balanced amplifiers are twice bigger power consumption and twice bigger occupied space compared to single ended amplifier. These disadvantages sometimes can make them not applicable.

Another approach, using a novel matching technique allowing achieving simultaneously low noise figure and good matching for such type of amplifiers is described in the presented paper.

MICROWAVE TRANSISTOR AS TWO PORT NETWORK

At microwave frequencies transistors are usually presented as two port networks, which are characterized with S-parameters. Such two port network

with defined load and source impedances is presented schematically on Fig.1.

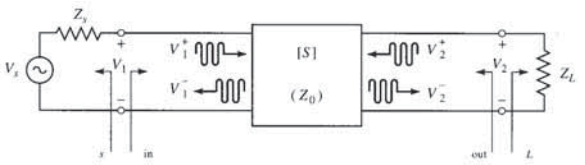

Fig. 1. Two-port network with specific source and load impedances

The three types of power gains for an arbitrary two-port network connected to source and load impedances, Z_S and Z_L may be defined as follows:

- Power Gain = $G = P_L/P_{in}$ is the ratio of power dissipated in the load Z_L to the power delivered to the input of the two-port network. This gain is independent of Z_S.
- Available Gain = $G_A = P_{avn}/P_{avs}$ is the ratio of the power available from the two-port network to the power available from the source. It depends on Z_S but not on Z_L.
- Transducer Power Gain=$G_T=P_L/P_{avs}$ is the ratio of the power dissipated in the load to the power delivered to the input of two port network. This depends on both Z_S and Z_L.

These definitions differ primarily in the way the source and load are matched to the two-port device. If the input and output are both conjugate matched, then the gain is maximized and $G = G_A = G_T$. Equations for these gains and reflection coefficients in terms of the *S* parameters of the active device can be defined, referring to Fig.1, as follows:

$$(1) \qquad G = \frac{P_L}{P_{in}} = \frac{|S_{21}|^2\left(1-|\Gamma_L|^2\right)}{\left(1-|\Gamma_{in}|^2\right)\left|1-S_{22}\Gamma_L\right|^2}$$

$$(2) \qquad G_A = \frac{P_{avn}}{P_{avs}} = \frac{|S_{21}|^2\left(1-|\Gamma_S|^2\right)}{\left|1-S_{11}\Gamma_S\right|^2\left(1-|\Gamma_{out}|^2\right)}$$

$$(3) \qquad G_T = \frac{P_L}{P_{in}} = \frac{|S_{21}|^2\left(1-|\Gamma_S|^2\right)\left(1-|\Gamma_L|^2\right)}{\left|1-\Gamma_S\Gamma_{in}\right|^2\left|1-S_{22}\Gamma_L\right|^2}$$

Where

$$(4) \qquad \Gamma_L = \frac{Z_L - Z_0}{Z_L + Z_0},\ \Gamma_S = \frac{Z_S - Z_0}{Z_S + Z_0}$$

And

$$(5a) \qquad \Gamma_{in} = \frac{Z_{in} - Z_0}{Z_{in} + Z_0} = S_{11} + \frac{S_{12}S_{21}\Gamma_L}{1 - S_{22}\Gamma_L}$$

$$(5b) \qquad \Gamma_{out} = \frac{Z_{out} - Z_0}{Z_{out} + Z_0} = S_{22} + \frac{S_{12}S_{21}\Gamma_S}{1 - S_{11}\Gamma_S}$$

In general to obtain good input matching it is necessary input reflection coefficient of two port network Γ_{in} to be close to zero. From equation 5a can be seen that Γ_{in} depends on active component parameters (S_{11}, S_{21}, S_{12}) and on load reflection coefficient Γ_L. This means that we can manipulate input reflection coefficient of two port network by changing load impedance.

DESIGN OF MICROWAVE LOW-NOSE AMPLIFIER (LNA) WITH IMPROVED INPUT MATCHING

The main goal in designing low nose amplifiers is obtaining proper reflection coefficient from input matching network. This coefficient must coincide with optimum reflection coefficient for obtaining minimum noise figure of active component. Usually this coefficient is different from conjugate machining and this is the reason Γ_{in} of LNA's not to be zero. It is possible to design proper input matching network and then to choose load impedance, which will minimize input reflection coefficient of the two port network. In this case amplifier will be simultaneously matched for obtaining minimum nose figure and conjugate matched with source. In general for single stage amplifier this will worse output matching. The problem can be solved by adding second stage in amplifier configuration. Then using inter-stage matching circuit we can chose proper reflection coefficient to make $\Gamma_{in} = 0$ and then output matching circuit can be designed to make $\Gamma_{out} = 0$.

The approach, presented above was proven by designing microwave LNA, suitable for using in Ku band satellite communications working in frequency band from 10.7GHz to 12.8GHz. It was designed on Arlon 25N substrate with 0.51mm thickness, dielectric constant 3.38 and loss tangent 0.0025. Used transistors are NE3210 low noise hetero-junction FET, manufactured by NEC. The S-parameters of transistors and capacitors, provided by manufacturers were putted in simulator and circuit simulation was performed.

The first step in design is to define input matching circuit. In Fig. 2 reflection coefficients of input matching circuit and optimum reflection coefficient of transistor are shown. As can be seen, there is coincidence between them which means that transistor is matched for obtaining minimum noise figure.

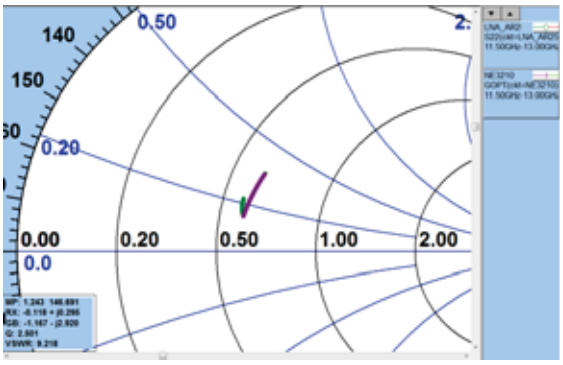

Fig. 2. Reflection from input matching circuit and transistor Γ_{opt}

Once input of the amplifier is matched, the interstage and output matching circuit can be designed, using optimization procedure in order to achieve good input and output matching. Simulated S-parameters and noise figure of LNA model are shown in fig. 3 and fig. 4.

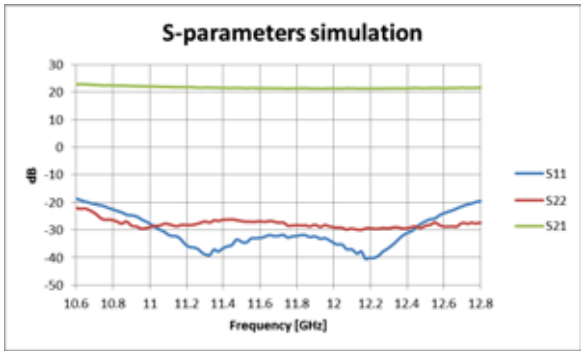

Fig. 3. Simulated S-parameters of LNA

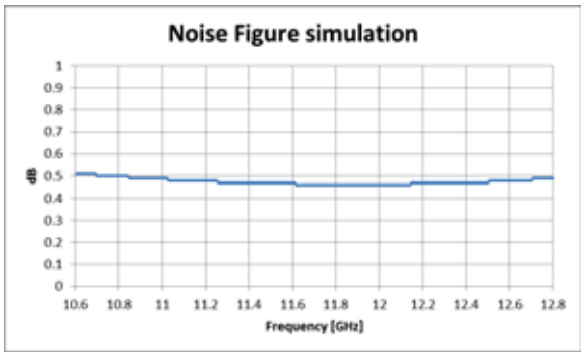

Fig. 4. Simulated noise Figure of LNA

The input and output reflection coefficients are lower than 0.1 and noise figure is lower than 0.5 dB. Simulated amplifier has low noise figure and good matching with source and load. To gain real inside how circuit works the simulated layout of amplifier was manufactured and measured. Measurement results are presented graphically in Fig. 5 and Fig. 6. Some difference between measured and simulated results may be caused by the tolerances in component parameters and by reflections from input and output connectors used for measurements. Measured input reflection coefficient is lower than 0.13 and measured noise figure is about 0.65 dB.

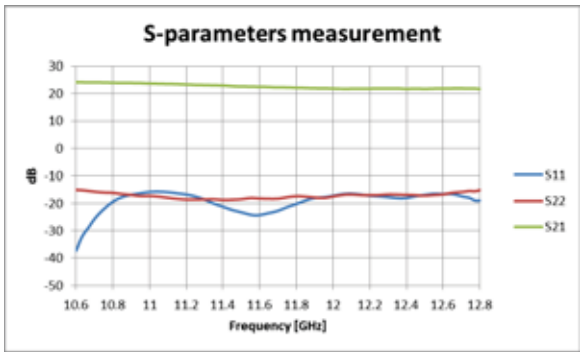

Fig. 5. Measured S-parameters of LNA

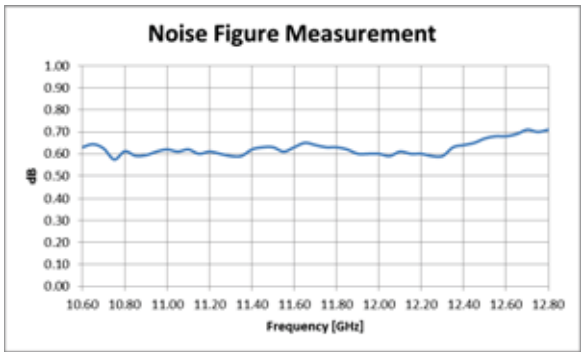

Fig. 6. Measured noise Figure of LNA

CONCLUSION

A design of microwave low-noise amplifier with improved input matching was presented in this paper. As was explained this is critical parameter for some communication systems. Practically the proposed method for enhancing this parameter, by using non-unilateral characteristic of microwave transistors was proved by model measurements.

References

[1] Pozar "Microwave Engineering 4ed"

[2] Vendelin Rohde, Pavio "Microwave circuit design using linear and nonlinear techniques"

ALGORITHM FOR DETECTION OF MUSCLE CONTRACTIONS IN THE EMG SIGNAL, FOR USE IN ACTIVE PROSTHESIS

Viktor A. Nedialkov

Technical University of Sofia, Bulgaria
Faculty of Telecommunication, TU-Sofia, "Kl. Ohridsky" str. 8, 1000 Sofia, Bulgaria

Abstract

An active prosthesis needs a reliable and easy real-time algorithm for detection of the muscle contraction. An algorithm based on the Pan-Tompkins ECG QRS detection algorithm is proposed. It uses band-pass filter and subsequent differentiation, squaring and moving averaging. The output signal is then compared to set of thresholds to determine the contraction of the muscle and its strength.

1. INTRODUCTION

Skeletal muscle is organized functionally on the basis of the motor unit (fig. 1). The motor unit is the smallest unit that can be activated by a volitional effort, in which case all constituent muscle fibres are activated synchronously. The component fibres of the motor units extend lengthwise in loose bundles along the muscle. In cross section, however the fibres of a given motor unit are interspersed with fibres of other motor units. Thus the component muscle fibres of the single motor unit (SMU) constitute a distributed, unit bioelectric source located in a volume conductor consisting of all other muscle fibres, both active and inactive. [5]

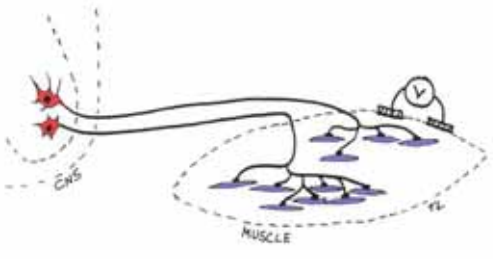

Fig.1

The evoked extracellular field potential from the active fibres of an SMU has a triphasic form of brief duration (3-15ms) and an amplitude of 20-2000 uV, [4] (fig 2) depending on the size of the motor unit. Due to the small size of the SMU the recording of the SMU action potential is only possible with needle electrodes. When using surface electrodes the recorded signal consists of many SMU action potentials form different depths. The resultant signal has a frequency range from 25Hz to several thousand Hertz and amplitude in the range of 20-2000 uV (fig. 3)

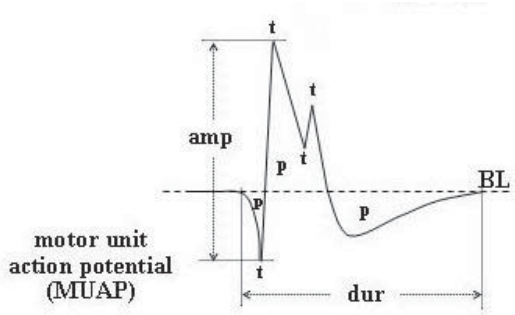

Fig. 2

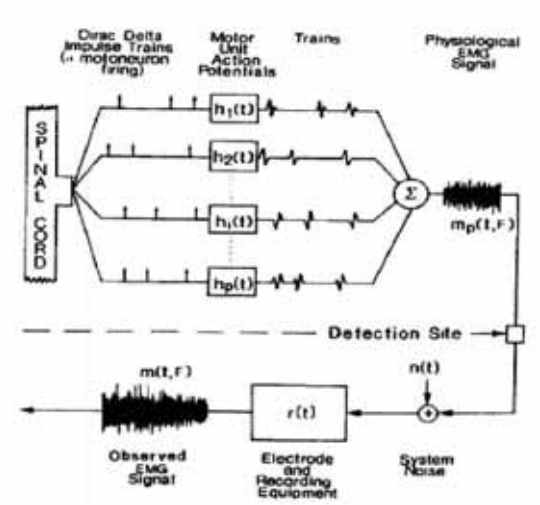

Fig. 3

The most frequently used algorithms for detecting muscle contraction consists of simple integration of the EMG signal. This is simple enough and can be implemented even with hardware means only, but does not provide enough sensitivity and signal to noise separation.

Pan and Tomkins [1] have proposed a real-time algorithm for detection of the ECG QRS complex

based on analysis of the slope, amplitude and width of QRS complexes. The algorithm includes a series of filters and methods that perform low-pass, high-pass, derivative, squaring, integration, adaptive thresholding, and search procedures. Figure 4 Illustrates the steps of the algorithm in schematic form.

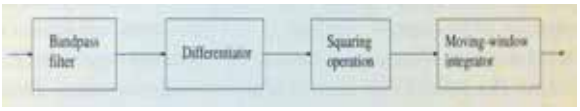

Fig. 4

The band-pass filter eliminates the noise from electrical interference and the low-frequency noise (baseline drift, P and T wave). The derivative operator further suppresses the low frequency components of the P and T wave and motion artifacts and provide large gain on the high-frequency components. The squaring makes the result positive and further emphasize high-frequency components. The subsequent moving average integration smooth the multiple peaks within the duration of a single QRS complex. The a set of thresholds are calculated for the signal and the noise.[2] A result of the Pan and Tompkins algorithms is shown on figure 5.

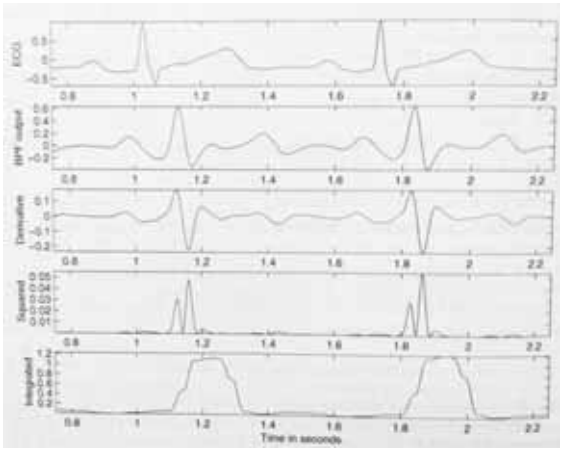

Fig. 5

2. METHODS

A dedicated amplifier was designed for the development of this algorithm. It is a one channel differential amplifier with a Driven Right Leg feedback circuitry for suppressing artifacts. The frequency range of the amplifier is 25Hz – 500Hz. This range is chosen to eliminate the low frequency noise witch is mostly below 25Hz. The upper cutoff frequency is chosen so that the signal will include the most of the EMG signal and to ease the signal processing. The electrical line interference is supressed by a Driven Right Leg feedback circuitry. A dedicated filter for the 50 Hz power line interference is not suitable because this frequency is in the range of the EMG signal. The sampling rate of the ADC is chosen to be 2000Hz.

The digital signal is then send via USB to a PC where a specially developed software EmgLab will make the signal analysis.

The use of Pan-Tompkins algorithm was inspired by the insight that the EMG signal can be very random and depends on the MUPs activated, the place and size of the surface electrodes used. This is why a pattern recognition is very difficult and not reliable enough. On the other hand this algorithm is very sensitive to the power of the signal witch is directly related to the strength of contraction.

The low-pass and high pass-filters used in the original Pan-Tomkins algorithm are omitted because in the frequency band of the digitized signal the low-frequency and high frequency noise is already filtered.

The steps used in the algorithm are the following:

1. Derivative operator: The derivative operation used is specified as:

$$y(n) = 1/8[2x(n) + x(n-1) - x(n-3) - 2x(n-4)]$$

2. Squaring: $y(n)^2$ – this makes the result positive and emphasizes the large differences

3. Moving average: The moving average smooth the multiple peaks from the squaring operation:

$$y(n) = 1/N[x(n-(N-1)) + x(n-(N-2)) + x(n)]$$

The window width is chosen to be N=500 in the proposed algorithm.

4. Adaptive thresholds: In this step it is important to find accurately the onset and the offset of the muscle contraction. Since the muscle can by contracted slowly or very rapidly a slope analysis is not suitable. Therefore only amplitude threshold is used which is defined as:

$$THR = 0.1*MAX\_CONTRACTION$$

3. EXPERIMENTS

The algorithm is tested on different muscles with real-time signal processing.

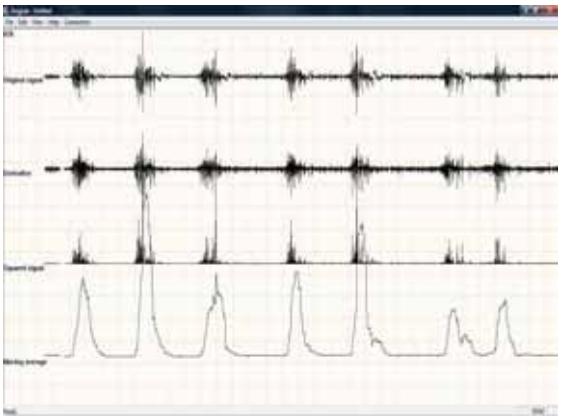

Fig. 6. Biceps branchii

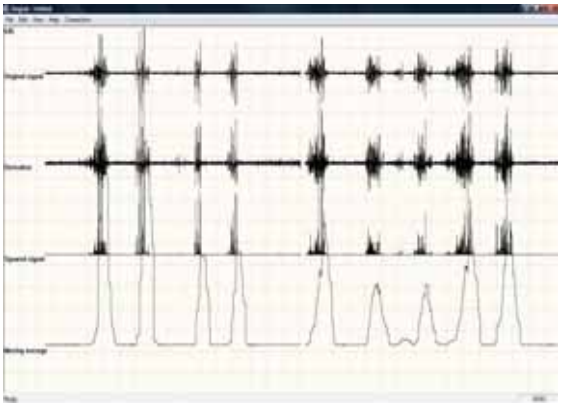

Fig. 7. Flexor radialis

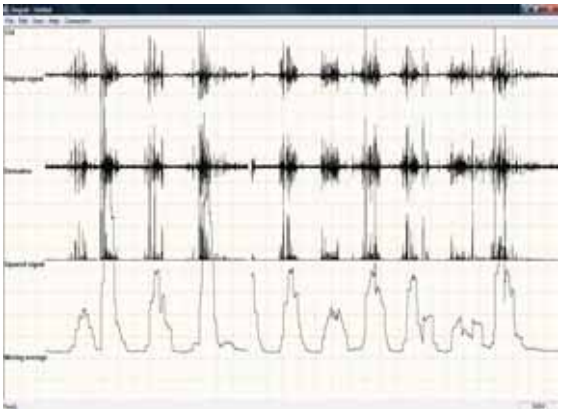

Fig. 8. Rectus femoris muscle

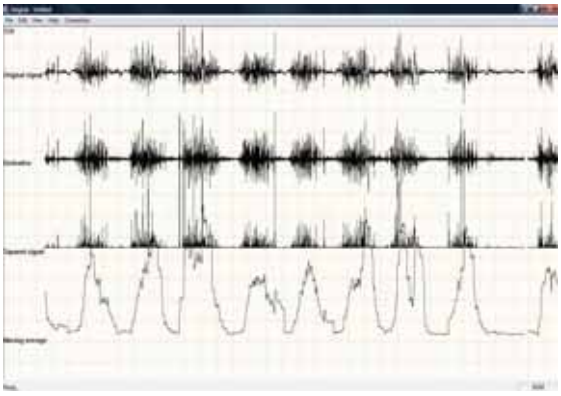

Fig. 9. Rectus femoris during walking

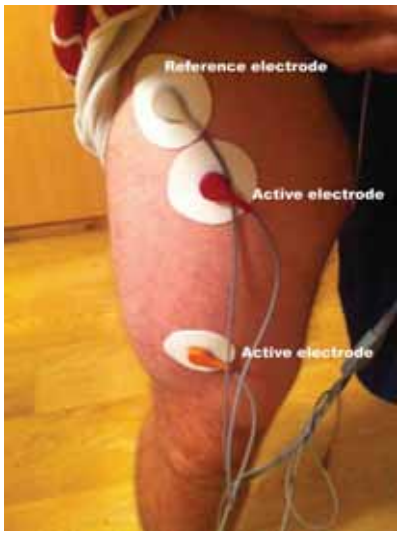

Fig. 10. Electrode placement for the Rectus femoris experiment

4. CONCLUSION

The algorithm gives very good results on the detection of the muscle contraction of different muscles. During walking the work of the muscle visible and the onset and offset of the contraction can easily be detected.

Further experiments are needed to tune the size of the Moving Average N.

References

[1] Pan J. and Tompkins W. J. "A real-time QRS detection algorithm." IEEE Transaction on Biomedical Engineering, 32:230-236, 1985

[2] Rangaraj M. Rangayyan "Biomedical Signal Analysis" Wiley-Interscience

[3] Joseph Bronzino "The Biomedical Engineering Handbook" CRC Press

[4] И. Даскалов, И. Стамболиев "Електромедицинска диагностична техника", Техника

[5] Webster J., "Medical Instrumentation – application and design" John Wiley & Son

FRACTAL CHARACTERISTICS OF DIGITAL IMAGES AND THEIR WAVELET TRANSFORMS

I. P. Soloviev

St. Petersburg State University, Math. & Mech. Faculty, i.soloviev@spbu.ru

M. V. Videneeva

St. Petersburg State University, Math. & Mech. Faculty, mvmilko@gmail.com

Abstract

We consider two methods to obtain classification signs for some classes of biomedical preparation images. The first method is based on the computation of the fractal signatures vector. The second one calculates fractal signatures for a set of wavelet transforms of the initial image. The images are represented both in gray scale and HSV (Hue, Saturation, Value) palettes. Experiment results show that the best separation for given classes is achieved by application of the second method and using H-component of HSV.

1. INTRODUCTION

When analyzing and classifying digital images we have to choose an appropriate method of investigation which is oriented on special range of application and based on mathematical and computer models. To analyze textures one can use both statistical and morphological methods, fractal and multifractal ones lead to good results for biomedical preparations images. [2,9].

We consider two based on fractal characteristics approaches to image analysis and classification. The both methods use fractal signature of a color image transformed to the gray scale palette (G) or presented by the component H in HSV palette. In both cases the image is considered as a function F of integer coordinates, i.e. a two-dimensional surface [6].

The first method uses a vector of fractal signatures for a given image, where fractal signatures are obtained in accordance with [8] (Fractal signature method). The second one is based on obtaining fractal characteristics of the image wavelet transforms. Fractal signature method consists in the calculation of the area of so called δ-parallel body for the surface of the graphic of a function F. By δ-parallel body one mean the set of points being at the distance not greater than δ from the surface of graphics of F; these points form a blanket» with width 2δ. Using the "blanket" volume we may obtain the approximate value A_δ of the surface area of the F graphics. The ratio $\log A_\delta / \log \delta$ is called fractal signature. By changing δ in an interval [1,N] one can obtain a fractal signatures vector which we consider as the image characteristics.

To perform wavelet transform we use Gauss function and its second order partial derivatives, because they have good localizing properties [1].

We apply such a transform to a given digital image and then calculate the fractal signature of the obtained wavelet transform that we consider as an image – wavelet image. By changing the scale value in empirically selected range we obtain a set of wavelet images and the vector of corresponding them fractal signatures. In this case fractal signatures are calculated for $\delta = 1,2$.

Thereby, in each method we obtain a vector of fractal signatures: in the first method — by changing δ in the second one — by calculating fractal signature for every wavelet image. To compare images from different classes we compare their fractal signature vectors. The less the distance between vectors corresponding images A and B, the more probability that A and B are in the same class. Experiments allows us to select a method that gives a better separability for given classes of images. We also compare the results for gray scale and HSV (H component) representations of an image. For almost all of the images under investigation the using H component gives better classification results.

2. METHODS DESCRIPTION

The given image is presented by a discrete function F (in gray scale or HSV (H component) palette: F =

$\{X_{ij}, i=0,1,\ldots,K, j=0,1,\ldots,L\}$, where X_{ij} —is (i,j) pixel intensity, K, L define the image size. In points with real coordinates F is redefined by its value on the left end of the integer interval. Hence one can consider a surface of the graphic of F and calculate its area.

2.1. Fractal signature method

The method is based on the B. Mandelbrot idea about the approximate calculation of the length *L* of a coastline which has complex fractal structure [7].

Consider all the points with distances to the coastline of no more than δ. They form a strip of width 2δ. Then the strip area divided by 2δ is an approximation to $L(\delta)$. The length increases as δ decreases. At the same time Mandelbrot noted that there is an interval for δ in which the value $L(\delta)$ becomes stable.

In [8] athors applied this idea to calculate the approximate value of the surface area of the graphic of the function presenting a digital image. They construct a special neighbourhood of the surface (δ-parallel body) calculated the body volume and divided it on the height. Changing δ one can obtain several approximate values for the surface area.

We define δ-parallel body [5] as the set of points being at the distance not greater than δ from the surface of graphics of F. They form a "blanket» with width 2δ having upper (u_δ) and bottom (b_δ) bounds which are calculated in each point of the image on its intensity and the intensity of neighbours. The formulas are given in [8,10].

The volume is calculated as the following

$$Vol_\delta = \sum_{i,j} u_\delta(i,j) - b_\delta(i,j) \qquad (1)$$

To calculate approximations to the surface area we may use two variants:

$$A_\delta = Vol_\delta / 2\delta, \qquad (2)$$

or

$$A_\delta = \frac{Vol_\delta - Vol_{\delta-1}}{2}. \qquad (3)$$

As for fractal surfaces (3) is more preferable, we use it. Fractal signature S_δ is defined as

$$S_\delta = \frac{\log A_\delta}{\log \delta}.$$

For $\delta \in [1, N]$ the sequence S_δ is calculated. The approximate value of S_δ is obtained by the least square method and is the slope of the line (in log-log scale) fitted to

$(\log(\delta-1), \log A_{\delta-1}), (\log\delta, \log A_\delta)$ and $(\log(\delta+1), \log A_{\delta+1})$

To compare two images one should to find the distance between their fractal signature vectors.

2.2. Wavelet transform method

We apply a wavelet transform [3,4] to the discrete function presenting the image. The transform reads

$$W(a, b_1, b_2) = \text{as } \frac{1}{a}\sum_{x=0}^{K-1}\sum_{y=0}^{L-1}\varphi\left(\frac{x-b_1}{a}, \frac{y-b_2}{a}\right)F(x,y), \qquad (4)$$

where a – scale parameter, b_1, b_2 – shifts on coordinate axis, φ – wavelet.

As a wavelet we use the sum of the second order partial derivatives of Gauss function:

$$\varphi(x,y) = \exp\left(-\frac{x^2}{2} - \frac{y^2}{2}\right) * (x^2 + y^2 + 2xy - 2). \qquad (5)$$

Such a wavelet has narrow energy spectrum and seems to be preferable when higher order singularities are analyzed [1]. As experiments show, though higher order derivatives allows obtaining more exact results than the initial function, the using derivatives higher than the second order complicates calculations without the accuracy increasing.

For the function presenting given image we fix *a* parameter and perform wavelet transform in accordance with (4). Here b_1, b_2 change from 1 to K, L respectively, where K and L define the image size. The obtained set we consider as a new "image" (in coordinates (b_1, b_2) that has the same size as the initial one.

By changing a in an interval (comparable with the interval of δ) we construct a series of images corresponding to the initial one. Then for every image from the set we calculate its fractal signature. The vector of fractal signatures is the image characteristic.

3. NUMERICAL EXPERIMENTS

We considered the biomedical preparation images of two different classes: healthy liver and Fatty Liver Disease (FLD) (Figure 1 and Figure 2). The size of all images is 300x300. In each class 5 images were selected.

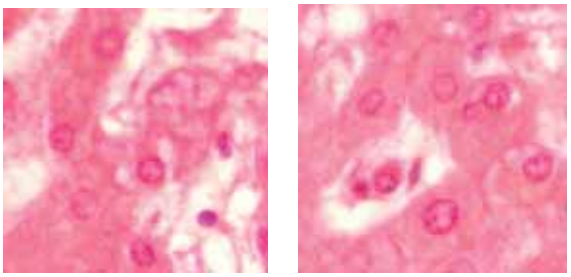

Fig. 1. Healthy liver images

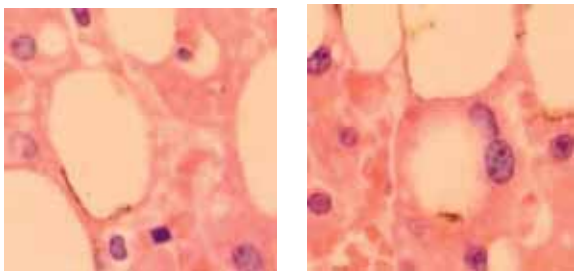

Fig. 2. Images of liver with FLD

Note that the images were beforehand classified by an expert.

The application of the first method when using HSV palette did not lead to a separation of images (Fig. 3)

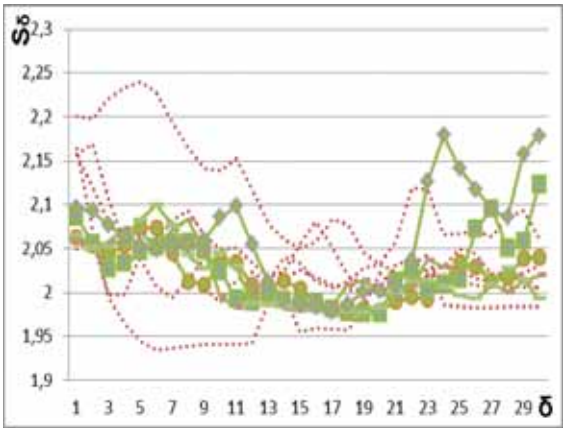

Fig. 3. The result of the first method in HSV palette

The vector size (30) was selected empirically: for δ >30 fractal signature values changed insignificantly. For the second method empirical estimation for scaling parameter was 10.

The application of the second method when using HSV palette demonstrated good separability of fractal signature vectors, and ipso facto two classes of images.

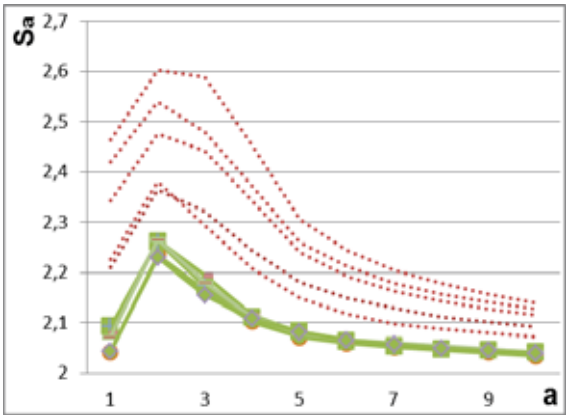

Fig. 4. Separation of vectors for two classes of images in the second method in HSV palette

The praphic illustrated the dependence fractal signature on the scale parameter *a*. Dotted lines denote the graphics for healthy liver, solid lines – graphics for FLD images. Hence wavelet transform with the following application of fractal signature method allowed us to separate two given classes of images.

The first method with using gray scale palette did not result in the separation of two classes. For obtained vectors we also considered graphics of their average, maximum and minimum values. As it is shown for maximal values on Fig. 5, this experiment did not improve the situation

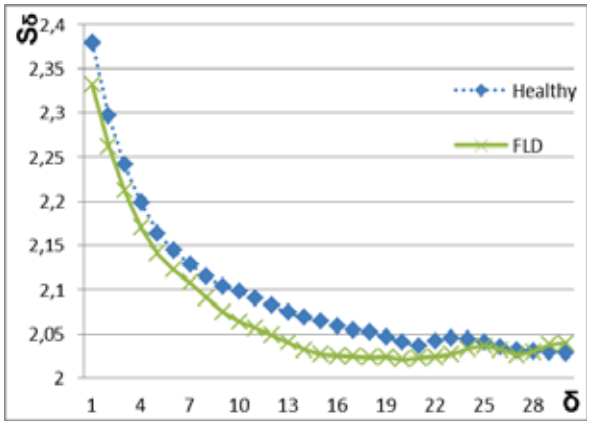

Fig. 5. Closeness of vectors of maximum for the first method in gray scale palette

The second method in grayscale palette was not successful (Figure 6).

We also considered the class of images of the liver with plephora and applied the described methods by the above scheme. The results of the experiments for this class seemed to be close to the re-

sults for two considered classes: the combination of the second method and HSV palette (H component) led to the separation of the images by the chosen characteristic. The results are summed up in the following table, where "+" means the success of experiments.

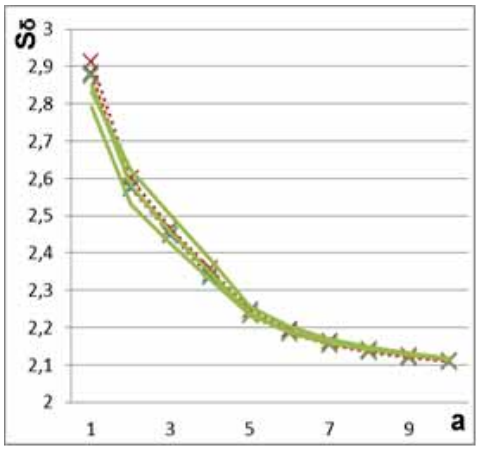

Fig. 6. Closeness of vectors of maximal values for the second method in gray scale palette

palette	method 1	method 2
HSV	-	+
grayscale	-	-

4. CONCLUSION

We performed the comparison of two methods of analysis of some classes of digital images. Both methods use fractal signature vector as a classifying sign. The first method forms the vector of fractal signatures obtained for a sequence of δ-parallel bodies when $\delta \in [1, N]$. The second one at first forms a sequence of wavelet transforms of the image by changing the scale parameter and then calculates fractal signatures for this sequence when $\delta \in [1,2]$. For both methods the results were more exact when using HSV palette (component H). Experiments show that wavelet transform may successfully applied to distinguish images with similar texture.

Acknowledgements

The work was partially supported by the grant RFBR 13-01-00782.

References

[1] K. A. Alekseev. Around the CWT. http://matlab.exponenta.ru/wavelet/book3/4.php (in Russian)

[2] N. Ampilova, E. Gurevich, I. Soloviev. Application of Modified Fractal Signature & Regny Spectrum Methods to the Analysis of Biomedical Preparations Images. Proc. 6 Int. Conf. CEMA11, 6-8 Oct. 2011, Sofia, Bulgaria. p. 96-100.

[3] N. M. Astaf'eva, "Wavelet Analysis: Theoretical Backgrounds and Application Examples," Usp. Fiz. Nauk 166 (11), 1145–1170 (1996). (in Russian)

[4] C. K. Chui, An Introduction to wavelets. M. Mir (2001). (in Russian)

[5] Falconer K.J. Fractal Geometry. Mathematical Foundations and Applications. — John Wiley & Sons, 1990.

[6] R. Gonzalez, R. Woods, Digital Image Processing.Tekhnosfera, (2006) (in Russian)

[7] B. B. Mandelbrot, The Fractal Geometry of Nature San Francisco, CA: Freeman, 1982

[8] Peleg Shmuel, Naor Joseph, Hartley Ralph, Avnir David. Multiple Resolution Texture Analysis and Classification. IEEE Transactions on pattern analysis and machine intelligence, vol. PAMI-6, NO. 4, July 1984

[9] Soloviev, N. Ampilova, E. Gurevich. On implementation of a neural network classifier for some classes of biological and medical preparation images. Proc. 7 Int. Conf. CEMA12, 8-10 Nov. 2012, Athens, Greece. P. 94-97.

[10] Tang Y. Y., Hong Ma, Dihua Xi, Xiaogang Mao, C. Y. Suen. Modified Fractal Signature (MFS): A New Approach to Document Analysis for Automatic Knowledge Acquisition. – IEEE Trans. Knowledge and Data Eng., vol.9. no. 5, 1997, pp. 742-762.

IMAGE SEGMENTATION ALGORITHM BASED ON MULTIFRACTAL SPECTRUM COMPUTING

N. B. Ampilova

St. Petersburg State University, Math. & Mech. Faculty, n.ampilova@spbu.ru

Y. V. Shupletsov

St. Petersburg State University, Math. & Mech. Faculty, shupaag@mail.ru

Abstract

In the image analysis problem segmentation algorithms are very important. We can use classical algorithms based on morphological analysis. But it is well known that for image having complex structure, e.g high resolution images, classical approach may fail to achieve good results. The solution is to use multifractal analysis that gives an information about the geometric distribution of the singularities of the image. In this work we apply the algorithm of direct calculation of multifractal spectrum for image segmentation. Fractal dimensions for level sets are calculated by fractal signature method. Experimental results for 2 classes of biomedical preparations images are given.

1. INTRODUCTION

Image segmentation is the process of partitioning a digital image into multiple segments (sets of pixels). The goal of segmentation is to simplify the representation of an image so the obtained image may be easier to analyze. This method is used to locate objects and boundaries in images. In each segment all the pixels are similar with respect to some characteristics or computed property such as color or intensity.

Image segmentation is widely used in machine vision, medical imaging, object detection, recognition tasks. In order to effectively solve the domain's segmentation problems this technique must be combined with specific knowledge in the subject area.

Classical methods applied in image segmentation are methods of mathematical morphology: thresholding, edge detection (line, curve) [6,7].

For digital images with very high spatial resolution classical segmentation methods fail to give homogeneous segments and usually give very sparse results. As it was mentioned in [9], texture approach and fractal analysis are not appropriate methods, but "multifractal analysis is the perfect tool to analyze a highly varying regularity from point to point".

Multifractal analysis methods are based on a partition of the image on the set such that every of them has its own fractal dimension. The set of these dimensions characterizes the image and is called multifractal spectrum. To obtain such a partition we should factorize the image points in accordance with a sign. As this sign one can use density function [10], or Holder exponents [9]. The most common approach to calculate fractal dimensions is to use capacity dimension. When using multifractal methods we match to the image a measure and suppose that it is distributed according to exponential law: the measure of a partition cell is approximately equal to the size of the cell in a power. Multifractal spectrum may be obtained by calculation of the Regny spectrum and the following Legendre transform [4], by using generalized statistical sum [4] or by direct calculation by using density function [10].

The choice of the method depends on the problem. If the task is to obtain a spectrum then it is sufficient to compute the Regny spectrum. If our purpose is to use the partition on the sets for segmentation problem we have to devote attention to the separating sign choosing.

In [2] we considered the algorithm of direct calculation of multifractal spectrum based on the calculation of a density function at each point of the image.

In this work we reveal a dependence of the density function (and *ipso facto* the result of segmentation) from the measure and use fractal signature method [1,3] which allows us to make calculations more effective comparing capacity dimensions computing. Experimental results for 2 classes of biomedical preparations images are given.

2. METHOD DESCRIPTION

Let μ be a measure defined through pixel intensities. For $\square\in\square^2$ we denote $\square(\square,\square)$ a square of length r with center x. We describe $\mu(\square(\square,\square))=\square^{\square(\square)}(\square)$ with $\square(\square)$ the density function and *k* some constant. The local density function of *x* is defined as

$$\square(\square)=\lim_{\square\to 0}\frac{\log\mu(\square(\square,\square))}{\log\square} \quad (1)$$

The set of all image points x with local density α is a level set

$$E_\alpha=\{x\in R^2 : d(x)=\alpha\}\ . \quad (2)$$

Thus we obtain a point categorization $\{E_\alpha : \alpha\in R\}$ of the image with a multifractal spectrum defined as

$$\{f(\alpha):\alpha\in R\}=\{\dim(E_\alpha):\alpha\in R\}\ . \quad (3)$$

The density function describes how locally the measurement μ satisfiers the power law behavior. It measures the non-uniformity of the intensity distribution in the square $B(x,r)$.

We note that using (2) may lead to considerable increasing the number of level sets and segmentation may be useless. So in practice one consider sets

$$E(\alpha,\varepsilon)=\{x\in R^2, d(x)\in[\alpha,\alpha+\varepsilon)\} \quad (4)$$

The measure $\mu(B(x,r))$ may be calculated by several ways. We used the sum of intensity pixels in the square and the sum of Laplacians in the square.

1. $\mu(B(x,r))$ — the sum of intensity pixels in the square withy side r and center x. $\mu(B(x,r))=\int\limits_{\mu(B(x,r))}\int I(y)dy$,

where *I(y)* — is the pixel intensity in $y\in B(x,r)$.

In discrete case

$$\mu(B(x,r))=\sum_{y\in B(x,r)}I(y)\ . \quad (5)$$

2. $\mu(B(x,r))=\int\limits_{\mu(B(x,r))}\int\nabla^2(I(y))dy$, where ∇^2 — the Laplace operator.

In discrete case in accordance with [6] we have

$$\mu(B(x,r))=\sum_{y\in B(x,r)}L(y)\ , \quad (6)$$

where $L(y)=8I(y)-\sum_{z\in B(y,2)\setminus y}I(z)$.

It was shown in [4] that namely using Laplacian resulted in the separation of classes of connective tissues in accordance with obtained spectra.

The density $d(x)$ is obtained as the slope of the line fitted to the data $\{\log r,\log\mu(B(x,r))\}$ by the least square method. Then we take a discrete set $\{\alpha_i\}$ from an interval (1,2) and find for each α_i the point set $E(\alpha_i,\varepsilon)$ (ε=0.1) according to (4).This set contains all the pixels whose densities are close to α_i.

The fractal dimension $f(\alpha_i)$ is computed as the Minkovsky dimension by the fractal signature method.

3. NUMERICAL EXPERIMENTS

The experiments were performed for two classes of liver: healthy (a) and fatty liver disease (b). The examples of these images are shown on Fig.1.

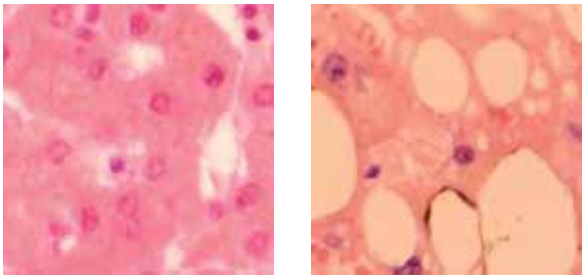

a b

Fig. 1. Liver images: a — healthy liver, b — fatty liver disease

We consider the dependence of segmentation results on the measure choice.

3.1. Measure is the sum of pixel intensities

For given images the results of calculation of $E(\alpha,\varepsilon)$ were the following. The sets containing the most number of points was obtained for α = 1.6. For α = 1.5 the set was not so dense. The rest of

sets were almost empty. This situation is illustrated on Fig.2, where black color means the point belongs to the set.

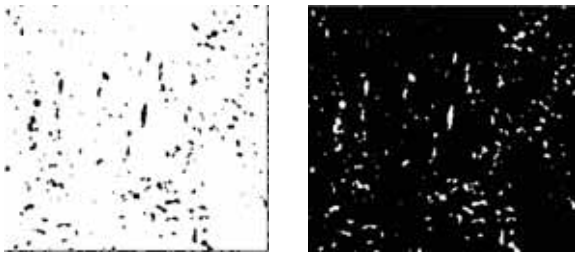

a b

Fig. 2. $E(\alpha,\varepsilon)$ for healthy liver: α = 1.5 (a) and α = 1.6(b)

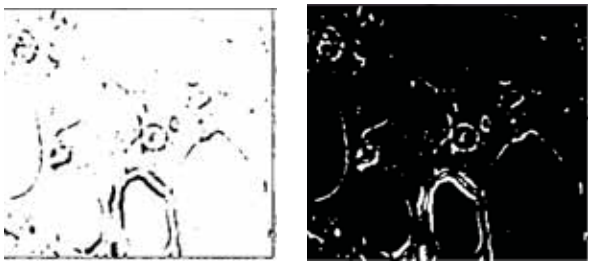

a b

Fig. 3. $E(\alpha,\varepsilon)$ for FLD: α = 1.5 (a) and α = 1.6(b)

Multifractal spectrum:

α	Healthy liver	Fatty liver desease
1.0	0	0
1.1	0.4352	0.9009
1.2	0.4352	0.9009
1.3	0.474	0.493
1.4	0.474	0.493
1.5	0.4988	0.5024
1.6	1.0538	0.8488
1.7	0	0.0591
1.8	0	0.1042
1.9	0	0

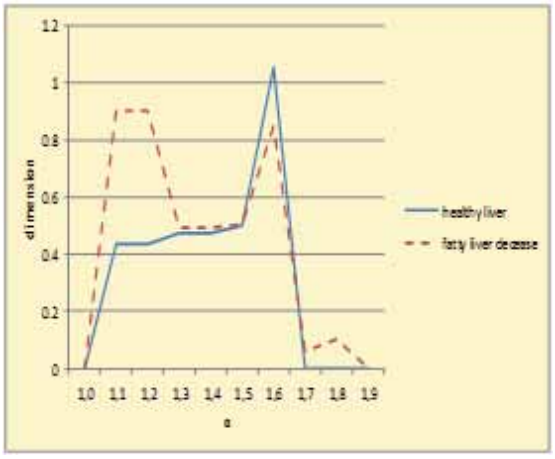

Fig. 4. Graphics of spectra for the measure as the sum of pixel intensities

3.2. Measure is the sum of Laplacians

In this case the density function (that depends on the measure) generates another partition on level sets and, as a consequence, another spectra. The most part of the image pixels belong to $E(\alpha,\varepsilon)$ with α = 1.0/

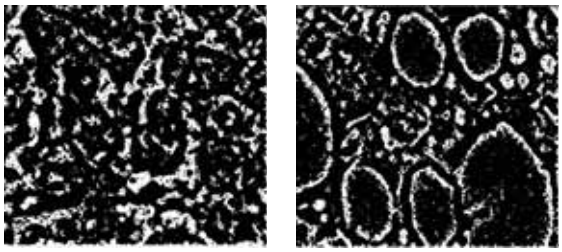

a b

Fig. 5. $E(\alpha,\varepsilon)$ for α = 1.0:(a) –healthy liver,(b)– FLD

Multifractal spectrum:

α	Healthy liver	Fatty liver desease
1.0	0.7291	0.7509
1.1	0.4376	0.499
1.2	0.4376	0.499
1.3	0.3986	0.4804
1.4	0.3986	0.4804
1.5	0.3932	0.4878
1.6	0.4032	0.5122
1.7	0.3962	0.5172
1.8	0.3921	0.4787
1.9	0.396	0.5122

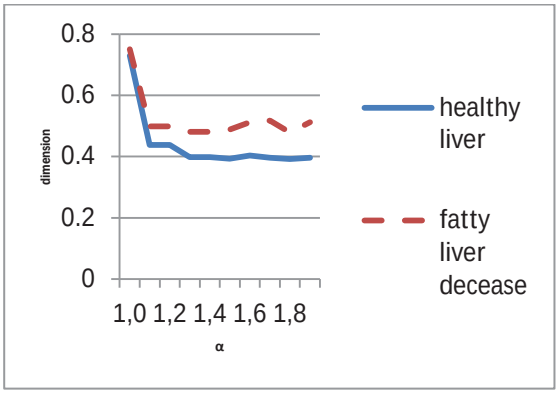

Fig. 6. Graphics of spectra for the measure with Laplacian

CONCLUSION

We presented a segmentation method based on a direct calculation multifractal spectrum. A categorization of the image points is performed by using density function that characterizes intensity changes in the neighbourhood of a given point. Two methods of the measure calculation were consid-

ered —- the sum of pixel intensities and the measure using Laplacian.

The experiments show that image segmentation based on using density function is a practical tool for analysis. Moreover, using the Laplacians leads to better segmentation and separability of multifractal spectra.

Acknowledgements

The work was partially supported by the grant RFBR 13-01-00782.

References

[1] N. Ampilova, E. Gurevich, I. Soloviev. Application of Modified Fractal Signature & Regny Spectrum Methods to the Analysis of Biomedical Preparations Images. Proc. 6 Int. Conf. CEMA11, 6-8 Oct. 2011, Sofia, Bulgaria. p. 96-100.

[2] N. Ampilova, I. Soloviev, Y. Shupletzov. Multifractal spectrum as a classification sign for biomedical preparations images. Proc. 7 Int. Conf. CEMA12, 8-10 Nov. 2012, Athens, Greece. p.98-101.

[3] N. Ampilova, I. Soloviev, Y. Shupletzov. On some aspects of the fractal signature method. Proc. 8 Int. Conf. CEMA13, 17-19 Oct. 2013, Sofia, Bulgaria. p.80-84.

[4] Ashvin B. Chhabra, Charles Meneveau, Roderick V. Jensen and K.R. Sreenivasan.Direct determination of the f(α) singularities spectrum and its application to fully developed turbulence - Physical Review A, Volume 40, Number 9, November 1,1989. pp. 5284-5294.

[5] Falconer K.J. Fractal Geometry. Mathematical Foundations and Applications. – John Wiley & Sons, 1990.

[6] R. Gonzalez, R. Woods. Digital image Processing, 2002, Prentice Hall.

[7] Linda G.Shapiro, George C. Stockman. Computer Vision, New Jersey,Prentice Hall, 2001, p.279-325. (ISBN 0 -13-030796-3).

[8] Y. Shupletsov. On some aspects of direct calculation of the multifractal spectrum. Proc. Conf.«Herzenovskie chtenia-2014», 14-18 April, 2014, Saint-Petersburg, Russia, p.247-251. (in Russian).

[9] M. Voorons, Y. Voirun, G. B. Benie, K. Fung. Very high spatial resolution image segmentation based on the multifractal analysis. , 2012, ISPRS (International Society for Photogrammetry and Remote Sensing) congress; Available at: http://www.isprs.org/proceedings/XXXV/congress/comm7/papers/7.pdf.

[10] Xu Y., Ji H., Fermüller C. Viewpoint Invariant Texture Description Using Fractal Analysis. — International Journal of Computer Vision, no. 83, 2009, pp. 85–100.

ALGORITHMS OF INTERPOLATION AND VISUALIZATION OF LOW FREQUENCY MAGNETIC FIELD BY USING EXPERIMENTAL DATA

B. Kudrin

St. Petersburg State University, Faculty of Math. & Mech., Postgraduate student at Comp. Sci. Dept, 198504, SPb, Universitetsky pr.28, bogdan.kudrin@gmail.com

V. Nikolov

Faculty of Telecommunication,Techical University of Sofia

Abstract

For a special magnetotherapy device (magneto bed) the magnetic field is measured in special points and obtained as a set of scalars. The measurement points are: the centers of coils and the middle of the interval between centers. At any moment only one pair of coils is active. The order of the choice of pairs of coils is defined by a data table. We present the algorithms of the interpolation of magnetic induction value in a given point of an interval and visualization of results.

1. INTRODUCTION

For a magneto bed it is possible to measure the induction value in the coils centers and in the middle of the connecting them line. The results are scalar.In [1] we proposed a mathematical model for the interpolation on the obtained data. In this work we describe the algorithms of interpolation and visualization of results.

2. THE STATE OF THE PROBLEM

We consider the following magnetotherapy device.

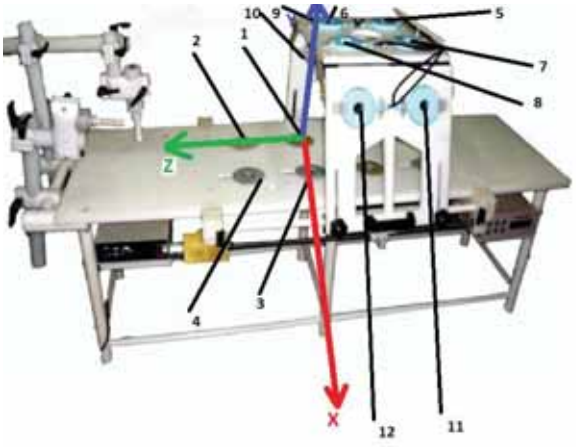

Fig. 1. Magnetotherapy device

The number of every coil and the coordinate system XYZ are shown on the Fig.1. Measurement has been done for every pair of coils. The first coil of pair is denoted by "A" in the table and the second coil in the pair by "B". In the table there are coordinates of every point of measurement. For every pair of coils the measurements have been done at 3 points. The first and the second points are in the centers of the two coils and the third point of measurement is on the middle of the line between the centers of two coils of the pair. In every moment only one pair of coils is active. In the process of the system functioning every pair of coils is active by turns, and a movement of magnetic field occurs. The order of the choice of pairs of coils is defined by a data table. It is necessary to provide interpolation on the line of every pair of coils on the base of result of measurement in three points and visualize results.

3. MATHEMATICAL MODEL

As it was shown in [1] the most appropriate model in this case is L'Agrange one-dimensional square interpolation. The formulas for calculation are given below.

Here f_i are experimentally obtained values in interpolation nodes: $f_{\square}$ and f_2 are values in centers, $f_{\square}$ – in the middle of the segment.

For a point (x,y,z) consider the polynomial

$$\square(x,y,z) = \prod_{\square=\square,\square\neq i}^{2} \frac{\sqrt{(x-x_i)^2+(y-y_i)^2+(z-z_i)^2}}{\sqrt{(x_{\square}-x_i)^2+(y_{\square}-y_i)^2+(z_{\square}-z_i)^2}}$$

such that

$$\square(x_i,y_i,z_i) = \square, i \neq \square$$

$\square_i(x_i, y_i, z_i) = \square$,

where l_i – the basic polynomial for the node (x_i,y_i,z_i).

Interpolation polynomial has the form:

$$L(x, y, z) = \sum_{\square=\square}^{2} f_{\square} \cdot \square(x, y, z)$$

where f_n – the value obtained by the measurement in the point (x_n,y_n,z_n).

Hence to obtain the interpolation value in a point we should calculate the interpolation polynomial in this point.

4. VISUALIZATION CHOICE

As the electromagnetic induction value continuously depends on the point position, for any given pair of coils we at first calculate the induction value in all the points of the segment by step 1 mm. Then we show the obtained distribution of the induction values in a special area in the interface in accordance with the following scheme (B denotes the induction value).

$B \in [\square, \square]$ –> blue
$B \in [\square, \square]$ –> lightblue
$B \in [\square, \square]$–>yellow
$B \in [\square, d]$ –> orange
$B > d$ –> red

The user can choose the values of parameters a,b,c,d defining the color distribution. In this implementation the segment [0, d] is partitioned on 5 equal parts, where d is the maximal value of induction in the points calculated. Thus the diagram of color distribution is in agreement with the position of the point the user choose to interpolate.

5. ALGORITHMS

5.1. Interpolation algorithm

1. Choose the row from data file (the pair of active coils)
2. Write chosen data into the array for interpolation
3. Select a point for interpolation
4. Interpolation
5. Is a new pair was chosen?
   Yes – go to 1
   No – go to 4

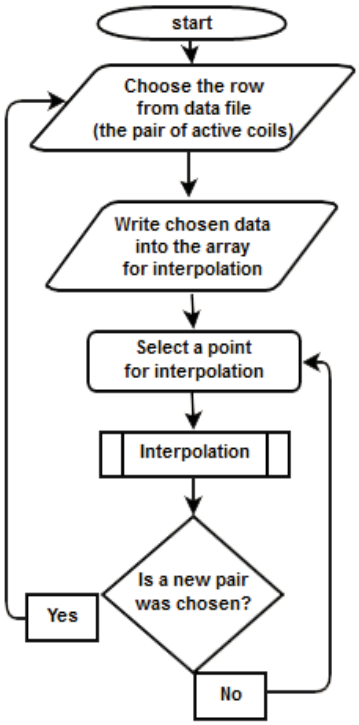

Fig. 2. Interpolation algorithm

5.2. Visualization algorithm

1. Choose the row from data file (the pair of active coils)
2. Write chosen data into the array for interpolation
3. In cycle interpolation in the points of the segment connecting the centers of coils by step 1 mm
4. Visualization of color distribution diagram

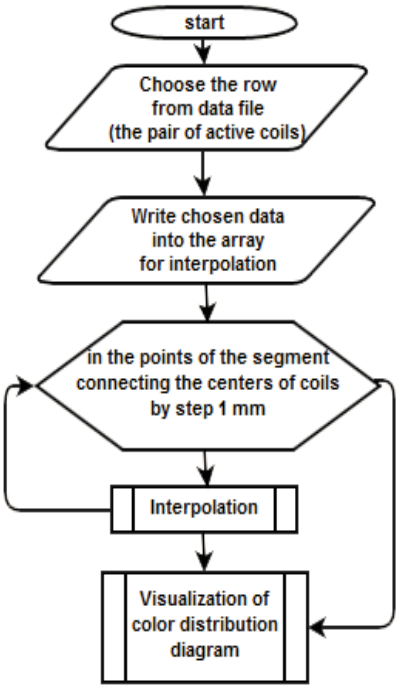

Fig. 3. Visualisation algorithm

5.3. The combined algorithm

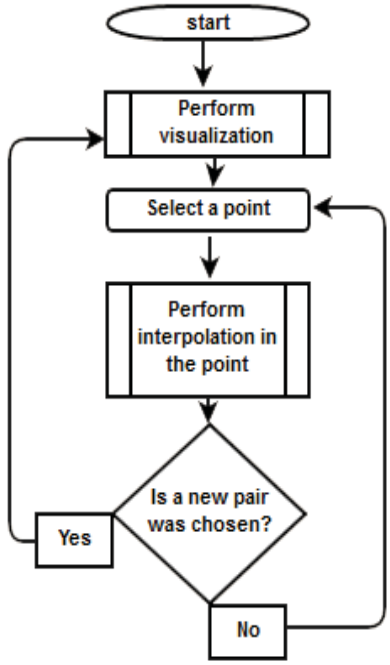

Fig. 4. Combined algorithm

1. Perform visualization
2. Select a point
3. Perform interpolation in the point
4. Is a new pair was chosen?
   Yes — go to 1
   No — go to 2

6. USER INTERFACE

The interface is shown below, digits note main fields.

Fig. 5. User interface

The user poinst the path to the input file with data obtained in results of experiments (element Input file has .txt format, columns are separated by tab symbol. In the field 2 one can chose a pair of coils (row number in the data table). Elements 3 and 4 are for input of the interpolation point. In 3 we select a point by slider, by using 4 we should point a distance the interpolation point from the left end of the segment. When changing data in 3 or 4 the result of interpolation is shown in 5 in real time. Note that color distribution diagram is drawn in element 6 immediately after the choice of coils, in doing so the position of slider corresponds the diagram.

All the described areas of the interface are shown on Fig. 5.

CONCLUSION

The algorithm of interpolation and visualization of value electromagnetic induction by using experimental data has been designed and implemented. Interpolation in a given point is performed in real time.

Acknowledgements

The work was partially supported by the grant RFBR 13-01-00782.

References

[1] B. Kudrin, V. Nikolov, D. Dimitrov. On the mathematical model of interpolation of low frequency magnetic field using experimental data. Proc. 9 Int. Conf. CEMA14. 16-18 Oct. 2014, Sofia, Bulgaria, p.

[2] D. Dimitrov. Medical Systems for Influence of Electromagnetic Field on the Human Body (in Bulgarian), Sophia, Technical University, 2008.

[3] Bekiarski Al., Sn. Pleshkova, Microphone Array Beamforming for Mobile Robot, The 8th WSEAS International-Conference on CIRCUITS, SYSTEMS, ELECTRONICS, CONTROL &SIGNALPROCESSING, (CSECS'09), Puerto De La Cruz, Spain, 2009, pp.146-150

[4] Alexander Bekiarski, Snejana Pleshkova, Svetlin Antonov, "Real Time Processing and Database of Medical Thermal Images", 4rd INTERNATIONAL CONFERENCE on Communications, Electromagnetics and Medical Appli-cation (CEMA'11), Sofia,2011, pp.101-106

[5] Stamboliev I., Medical equipment, Technika, Sofia, 1989

ON MODELLING OF DIFFUSION LIMITED AGGREGATION PROCESSES ON TRIANGULATION NET

N. B. Ampilova

St. Petersburg State University, Math. & Mech. Faculty, n.ampilova@spbu.ru

A. M. Batyukov

St. Petersburg State University, Math. & Mech. Faculty, batsun@gmail.com

Abstract

The implementations of diffusion-limited aggregation algorithms both on the plane lattice and a surface approximated by irregular triangulation net are described. The optimization of the method based on the a priori estimation of the sticking probability of a particle to the aggregation (joining coefficient) has been proposed and realized. The algorithm complexity estimation and results of numerical experiments are described.

1. INTRODUCTION

Many processes both in nature and society have chaotic dynamics resulting in appearance of complex fractal structures characterized by statistical (noncomplete) recurrence.

These objects are often called by chaotic fractals. Fractal clusters are the class of chaotic fractals such that their density decreasing when the cluster grows.

The investigation of fractal clusters began with a theoretical model of Diffusion Limited Aggregation (DLA) process that describes the aggregation of particles in conditions of their random walking. Later the models of Cluster-Cluster Aggregation (CCA) and Reaction-Limited Cluster Aggregation (RLCA) were proposed. One can find their detail description in [5].

The DLA model describes the growth of groups of particles (called aggregates) when the particles perform random (Brownian) walks on the sides of rectangle lattice on the plane. This model was considered in [4] by Witten and Sander and by Pinski in [7]. It seemed to be widely applicable for simulation such processes as metal deposition in electrolysis, propagation of electric discharge in dielectric breakdown, diffusion in liquids and gases.

Implementation of algorithms for DLA modelling is rather time-consuming. There are variants of optimization for the Pinski algorithm that result in a reducing run-time for aggregates containing a large number of particles. Some of them are given in [6]. One way of optimization is to allow walking for one step on the distance more than 1. Another way is to specify an initial vector of translational motion for a particle and add this vector to the particle free movement on every step of walking.

In [1] we implemented the optimization of basic algorithm for DLA model on the plane, which was based on the calculation of a priori estimations of the probabilities of a particle joins to boundary points of the aggregate. That reduced run-time more than 10 times in average.

A natural generalization of the algorithm DLA on the plane is to consider a surface in R^3. Such an algorithm was proposed and implemented in [2], where the surface was approximated by irregular triangular net. The implementation of the algorithm shows that, as in case of the plane, the construction of an aggregate from a large number of particles requires a great deal of time.

In this work we propose an optimization method for DLA on irregular triangular net by using a priori estimation of joining probability. As in [2] we assume that transitions between triangles of the net have different probabilities. Experiments show that we obtain considerable run-time reducing for repeated construction of aggregate.

2. DLA MODEL ON THE PLANE

In accordance with basic DLA model particles walk on sides of rectangular lattice. Particles join to the aggregate one by one. The aggregate formation starts with a particle being in the lattice coordinate

origin. The initial position of the following particle is defined in a random way. This particle starts walking on the lattice sides, in doing so on every step it may move with the probability $^1/_4$ to one of points which are one the distance 1 from it. The process continues for as long as the particle became adjacent with a particle from the aggregate. Then it connected with the aggregate by a segment and is considered as the aggregate part. This process is repeated.

In practice one should consider additional restrictions: a particle is thrown in a given neighbourhood of the aggregate, being the number of walking steps is supposed not greater than N. If the particle does not join to the aggregate for N steps, we consider the following one.

3. OPTIMIZATION OF DLA MODEL ON THE PLANE

In [1] we describe an implementation of the based algorithm which used a priori estimation of joining coefficients. This estimation depends on the initial distance between points: if two points are on the distance *a* on X and *b* on Y then the joining coefficient for them is $\frac{1}{4^{a+b}}$.

For each particle throwing on the plane with using of its initial coordinates we calculate all the joining coefficients to the boundary points of the aggregate. Then according to the coefficients we construct a distribution function ["numerical distribution function", 3] and chose randomly a number from the function value area. The proimage of the number determines the point of the aggregate which the particle joins to.

Hence, we do not consider all the possible paths by which a particle can join to the aggregate and lost an information. But experiments show that such an approach leads to the considerable run time reducing, in doing so the structure of the cluster practically does not differ from the results given by the classical model.

Given M points on the rectangle lattice we calculate joining coefficients for all pairs of points and form of them matrix G with size MxM such that G(i,j) is the a transition probability for a particle to move from the point i to j. It is easy to understand that for the pairs of points that have the same values $s = a + b$ joining coefficients are also the same and equal to $^1/_{4^s}$. Hence it is not necessary to use a matrix to save obtained values. However such a matrix will be useful in the sequel.

4. ADAPTATION OF DLA MODEL FOR TRIANGULAR NET

In [2] authors described an implementation of DLA algorithm on irregular triangular net. The initial particle is in a given triangle. Next, a new particle initiates its random walk on the net. On every step the particle can move to one of adjoining triangle with a probability depending on lengths of sides, providing that one particle only can occupy each triangle. For any adjoining triangles 1 and 2 the particle transition probability to move from 1 to 2 is calculated by the formula,

$$P(1 \to 2) = \frac{^1/_a}{^1/_a + {}^1/_b + {}^1/_c} \qquad (1)$$

where a, b, c – are lenths of sides for the triangle 1 (Fig.1).

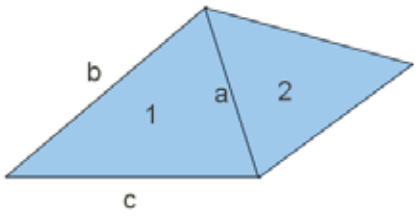

Fig. 1. Calculation of the transition probability

As the example of the application of the described algorithm the process of a matter distribution on bone surface was modelled. As in the case of the plane, to computer aggregation consisting from a large number of particles we need a considerable time.

5. OPTIMIZATION OF DLA MODEL FOR TRIANGULAR NET

Construct on a given area of the surface an irregular triangular net. Let the number of triangles to be M.

Consider an oriented graph $\square_{\square}$ with M vertices. To every triangle M_i we match a vertex i in $\square_{\square}$. There is the edge (i,j) iff M_i и M_j have a common side. Every edge (i,j) has a weight $\square(i, \square)$ calculated in accordance to (1).

Consider all the paths on $\square_{\square}$ that have the length not greater than N. The weight of a path between i and j is a production of weights of all the edges.

Choice coefficient for vertex i and j we define as the sum of weights of all the paths by length not greater than N between the vertices. The obtained coefficients save in a matrix G with size MxM.

To obtain the choice coefficients we use the following algorithm. Let on the initial step $\square = \square_{\square}$, where $\square_{\square}$ consists of weights of all the paths by length 1, i.e $\square(i, \square) = \square(i, \square)$. Form $\square_2$ containing weights of all the paths by length 2 by the following way. For a given pair (i,j) consider all the edges starting from j: $\square(\square, \square)$. There are not greater than 3 such edges because every triangle has not greater than 3 adjoining ones. Then we calculate length of the path by length 2 as $\square(i, \square) = \square(i, \square) \square(\square, \square)$ and set $\square_2(i, \square) = \square(i, \square)$. Hence, given $\square_{\square}$ we construct $\square_{\square+\square}$ by above way. Summing up all $\square_{\square}$ for k=1,…N we obtain G.

Time complexity for the algorithm of G construction is $O(NM^2)$. By the definition on the path weight (transition between vertices are independent) we do not need to save all the $\square_i$ obtained to the step k, but only G_1, G_k and G. Thus the memory size is proportional to M^2.

The modelling of particles throwing is performed in accordance with choice coefficients by the same way as for the plane. For T particles time complexity is $O(TM)$.

We see that as opposed to the case of the plane, for the modelling on a surface the matrix structure is essential. In fact this matrix saves an information about the triangulation structure.

The calculation of G for M large enough is time-consuming and when computing the aggregate one time we do not obtain a considerable advantage. But, as a rule, the studying of dynamics of processes on a surface to collect statistical data requires repeated experiments. Hence it is the great advantage that G is calculated one time and reused in what follows without changing.

We implemented two algorithms to construct an aggregate on irregular triangle net: proposed in [2] and based on a priori estimation and choice coefficients. The experiments were performed for the surface $\frac{x^2}{4} + \frac{y^2}{4} - z^2 = 1$ and the following parameter values: NA (the number of aggregate) is equal to 1 and 10, N = 300, M = 5000, T = 1000. Run times are shown in the table.

NA	Basic algorithm	Optimized algorithm
1	26 m. 12 s.	29 m. 43 s.
10	4 h. 47 m. 33 s.	31 m. 58 s.

6. CONCLUSION

The optimization of the algorithm of the construction of aggregate in accordance with DLA model on irregular triangle net has been designed and implemented. It is efficient when repeating experiments. Such an optimization may be applicable to other models of cluster forming.

Acknowledgements

The work was partially supported by the grant RFBR 13-01-00782.

References

[1] Batyukov A.M., Ampilova N.B. The modified algorithm DLA modelling. – Nauchno-tehnicheskie vedomosti SPbGPU. Informatika. Telekommunikacii. Upravlenie. Vipusk 3(174)/2013, ISSN 2304-9766 - СПб.: Izd. RPGU im. A. I. Gerzena, 2013, p.233-238. (in Russian)

[2] Evseev A.A., Nechaeva O.I. Kletochno-avtomatnoe modelirovanie diffuzionnih protsessov na trianguliatsionnih setkah. – Prikladnaia discretnaia matematika. Vipusk 4(6)/2009 - Tomsk: Izd. Tomskogo un-ta., 2009, p. 72-83. (in Russian)

[3] Knuth D. The Art of Computer Programming, vol.2. Seminumerical Algorithms, 3-ed edition. - 2001

[4] Pinski A. Diffusion-limited aggregation. - Physical Review. The American Physical Society. USA. - 1981.

[5] Smirnov B.M. Phisika fractalnih clasterov. // M., Nauka – 1991. (in Russian)

VISUALIZATION OF THE STUDY FOR SPACE-TIME CONFIGURATION OF THE ELECTROMAGNETIC FIELD EMITTED BY EQUIPMENT FOR MICROWAVE THERAPY

Antoniya P. Petrova, Dimitar C. Dimitrov

Faculty of Telecommunications, Technical University of Sofia, Bulgaria
1000 Sofia, "Kl. Ohridsky" str.8
E-mail: tony.petrova@gmail.com

Abstract

The aim of this paper is to show the real dimensions of space - time configuration of the electromagnetic field in a near field area brought by symmetric and asymmetric dipole antenna used in microwave therapy. The bandwidth of these devices is in the range of 2 GHz to 3 GHz, thus resulting in a more effective treatment. These frequencies and wavelengths are the most efficient and enables much more deeply and better adjustability of the action intensity of warming. It's difficult to be provided one exact mathematical description of electromagnetic field in this area taking in account deformation of this field because of live tissues additionally. Because of that one experimental investigation of electromagnetic field in the patient's area would be useful in this case.

1. INTRODUCTION

The experimental measurements of the electromagnetic field in actual clinical environment were carried out for the most commonly used therapy modes, i.e. uninterrupted radio emission and in the near field area of emission since this is the interesting are when speaking for medical physiotherapy systems. The energy in the near field area emitted by an antenna with maximum allowed size ans yet still small compared to the wavelength is mostly reactive. Thus the accumulated energy is transmitted periodically between the antenna and the the near field area. The reactive near-by field extends from the antenna to a distance "R" from the antenna, which in our case is equal to 30 cm.

2. THEORETICAL SOLUTION

When it comes to medicine, wavelengths of 12.2cm, 12.4cm and 12.6 cm are most commonly used, which are close to UHF. In fact, the equipment is mainly operating at power up to 200W and 2450 MHz wave frequency. For the conducted measurements exploring the space-time configuration of patient area is used transmission frequency close to the most commonly used frequency - 2.45 GHz with a wavelength of 12.44 cm.

When irradiating of homogeneous tissue, the heat is distributed in depth exponentially. It is clear that the distribution of endogenous heat inside the body is mainly determined by the space-time configuration of the electromagnetic field created by emitters in medical microwave therapy, therefore, the knowledge of this configuration is essential for achieving the desired healing effect.

The discovery of analytical and mathematical calculation models for exploring of space-time configuration of the electromagnetic field created by the emitter boils down to the calculating of the parameters of the radiation field from the emitting surface in general and in particular concerning the patient area. The generated heat is determined by the geometry of the emitters of the microwave device (its antennas), how they were positioned on the body, the frequency of the electromagnetic field, the electrical conductivity of the tissue and their dielectric properties.

Figure 1 and Figure 2 show the two experimental settings.

Fig. 1. Setting with asymemetric dipole antenna

Fig. 2. Setting with symemetric dipole antenna

Measurements of power density were carried out at various points along the legth of the patient's bed. The purpose of measurement is to determine the space configuration of the electromagnetic field in the near field area of the antenna system (surface of the patient), as well as to determineing the intensity maximums created by the antenna. In this case it could be usefull to deal with relative units of power. Of course, these values refer to the absolute values with a coefficinet. Two types of antennas are measured according to the treated area of patient's body at a distance of 30 cm from the patient bed. [1]

3. RESULTS AND ILLUSTRATION OF THE EXPERIMENTAL INVESTIGATION OF THE ELECTROMAGNETIC FIELD

The first one is an asymmetric vibrator which is typically used for already determined areas (eg elbow, wrist, knee, foot) or by paediatrics. The second antenna is symmetrical vibrator used for treating areas like a neck, shoulders back or pelvis. [2]

Due to high levels of both types of antennas attenuators were used to reduce the signal strength. For the measurements of the first antenna were used 70 dB and 80 dB power reduction, while the second the reduction was only 40 dB. A special device for measuring the power of the electromagnetic field was used in the experimet - HF Analyser 38B by GigaHerzt Solution company and the period for measuring the values was 3 seconds. The measurement device and the antennas with which the data were obtained are shown in Figure 3 and Figure 4.

As you know, essential in measuring here is the polarization of the antenna - whether it is vertical or horizontal. With the antenna attached the meter measures the vertically polarized component, if the display is positioned horizontally. By rotating the meter around its longitudinal axis you will be able to pick up any polarization plane. Due to the physics of wave generation it is not possible to reliably measure the customary "power density" (W/m^2) in the close vicinity of the source of radiation. For the instruments described here, the distance should be in excess of 30 cm. For the measurements were taken the peak values of the power density through the special option of the HF Analyzer.

Fig. 3. The metering device and antenna

Fig. 4. The measuring antenna

In Table 1, Table 2 and Table 3 are shown in relative units of the measured power values of the field, as well as the length of the patient bed, and perpendicular to it at the asymmetric dipole antena. Figure 5, Figure 6 and Figure 7 show the results graphically, at 70 dB and 80 dB gain.

Table 1. Relative values of the measured power P in perpendicular placement of the antenna in the patient area, 70 dB gain

Lenght, cm	1	2	3	4	5	6	7	8	9
Power P, relative units, 70 dB gain	12.7	15.48	15.7	19.3	16.2	16	8.5	11.87	12

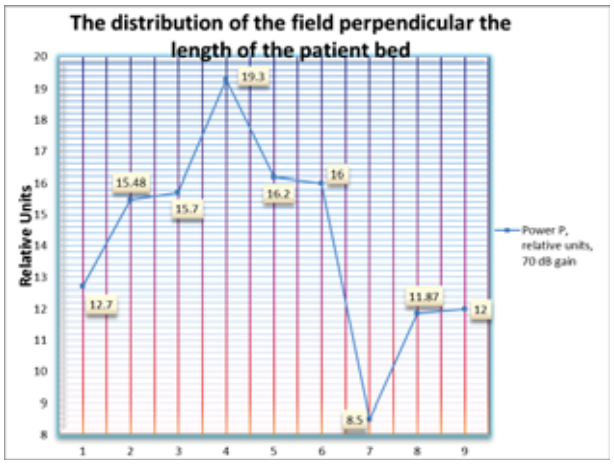

Fig. 5. Graph of the measured values of the power P in perpendicular placement of the antenna in the patient area, 70 dB gain

Table 2. Relative values of the measured power P in perpendicular placement of the antenna in the patient area, 80 dB gain

Lenght, cm	1	3	5	7	9	11	13	15
Power P, relative units, 80 dB gain	1.44	1.21	0.93	1.51	1.7	1.61	1.71	1.1
Lenght, cm	17	19	21	25	30	35	40	
Power P, relative units, 80 dB gain	0.81	1.07	0.83	0.65	1	0.35	0.58	

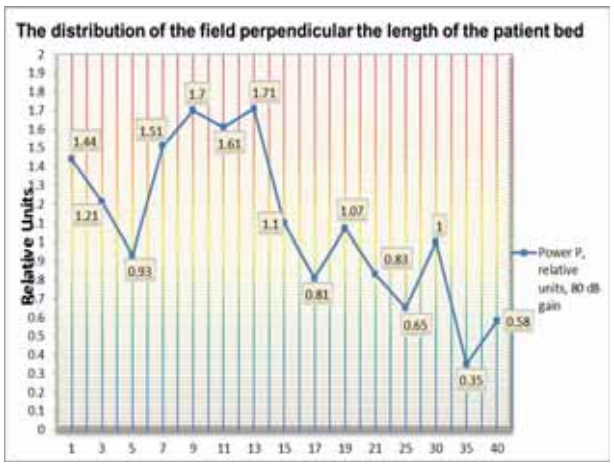

Fig. 6. Graph of the measured values of the power P in perpendicular placement of the antenna in the patient area, 70 dB gain

Table 3. Relative values of the measured power P in parallel placement of the antenna in the patient area, 80 dB gain

Lenght, cm	0	5	10	15	20	25	30	35
Power P, relative units, 80 dB gain	1.63	1.1	0.7	1.01	0.95	0.7	0.68	0.65

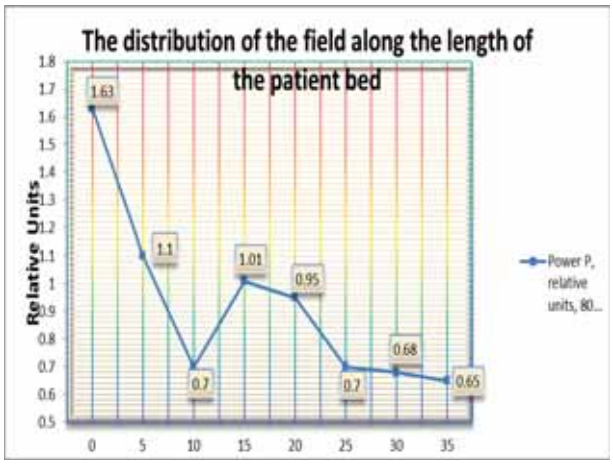

Fig. 7. Graph of the measured values of the power P in parallel placement of the antenna in the patient area, 70 dB gain

Table 4 and Table 5 show the relative units of the measured power values of the field, as well as the length of the patient bed, and perpendicular to it at a symmetric dipole antena. Figure 8 and Figure 9 depicts the results graphically at 40 dB gain.

Table 4. Relative values of the measured power P in perpendicular placement of the antenna in the patient area, 40 dB gain

Lenght, cm	0	2,5	5	7,5	9	11,5	13	15	17,5	20	22,5
Power P, relative units, 40 dB gain	8.45	17.35	16.18	17.6	18.05	36.51	38.92	36.37	36.84	37.3	24.94
Lenght, cm	25	27,5	29	32,5	35	37,5	40	45	50	55	60	65
Power P, relative units, 40 dB gain	25.55	26.1	32.32	29.7	27.9	23.93	27.75	27.4	26	30.5	26	28.34

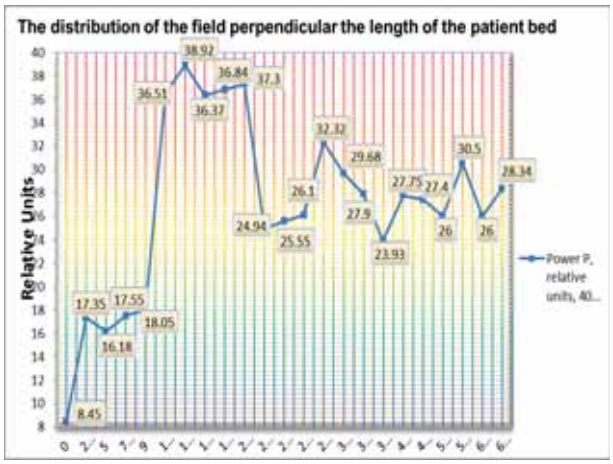

Fig. 8. Graph of the measured values of the power P in perpendicular placement of the antenna in the patient area, 70 dB gain

Table 4. Relative values of the measured power P in parallel placement of the antenna in the patient area, 40 dB gain

Lenght, cm	0	5	10	15	20	25	30	35
Power P, relative units, 40 dB gain	28.1	27.4	28.6	23.7	31.65	29.06	26.5	23.4

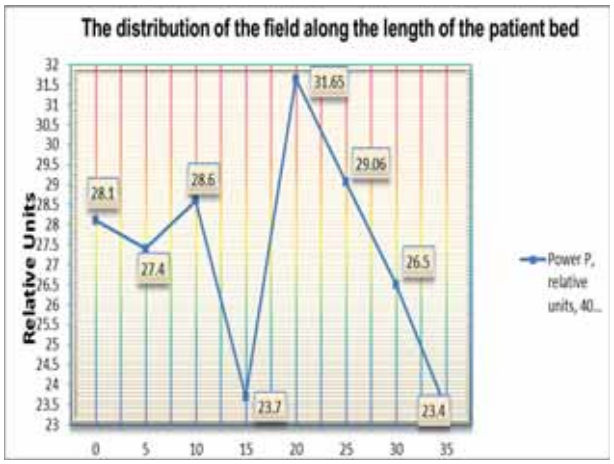

Fig. 9. Graph of the measured values of the power P in parallel placement of the antenna in the patient area, 70 dB gain

7. CONCLUSION

In conclusion we can say that these waves penetrate deep into the human body and have very good therapeutic effect, which leads to their frequent use. Therefore, it is necessary to study them and in particular the characteristics of the electromagnetic field at the near field area, together with the optimization of the space-time configuration of the electromagnetic field. This is crucial to achieve the desired therapeutic effect.

References

[1] D. Dimitrov, Medical systems influence of electromagnetic fields on human,education book, TU-Sofia,2007

[2] W. Y. Riadh, "Electromagnetic Fields and Radiation (Human Bioffects and Safety)",Marcel Dekker Inc. Canada,2001,ISBN 0-8247-0877-3

DESIGN OF RADIO CHANNEL FOR DVB-T SYSTEM

Lidia Jordanova, Georgi Karpov, Dobri Dobrev

Technical University of Sofia
Faculty of Telecommunication, Technical University of Sofia,
8, Kl.Ohridski, str.1000 Sofia, Bulgaria
Email: jordanova@tu-sofia.bg, karpov21g@gmail.com, dobrev@tu-sofia.bg

Abstract

The paper deals with the influence of transmitter parameters, the distance between transmitter and receiver, the propagation losses, the channel coding and modulation on the quality of received video information in DVB-T systems. A mathematical model to determine the dependence of field strength from distance to DVB-T transmitter is presented. Expressions for calculating of minimum carrier-to-noise ratio (CNR) at the input of DVB-T receiver, necessary for quasi-error-free reception, are given. The dependence of minimum mean field strength at the receiver input from CNR is derived and the algorithm for determination of maximum distance to the transmitter is described.

1. INTRODUCTION

The main difficulty in terrestrial television broadcasting systems is multipath radio signal propagation that causes intersymbol interference (ISI), from where, the bit error probability in received video and audio information, increases. As is known, required quality of the received digital TV programs is achieved when BER at the input of MPEG-4 demultiplexer is less then 10^{-11}. This criteria corresponds to Quasi Error Free (QEF), it means less than one uncorrected error event per hour of system's work [1]. In DVB-T systems the criteria for QEF receiving can be achieved by using two-step Reed-Solomon - convolutional channel coding, COFDM method of transmitting the signal through radio channel and special diversity antennas with received signals combining [2].

For evaluating the quality of received TV programs in DVB-T system, the three different criteria are used: the carrier-to-noise ratio (CNR) required for quasi-error-free reception, the available useful data rate and the field strength required for different reception modes. There are four reception modes, namely, fixed reception with rooftop antenna, portable outdoor and indoor reception and mobile reception. Specific for mobile reception is that receiver moves relative to the transmitter, this causes Doppler effect in communication channel.

The planning of digital terrestrial broadcasting systems can be divided into two main stages. The first step is to define the dependence of field strength from distance to transmitter antenna, taking into account conditions of signal propagation, requirements to percentage of coverage and percentage of time, during which the given reception quality is supported. The second stage of the planning is determination of minimum median field strength at the receiver input, required for quasi-error-free reception for different parameters of DVB-T signal and different reception conditions. After the minimum median field strength is calculated, the service zone of a given DVB-T transmitter can be estimated, using dependences from the first step of design.

The aim of this research is to derive relationships for determination of field strength at the receiver input that is required for quasi-error-free reception, considering the parameters of DVB-T transmitter and receiver and distance between them, the communication channel parameters, the modulation type and parameters of channel codes.

2. DEPENDENCE OF FIELD STRENGTH FROM DISTANCE TO TRANSMITTER

Dependences of field strength E (dBμV/m) against distance d (km) to transmitter antenna are given in form of tables and graphics in ITU-R recommendations. The values are obtained on the base of measurements and theoretical considerations and ensure that value of field-strength is exceeded for 50% of locations for time percentages 50%, 10% and 1% of system work. These dependences correspond to equivalent radiated power (ERP) of 1 kW in the direction of the reception point, or respectively, 1.637 kW equivalent isotropic radiated power (EIRP), and receiver antenna height 10 m

above ground level. The recommendation contains dependence of E from d for different frequency bands, transmitter antenna heights and geographical zones.

When developing the algorithm of designing the DVB-T system, it is necessary to derive dependence of field strength from distance to transmitter. This requires the selection of an adequate model that describes losses in communication channel. Suitable for this purpose is semi-empirical Hata-Okumura model. Number of modifications of this model exists, as comparison suggests that the ITU-R P.529-3 model is the most suitable for general use and for frequencies above 500 MHz and is the most close to Okumura model [3].

Modified model ITU-R P.529-3 of Hata-Okumura model for determination of propagation losses L (in dB) has the following form:

$$L = 69.82 + 6.16 * \lg(f) - 13.82 * \lg(h_t) - \\ - \alpha(h_r) + \left[44.9 - 6.55 * \lg(h_t)\right] \lg(d)^b , \quad (1)$$

where f is working frequency in MHz, h_t – transmission antenna height in m, $\alpha(h_r)$ – gain correction factor of receiver antenna, considering antenna height h_r, in dB, d – distance between transmitter and receiver in km.

For determination of receiver antenna correction factor, the following expression is used:

$$\alpha(h_r) = \left[1.1 * \lg(f) - 0.7\right] h_r - \\ - \left[1.56 * \lg(f) - 0.8\right]. \quad (2)$$

The value of power index b for d ≤ 20 km is 1, and for d > 20 km it is calculated with the following formula:

$$b = 1 + \left(0.14 + 1.87 * 10^{-4} * f\right) * d^{\Delta} + \\ + \left(1.07 * 10^{-3} * h_t^{\Delta}\right) * d^{\Delta}, \quad (3)$$

where

$$d^{\Delta} = \left[\lg(d/20)\right]^{0.8} \text{ and} \quad (4)$$

$$h_t^{\Delta} = h_t \Big/ \left(1 + 7 * 10^{-6} * h_t^2\right)^{1/2}. \quad (5)$$

This model is suitable for use over the following ranges of input parameters:

150 MHz ≤ f ≤ 1500 MHz,
30 m ≤ h_t ≤ 200 m,
1 m ≤ h_r ≤ 10 m,
1 km ≤ d ≤ 100 km.

By known equivalent isotropic radiated power of transmitter (EIRP) in dBW, signal propagation losses from transmitter to receiver L in dB and radiated signal frequency f in MHz, the power flux density at receiving point Φ in dBW/m^2 can be found, as for the purpose following expression is used:

$$\Phi = EIRP - L + 20\lg f - 38.55 \quad (6)$$

The following formula is obtained to determine field strength at receiver point E is dBμV/m:

$$E = \Phi + 120 + 10\lg\left(Z_{c0}\right) = \Phi + 145.76 , \quad (7)$$

where Z_{c0} = 120π is free space wave impedance.

Dependences of field strength from distance to transmitter for three transmitter antenna heights are shown on Fig. 1. The dependences refer to the case, when EIRP = 32.15 dBW, and f = 600 MHz.

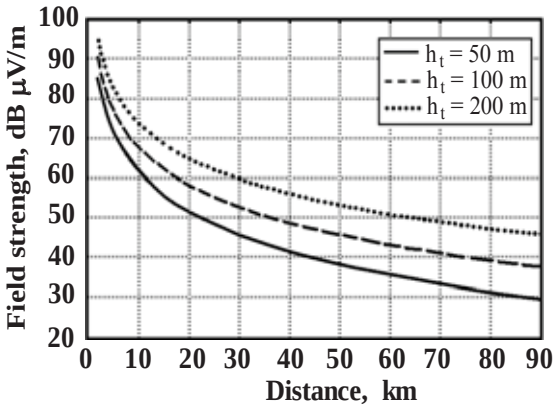

Fig. 1. Field strength for a given distance to receiver and transmitter antenna height

If the output transmitter power P_t in W is given, the following expression is used to calculate EIRP in dBW:

$$EIRP = 10\lg(P_t) + G_t - L_{\Sigma} \quad (8)$$

where G_t is the gain of transmitter antenna in dBi and L_{Σ} is the transmitter feeder losses in dB.

3. ACCEPTABLE CNR AT THE INPUT OF DVB-T RECEIVER

To provide QEF reception, it is necessary BER at the output of channel decoder not to exceed 10^{-11}.

The value of BER depends on CNR at the input of DVB-T receiver, roll-off factor *α* of digital filter at the output of demodulator (α = 0.35), code rates of Reed-Solomon code and convolutional code, modulation method (number of bits per symbol, m) and working mode of the system (2K or 8K).

In DVB-T systems the shorted Reed-Solomon code RS(204,188,8) is used with rate $R_{RS} = 0.92$. The convolutional code rate R_C can be 1/2, 2/3, 3/4, 5/6 and 7/8. For modulation of subcarriers the following methods are used: QPSK, 16QAM и 64QAM (value of m for these modulations are respectively 2, 4 and 6).

The two modes of work of DVB-T system differs in number of subcarriers in OFDM symbol, that is 1705 (2k) and 6817 (8k). In both modes the ratio of guard interval length (τ) and OFDM symbol length (T_U) can be τ/T_U = 1/4, 1/8, 1/16 and 1/32.

Also, the type of communication channel must be considered when determining the CNR. The channel is characterized with Rice fading when right path between transmitter and receiver exists, and when there is no right sight, the channel is characterized with Rayleigh fading and received radio signal is formed from reflected copies of transmitted signal. The channel with more complex conditions of signal propagation requires higher values of CNR ratio at the input of receiver.

In [4] are given expressions for determining the dependence of BER at the output of channel decoder from CNR at the input of DVB-T receiver, from covolutional code rate R_C and modulation type. These dependences are used to calculate the minimum CNR, required for QEF reception. Obtained values of CNR (in dB) for Rice and Rayleigh channels, when reception is fixed (FR), portable outdoor (PO), portable indoor (PI) and mobile (MO) are given in Table 1.

Table 1. Acceptable values of CNR

Modulation	R_C	Race channel	Rayleigh channel	
		FR	PO/PI	MO
QPSK	1/2	5,9	8,2	11,1
QPSK	2/3	7,9	10,2	13,2
QPSK	3/4	9,1	11,6	14,5
QPSK	5/6	10,3	12,8	15,8
QPSK	7/8	11,3	15,4	16,9
16-QAM	1/2	11,6	13,5	16,8
16-QAM	2/3	14,1	16,4	19,4
16-QAM	3/4	15,7	17,2	21,1
16-QAM	5/6	16,9	19,4	22,4
16-QAM	7/8	17,5	21,3	23,1
64-QAM	1/2	17,2	18,1	22,4
64-QAM	2/3	19,5	21,8	24,8
64-QAM	3/4	21,2	22,2	26,6
64-QAM	5/6	22,7	25,2	28,2
64-QAM	7/8	23,7	26,6	29,3

4. DEPENDENCE OF FIELD STRENGTH FROM ACCEPTABLE CNR

Large numbers of experimental and theoretical researches were conducted with purpose to find the dependence of field strength at the receiver input from minimum CNR, at which the QEF reception is provided. Obtained results for different conditions were described in detail and documented in resolutions of Regional Radio communication Conference (RRC-06) of ITU-R from 2006 year [5].

The following dependence was derived to determine the minimum field strength at receiving place E_{min} (in dBμV/m), necessary for QEF reception [5]:

$$E_{min} = P_{r\,min} - G_r - 10\lg\left(\frac{1.64\lambda^2}{4\pi}\right) + L_f\,, \qquad (9)$$

where $P_{r\,min}$ is acceptable minimum signal level at the DVB-T receiver input in dBW, G_r – receiver antenna gain related to half-dipole in dBi and λ – receive signal wave length in m, L_f – receiver feeder losses in dB.

The minimum level of receive signal is limited by acceptable values of CNR parameter and noise power P_n at receiver input:

$$P_{r\,min} = CNR + P_n\,. \qquad (10)$$

Values of CNR, which depend on type of communication channel, selected scheme of OFDM signal subcarrier modulation, convolutional code rate and receiving mode are given in Table 1. Levels of outer and inner noises at the input of DVB-T receiver are defined by formula:

$$P_n = 10\lg(k) + 10\lg(B_n) + 10\lg(T) + NF_r\,.' \qquad (11)$$

where $k = -1.38.10^{-23}$, W/K.Hz is Boltzmann's constant, B_n – receiver noise bandwidth in Hz (for channel bandwidth 8 MHz B_n = 7,61 MHz) , T = 290 K –

absolute temperature, NF_r – receiver noise figure in dB (according to ITU-R recommendations for DVB-T receivers NF_r = 7 dB).

Minimum mean field strength E_{med} at receiving place is used for design of DVB-T channel. Except E_{min}, it depends on the receiving mode and is calculated using following expressions:

$$E_{med} = E_{min} + P_{mmn} + C_l \quad \text{«FR»} \tag{12}$$

$$E_{med} = E_{min} + P_{mmn} + C_l + L_h \quad \text{«PO»} \tag{13}$$

$$E_{med} = E_{min} + P_{mmn} + C_l + L_h + L_b \quad \text{«PI»} \tag{14}$$

Coefficients used in these expressions, whose values are given in dB, account influence of following factors: man-made noise (P_{mmn}); characteristics of area of receiver location (C_l); losses from changing the height of receiver antenna relative to reference value, that is accepted to be 1.5 m above ground level (L_h) and mean building entry loss (L_b).

Dependences of mean minimum field strength in receiving place E_{med} (in dBμV/m) from minimum CNR value at the input of receiver (in dB) for fixed reception with rooftop antenna, portable outdoor reception and portable indoor reception are shown on Fig. 2. To obtain these dependences it is accepted that f = 600 MHz, L_f = 4 dB G_r = 11 dBi, and recommended by ITU-R values of coefficients from (11) - (13), namely P_{mmn} = 0 dB, C_l = 13 dB, L_h = 17 dB and L_b = 8 dB.

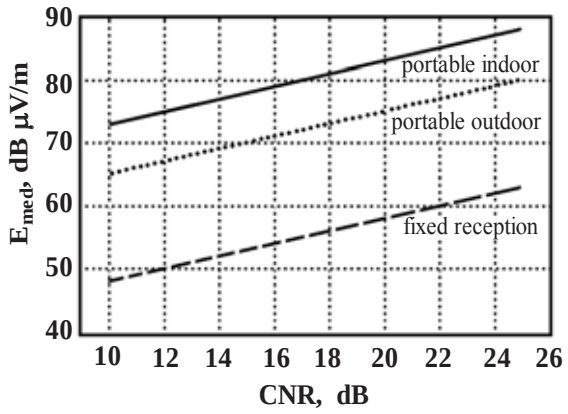

Fig. 2. Minimum median field strength corresponding to minimum CNR

Using obtained dependences easily can be found value of E_{med} necessary for minimum CNR and for QEF reception. For example, if modulation of subcarriers in OFDM symbol is 16QAM, convolutional code rate is R_C = 3/4, from Table 1 the following values of CNR are obtained: 15.7 dB (fixed reception) and 18.1 dB (portable indoor and outdoor reception). To ensure these values of CNR it is necessary field strength at receiving place E_{med} to be not less then 53.9 dBμV/m – for fixed reception (FR), 73.3 dBμV/m – for portable outdoor (PO) reception and 81.3 dBμV/m – for portable indoor (PI) reception.

5. SERVICE ZONE OF DVB-T TRANSMITTER

Service zone of DVB-T transmitter is characterized by field strength that is above minimum mean field strength E_{med}. As already explained, E_{med} depends on minimum acceptable C/N ratio at the input of receiver, radiated signal frequency f, receiver antenna gain G_r, noise parameters of receiver (B_n and NF_r) and selected above additional factors.

Minimum acceptable values of CNR parameter, taking into account modulation scheme, convolutional code rate and type of communication channel are given in Table 1. According to catalog data receiver antenna gain value typically varies in range from 5 to 40 dBi depending on number of its elements and its shape. Values of other parameters are chosen according to ITU-R recommendations for DVB-T systems.

To determine maximum acceptable distance between transmitter and receiver d_{max}, dependences given in the second section of the publication could be used, or graphical dependences from ITU-R recommendations, similar to those shown on Fig. 1. Accepting, transmitted EIRP is 32.15 dBW, radiated signal frequency f = 600 MHz and values of parameter E_{med} are 55.4 dBμV/m (for FR), 72.4 dBμV/m (for PO reception) and 80.4 dBμV/m (for PI reception). Then, to provide QEF reception for 95% of locations in service area for 50% of the time of transmitter work, it is necessary d_{max} not to exceed values given in Table 2.

Table 2. Maximum distance between transmitter and receiver in km

h_h, m	50	100	200
FR	15.7 km	25.2 km	43 km
PO	4.9 km	7.35 km	11.55 km
PI	2.7 km	4.2 km	6.25 km

6. CONCLUSION

Dependences for determination of field strength at receiving place, given in this publication, allow take into account parameters of DVB-T transmitter and

receiver, conditions of radiated radio signal propagation and mode of its receiving. These dependences are used for development of software, used for resolving some important problems, related to construction of terrestrial television networks. These problems are: determination of output power, antenna gain and antenna system directional properties for DVB-T transmitters and its service zone, creating conditions for QEF reception, while changing radio signal propagation conditions and signal reception mode and other.

8. APPENDIX AND ACKNOWLEDGMENTS

The research described in this paper is supported by the Bulgarian National Science Fund under the contract DDVU 02/74/2010.

References

[1] ETSI EN 300 744, Digital Video Broadcasting: Framing structure, channel coding and modulation for digital terrestrial television, 2009.

[2] W. Fischer, Digital Video and Audio Broadcasting Technology, Springer, 2008.

[3] Radiofrequency Planning Group Document: SP 2/01: Investigation of Modified Hata Propagation Models, Australian Comm. Authority, April 2001.

[4] L. Jordanova, G. Karpov, D. Dobrev, *Parametrical analysis of DVB-T channels*, Proceedings of the XLIX-th Int. Conference on ICEST, Nis, 2014 (in press).

[5] ITU: Final acts of the RRC-06 for planning of the digital terrestrial broadcasting service in parts of Regions 1 and 3 in frequency bands 174 - 230 MHz and 470 - 862 MHz, 2006.

[6] ETSI TR 101 190, Digital Video Broadcasting: Implementation Guidelines for DVB Terrestrial Services – Transmission Aspects, 2011.

ISOTROPIC MULTI-HOP MODEL FOR WIRELESS SENSOR NETWORKS

Zlatan Ganev

Department of Electrical Engineering, Technical University of Varna, 9010 Varna, Bulgaria,
E-mail: zganev@gmail.com

Sava Savov

Department of Electrical Engineering, Technical University of Varna, 9010 Varna, Bulgaria,
E-mail: sava.savov12@gmail.com

Abstract

This article deals with idealized isotropic model of data transmission. This is a model by which data to base station does not arrive directly, but by the means of multi-hop method. Thus data transmission energy is considerably reduced and network life is prolonged, which is a main task of any designer.

In this article a particular example of multi-hop data transmission is pointed out, as energy model is simulated with Matlab and results visualized with appropriate graphics.

1. INTRODUCTION

Wireless sensor networks (WSN) are networks with a decentralized structure in which information is wirelessly transmitted, mostly through radio or optical connection and there are high expectations for size and lifetime of the nodes. This network types are preferred when building infrastructure is difficult or uneconomic or network is of temporary purpose.

Devices compactness and possibility of rapid deployment of WSN makes them extremely suitable for emergency situations: fires, floods and other natural disasters [1].

The so far given characteristics lead to certain requirements: low power consumption (as it works with limited autonomous power supply); small size of sensor nodes; security and protection of data transmitted.

It is typical for WSN nodes to have a limited scope for data transmission. In most cases, packets of information are transmitted from source to receiver, passing through many intermediate nodes. This method allows for the level of energy used to be reduced, but on the other hand imposes the condition of dynamic routing of transmission [2].

2. ENERGY MODEL

A main challenge in the design of an energy coefficient wireless network is that sending a bit of information through free space directly from node A to node B in curs an energy cost Et, which is a strong function of the distanc*e d* between then odes and can be represented in the follow in g form:

$$Et = \beta \times d^n \qquad (1)$$

with n > 1 as the path-loss exponent (a factor that depends on the RF environment, and is generally between 2 and 5). β is a proportionality constant describing the over head per bit. Given this greater than linear relationship between energy and distance, using several short intermediate hops (Fig. 1) to send a bit is more energy-efficient than us in gone longer hop [3,4,5,6].

This model does not take into account the energy for calculations and for operation of the receiver at each node.

Fig. 1. Multihop networks, using several intermediate nodes to send information

3. RESULTS FROM SIMULATIONS

3.1. Example one

Weas sume that n = 4, which is a common case in indoor environments, and β = 0.2 femtojoules/meter

n. Than one hop over 50 meters requires 1.25 nanojoules per bit (Fig. 2), where as five hops of 10 meters (Fig. 3), according (1), require only 5 × 2 picojoules per bit [1]. This is graphically shown in Figure 4.

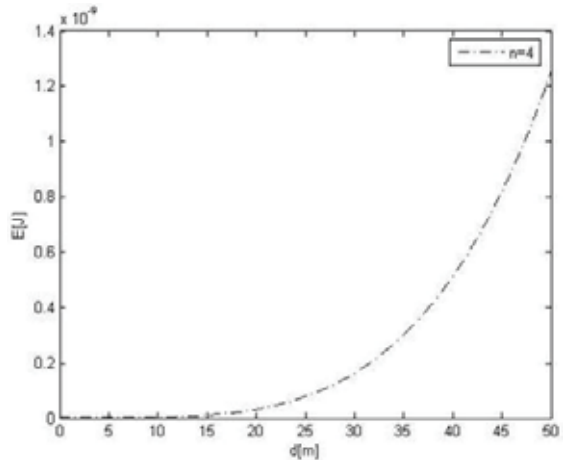

Fig. 2. One hope transmission (n=4,d=50m)

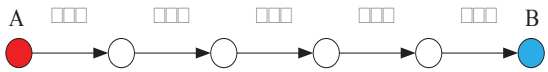

Fig. 3. Multi hop networks, using five intermediate hopes to send information

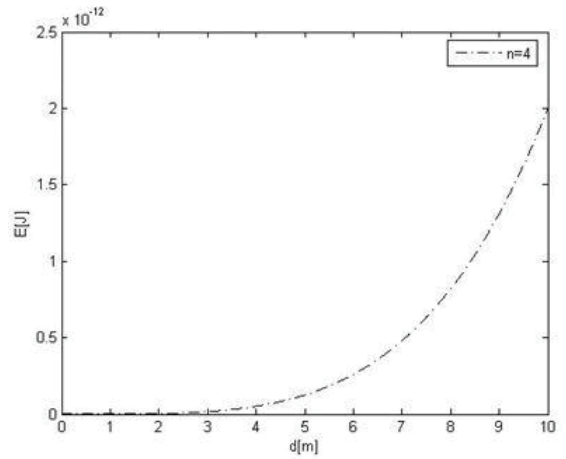

Fig. 4.Multi-hop transmission (n=4,d=10m)

The multi hop approach in this example reduces transmission energy by a factorof125.

3.2. Example two

Now weas sume that n = 4, and β = 0.2 femtojoules/meter *n*. Than one hop over 50 meters requires 1.25 nanojoules per bit (Fig. 2), where as ten hops of 5 meters (Fig. 5) require only 10 × 0.125 picojoules per bit. This is graphically shown in Figure 6.

Fig. 5. Multihop networks, using ten intermediate hopes to send information

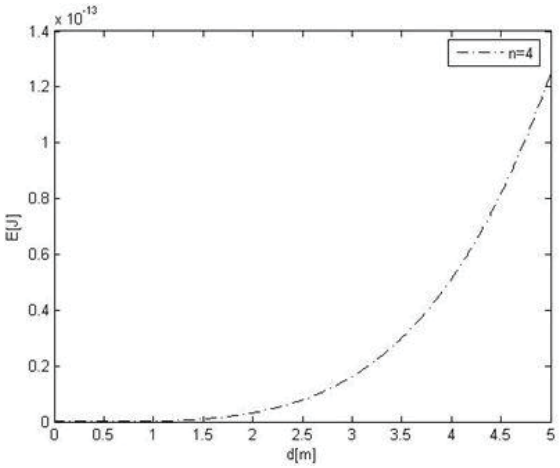

Fig. 6.Multi-hop transmission (n=4,d=5m)

The multi-hop approach in this example reduces transmission energy by a factor of 1000.

3.3. Example three

Now weas sume that n = 4, and β = 0.2 femtojoules/meter *n*. Than one hop over 50 meters requires 1.25 nanojoules per bit (Fig. 2), where as ten hops of 2 meters (Fig. 7) require only 25 × 0.0032 picojoules per bit. This is graphically shown in Figure 8.

Fig. 7. Multihop networks, using ten intermediate hopes to send information

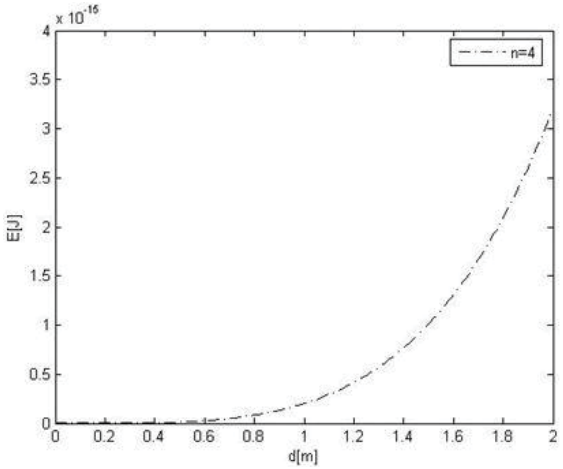

Fig. 8.Multi-hop transmission (n=4,d=2m)

The multihop approach in this example reduces transmission energy by a factor of 15625.

3.3. Example four

Now weas sume that n = 4, and β = 0.2 femto-joules/meter *n*. Than one hop over 50 meters requires 1.25 nanojoules per bit, where as ten hops of 1 meter (Fig. 9), require only 50 × 0.0002 picojoules per bit. This is graphically shown in Figure 10.

Fig. 9. Multihop networks, using ten intermediate hopes to send information

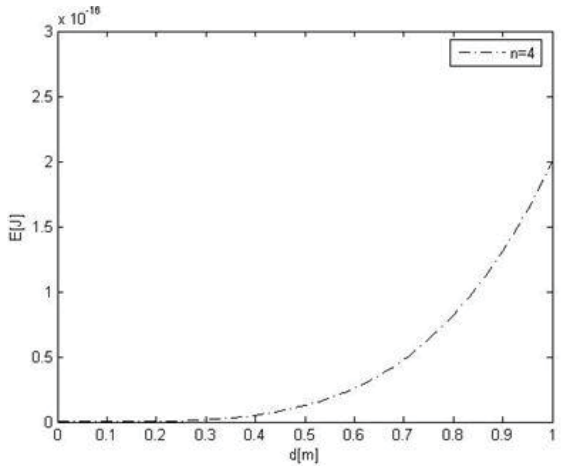

Fig. 10. Multi-hop transmission (n=4,d=1m)

The multihop approach in this example reduces transmission energy by a factor of 125000.

4. CONCLUSION

In this article we present idealized isotropic multi-hop model for wireless sensor networks. This model does not take into account transmission irregularity, shadowing effects and the energy for calculations. It also does not take into consideration the energy for signal amplification in the different nodes, which are used as active repeaters.

The main purpose was to demonstrate that the energy for transmission of information between two nodes (A and B) can be reduced significantly by using a multi-hop route. It is found through simulations in Matlab environment that the energy transmission is highest in the direct transmission (one-hop) and lowest in the multi-hop approach in example four, where we use 50 hopes. The transmission energy there reduces by a factor of 125000.

5. Appendix and acknowledgments

The authors are supported by the Program "Human Resources Development" of the Bulgarian Ministry of Youthand Education, Project BG051PO001-3.3.06-0005 , ОП 'РЧР.

References

[1] Ганев З., Савов С., ,,Приложение на безжични сензорни мрежи", Юбилеен конгрес на ТУ-Варна, 2012 г.

[2] Ганев З., Димова Р., ,,Безжични сензорни мрежи", Годишник на ТУ - Варна, 2011 г.

[3] J. L. Gao, Energy Efficient Routing for Wireless Sensor Networks, Ph.D. dissertation, University of California, Los Angeles, 2000.

[4] J. M. Rabaey, M. J. Ammer, J. L. Silva, D. Patel & S. Roundy, "Pico Radio supports ad hoc ultra-low power wireless networking", IEEE Computer, Vol. 33, July, 2000, pp. 42-48.

[5] Katayoun Sohrabi, On Low Power Self Organizing Sensor Networks, Ph. D. theses, University of California, Los Angeles, 2000.

[6] Karakehayov Z., Sensor Networks, Technical University of Sofia (In Bulgarian).

LOG-NORMAL SHADOWINGMODEL FOR WIRELESS SENSOR NETWORKS

Zlatan Ganev

Department of Electrical Engineering, Technical University of Varna, 9010 Varna, Bulgaria,
E-mail: zganev@gmail.com

Sava Savov

Department of Electrical Engineering, Technical University of Varna, 9010 Varna, Bulgaria,
E-mail: sava.savov12@gmail.com

Abstract

In this paper two cases of propagation are considered: a) two- floor propagation and b) three-floor propagation in one office building. Additional losses are caused by radio waves going through ceilings and reflections and diffractions from walls and edges.

"Log-normal shadowing model" is used here for predicting large-scale coverage for wireless sensor networks. Applying this model helps one to estimate the energy capacity of WSN (wireless sensor network), before such systems to be deployed.

First, we calculate path loss exponent (n) and then standard deviation (σ), assuming Gaussian noise in the channel. Second, we estimate the received power (Pr) at given distance (d) and predict the likelihood that the received signal level at this distance will be greater than given threshold γ:Pr[Pr(d) > γ]. Finally, we find out the percentage U(γ) of the area with a radius d, where received signal will be greater than a certain threshold γ.

1. INTRODUCTION

Our radio propagation model is derived on a combination of analytical and empirical methods. The empirical approach is based on "*curve-fitting*" method applied to measured data. All propagation factors are taken into consideration, both known and unknown, through *actual power measurements*. However, the validity of an empirical model at certain frequency or environment, can only be established by proper measurements.

2. PROPAGATION MODEL

This is an empirical model that try to approximate analytically the results of measurement. The path-loss function of the distance can be represented in the following form [1 - 3]

$$\mathrm{PL(d)} = \mathrm{PL(d_0)(d/d_0)^n} \tag{1}$$

or in logarithmic form [4 - 5]

$$\mathrm{PL_{dB}(d)} = \mathrm{PL_{dB}(d_0)} + 10\mathrm{n\lg(d/d_0)} + \mathrm{X_\sigma} \tag{2}$$

where (d) is the distance, (d_0) is the reference distance, and (X_σ) is a Gaussian noise power (in dB). Here MMSE (*minimum mean square error*) estimation about the path-loss exponent (n) is applied and the standard deviation (σ) is found.

The reference distance for *indoor propagation model* usually is assumed to be d_0 = 1 m, and the path loss there in our case is assumed to be $PL(d_0) = -32\,dB$.

The sum of squared errors that should be minimized is [6]

$$\mathrm{S(n)} = \sum_{k=0}^{N} \left(\mathrm{p_k} - \mathrm{q_k n}\right)^2 \tag{3}$$

where new coefficients

$$\mathrm{q_k} = -10\lg(\mathrm{d_k}/\mathrm{d_0}) \tag{4}$$

and

$$\mathrm{p_0} = 0,\ \mathrm{p_k} = -\mathrm{p(d_k)} + \mathrm{p_0} \tag{5}$$

are introduced. For the MMSE algorithm S(n) is found by the following simple quadratic expression

$$\mathrm{S(n)} = \mathrm{A} - 2\mathrm{Bn} + \mathrm{Cn^2} \tag{6}$$

with new defined coefficients

$$\mathrm{A} = \sum_{k=0}^{N} \mathrm{p_k^2};\ \ \mathrm{B} = \sum_{k=0}^{N} \mathrm{p_k q_k};\ \ \mathrm{C} = \sum_{k=0}^{N} \mathrm{q_k^2} \tag{7}$$

(k = 1,2,…,N). Here N is the *total number of the measurements*, while (k=0) is related to the reference point. The *necessary condition for minimum*

$$\frac{dS}{dn} = 0 \quad (8)$$

leads to the following equation for the path-loss exponent n

$$n = B / C \quad (9)$$

It can be shown that an appropriate expression for the *standard deviation* is

$$\sigma[dB] = \sqrt{S(n)/N} \quad (10)$$

In general, a greater number of measurements are needed to reduce σ.

3. RESULTS FROM SIMULATIONS

3.1. Calculation of the path loss exponent (n) and the standard deviation (σ) using measured results

Here we presented two different *best fit lines*:

a) "the two-floor results" of measurements (with circles);

b) "the three-floor results" of measurements (with squares).

The range of measurements is: d = [10–34m]. In these experiments the carrier frequency is f = 914 MHz.

Both best fit lines (with *linear regressions*) are shown by dashed lines in Fig.1.

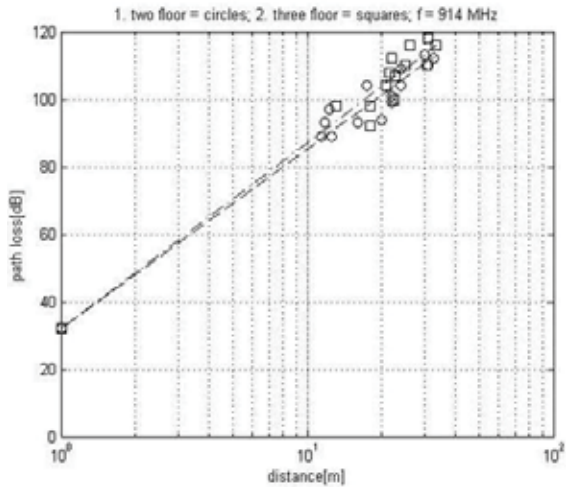

Fig. 1. Best fit linear regressions

More accurate results for the parameters of both linear regression lines are:

a) (two-floor) $n_1 = 5.32$; $\sigma_1 = 3.76$ dB;

b) (three-floor) $n_2 = 5.52$; $\sigma_2 = 4.36$ dB.

We observe one interesting and expected result from these simulations: the power parameter (n) for the case of "three-floor" is higher than the same parameter for the case of "two-floor". This event can be explained by additional "through-ceiling propagation".

3.2. Statistical data processing of the obtained results

a) two-floor case at distance d = 30m

a1) estimation of the received power (at d=30m)

It is given by the following equation [5]

$$P_r(d) = -32dB - 10n \lg(d/d_0) \quad (11)$$

It can be found for this distance the following power

$$P_r(d = 30m) = -32dB - 10(5.32)\lg(30/1)$$
$$= -110.58dB$$

A Gaussian random variable having zero mean and standard deviation $\sigma_1 = 3.76$ dB could be added to this value to simulate random shadowing effects at *d*=30m.

a2) likelihood prediction of the received signal - to be greater than the level "γ" (here γ = –113 dB).

The probability that the received signal level will be greater than γ = –113dB is given by the following equation [5]

$$Pr[P_r(d) > \gamma] = Q\left(\frac{\gamma - Pr(d)}{\sigma 1}\right) =$$
$$Q\left(\frac{-113+110.58}{3.76}\right) = Q(-0.644) = 0.740 = 74\% \quad (12)$$

where new auxiliary function (for argument z < 0) is involved [5]

$$Q(z) = 0.5[1 + erf(z/\sqrt{2})] \quad (13)$$

and erf(x) is the "error function" (this special function is available in Matlab).

a3) percentage prediction of the area within a d=30 m radius (that receives signals with a level greater than "γ").

The probability that the received signal level will be greater than γ= -113dB is presented by the follow n g equation [5]

$$U(\gamma)=0.5\{1+\exp(1/b^2)[1-\text{erf}(1/b)]\} \quad (14)$$

where erf(x) is already defined function above and the new parameter here is

$$b = (10\text{nlge})/(\sigma\sqrt{2}) = 4.345 \quad (15)$$

The value obtained by (14) is U = 89.3% (of the area that receives coverage above – 113 dB) .

b) three-floor case at distance d = 26m

Similar analysis is performed here.

b1) estimation of the received power (at $d = 26\text{m}$). It is given by (11)

$$P_r(d = 26\text{m}) = -32\text{dB} - 10(5.52)\lg(26/1) = -110.1\text{dB}$$

A Gaussian random variable having zero mean and standard deviation σ_2 = 4.36 dB could be added to this value to simulate random shadowing effects at d=26m.

b2) likelihood prediction of the received signal - to be greater than the level "γ" (here γ = –116 dB).

The probability that the received signal level will be greater than γ = –116 dB is given by (12)

$$\Pr[P_r(d) > \gamma] = Q\left(\frac{\gamma - \Pr(d)}{\sigma 2}\right) = Q\left(\frac{-116+110.1}{4.36}\right) = Q(-1.352) = 0.912 = 91.2\%$$

where the function Q(z) is defined by (13).

b3) percentagepredictionof the area within a d = 26 m radius (that receives signals with a level greater than "γ").

The probability that the received signal level will be greater than γ = –116 dB is found by equations (14) and (15).

Here

$$b = (10\text{nlge})/(\sigma\sqrt{2}) = 2.423,$$

and for the percentage is obtained the following value U = 88.2 % .

4. CONCLUSION

The log-normal distribution describes the random *shadowing* effects which occur over a large number of measurement locations which have the same T-R (transmitter – receiver) separation, but have different levels of clutter on the propagation path. This phenomenon is referred to as "*log-normal shadowing model*". This model implies that measured signal levels at a specific T-R separation have a Gaussian (normal) distribution about the distance-dependent mean, where the measured signal levels (received power) have values in dB units. The standard deviation of the Gaussian distribution that describes the shadowing has also units in dB. Thus, the random effects of shadowing are easily accounted for the case of Gaussian distribution.

The closed reference distance d0, the path-loss at this distance PL(d0), the path- loss exponent n, and the standard deviation σ, statistically describe the path-loss model for an arbitrary location having a specific T-R separation, and this model may be used in computer simulation to provide received power levels for random locations in communication system design and analysis.

In practice, the values of n and σ are computed from measured data (as described above), using linear regression, such that the difference between the measured and estimated path losses is minimized in a mean square error sense (*MMSE method*) over a wide range of measurement locations and T-R separations.

In our case is visible that the path loss constant (parameter n) is bigger for the case in "three-floor" than the case in "two- floor" example. This can be explained by the additional shadowing effects for the "three-floor" example.

Our "*best-fit model*" (with linear regression) could be applied to variety of scenarios in the area of WSN. We can apply this model in different kind of environments, with different carrier frequencies and distances.

5. APPENDIX AND ACKNOWLEDGMENTS

The authors are supported by the Program "Human Resources Development" of the Bulgarian Ministry of Youth and Education, Project BG051PO001-3.3.06-0005, OP 'RCR.

References

[1] H. Karl. A. Willig, "Protocols and architectures for wireless sensor networks", John Wiley & Sons, 2005.

[2] Azar, Y., Wong, G. N., Wang, K., Mayzus, R., Schulz, J. K., Zhao, H., Gutierrez, F., Hwang, D., Rappaport, T. S., 28 GHz Propagation Measurements for Outdoor Cellular Communications Using Steerable Beam Antennas in New York City, toappear in the 2013 IEEE International Conference on Communications (ICC), Jun 9-13, 2013.

[3] Alejandro Martınez-Sala, Jose-Marıa Molina-Garcia-Pardo, Esteban Egea-Lopez, Javier Vales-Alonso, Leandro Juan-Llacer, and Joan Garcıa-Haro, "An Accurate Radio Channel Model for Wireless Sensor Networks Simulation", Journal of communications and networks, vol.7, No4, Dec 2005.

[4] Claude Oestges, "Propagation Modelling for Wireless Sensor Networks", Report, Catholique Universite de Louvain, 2005.

[5] T. Rappaport., "Wireless Communications (Principles and Practice)", 2nd ed., Prentice Hall, 2002.

[6] S. Savov, Z. Ganev, "Indoor Propagation Path Loss Modelling for Wireless Sensor Networks", ICEST Nis, Serbia, Jun 2014.

ON THE LIMITATIONS OF GAIN CALIBRATION IN HARMONIC REJECTION MIXERS

Ludwig Lubich

Technical University of Sofia, Faculty of Telecommunications
1000 Sofia, 8 Kl. Ohridski Blvd
lvl@tu-sofia.bg.

Abstract

The paper deals with the number of harmonics that can be completely rejected simultaneously in harmonic rejection mixers using only gain calibration. The restrictions on the combinations of rejected harmonics are examined too. The results are also applicable to harmonic rejection in digital domain.

1. INTRODUCTION

Harmonic rejection mixers (HRM) have been increasingly used in wideband receivers as they alleviate the harmonic mixing problem and thus considerably relax the preselect filtering requirements. An HRM is a complex mixer, consisting of several parallel operating conventional hard switching mixers, driven by a multiphase local oscillator (LO). The HRM output signal is a weighted sum of the signals down converted by the individual mixers [1]. The HRM can be seen as a single perfect multiplier, driven by an *effective* LO waveform, in which some harmonics are eliminated.

There are numerous implementation options for HRMs, but the basic principle can be illustrated by Fig. 1. It can be easily realized that the effective LO waveform is by its nature a sampled sinusoid. Therefore it contains only harmonics of orders $kN \pm 1$, where k=1, 2, ... So, the nearest interferer, which should be suppressed by the preselect filters is at $N \pm 1$ f_{LO} (assuming a zero-IF receiver).

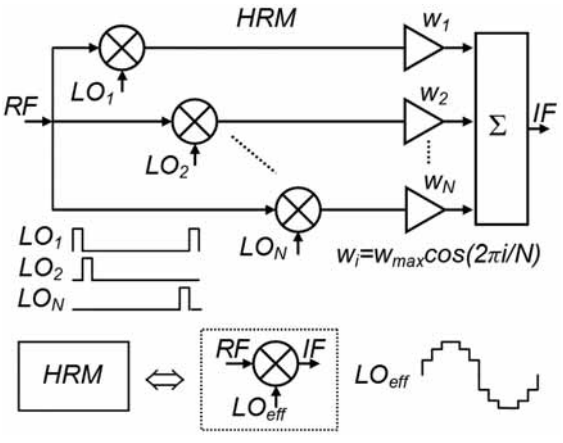

Fig. 1. HRM operation principle

Unfortunately harmonic rejection ratios (HRR) of HRMs are typically limited to 30-40 dB due to gain and phase mismatches [2]. HRR can be enhanced by gain and phase calibration [3]. Simultaneous calibration of both phases and gains however, increases complexity of HRM. Hence, many HRMs employ only gain calibration [4, 5, 6].

Another efficient way for HRR improvement is to perform the suppression of harmonic interferers partly [1, 2, 7, 8] or entirely [9] in digital domain. In [1, 2, 7, 8] adaptive cancellation is used. In [9] the harmonic rejection (HR) problem is formulated and treated as a problem from the area of multiuser detection and an MMSE equalizer is derived for the suppression of the harmonic interferers. These two approaches to digital HR appear to be completely different, but in both cases, although different tools are used, the proper weighting factors are found and applied to form a weighted sum of the individual mixer outputs. From this perspective, the proposed HRMs with digital interference suppression can be seen as HRMs with gain calibration only.

In this paper we determine the number of harmonics that can be completely rejected simultaneously in presence of phase mismatches using gain calibration only. In addition, the restrictions on the combination of these harmonics are investigated. The results are also applicable to HRMs employing digital domain HR techniques.

The rest of the paper is organized as follows:

In Section 2 the system model is presented and the conditions for HR as a system of linear equations are expressed. In Section 3 this equation system is examined from the viewpoint of finding the allowa-

ble combinations of harmonics, that can be completely rejected simultaneously. In section 4 examples for some typical scenarios are presented and discussed.

2. THE HRM MODEL

The effective LO waveform can be expressed as:

$$LO_{eff} = \sum_{i=1}^{N} LO_i(t) w_i \,, \qquad (1)$$

where $LO_i(t) = p(t) * \sum_{n=-\infty}^{\infty} \delta(t - nT_{LO} - t_i)$ and $p(t)$ denotes the single effective pulse, which multiplies the RF signal in each HRM path. The convolution with $p(t)$ is equivalent to a mild filtering of the effective LO waveform and usually does not play a significant role in the rejection of the LO harmonics. Therefore, it will be ignored in the rest of the paper, excluding an important special case. Also, without loss of generality $T_{LO} = 1$ will be assumed. Furthermore, the path count N will be assumed to be even, as odd values result in implementation disadvantages.

The Fourier series coefficients of the effective LO waveform, ignoring the scale factors, are given by:

$$c_k = \sum_{i=1}^{N} w_i e^{jk\theta_i} \,, \qquad (2)$$

where $\theta_i = -(2\pi i / N + \varphi_i)$ and φ_i is the phase error of the i-th LO pulse train.

The path gains, needed to reject the DC component and the harmonics of the orders from 1 to $N-1$ are the solution of the following system of $N-1$ linear equations:

$$\mathbf{A}\mathbf{w} = \mathbf{b} \qquad (3)$$

where

$$\mathbf{A} = \begin{bmatrix} 1 & 1 & \cdots & 1 \\ e^{j\theta_1} & e^{j\theta_2} & \cdots & e^{j\theta_N} \\ e^{j2\theta_1} & e^{j2\theta_2} & \cdots & e^{j2\theta_N} \\ \vdots & \vdots & \ddots & \vdots \\ e^{j(N-1)\theta_1} & e^{j(N-1)\theta_2} & \cdots & e^{j(N-1)\theta_N} \end{bmatrix},$$

$\mathbf{w} = [w_1\ w_2\ \ldots\ w_N]^T$, $\mathbf{b} = [1\ e^{j\alpha}\ \ldots\ 0]^T$, and α is the phase angle of the LO fundamental component.

We seek real solutions only. Complex solutions are inapplicable, because the two quadrature components of the LO harmonics are not available separately in the HRM hardware. So, the multiplication with complex weighting factors cannot be implemented.

A widely used HRM implementation option is to use double LO pulses of the form $p_D = p(t) - p(t - T_{LO}/2)$ ensuring even HR. Then the number of HRM paths is reduced by half and will be denoted by M. Such HRMs will be designated here as M-path HRMs in contrast to N-path HRMs described before. The LO phase shifts in M-path HRMs are π/M. The HR equation system consists of $M-1$ equations for odd HR only.

Both N-path and M-path HRMs can be simplified if one of the path gains is constrained to be zero (i. e. this path does not exist in the hardware). Then the number of unknown path gains reduces by one.

3. HR EQUATION SYSTEM EXAMINATION

3.1. HRM without phase errors

Within the restriction to real solutions it is convenient to split the equations into real and imaginary parts using the Euler's formula. We obtain a new system

$$\mathbf{C}\mathbf{w} = \mathbf{d} \qquad (4)$$

where

$$\mathbf{C} = \begin{bmatrix} 1 & \cdots & 1 \\ \cos(\theta_1) & \cdots & \cos(\theta_N) \\ \cos(2\theta_1) & \cdots & \cos(2\theta_N) \\ \vdots & \ddots & \vdots \\ \cos[(N-1)\theta_1] & \cdots & \cos[(N-1)\theta_N] \\ \cos[(N-2)\theta_1] & \cdots & \cos[(N-2)\theta_N] \end{bmatrix}$$

and $\mathbf{d} = [1\ \cos\alpha\ \cos 2\alpha\ \ldots\ \cos(N-2)\alpha]^T$, are a $(2N-2)\times N$ real-valued matrix and a $(2N-2)\times 1$ real-valued vector, respectively. Furthermore, it is suitable to scale the first and the N-th equations by $1/\sqrt{N}$ and the remaining ones by $\sqrt{1/N}$.

The equations from $N+1$-st to the the $2N-2$-rd are superfluous, as the $N+1$-st equation has all zero coefficients, and each of the rest equations duplicates one of the equations from the fourth to the $N-1$-st.

Let us create a new reduced equation system

$$\mathbf{Gw} = \mathbf{h} \qquad (5)$$

where $\mathbf{G}$ is a matrix formed from the first N rows of $\mathbf{C}$ and $\mathbf{h} = [\alpha \ \alpha \ \ldots]^T$ is an N-element vector.

It can be easily proven that in the absence of phase errors $\mathbf{G}$ is an orthogonal matrix. As a result the system (5) has a unique solution.

3.2. Examination of the perturbed system

An orthogonal matrix is the best conditioned matrix. This implies that in the presence of sufficiently small phase errors $\boldsymbol{\varphi} = [\varphi_1 \ \varphi_2 \ \ldots \ \varphi_N]^T$ the perturbed system $\mathbf{G}(\boldsymbol{\varphi})\mathbf{w} = \mathbf{h}$ will not only have a unique solution $\mathbf{w}(\boldsymbol{\varphi})$ but its scatter will be small. Therefore, in the presence of phase errors, the path gains in an HRM can be adjusted for perfect suppression of the DC component and the harmonics up to and including $N/2-1$-st. In addition, the path gains will be nearly equal to their nominal values.

It is useful to prove that additional harmonics cannot be completely rejected. If one of the two equations, related to a harmonic of order k_{add}, $N/2 < k_{add} < N-1$, is satisfied by $\mathbf{w}(\boldsymbol{\varphi})$, then $\mathbf{r}(\boldsymbol{\varphi})\mathbf{w}(\boldsymbol{\varphi}) = 0$, where $\mathbf{r}(\boldsymbol{\varphi})$ is the corresponding row of $\mathbf{C}$, e. g. the one with cosine coefficients. It is difficult to find an expression for $f(\boldsymbol{\varphi}) = \mathbf{r}(\boldsymbol{\varphi})\mathbf{w}(\boldsymbol{\varphi})$. So we find its derivative

$$\left.\frac{\partial[\mathbf{r}(\boldsymbol{\varphi})\mathbf{w}(\boldsymbol{\varphi})]}{\partial\varphi_i}\right|_{\boldsymbol{\varphi}=0} = \left.\frac{\partial\mathbf{r}}{\partial\varphi_i}\right|_{\boldsymbol{\varphi}=0}\mathbf{w}(0) + \mathbf{r}(0)\left.\frac{\partial\mathbf{w}}{\partial\varphi_i}\right|_{\boldsymbol{\varphi}=0} \qquad (6)$$

Using implicit differentiation we find

$$\left.\frac{\partial\mathbf{w}}{\partial\varphi_i}\right|_{\boldsymbol{\varphi}=0} = -[\mathbf{G}(\mathbf{0})]^{-1}\left.\frac{\partial\mathbf{G}}{\partial\varphi_i}\right|_{\boldsymbol{\varphi}=0}\mathbf{w}(\mathbf{0}). \qquad (7)$$

After performing substitutions and simplifications, we obtain:

$$\left.\frac{\partial[\mathbf{r}(\boldsymbol{\varphi})\mathbf{w}(\boldsymbol{\varphi})]}{\partial\varphi_i}\right|_{\boldsymbol{\varphi}=0} = -\sqrt{N}\sin\left(k_{add}\,i\,\frac{\pi}{N}\right)w_i, \qquad (8)$$

hence $\dfrac{\partial[\mathbf{r}(\boldsymbol{\varphi})\mathbf{w}(\boldsymbol{\varphi})]}{\partial\varphi_i} \neq 0$ in the general case. Therefore in the general case $\mathbf{r}(\boldsymbol{\varphi})\mathbf{w}(\boldsymbol{\varphi})$ cannot be constant and, in particular, cannot be zero. In a similar way this can be proven for additional equations with sine coefficients. Hence, additional harmonics cannot be completely rejected.

However, the perfect suppression of the k-th harmonic can be traded off for perfect suppression of its "symmetrical", $(N-k)$-th harmonic, where $k < N/2$. This is possible, because the corresponding matrix rows for the two symmetrical harmonics are identical in the unperturbed case. The scatter of the solution will be somewhat larger, as the phase errors will be multiplied by $(N-k)$ instead of k.

The simultaneous complete suppression of two symmetrical harmonics is, however, problematic. Assume, that in the system present e. g. the cosine equations for the k-th and $(N-k)$-th harmonics. By subtracting the first one from the second one we obtain a new equation. The solution of the system will not change if one of the two original equations is replaced by the new one. The coefficients of the latter will be approximately $-\varepsilon_i N \sin(\pi k i / N)$, so they will be completely random, unlike the coefficients of the remaining equations, where the random phase errors are added to much larger fixed angles. As a result some combinations of phase errors will cause very large path gains and even inconsistency of the system. It can be proven that the power of white noise, transferred to the HRM output from the output of the preceding RF amplifier is proportional to the sum of the squares of the path gains. Hence, in this case the HRM output noise can exceed many times that in the case of a solution, nearly equal to the nominal path gains. Since the fundamental magnitude is constant, a catastrophic SNR degradation can occur.

Similar problems arise when the HRM is calibrated for a complete rejection of the "middle", *N/2*-nd harmonic, because the corresponding sine equation has coefficients, roughly proportional to the respective phase errors. So the receiver will be susceptible to strong interferers at $N f_{LO}/2$.

3.3. Implementation implications

In the case of an N-path HRM the consistent system of HR equations has N or $N-1$ equations in the form (4), depending on whether there is a zero-gain path. The first three equations ensure the

DC suppression and define the fundamental magnitude and angle. The remaining equations ensure the harmonic rejection. Given that two equations per a rejected harmonic are required and only even values of N are preferred for implementation reasons, it is advisable for the *N*-path HRMs to be implemented with a zero-gain path. Otherwise one path will be superfluous.

A limitation of the HRM with one zero-gain is that they have a "native" phase angle of the fundamental tone due to the fixed position of the effective LO zero crossing. In this case the modification of the fundamental angle by path weight adjustment results in an increased level of the $N/2$-th harmonic.

For M-path HRMs the consistent HR equation system consists of M or $M-1$ equations depending on whether there is a zero-gain path. Based on considerations, similar to those for the N-pat HRMs, it is advisable to choose even values of M, or to implement HRMs with one zero-gain path, if M is odd.

The M-th harmonic causes the same problems in the M-path HRM, like the $N/2$-nd harmonic in their N-path counterparts. However this can be avoided here, if an even value of M is chosen. In this case the problematic harmonic would be already suppressed owing to the use of bipolar LO pulses, as far as good symmetry is achieved.

4. EXAMPLES AND DISCUSSION

To illustrate the theory we shall examine some examples. We assume that phase errors are uncorrelated normally distributed with $\sigma_\varphi = 1$, and the path gains are initially equal to the nominal values corresponding to zero phase errors. In each of the examples, the calibrated path gains for 20 consecutive realizations of phase errors will be presented.

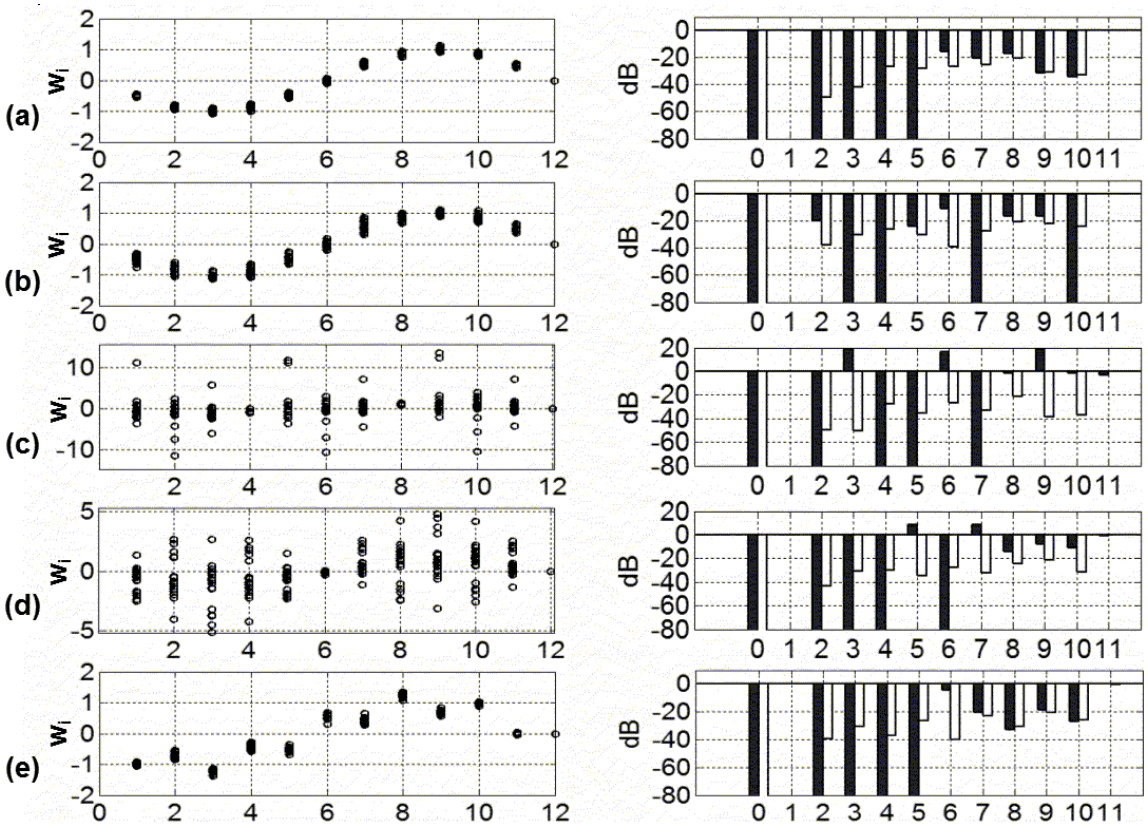

Fig. 2. Path gains after calibration for 20 realizations of a 12-path HRM and the effective LO harmonic levels for one typical its realization after and before calibration. Completely rejected harmonics of the orders 2, 3, 4 and 5 (a) and 3, 4, 7 and 10 (b). Simultaneous rejection of one pair of symmetrical harmonics (c). Complete rejection of the harmonic of the order N/2 (d). Fundamental tone shifted by 15° from its native value (e).

An N-path HRM with N=12 with one zero-gain path will be examined. The consistent system consists of 11 equations – the first one is for the DC rejection, the next two equations define the fundamental magnitude and angle, and the remaining 8 equations ensure complete suppression of 4 harmonics.

We choose the harmonics of the orders 2, 3, 4 and 5 to be completely rejected. The solution has minimal scatter (Fig. 2a). Each of the above harmonics can be exchanged for its symmetrical one without compromising the HRM performance. For example, we can completely suppress the harmonics of the orders 10, 3, 4 and 7 (Fig. 2b). However, the calibration for simultaneous rejection for example of the 5-th and 7-th harmonics results in very large gain scatter (Fig. 2c). If the N□2-nd, the 6-th harmonic in our case, is entirely rejected the solution has very large scatter again (Fig. 2d).

As can be expected, the calibration for a complete rejection of a set of harmonics worsens (but not necessarily) the HRRs for the remaining harmonics (Fig. 2 a-e). This can be especially strongly pronounced if a pair of symmetrical harmonics and/or the middle, N□2-nd harmonic is completely rejected (Fig. 2 c, d). An HRR degradation for the N□2-nd harmonic occurs in the case when a HRM with a zero-gain path is forced to operate with fundamental angle, different from its "native" one (Fig. 2 e)

For the M-path HRMs similar observations can be made as for their N-path counterparts.

5. CONCLUSIONS

The investigations of limitations of the gain calibration in HRMs showed that perfect suppression can be achieved only for $N/2-2$ and $\lfloor M/2-1 \rfloor$ harmonics in N-path and M-path HRMs, respectively. Calibration for perfect suppression of a given set of harmonics worsens the rejection of the remaining harmonics. Attempts for complete suppression of the middle harmonic or a pair of symmetrical harmonics can result in extremely large path gains and SNR degradation. In addition, convergence issues in the algorithms for calibration or digital domain HR can be expected.

As the RF spectrum gets more and more crowded, the probability for interference scenarios with a simultaneous presence of strong blockers at pairs of symmetrical LO harmonics will increase. This implies that the stopband of the preselect filters should begin at N□□/2 if only gain calibration is employed. Additional phase calibration or increase of path count of the HRM would be needed if more relaxed filter requirements are desired.

It is advisable that N-path HRMs are implemented with even N and one zero-gain path, whereas M-path HRMs are implemented with even M.

References

[1] Zhiyu Ru et al., "Digitally-Enhanced Software-Defined Radio Receiver Robust to Out-of-Band Interference", *IEEE Journal of Solid-State Circuits*, vol. 44, 15 Dec. 2009, pp. 3359–3375.

[2] N. A. Moseley et al., "A Two-Stage Approach to Harmonic Rejection Mixing Using Blind Interference Cancellation," *Circuits and Systems II: Express Briefs, IEEE Transactions on* , vol.55, no.10, Oct. 2008, pp. 966-970

[3] W. L. Ng, S.Y. Zheng et al., "A 0.9GHz–5.8GHz SDR receiver front-end with transformer-based current-gain boosting and 81-dB 3rd-order-harmonic rejection ratio", *Proceedings of the ESSCIRC 2013*, 16-20 Sept. 2013, pp.181-184.

[4] Van Liempd et al., "IIP2 and HR calibration for an 8-phase harmonic recombination receiver in 28nm", *Custom Integrated Circuits Conference, 2013 IEEE*, 22-25 Sept. 2013, pp. 1-4.

[5] H.-K. Cha et al. "A CMOS Wideband RF Front-End With Mismatch Calibrated Harmonic Rejection Mixer for Terrestrial Digital TV Tuner Applications," *IEEE Transactions on Microwave Theory and Techniques,* , vol. 58, no. 8, Aug. 2010, pp. 2143-2151.

[6] S. Uemura et al. "A 1.15V Low Power Mobile ISDB-Tsb/Tmm/T and DVB-T Tuner SoC in 40nm CMOS", *Symposium on VLSI Circuits*, 12-14 June 2013, pp. C76-C77.

[7] C. Li et al., "Adaptive filter based low complexity digital intensive harmonic rejection for SDR receiver", *Acoustics, Speech and Signal Processing, 2013 IEEE International Conference on*, 26-31 May 2013, pp. 2712-2715.

[8] T.Yamaji et al., "A 6-phase harmonic rejection down-converter with digital assist", *IEEE Symposium on VLSI Circuits, 2010*, 16-18 June 2010, pp. 181-182.

[9] W. Namgoong, "Digital Equalization of a Polyphase Harmonic Mixer", *IEEE Transactions on Circuits and Systems—II: Express Briefs*, Vol. 60, No. 8, August 2013, pp. 467-471.

Acknowledgment

The research in this paper is supported by grant DDVU 02/74-7.

THE BENEFITS OF IEEE 802.11AC STANDARD: COMPARISON WITH 802.11N WIRELESS NETWORK AND EXPERIMENTAL INVESTIGATIONS FOR REAL-TIME SERVICE TRANSMISSION

Arnoldas Matusevičius, Tomas Adomkus, Lina Narbutaitė, Rasa Brūzgienė

Department of Telecommunications, Kaunas University of Technology
Studentu str. 50-452, Kaunas, Lithuania, LT- 51368
E-mail: tomas.adomkus@ktu.lt

Abstract

Today's users want to be connected to a wireless network not only at home, but in any place at any time. Due to this, the users' demands on the mobility, data security and the Quality of Services (QoS) are increasing rapidly. Wireless networks are good choice for the users' mobility, however it have a number of disadvantages, as the limited network's bandwidth, the problems of data security and the pollution of the radio ether. That is the reason for use a more flexible and more adaptable wireless network, based on a relatively new Wi-Fi standard - IEEE 802.11ac. The wireless network over 802.11ac standard is more advanced due to the extended coverage of the radio signals and improved network's bandwidth. According to this, the authors compared 802.11ac with 802.11n by the network's parameters of these standards (the throughput, the signal level) in different conditions. In order to evaluate the benefits of IEEE 802.11ac wireless network to the transmission of the telecommunication services the authors created an experimental wireless network over 802.11ac standard and investigated the quality parameters of Voice over Internet Protocol (VoIP) as a Real-time service. The impact of the transmission of Non Real-time services (video streaming, FTP and HTTP) as an additional network traffic during the transmission of VoIP service was investigated also. The results of these investigations and the conclusions, based on the simulation and experimental investigations in the wireless networks over different 802.11ac and 802.11n standards, are presented in this paper.

1. INTRODUCTION

Currently, the real-time services and the wireless networks (Wi-Fi) are very popular and widely used [1,2]. However, these real-time services have very strict requirements for their quality characteristics [3]. The latter are directly dependent on the channel bandwidth. This problem was solved with the new next generation 802.11ac standard [4-6]. IEEE 802.11ac wireless standard is able to provide a theoretical data rate of 3.5 Gbps with the channel width of 160 MHz for 4 streams at 256-QAM modulation. This is indeed an impressive speed compared to the 802.11n standard, which is currently widely in use now [7]. IEEE 802.11n standard provides a maximum theoretical data rate of 1.3 Gbps.

In order to compare the 802.11n and 802.11ac wireless standards in theoretical and practical view, the simulation and experiments of it throughput, the signal strength are presented in this paper. Then, to make sure that the 802.11ac standard is able to transmit multiple streams of a real-time service, the authors carried out the experiments, which investigate the quality of VoIP service, continuously increasing the number of active TCP sessions in the network. The results of these investigations and the conclusions are presented in this paper.

2. COMPARATIVE ANALYSIS OF SIMULATED PARAMETERS OVER IEEE 802.11N AND 802.11AC WIRELESS NETWORKS

In order to evaluate the possibility of the user as a mobile user of a wireless network, it is necessary to compare two different IEEE 802.11n and 802.11ac standards in accordance to their signal coverage and throughput. The authors used *Ekahau Site Survey* software tool for the simulation of throughput and received signal strength in the wireless networks based on 802.11n and 802.11ac standards. The selected access point (AP) is working on 802.11n and 802.11ac standards in 5GHz frequency band. The simulation was done in LOS (Line of Sight) and NLOS (Non-Line of Sight) conditions of the wireless networks. It has been used the wall of a 20 cm thick in NLOS conditions. The comparison of the throughput by using the different wireless standard is presented in Figures 1 and 2.

The average simulated throughput is 280 Mbps in LOS conditions (Fig. 1). The average simulated throughput is 150 Mbps in NLOS conditions, when the distance from access point to the user was 6 m. If the user is 40 m away from the AP (NLOS conditions), the average simulated throughput is 60 Mbps.

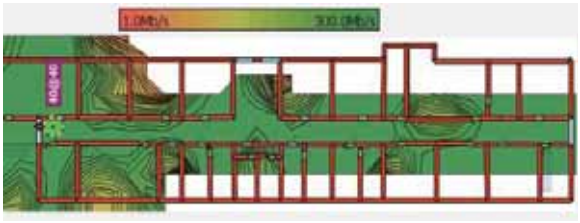

Fig. 1. The simulated throughput in the 802.11n wireless network

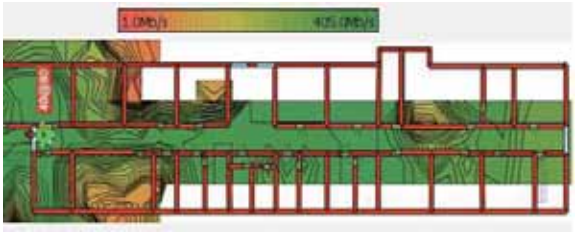

Fig. 2. The simulated throughput in the 802.11ac wireless network

The results from the 802.11ac throughput simulation (Fig. 2) showed that the average throughput is 350 Mbps in LOS (Line of Sight) conditions. In this case, the distance from AP to the user was 1 m. Due to this the simulated throughput in the 802.11ac wireless network is 43% bigger than the throughput in the 802.11n network.

As the user quite often uses Wi-Fi in NLOS conditions, the 802.11ac standard is more effective in this way also. The average throughput is 250 Mbps in NLOS (Non-Line of Sight) conditions, when the distance from access point to the user was 6 m, and 65 Mbps, when the distance was 40 m. That means the simulated throughput in 802.11ac network differences in 120 Mbps, when the distance is 6 m, and in 5 Mbps, when the distance is 40 m.

The signal strength is the most basic requirement for a wireless network, because low signal strength means unreliable connection and/or low data throughput. The simulated signal strength in 802.11n and in 802.11ac wireless networks is presented in Figures 3 – 4.

According to the results in Figures 3, 4 it can be stated, that the signal strength in 802.11ac wireless network is more influenced by the obstacles (walls, partitions, etc.) than in 802.11n. This is because of the channel bandwidth, used in 802.11n [8].

Due to the results from the simulations, the 802.11ac wireless network provides 3 times faster connection than 802.11n, but its signal strength is more influenced by the obstacles.

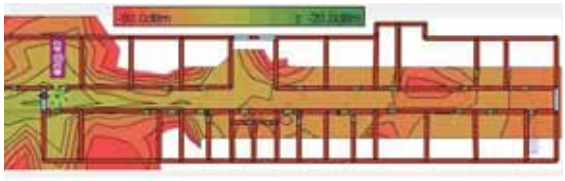

Fig. 3. The simulated signal strength in the 802.11n wireless network

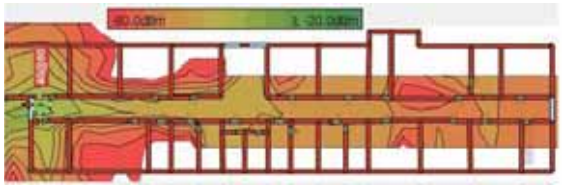

Fig. 4. The simulated signal strength in the 802.11ac wireless network

3. EXPERIMENTAL INVESTIGATIONS FOR THE THROUGHPUT EVALUATION OVER IEEE 802.11N AND 802.11AC WIRELESS NETWORKS

After the simulations, it is necessary to investigate the parameters of the wireless networks based on 802.11n and 802.11ac standards. The experiments were carried out in the 4th floor of the building at Kaunas university of technology, Department of Telecommunications. Its layout corresponds to the scheme, used during the simulations. The structure of the experimental network and LOS/NLOS conditions is presented in Figure 5. The parameters, which were investigated: the throughput and the signal strength. The results of the investigated throughput of 802.11n and 802.11ac wireless networks in NLOS conditions are presented in Figures 6, 7. The results in Figure 8 show the ratio of the throughput between the different standards in accordance to the signal strength.

According to the results of the investigated throughput in NLOS conditions, it can be seen, that the distance between the AP and the user influences the throughput of 802.11ac wireless network. In this case, the average throughput of 802.11ac wireless network is 281 Mbps in 6 m distance and only 45 Mbps in 40 m distance. The average throughput of 802.11n wireless network is only 7% less in the distance of 40 m from AP.

The ratio of the investigated throughput between the different standards shows that the investigated throughput differences in ~ 4 times if the received signal strength indication (RSSI) is -65 dBm. In this case, the signal strength of 802.11n wireless network in NLOS conditions is more appropriate for the wireless connections.

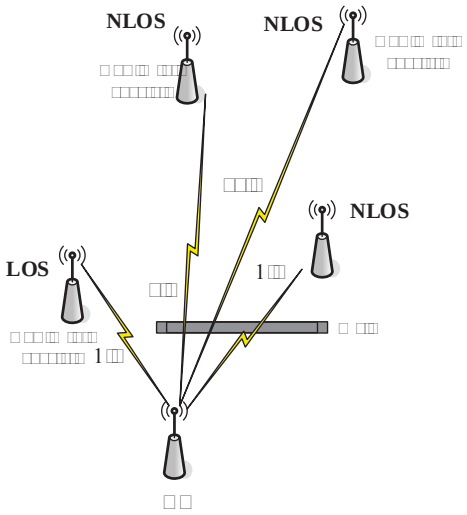

Fig. 5. The structure of the experimental network and its LOS/NLOS conditions

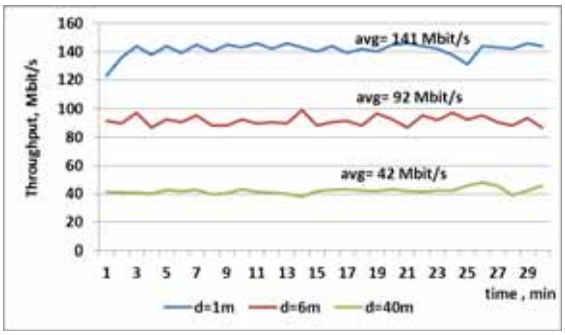

Fig. 6. The investigated throughput of 802.11n wireless network in NLOS conditions

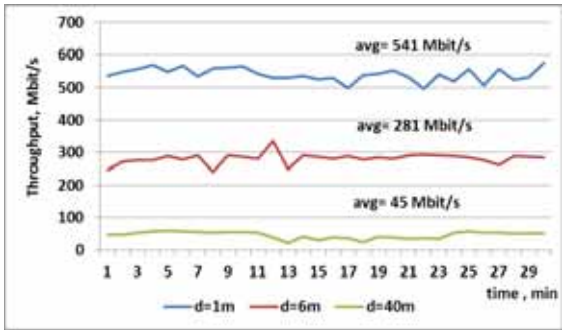

Fig. 7. The investigated throughput of 802.11ac wireless network in NLOS conditions

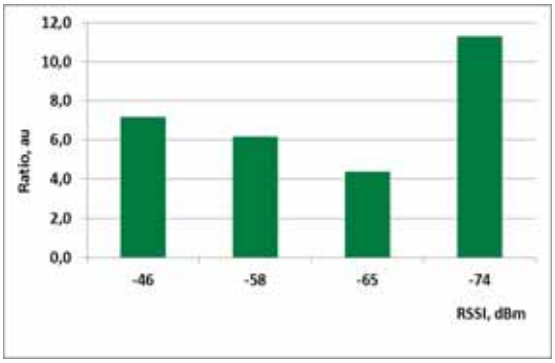

Fig. 8. The ratio of the investigated throughput between the different standards

The investigated throughput of 802.11ac wireless network in LOS conditions is presented in Figure 9.

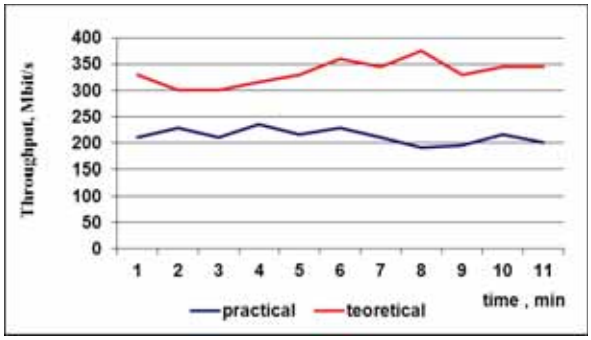

Fig. 9. The comparison of 802.11ac throughput in LOS conditions

Its comparison with the results from the simulations is presented also in this Figure. It can be seen, that the investigated 802.11ac wireless connection is 1.5 times faster than the simulated.

In order to evaluate the 802.11ac throughput in realistic conditions, it is necessary to investigate the impact of traffic load on it (Fig. 10).

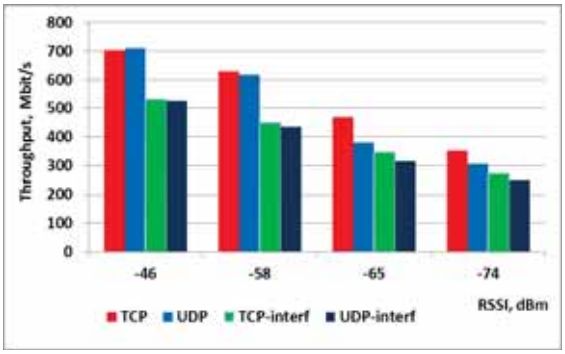

Fig. 10. The influence of the traffic load to the 802.11ac throughput

According to the results in Figure 10, if the signal strength is falling and there are the additional loads in the network TCP (*Transmission Control Protocol*), UDP (*User Datagram Protocol*) sessions) the throughput of 802.11ac wireless network can be reduced in 2 times. However, even the throughput can be reduced the wireless network of 802.11ac standard provides access to a faster Wi-Fi connection than 802.11n.

4. THE EXPERIMENTAL EVALUATION OF VOIP QOS OVER IEEE 802.11AC WIRELESS NETWORK

The broadcasting of Real-time services, such as VoIP, depends on the quality of the communication process over wireless connection and its continuity.

The throughput, the packets' delay and loss, the signal level are the main QoS parameters for VoIP service transmission over wireless network. Due to this, the experimental investigations were carried out in order to evaluate the QoS parameters of VoIP service transmission over 802.11ac wireless network. The structure of the experimental 802.11ac wireless network is presented in Figure 11.

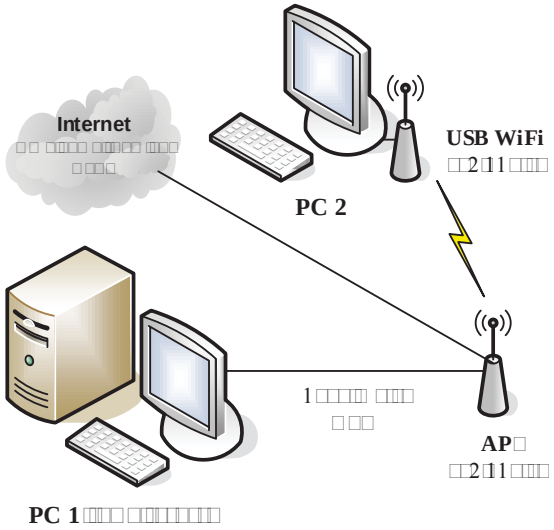

Fig. 11. The structure of the experimental network

This experimental 802.11ac wireless network consists of two computers, both of them were working as a VoIP users, and the wireless access point (AP). The model of the access point was D-Link DIR 850L, which is working on 802.11n and 802.11ac standards. It has four MIMO antennas and dual band (2.4 GHz; 5 GHz) performance up to 1167 Mbps. The measurements were made using *Jperf 2.0.2v, InSSIDer, SJ Phone, Wireshark 1.12.0 Network Analyzer software*. G.711 voice codec was used for VoIP service transmission. The distance from AP to the user was 1 m.

The experimental investigations have been carried out for three different scenarios. At first, only VoIP calls were made in the experimental 802.11ac network without any additional traffic in the network. The results for the delay and the jitter of VoIP service transmission over IEEE 802.11ac wireless network are presented in Figure 12 and Figure 13. According to the results in these Figures, it can be stated, that Voice over IP transmission in 802.11ac wireless network is performed with a high quality, if there is no any additional traffic in the network.

The average delay of VoIP packets was 45.56 ms and the average jitter – 13.44 ms, the loss of VoIP packets – 0 %.

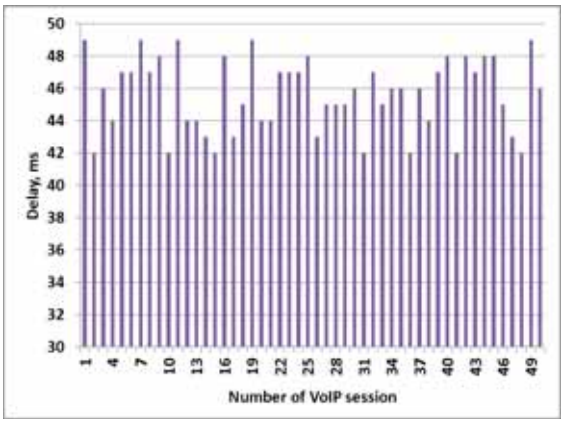

Fig. 12. The delay of VoIP packets transmission over 802.11ac network

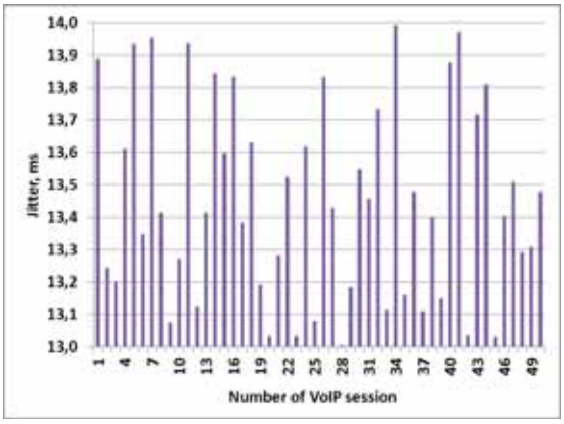

Fig. 13. The jitter of VoIP packets transmission over 802.11ac network

The transmission of VoIP service with the additional traffic over the 802.11ac network was done during the second and the third scenarios. The additional traffic (for the second scenario) was created from the HD (High Definition) video and FTP (File Transfer Protocol) transmissions to the VoIP user (PC2 in Figure 11) at the same time, when VoIP calls were made.

The results of the QoS parameters for VoIP service during the second scenario are presented in Figures 14 - 16.

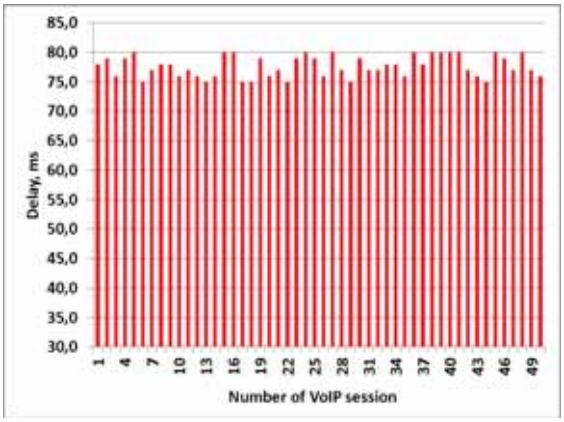

Fig. 14. The delay of VoIP packets transmission with the additional video/FTP traffic over 802.11ac network

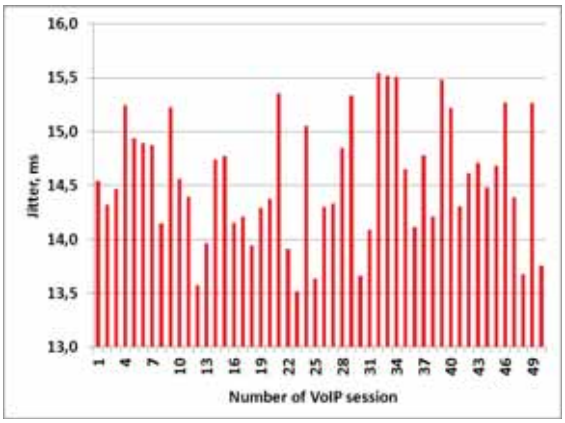

Fig. 15. The jitter of VoIP packets transmission with the additional video/FTP traffic over 802.11ac network

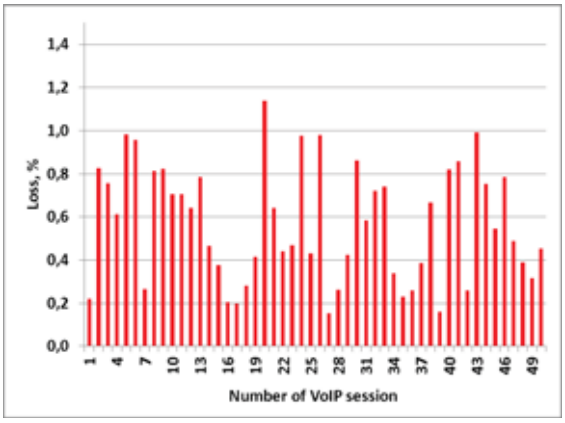

Fig. 16. The loss of VoIP packets transmission with the additional video/FTP traffic over 802.11ac network

The results of the investigations during the second scenario showed, that the additional traffic over 802.11ac wireless network influences the quality of VoIP service. However, such influence was observed only to minor changes in the voice calls, which the user felt as a voice jerking. In this case the average delay of VoIP packets was 77.6 ms and the average jitter – 14.7 ms. The loss of VoIP packets was 0.7 %.

The additional traffic from the HD video, FTP and HTTP (Hyper Text Transfer Protocol) transmissions was created to the VoIP user at the same time, when VoIP calls were made during the third scenario. The results of these investigations are presented in Figures 17 – 19.

As it seen from the results in Figures 17–19, the transmission of VoIP service is affected by the additional video/FTP/HTTP traffic, because the average loss of VoIP packets is 2 %. Such loss of VoIP packets value exceeds the recommended limit of 1 % accord to the ITU-T G.711 recommendation. The average delay of VoIP packets was 229 ms and the average jitter – 16.23 ms. In this way, the user felt many negative things, like voice jerking or echo, however the transmission of VoIP service was not braked. So generally, the IEEE 802.11ac standard allows the transmission of VoIP service over the wireless network.

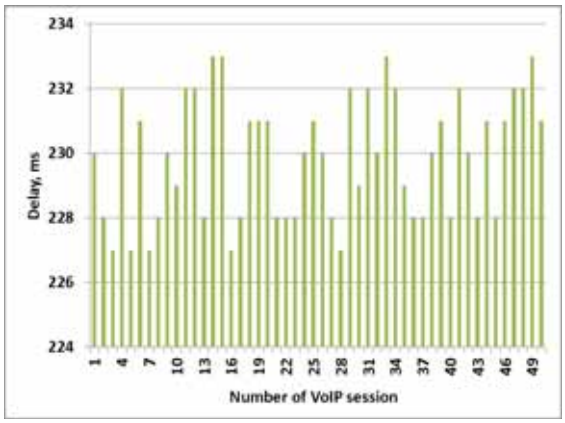

Fig. 17. The delay of VoIP packets transmission with the additional video/FTP/HTTP traffic over 802.11ac network

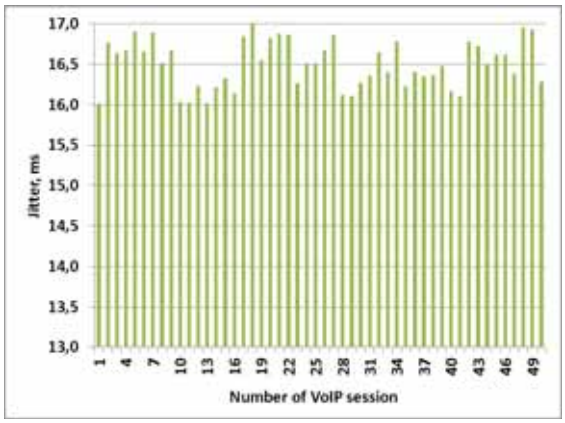

Fig. 18. The jitter of VoIP packets transmission with the additional video/FTP/HTTP traffic over 802.11ac network

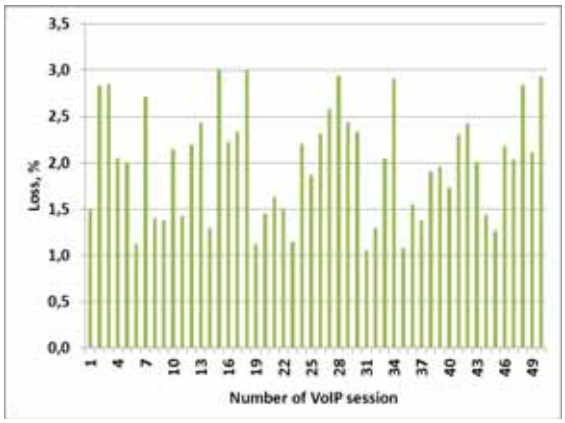

Fig. 19. The loss of VoIP packets transmission with the additional video/FTP/HTTP traffic over 802.11ac network

5. CONCLUSIONS

In this paper, the authors investigated the IEEE 802.11ac wireless network and compared it with IEEE 802.11n. According to the obtained results, it can be stated, that the 802.11ac wireless network provides 3 times faster connection than 802.11n, but its signal strength is more influenced by the obstacles.

The investigation of the VoIP QoS over 802.11ac showed that VoIP transmission is performed with a high quality, if there is no additional traffic in the network. The additional traffic as HD video, FTP and HTTP in the 802.11ac network influences the average loss in 2 % for VoIP packets.

References

[1] Eng Hwee Ong, Jarkko Kneckt, Olli Alanen, Zheng Chang, Toni Huovinen and Timo Nihtila. "IEEE 802.11ac: Enhancements for Very High Throughput WLANs Personal Indoor and Mobile Radio Communications (PIMRC)", *in Proceedings of IEEE 22nd International Symposium*, 2011, pp. 849 – 853.

[2] Lochan Verma, Mohammad Fakharzadeh and Unghyun Choi. "WiFi on Steroids: 802.11ac and 802.11ad", *IEEE Wireless Communications*, Vol. 20, No. 6, 2013, pp. 30 – 35.

[3] Emna Charfi, Lamia Chaari, and Lotfi Kamoun. "PHY/MAC Enhancements and QoS Mechanisms for Very High Throughput WLANs: A Survey", *IEEE Communications Surveys & Tutorials*, Vol. 15, No. 4, 2013, pp. 1714 – 1735.

[4] Ali A. Khavasi; Mojtaba Aajami; Hae-Ryeon Park; Jung-Bong Suk. "Video transmission over IEEE 802.11ac downlink multi-user: max-min fair link adaptation strategy", *Electronics Letters*, Vol. 50, No. 12, 2014, pp. 898 – 900.

[5] Oscar Bejarano, Edward W. Knightly and Minyoung Park. "IEEE 802.11ac: From Channelization to Multi-User MIMO", *IEEE Communications Magazine*, Vol: 51 , No. 10, 2013, pp. 84 – 90.

[6] Yu H., Kim T. "Beamforming transmission in IEEE 802.11ac under time-varying channels", *The scientific world journal*, Vol. 2014, 2014, pp. 920 – 937.

[7] Brūzgienė, Rasa; Narbutaitė, Lina; Adomkus, Tomas; Cibulskis, Romualdas. "The impact of video streaming on quality of experience over 802.11n dual Band networks: experimental evaluation", *Electronics and electrical engineering*, Vol. 20, no. 6, 2014, p. 158-161.

[8] F. Heereman, W. Joseph, E. Tanghe, D. Plets and L. Martens. "Prediction of Range, Power Consumption and Throughput for IEEE 802.11n in Large Conference Rooms Antennas and Propagation (EUCAP)", *in Proceedings of the 5th European Conference*, April 2011, pp. 692 – 696.

USING EMBEDDED SOFTWARE FOR ACHIEVING HIGHER PRECISION IN POWER DETECTORS

Boyan Ivanov Ivanov

Ph.D. Student, Sofia University "St. Kliment Ohridski",
Faculty of Physics, Department of Radio Physics and Electronics
Postal address: Sofia 1712, Mladost-3 bl.329 ent.2 apt.33
T. +359 885 088 457; E. boyan.ivanov@phys.uni-sofia.bg

Abstract

Accurate power measurement is essential in satellite communication systems, particularly for power generated by BUCs, due to regulations for the transmitted power connected with issues like transponder saturation, power limits for VSAT system connected with intermodulation interferences, etc. Many of the more expensive and powerful BUCs have integrated power detectors as a feature, but this is not the case with low power and customer defined devices, where output power is calculated on the basis of the gain of the device. On the other hand this gain is dependent from frequency, temperature, ageing and other factors. Here comes the need of an accurate power detector module. There are many power detectors present, but they also suffer from the same "symptoms" of frequency and temperature non-linearity, which again bring us to the problem of precise measuring of generated power.

As a solution of this problem a power measuring device will be presented. Its main feature is an embedded software algorithm which using data from internal temperature sensor, data for the used frequency, and reading from a power detector micro-chip, calculates an accurate power value based on a predefined calibration tables. These tables are populated with data measured in closely monitored environment and signal power generated and measured by high quality calibrated laboratory equipment.

The achieved results are real time readings with error of less than 0.5dB of the power generated by a Ku-band BUC in the whole frequency range and in a wide temperature range. This gives us the possibility of controlling output power more accurately and use the maximum permitted power for our up-links instead of using less power as a buffer for not transmitting more than expected.

1. INTRODUCTION

Power measuring is tightly connected with history of design and usage of RF equipment. Since early days there are three basic methods for sensing and measuring average power at RF and microwave frequencies. Each of the methods uses a different kind of device to convert the RF power to a measurable DC or low frequency signal. The devices are the thermistor, the thermocouple, and the diode detector.

In modern days power measuring has become very accurate in laboratory power meters using the previously mentioned methods. With the development of microchip technology, there is a high demand for smaller and more accurate power detectors. Most of the contemporary powers detecting MMICs are giving accurate linear reading just for a specific frequency range and surrounding conditions. Combining the power of digital microprocessors and embedded software with power detecting MMICs, these devices can be used in ranges where the results are non-linear, and achieve results with reasonable accuracy.

2. MAIN TEXT

Creating a small portable power meter with accurate results is challenging task. If used only analog technology this device may not be able to meet dimension and price requirements especially in higher frequency ranges. Using digital microprocessors with embedded software can reduce the requirements for the initial power detecting microchip without compromising the accuracy of the power reading. The main problem is that most power detectors' output signal is linearly proportional to the measured power only in specific ranges of frequencies and temperatures. Outside this ranges the detectors are still working but the proportionality with the power levels measured is no more linear. This non-linearity and the deviation of the output signal because of temperature change are the main sources of error in power measurement. This error can be significantly reduced by using digital microprocessors. If this non-linear characteristic is measured in a controlled calibrated laboratory the user will know how the detector is acting outside of its linear range. If enough of these measurements for different frequencies and temperatures are made, a

full picture of the detector's characteristic can be made. In software aspect these measurements can be viewed as a multidimensional array of data of corresponding output voltage to a specific power level and second or third variable parameter. For example reduction of the error from frequency and temperature deviation is needed, then a three dimensional array of data which stored output voltage values corresponding to a specific power level, frequency and temperature is necessary. This process will be referred as calibration of the detector. For the purpose of calculating actual power level from these calibration measurements a backward calculation using interpolation or extrapolation is done, for this purpose the microprocessor need to have the current temperature, frequency and detector's output voltage. The frequency is inputted as a parameter via the communication protocol, the temperature is measured from the same temperature sensor used during the calibration and the detector's voltage is measured directly on the ADC input.

In this article software and hardware requirements and solutions will be discussed, as well as the needed laboratory equipment and procedure for calibrating the detector. In parallel an example of real device of this kind with real parameters and results will be given, for the purpose of better understanding of the problem and its solution.

2.1. Power meter requirements

A device called power meter is required to measure accurate microwave power levels and return a corresponding message for the user or other equipment to be used. There are several requirements towards the power detector module.

2.1.1. Accuracy

The main requirement is accuracy: this means the error between detector readings and real power of the microwave signal to be as small as possible.

2.1.2. Frequency range

Another requirement is the operating frequency range in which the accuracy is maintained in certain level.

2.1.3. Operating conditions

Third important requirement is operating conditions, such as temperature range, humidity levels etc.

2.1.4. Others

Additional requirements towards the detector module are physical dimensions, type of connection with power transmitting structure (waveguide or cable), coupling and others.

As an example a power meter for Ku-band BUC output power is presented. It must operate in the frequency range from 14 to 14.5 GHz, and in conditions from -50 to +70˚C. Its accuracy must be less than 0.5dBm error. It should be connected at the waveguide exit of the BUC.

2.2. Hardware requirements

Power meter is created by several basic modules and each one has its own requirements.

2.2.1. Power detector microchip

Power detector microchip is the main module of the power meter. Its function is to detect microwave power and produce a DC voltage corresponding to the power level in its dynamic range. In the ideal case the produced DC is in linear scale proportional to the measured RF power. In reality the linear part of it power-DC characteristic is in some part of the frequency range. Outside of this linear range the power detector chip is still outputting a DC voltage but in non-linear proportion to the RF power. Embedded software will be used to overcome this non-linearity and still read correct power levels.

2.2.2. Microprocessor

Microprocessor with at least two analog to digital convertor (ADC) channels is to be used for interpreting the power detector DC voltage. It is important that the ADC's sensibility is enough to make difference in the change of the detector's output voltage even in non-linear characteristic. Additional requirements towards the microprocessor are to have enough memory for storing software program and calibration data, faster clock for real time calculations, communication protocol for returning calculated power level and input of initial data for operating frequency and temperature, calibration data and other commands.

2.2.3. Other

Other devices that are part of the power meter are temperature stable reference voltage source and temperature sensor. Optional devices may be addi-

tional data memory, communications interface such as RF modem of RS-232 to USB converter etc.

In the example device a "Linear Technology" power detector linear in the 10MHz to 6 GHz frequency range is used. The microprocessor is 72MHz ARM Corex-M3 controller with 16 channels 12-bit ADC. For communications a 333MHz modem is used.

2.3. Software requirements and solutions

The requirements towards the software have several aspects.

2.3.1. Accuracy of calculation

The most important one is accuracy of calculation. This is achieved by storing as much calibration data as possible depending on the available memory. Another key issue for accurate calculation is that the precision of the calibration data must be at least 0.01 dBm for the power level. Stable reference voltage level is also critical for the accuracy; usually the supply voltage for microprocessors which is also used for reference for the ADC is not temperature stable enough. That is why before each measurement from the detector a measurement from a temperature stable voltage source is made to which the detector's output voltage is compared. This is done in the calibration procedure as well in the operating mode when calculating the measured power level.

2.3.2. Calibration data

The ideal case is when all the available memory is filled with data covering the whole range of frequencies and temperatures in which the device will be used. In this case the operating conditions will always be within the calibration data and interpolation will be used for calculating the measured value. If the calibration points are with smaller steps the error will be smaller. On the contrary if less calibration points are present the bigger error will be.

If for some reason the calibration process is compromised and there is partial calibration, sometimes the operating conditions will be outside of the covered calibration measurements, than extrapolation is the method for calculating the power level.

In both cases an algorithm for finding the closest data is needed. This can be achieved by using a second array of the same dimensions like the arrays of calibration data but filled with flags for valid data.

Additional array of temperature measured with the built-in temperature sensor during the calibration procedure is needed. The data in this array will be slightly different from the theoretical value and will be used in calculation of the power. The procedure for gathering this data will be discussed later in the calibration procedure description.

2.3.3. Communication protocol

Communication protocol is needed for interacting with the microcontroller for several reasons. They include: reading writing and editing calibration data; inputting operation frequency; reading measured power level; reading device parameters; updating the software; and any other features that can be performed from the microcontroller.

The communication can be done over any interface that is supported by the microcontroller (SPI, UART, and I2C) or with the help of peripheral communication device such as RF modems serial-to-USB convertors and others.

In the example device a 16x16x16 array is used for covering the whole range of frequencies from 14 to 14.5 GHz and a temperature range from -50 to 70˚C. For each temperature/frequency points an array with 16 power levels from -50 to 10 dBm and the corresponding power detector output voltage is recorded. The calibration memory was partially filled with only 3 calibration temperatures at 30, 50 and 70˚C. The frequency range was covered with 11 points with 0.05 GHz step.

2.4. Calibration equipment and procedure

The calibration process is very important for the proper calculation of the measured power in real operation.

The equipment needed for calibration is a temperature chamber for setting different calibration temperatures; power source capable of producing power levels in a broad dynamic range through the whole frequency range in which the power meter will be calibrated; laboratory calibrated power meter which is going to measure the real power at the calibrated power meter probe, this values will be added in the calibration database; PC which is going to synchronize the calibration process and communicate with the calibrated device to add the measured values.

The procedure consists of several steps which repeat for each desired calibration temperature. First

the temperature is set in the chamber, and then a frequency sweep is started with predefined calibration frequency values. For each frequency a power sweep is performed with power defined in the dynamic range of the power meter to be used. For each power level, the actual power in the power meter is measured with the laboratory calibrated power meter and then this value is send to the calibrated device together with the current frequency and temperature. Upon receiving this data in the form of a command to add new calibration value the microprocessor measures the voltage from the detector and stores it in the corresponding part of the calibration array.

Since the temperature is regulated from the chamber, the built-in temperature sensor might have a different reading. For that purpose upon each command for adding a new calibration value, a reading from the sensor is taken. After all points for the given temperature are taken a mean value from the built-in temperature sensor readings is saved in the microcontroller for making the calculations when the device is making the calculations of the power level measured at the probe.

After populating all the desired power levels with corresponding voltages for each frequency-temperature combination the calibration process is completed.

In the example device the calibration is done in a laboratory with a combination of HP VNA and 40W BUC from Wavestream as power source and HP power meter. Both this equipment and the calibrated device were connected with PC for the purpose of automatic calibration. The calibration software and UI was written in Python 2.7.

3. CONCLUSION

At the end of this article a conclusion can be made that the power of modern microprocessors in combination with proper software and calibration can extend the usage of power detector MMICs outside of the frequency range for which they were originally designed. The accuracy of such devices depends mainly on the number of calibration points recorded and on the algorithm for choosing the calibration values from which the actual power level is calculated.

In the example a calibration for frequency and temperature was made, but in theory it may be any other parameter that is including error in the measurement. The results in the test device were meeting the criteria of less than 0.5dBm error from the real power level with actual biggest error of 0.31 dBm.

ON THE MATHEMATICAL MODEL OF INTERPOLATION OF LOW FREQUENCY MAGNETIC FIELD USING EXPERIMENTAL DATA

B. Kudrin

St. Petersburg State University, Faculty of Math. & Mech., St. Petersburg, Russia

V. Nikolov

Technical University of Sofia, Faculty of Telecommunication, Bulgaria

Abstract

In the process of magneto-therapy often it's necessary to use space distribution of the value of magnetic induction in points of patient's area in which there is not preliminary measurement of the value of magnetic induction. It's important first of all for the points in the human body. In this case a preliminary measurement of the value of magnetic induction in some points out of the human body can be provided. In result a set of scalars can be obtained. Usually the sources of low frequency magnetic field are several coils which are situated around the human body. The measurement points are the centers of these coils and the point on the middle of the line between them. At any moment only one pair of coils is active. The order of the choice of the pairs is defined by a data table. The problem is to find the values of magnetic induction in some points between the active coils and to visualize results. The results of interpolation for every pair can be shown and a physician can observe a space distribution of the value of magnetic induction of running magnetic field.

1. INTRODUCTION

In the mathematical field of numerical analysis interpolation is a method of constructing new data points within the range of a discrete set of known data points.In engineering and science, one often has a number of data points obtained by sampling or experimentation, which represent the values of a function for a limited number of values of the independent variable. It is often required to interpolate (i.e. estimate) the value of that function for an intermediate value of the independent variable. This may be achieved by curve fitting or regression analysis.

A different problem which is closely related to interpolation is the approximation of a complicated function by a simple function. Suppose the formula for some given function is known, but too complex to evaluate efficiently. A few known data points from the original function can be used to create an interpolation based on a simpler function. Of course, when a simple function is used to estimate data points from the original, there are interpolation errors. However, depending on the problem domain and the used interpolation method used, the gain in simplicity may be of greater value than the resultant loss in accuracy.

When modelling magnetic field distribution one can use mathematical models and compute magnetic induction value in the points of a given lattice. In [1-3] the model of calculation of electromagnetic induction for two coils which are arbitrary disposed in 3D was described. The algorithms of calculation and visualization were also implemented.

For a large number of the lattice nodes the calculation may be time-consuming, so an application of interpolation methods is rather actual. We may calculate magnetic induction in a small number of points and obtain the induction values in other ones by interpolation. The results obtained in [4] show that such an approach leads to considerable reducing run time.

Results of measurements of electromagnetic induction are usually obtained as scalars and we have a problem of one-dimensional interpolation.

In this work we discuss a mathematical model for interpolation electromagnetic induction in a special magnetotherapy device – magneto bed. Interpolation nodes are the centers of two given coils and the middle of connecting them line.

2. TYPES OF INTERPOLATION

We discuss some types of interpolation methods that may be used in the case of one-dimensional interpolation.

2.1. Linear interpolation

One of the simplest methods is linear interpolation (sometimes known as lerp). Generally, linear interpolation takes two data points, say (x_a,y_a) and (x_b,y_b), and the interpolant is given by:

$$y = y_a + (y_b - y_a)\frac{x - x_a}{x_b - x_a} \text{ at the point } (x, y) \quad (1)$$

Linear interpolation is quick and easy, but it is not very precise. Another disadvantage is that the interpolant is not differentiable at the point x_k.The following error estimate shows that linear interpolation is not very precise. Denote the function which we want to interpolate by g, and suppose that x lies between x_a and x_b and that g is twice continuously differentiable. Then the linear interpolation error is

$$|f(x) - g(x)| \leq C(x_b - x_a)^2 \quad \text{where} \quad C = \frac{1}{8}\max_{y\in[x_a,x_b]}|g''(y)| \quad (2)$$

In words, the error is proportional to the square of the distance between the data points. The error in some other methods, including polynomial interpolation and spline interpolation (described below), is proportional to higher powers of the distance between the data points. These methods also produce smoother interpolants (Fig.1).

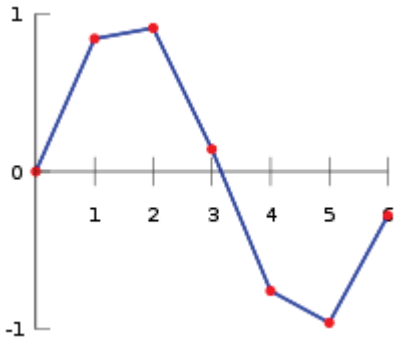

Fig. 1

2.2. Polynomial interpolation

Polynomial interpolation is a generalization of linear interpolation. Note that the linear interpolant is a linear function. We now replace this interpolant with a polynomial of higher degree.

Generally, if we have n data points, there is exactly one polynomial of degree at most $n-1$ going through all the data points. The interpolation error is proportional to the distance between the data points to the power n. Furthermore, the interpolant is a polynomial and thus infinitely differentiable. So, we see that polynomial interpolation overcomes most of the problems of linear interpolation (Fig.2).

However, polynomial interpolation also has some disadvantages. Calculating the interpolating polynomial is computationally expensive compared to linear interpolation. Furthermore, polynomial interpolation may exhibit oscillatory artifacts, especially at the end points. More generally, the shape of the resulting curve, especially for very high or low values of the independent variable, may be contrary to commonsense, i.e. to what is known about the experimental system which has generated the data points. These disadvantages can be reduced by using spline interpolation or restricting attention to Chebyshev polynomials.

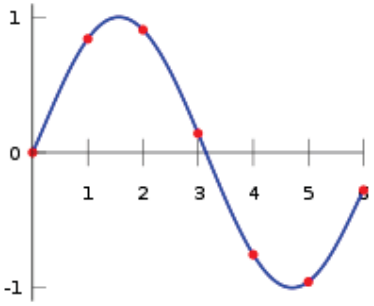

Fig. 2

2.3. Spline interpolation

Remember that linear interpolation uses a linear function for each of intervals $[x_k,x_{k+1}]$. Spline interpolation uses low-degree polynomials in each of the intervals, and chooses the polynomial pieces such that they fit smoothly together. The resulting function is called a spline. Like polynomial interpolation, spline interpolation incurs a smaller error than linear interpolation and the interpolant is smoother. However, the interpolant is easier to evaluate than the high-degree polynomials used in polynomial interpolation. It also does not suffer from Runge's phenomenon. It should be noted that minimal power for the spline is 3.

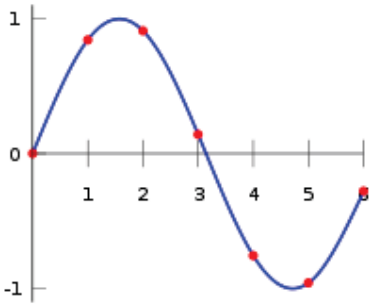

Fig. 3

3. INTERPOLATION OF THE VALUE OF MAGNETIC INDUCTION OF LOW FREQUENCY MAGNETIC FIELD IN THE CASE OF MAGNETIC BED

One new system for magneto-therapy is "magnetic bed" (Fig. 4).

The number of every coil and the coordinate system XYZ are shown on the Fig. 4. The first coil of pair is denoted by "A" in the table and the second coil in the pair by "B". In the table there are coordinates of every point of measurement.

For every pair of coils the measurements have been done at 3 points. The first and the second points are in the centers of the two coils and the third point of measurement is on the middle of the line between the centers of two coils of the pair. In every moment only one pair of coils is active. In the process of the system functioning every pair of coils is active by turns and a movement of magnetic field occurs. The order of the choice of pairs of coils is defined by a data table. It is necessary to provide interpolation on the line of every pair of coils on the base of result of measurement in three points and visualize results.

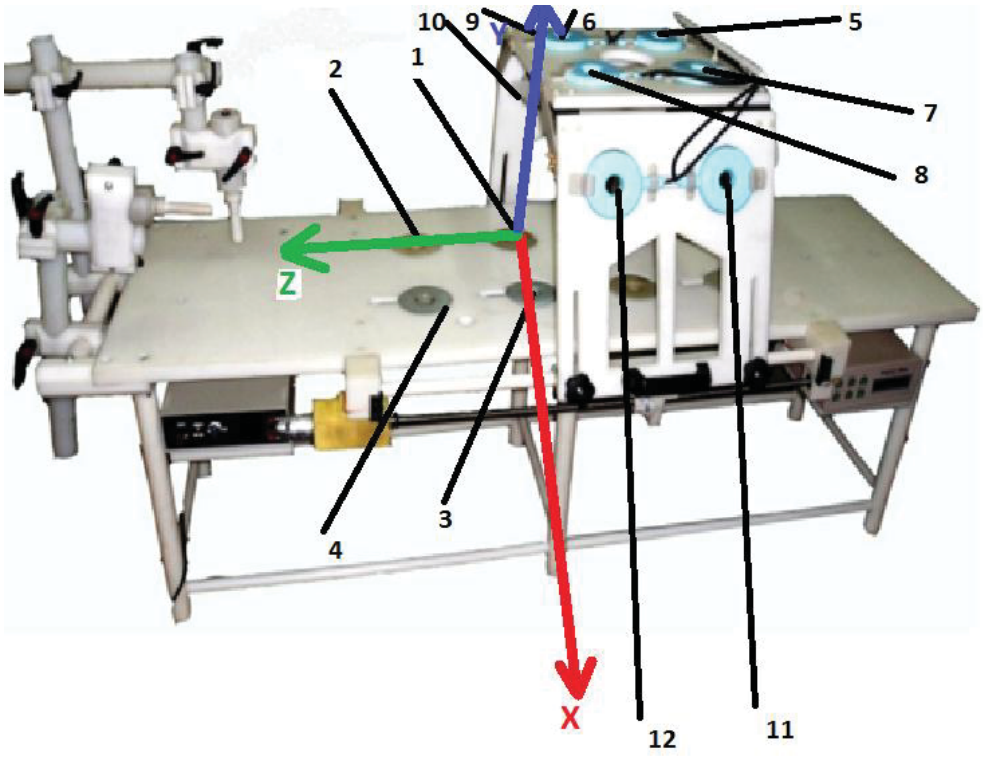

Fig. 4

The results of experimental measurement of the value of magnetic induction of low frequency magnetic field in different points according to Fig. 4 are shown in Table 1. This table can be saved as text file structured in accordance with the table (matrix 13 x 32). Interpolation can be done for points which are on the line containing interpolation nodes.

Taking into account the advantages and disadvantages of the interpolation methods we came to the decision to use one- dimensional square L'Agrange interpolation. The interpolation nodes are three points:

1. Centre of the first active coil. The coordinates of this node x_0 y_0 z_0 can be obtained from the columns 3, 4, 5 of the input file.
   The value of magnetic induction after experimental measurement in the node (x_0, y_0, z_0) is f_0 in the column 10 of the input file.
2. Centre of the second active coil. The coordinates of this node (x_2, y_2, z_2) can be obtained from the columns 7,8,9 of the input file . The value of magnetic induction after experimental measurement in the node (x_2, y_2, z_2) is f_2 in the column 11 of the input file.

Table 1

№	Coil A				Coil B				Value A mT	Value B mT	Average value mT	Distance mm
	№	axis			№	axis						
		X	Y	Z		X	Y	Z				
1	1	0	0	0	5	0	500	0	50	50	0.5	500
2	1	0	0	0	6	0	500	234	50	50	0.38	550
3	1	0	0	0	7	238	500	0	50	50	0.25	600
4	1	0	0	0	8	238	500	234	50	50	0.12	640
5	2	0	0	234	5	0	500	0	50	50	0.38	550
6	2	0	0	234	6	0	500	234	50	50	0.5	500
7	2	0	0	234	7	238	500	0	50	50	0.12	640
8	2	0	0	234	8	238	500	234	50	50	0.25	600
9	3	238	0	0	5	0	500	0	50	50	0.12	640
10	3	238	0	0	6	0	500	234	50	50	0.25	600
11	3	238	0	0	7	238	500	0	50	50	0.5	500
12	3	238	0	0	8	238	500	234	50	50	0.38	550
13	4	238	0	234	5	0	500	0	50	50	0.12	640
14	4	238	0	234	6	0	500	234	50	50	0.25	600
15	4	238	0	234	7	238	500	0	50	50	0.38	550
16	4	238	0	234	8	238	500	234	50	50	0.5	500
17	1	0	0	0	9	-130	333	0	50	50	1	360
18	1	0	0	0	10	-130	333	234	50	50	0.63	430
19	1	0	0	0	11	368	333	0	50	50	0.5	500
20	1	0	0	0	12	368	333	234	50	50	0.38	550
21	2	0	0	234	9	-130	333	0	50	50	0.63	430
22	2	0	0	234	10	-130	333	234	50	50	1	360
23	2	0	0	234	11	368	333	0	50	50	0.38	550
24	2	0	0	234	12	368	333	234	50	50	0.5	500
25	3	238	0	0	9	-130	333	0	50	50	0.5	500
26	3	238	0	0	10	-130	333	234	50	50	0.38	550
27	3	238	0	0	11	368	333	0	50	50	1	360
28	3	238	0	0	12	368	333	234	50	50	0.63	430
29	4	238	0	234	9	-130	333	0	50	50	0.38	550
30	4	238	0	234	10	-130	333	234	50	50	0.5	500
31	4	238	0	234	11	368	333	0	50	50	0.63	430
32	4	238	0	234	12	368	333	234	50	50	1	360

3. Middle of the line between points 1 and 2.The coordinates $(x_□, y_□, z_□)$ of this node can be calculated by using coordinates of the points 1 and 2.
   Then:

$$(x_□, y_□, z_□) = (\frac{x_0 + x_2}{2}, \frac{y_0 + y_2}{2}, \frac{z_0 + z_2}{2}) \qquad (3)$$

4. The value of magnetic induction after experimental measurement in the node $(x_□, y_□, z_□)$ is in the column 12 of the input file.

   For the point of interpolation (x,y,z) one can use the equation

$$□(x, y, z) = \prod_{□=0, □≠□}^{2} \frac{\sqrt{(x - x_□)^2 + (y - y_□)^2 + (z - z_□)^2}}{\sqrt{(x_□ - x_□)^2 + (y_□ - y_□)^2 + (z_□ - z_□)^2}}, \qquad (4)$$

$$□(x_□, y_□, z_□) = 0, □ ≠ □$$

$$□(x_□, y_□, z_□) = □□$$

where: l_i – basic polynomial for the node (x_i,y_i,z_i).

The interpolation polynomial is:

$$□(x, y, z) = \sum_{□=0}^{2} f_□ \cdot □(x, y, z) \,, □□□□□□□□□□□□□□□□□□□□ \qquad (5)$$

where f_n – the value of magnetic induction measured in the point (x_n,y_n,z_n).

□

4. CONCLUSION

We propose a mathematical model for interpolation of electromagnetic field in a special device of magnetotherapy — magnetic bed. Interpolation should be performed for the points of the line connecting

centres of two given coils. Measurements are made in the coils centers and in the middle of the connecting them line. These points are interpolation nodes. To solve the task we use square L'Agrange interpolation.

Acknowledgements

The work was partially supported by the grant RFBR 13-01-00782.

References

[1] N. Ampilova, D. Dimitrov, B. Kudrin. Mathematical modeling of low frequency magnetic field in systems for magnetotherapy. Proc. 8 Int. Conf. CEMA13, 17-19 Oct. 2013, Sofia, Bulgaria. p. 48-51.

[2] B. Kudrin, A. Dimitrov. An algorithm for visualization of low-frequency magnetic signals in systems for magnetotherapy. Proc. 8 Int. Conf. CEMA13. 17-19 Oct. 2013, Sofia, Bulgaria, p. 31-35.

[3] B. Kudrin, A. Dimitrov. Computer visualization of low frequency magnetic signals in systems for magnetotherapy with variable parameters. Proc. 8 Int. Conf. CEMA13. 17-19 Oct. 2013, Sofia, Bulgaria, p. 36-39.

[4] B. Kudrin, I. Soloviev. On interpolation methods of low frequency magnetic field in systems for magneto therapy. Proc. 9 Int. Conf. CEMA14. 16-18 Oct. 2014, Sofia, Bulgaria, p..

PZT AND MEMS APPLICATIONS FOR THE VESTIBULAR SYSTEMS

Tsvetan Kachamachkov

Technical University of Sofia, Bulgaria
Postal Sofia – 1309, „Sv. Troitsa" 303 - B - 39

Abstract

The paper presents a research in the area of PZT and MEMS uses for the vestibular systems. The following will introduce the anatomy and physiology of the inner ear and more specifically, the vestibular system. And some of the modern developments in the field of PZT and MEMS uses for the vestibular systems. It is important to note that holds medical devices more and compact and and that the interest in the field still continues to grow with the development of new devices and new methods for the PZT and MEMS uses in the field of the vestibular systems. Lead zirconium titanate is an intermetallic inorganic compound with the chemical formula Pb[ZrxTi1-x]O3 (0≤x≤1). Also called PZT, it is a ceramic perovskite material that shows a marked piezoelectric effect, which finds practical applications in the area of electroceramics. It is a white solid that is insoluble in all solvents. Microelectromechanical systems (MEMS)

1. INTRODUCTION

The following will introduce the anatomy and physiology of the inner ear and more specifically, the vestibular system, Figure 1 [1].

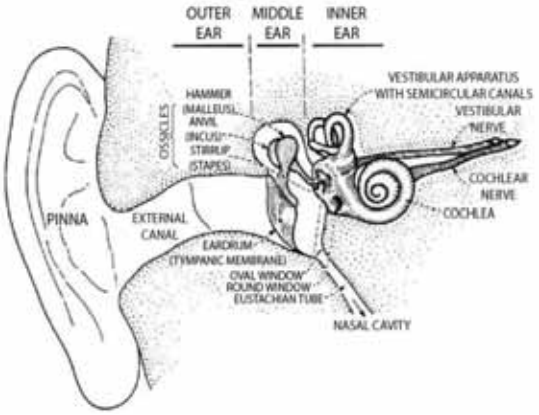

Fig. 1. Anatomy of the human ear [1]

The vestibular system, located in the inner ear, is used to maintain equilibrium bycoordinating motor responses, eye movements, and posture. Bycoordinating head and eye movements, the vestibular system allow for the eyes to remain fixed on a point when the head is in motion [4]. The vestibular organs include the otolith organs, the utricle and saccule, and the semicircular canals (Figure 2). Located within each of these organs are sensory mechanoreceptors in the form of hair cells. The vestibular hair cells respond to accelerations of the head or accelerations due to gravity. [3]

The human vestibular organs consist of the utricle, the saccule, and the three orthogonal semicircular canals. The human semicircular ducts, housed within the semicircular canals, are important in the detection of angular motion and in measuring the head's angular velocity. Three different semicircular ducts are located in different planes. The anterior and posterior ducts are located in the vertical plane at approximately right angles to each other. The lateral duct is in the horizontal plane when the head is tilted down □0□ (Figure 3).

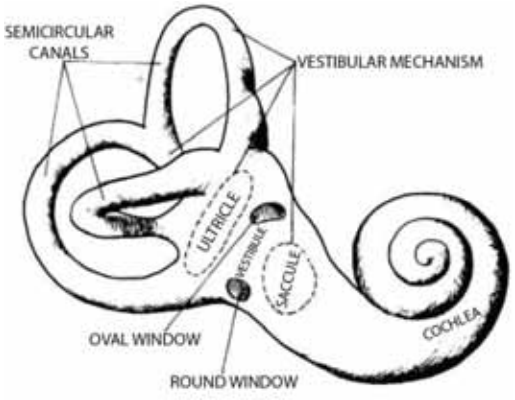

Fig. 2. Human vestibular organs [2]

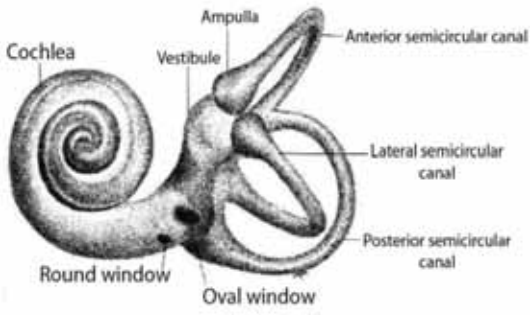

Fig. 3. Orientation of the human semicircular canals in the vestibular system [3]

Each duct forms two thirds of a circle and is ampullated at one end. The ampulla contains the sensory hair cells in a region referred to as the ampullary crest or crista (Figure 4).The ampullary crest contains the hair bundles embedded in a gelatinous mass, the cupula. When the head undergoes angular accelerations, the viscous endolymph in the semicircular ducts lags behind due to inertia and initiates fluid flow in the duct that results in pressure on the cupula (Figure 5). The motion of the cupula elicits a response in the hair cells (Kelly, 1981) [4].

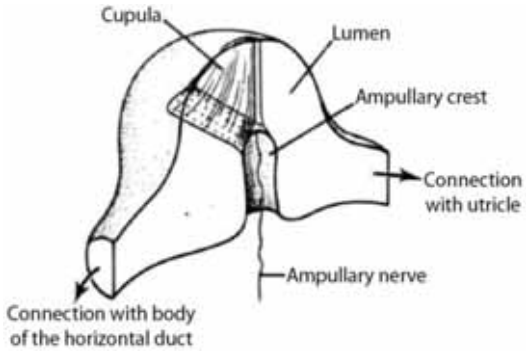

Fig. 4. The ampulla of the semicircular ducts. The ampullary crest contains hair cells embedded in a gelatinous layer, the cupula [4]

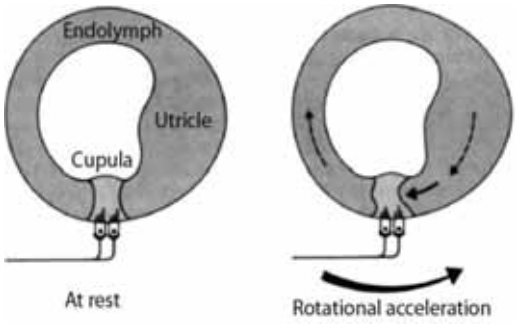

Fig. 5. Positioning of the cupula during angular accelerations [2]

During angular accelerations, the endolymph causes a force on the cupula resulting in a displacement of the cupula and the hair cells embedded in it the entire substance and its contents are referred to as the otolith membrane. The epithelium is connected to the otolithic membrane by a 5-8 μm thick column filament layer [5]. When the head is tilted, gravity will displace the otoconia, causing a disturbance in the gelatinous layer (Figure 6)

During angular accelerations, the endolymph causes a force on the cupula resulting in a displacement of the cupula and the hair cells embedded in it the entire substance and its contents are referred to as the otolith membrane. The epithelium is connected to the otolithic membrane by a 5-8 μm thick column filament layer [5]. When the head is tilted, gravity will displace the otoconia, causing a disturbance in the gelatinous layer (Figure 6).

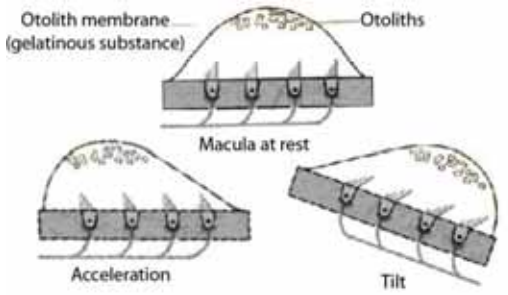

Fig. 6. Displacement of the macula during motion [2]

There is very limited research in the area of inner ear hair cell mechanics. Different techniques have been used to determine the mechanical stiffness of hair bundles. Glass whiskers are used to deflect hair bundles and the deflection is measured with video microscopy or with photodiodes [9].

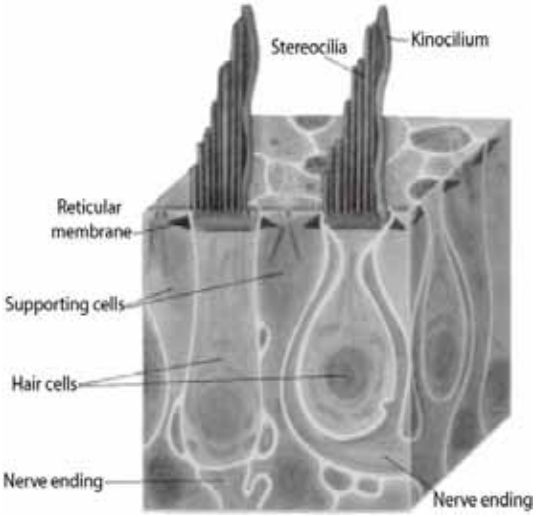

Fig. 8. Hair cells are separated by supporting cells [7]

Another method used to deflect the bundles involves using the stream from a water jet. The resulting stiffness values from previous works are shown in Table 1. These average stiffness values are for different animals and are from different parts of the vestibular and auditory systems. One study showed the relationship between different types of hair bundles in the utricle and their stiffness values. It was found that the striolar hair bundles (stiffness of 2.83-27.1×10^{-5} N/m) [10]. There has been no research to date comparing the measured location of the hair bundle within the utricle to its stiffness.

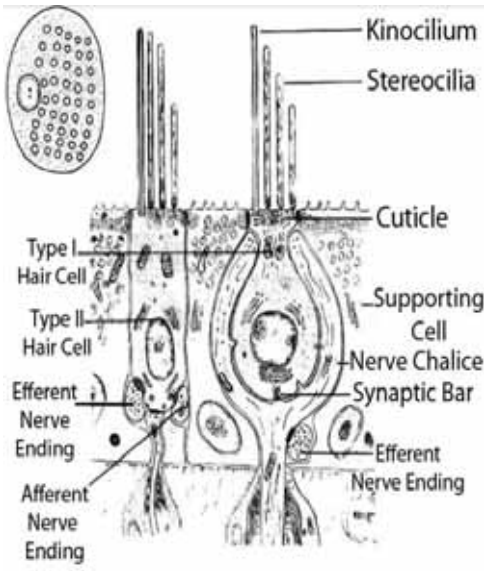

Fig. 9. Hair cell types [8]

Table 1. Experimental stiffness values [11]

INVESTIGATOR	STIFF-NESS ($\times 10^{-4}$ N/m)	HAIR CELL ORGAN
Ashmore (1984)	1.32	frog sacculus
Flock and streiloff(1984)	7.8 to 34.7	guinea pig cochlea
Streiloff and Flock (1984)	1 to 97.2	guinea pig cochlea
Crawford and fettiplace(1985)	6	turtle cochlea
Howard and Ashmore(1986)	2.56	frog sacculus
Howard and Hudspeth(1988)	6.3	bullfrog sacculus
Denk. Webb. And Hudspeth(1989)	3.41	frog sacculus
Russell. Richardson and Kossl(1989)	16 to 35	mouse cochlea
Szymko, Dmitri and saunders (1992)	5.4	chick cochlea

2. EXPERIMENTAL SETUP AND THE EQUIPMENT USED TO LOCATE AND MEASURE A HAIR BUNDLE'S STIFFNESS

A solution was developed to preserve the viability of the hair cells during testing. After measuring the extracellular fluid, or perilymph, in the inner ear of the turtle, it was determined that the fluid had a solute concentration of approximately 300 mOsm. Osmolality measurements were conducted using a VAPRO Vapor Pressure Osmometer 5520. An artificial perilymph (AP) solution was then developed to contain the same osmolality as the actual biological fluid. The solutes in Table 2 were added to one litter of deionized water. Also added were 10 mL of vitamins and 20 mL of amino acids. Once the AP solution was properly mixed, the pH was then measured. In order to get the pH close to the normal pH of blood and most extracellular fluids, the AP solution was titrated with hydrochloric acid until the pH was approximately 7.3-7.4. The AP solutions were stored in 100-mL aliquots, then frozen and thawed upon use.

Table 2. Solute concentrations mixed into a solution to be used during dissection and testing

Solute	milliMolar values (mM)	Mass (grams)
NaCl	144.0	8.415
NaH_2PO_4	0.7	0.084
KCl	5.8	0.432
$CaCl_2$	1.3	0.144
$MgCl_2$	0.9	0.086
HEPES	10.0	2.383
D-Glucose	5.6	1.001

The whiskers are made in a two step process from borosilicate glass rods pulled with a micropipette puller and microforge (Steolting Co.) to a tip diameter of 1-2 μm. Glass whiskers were used because of they were simple to manufacture with the equipment available and it was possible to produce whiskers with a very small stiffness value. The whisker is designed to be less stiff than the bundle so the pipette displacement is greater than the bundle displacement. The glass rods are first placed in the micropipette puller and a piece of clay is placed on the end of the rod. The coils are heated until the pipette begins to elongate due to the weight of the clay. Once the pipette is drawn to approximately 4 μm, the heat is turned off. The rod is then placed in a microforge (Steolting Co.) where it is heated again by a nickel-chromium filament. Another weight is attached to the bottom of the pipette and it is again drawn until the diameter is now 1-3 μm. Another pipette that has already been pulled to approximately 25 μm by the micropipette puller and shaped by the microforge to fit the contour of the slides is aligned perpendicular to the smaller pipette. Using a light sensitive adhesive, the smaller pipette is bonded to the tip of the larger pipette. The smaller pipette is then trimmed to a length of 600-900 μm. The smaller pipette is now referred to as the glass whisker (Figure 10) [10].

The (micromanipulator) Burleigh PCS-5100 was used in "Experimental Measurements of Vestibular

Hair Bundle Stiffness in the Red Ear Slider Turtle Utricle" to hold and manipulate the motion of the pipette. The micromanipulator (Figure 11) [12] utilizes piezoelectric (PZT) actuators to make very small, precise movements.

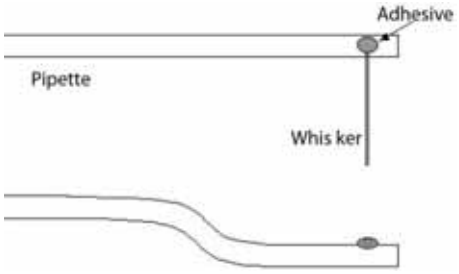

Fig. 10. Pipette with attached whisker [10]. The glass pipette is shaped to fit the contour of the slides on which the utricle is mounted

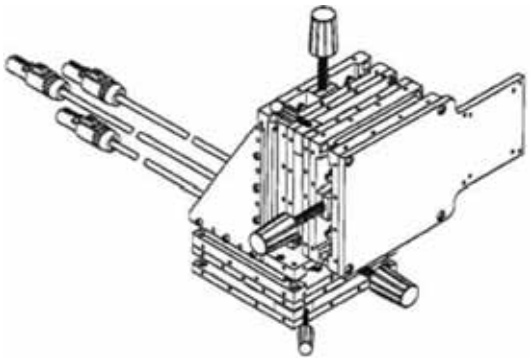

Fig. 11. Micromanipulator (Burleigh manual). The three large knobs on the micromanipulator are used to □ □□□□□□□the pipette in three orthogonal directions [12]

Three actuators allow for motion in three orthogonal directions, up and down, left and right, and forward and backward. An Axis Control Unit (ACU) controls the actual movement. Three knobs on the ACU correspond to the three different directions and are used to move the pipette in those directions (Burleigh manual). The PZT actuators and the ACU are used to position the whisker on the bundle and to produce a force on the bundle. In order to position the whisker in the vicinity of the bundle, screws located on the side of the stage are turned. The screws allow for greater movement, while the actuators and the ACU allow for smaller movements of up to 300 mm. The pipette is held by placing it in a groove on the micromanipulator and another plate is screwed on top to clamp it down, Figure 12.

The groove in the large aluminium plate holds the pipette when the smaller aluminium plate is screwed in to clamp down on the pipette. MEMS and PZT are being used in a device for diagnosing and treating hearing disorders [13]. Figure 13 illustrates a supersonic hearing assist device which includes a transducer 20, a cable 21, and a tuning circuit 22 which is mounted within an electronic housing 23. The transducer is held up against the mastoid process of the temporal bone. The transducer can also be applied to other surfaces of the human body, for example, the Wall of the ear canal, the middle of the human forehead, the human tooth, human clavicle, human spine, or other bones. In general the housing 23 includes a microphone for receiving sounds in the auditory frequency range and a device for amplifying and converting the frequencies to the supersonic range and for applying electrical signals to the transducer.

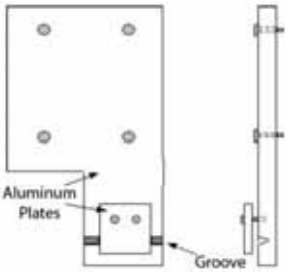

Fig. 12. Pipette holder [10]

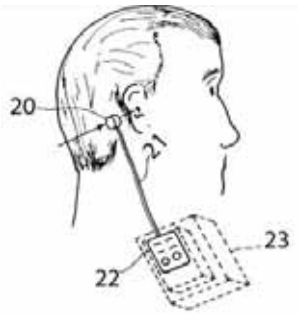

Fig. 13. Supersonic transducer formed in accordance with the invention being used as a hearing assist device

In figure 14, the transducer 20 is best described as a piezoelectric longitudinal vibrator and includes a central piezoelectric ceramic tube 25, a radiating surface or head mass 26, and an inertial or tail mass 27. The radiating surface and inertial mass are tied together by a tensioning rod 28 to keep the assembly from self destructing as a result of large displacements of the radiating surface.

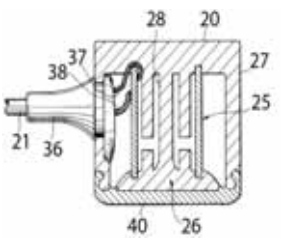

Fig. 14. Enlarged sectional view of the transducer [13]

According to Figure 15, the inertial mass 27 can be formed from separate components which include a generally cylindrical housing 30, a back plate 31, and a nut 32.

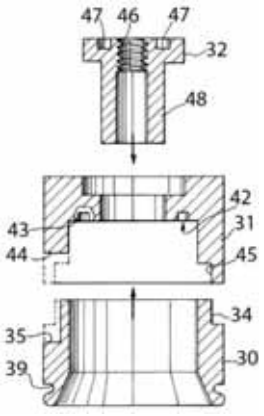

Fig. 15. Exploded sectional view of the tail mass assembly of the transducer [13]

3. CONCLUSION

Of the following, it can be concluded that PZT and MEMS are widely used in the field of research related to the vestibular system, and part of the modern and active developments in the field.

Both electrodes are etched back on both ends of the ceramic a small distance to allow for capture of the ceramic in the ceramic capture ring 42 of the back plate 31 and head mass 26 without resulting in a short circuit. When a voltage is applied across the electrodes of the ceramic, the ceramic either expands or contracts in thickness. This motion is inconsequential to the operation of the device. At the same time, the ceramic also contracts or expands in length and circumference. The expansion and contraction in length is what drives the head mass in a longitudinal vibration.

The ceramic material is selected from the family of lead zirconate titanate (PZT), more specifically from the PZT-4 and PZT-8 ceramics. These particular ceramic materials are selected for their especially low value of dissipation factor or loss tangent, the parameter which relates to the tendency of the ceramic to generate heat as a result of large applied electric fields. The low heat abilities of these materials markedly overshadow the attendant reduced displacement. The static "DC" longitudinal zero to peak displacement D of the cylindrical tube ceramic is given by the expression:

$$\square = \square_{\square\square} \cdot \square \cdot \frac{\square}{\square\square\square} \square \qquad (1)$$

where

d_{31} is the piezoelectric charge constant, typically in the range from 97 to 122×10^{-12} m/V for the PZT-8 and PZT-4, respectively,

V is the applied zero to peak voltage,
L is the length of the ceramic tube.
thk is the thickness of the ceramic tube Wall.

The displacements predicted by the above expression are modest, below the levels required for the hearing assist device. The resonant frequency emission typically increases by 35 to 40 dB.

References

[1] Brown, B.H., Smallwood, R.H., Barber, D.C., Lawford, P.V., Hose, D.R. (1998) *Medical Physics and Biomedical Engineering*. CRC Press, ISBN 978-0-7503-0368-2

[2] Klinke, R. (1986) *Physiology of Hearing*. Fundamentals of Sensory Physiology. Edited by R.F. Schmidt. New York: Springer-Verlag.

[3] Singh, R.P. (1980). *Anatomy of Hearing and Speech.* New York: Oxford University Press.

[4] Kelly, J.P. (1981). "*Vestibular System*." Principles of Neural Science. Edited by E.R. Kandel and J. H. Schwartz. New York: Elsevier North Holland, Inc.

[5] Kachar, B., Parakkal, M., Fox, J. (1989). *"Structural basis for mechanical transduction in the frog vestibular sensory apparatus"*: I. The otolithic membrane. Hearing Research 45: 179-190.

[6] Title - *Journal of morphology, Том 163* Journal of morphology published 1980 Original from the University of California Digitized Sept. 3. 2008

[7] Spoendlin, H. (1966). *"Ultrastructure of the Vestibular Sense Organ."* The Vestibular System and it Diseases. Philadelphia: University of Pennsylvania Press.

[8] Wersall, J. Bagger-Sjoback, D. (1974) *"Morphology of the vestibular sense organ."* Handbook of Sensory Physiology. Kornhuber, H.H. Ed., Berlin: Springer Verlag.

[9] Crawford, A.C. & Fettiplace, R. (1985). "The mechanical properties of ciliary bundles of turtle cochlear hair cells." Journal of Physiology 364: 359-379.

[10] Merkle, A.C. (2000). "Implementation of a Photoelectronic Motion Transducer for Measuring Sub-Micrometer Displacements of Vestibular Bundles." Master's Thesis, Virginia Tech.

[11] Szymko, Y.M., Dimitri, P. S., & Saunders, J. C. (1991). *"Stiffness of hair bundles in chick cochlea."* Hearing Research 59: 241-249.

[12] Experimental measurements of vestibular hair bundle stiffness in the red ear slider turtle utricle jennifer mary silverman thesis submitted to the faculty of the virginia polytechnic institute and state university in partial fulfillment of the requirements for the degree of master of

science in engineering mechanics j.wallace grant, chair don h. Morris ellengene h. Peterson july 31, 2002 Blacksburg, Virginia

[13] *Publication number US6068590 A* Publication type Grant Application number US 08/957, 189 Publication date May 30, 2000 Filing date Oct 24, 1997 Priority date Oct 24, 1997 Fee status Lapsed Also published as CA2248666A1, EP0912073A2 Inventors Axel F. Brisken Original Assignee Hearing Innovations, Inc. Export Citation BiBTeX, EndNote, RefMan - References to 13:

[14] Lan et al "Development of an Efficient Transducer Design Tool: Complete Finite Element Modeling of Transducer Performance Parameters on a PC", SPIE vol. 1733, 1992 p. 57-71.

[15] Lan et al Development of an Efficient Transducer Design Tool: Complete Finite Element Modeling of Transducer Performance Parameters on a PC, SPIE vol. 1733, 1992 p. 57 71.

[16] Camp "Underwater Acoustics", Wiley-Interscience, 1970

[17] Lan et al Development of an Efficient Transducer Design Tool: Complete Finite Element Modeling of Transducer Performance Parameters on a PC, SPIE vol. 1733, 1992 p. 57 71.

[18] Lenhardt et al "Human Ultrasonic Speech Perception," Science, vol. 253, p. 82-84 (1991).

[19] Mason "Physical Acoustics, Principles and Methods", vol. 1, Part A, Academic Press, (1964).

[20] Rosenthal et al "*Vibrations of Ferroelectric Transducer Elements Loaded by Masses and Acoustic Radiation*", IRE National Conventional Record 7, Part 6, 252.

[21] Shunichi Kono, et al, Some Consideration on the Auditory Perception of Ultrasound and Its Effects on Hearing, *Journal of the Accustical Society of Japan (1985)*.

[22] Tims et al Piezoelectric Ceramic Reproducibility (for 33 Mode Transducer Application), Proceedings of the 6th IEEE International Symposium on Applns. of Ferroelectics, Lehigh U., Bethlehem, PA, p. 6245 627, Jun. 8 11, 1986

[23] Tims et al Piezoelectric Ceramic Reproducibility (for 33 Mode Transducer Application), Proceedings of the 6th IEEE International Symposium on Applns. of Ferroelectics, Lehigh U., Bethlehem, PA, p. 6245-627, Jun. 8-11, 1986.

[24] Woollett, IRE International Convention Record 10, Part 6, p. 90, 1962.

ALGORITHM TO CALCULATE THE MAXIMUM VALUE OF THE LOW-FREQUENCY MAGNETIC FIELD USING MICROPROCESSOR AND MAGNETIC SENSORS

Vladimir Nikolov

Faculty of Telecommunication
TU-Sofia
Author Affiliation: Bulgarian
Postal address: Bulgaria, Sofia, PostCode 1000, boulevard Kliment Ohridski 8
T.+359 965 2278 ; F. .+359 965 2278; E. v_nikolov@tu-sofia.bg.

Abstract

In this article is considered the algorithm for measuring the low-frequency magnetic fields in the range 0,1 Hz to 100 Hz. The algorithm used to construct the apparatus for measuring low frequency magnetic fields generated by systems for magnetotherapy, using moving magnetic field. The possibility for simultaneously influence of low frequency magnetic field on different part of the human body is one additional advantage of systems for magnetotherapy, using moving magnetic field.

1. INTRODUCTION

During the past few decades, the advances in the theory and technology of modern electronics have led to improvements in medical diagnostic and therapeutic methods. As a result, bioelectric and biomagnetic phenomena have become increasingly important. Today it is not possible to imagine a hospital without electrocardiography and electro encephalography. The development of microelectronics has made the respective equipment portable and has increased its diagnostic power. Implantable cardiac pacemakers have made it possible for millions of people to return to normal life. The development of superconducting technology has provided the means to detect the weak biomagnetic fields induced by bioelectric currents. The latest advances in the measurement of electric currents flowing through a single ion channel of the cell membrane with the patch clamp have opened up completely new applications for bioelectromagnetism. With the patch clamp, bioelectromagnetism can also be applied to molecular biology, e.g. in developing new pharmaceuticals. These examples illustrate that bioelectromagnetism is a vital part of our everyday life. Modern bio-medical diagnostic technique involves two main groups of measuring instruments: ones for measuring bioelectric, bio-magnetic, etc. signals and imaging systems. Registration systems are non-invasive bio-signals – with sensors and electrodes attached to the surface of the body in the form of implants, needle electrodes or chemical sensors.

Measured magnetic field represents sinusoidal oscillation whose amplitude and repetition frequency change over time. The frequency of oscillation was varied between 0,1 Hz and 150 Hz. In such a repetition frequency oscillation sinusoidalnoto need to develop special algorithm by which it can in every moment of time to determine the maximum value of the signal.

Fig. 1

If measured value of amplitude of the curve in the classical way without the use of a special algorithm will not get correct measurement as at the time of measurement can be measured minimum or zero value.

Magnetic sensor - A small coil can be used as semiconductor for measurement of magnetic induction of low frequency magnetic field. The coil is made of dielectric on which reel is wound a copper wire with a thickness of 0,2 mm The coil is placed in a special housing with dimensions 15mm X 80 mm. It has a cylindrical shape and is easy to use by the physician. The coil is a small, because the magnetic field measured at fixed points in space.

2. PRINCIPLE OF THE ALGORITHM

Principle of the algorithm is as follows: For a short period of time eg 1 s made n number measurement. Largest measured value of the field for this period of time is determined for the maximum value of the field. In the algorithm are implemented additional conditions by which to reduce the error caused by disturbance die come in the area of measurement.

Fig. 2

Introduced the following conditions:

- Are defined maximum values of the measured field. When the measured value of the amplitude is greater than the maximum possible value, the measured value is ignored and then not be included in determining the maximum value of the measured magnetic field.
- Defining the Difference between maximum two adjacent measured values. When the difference between the two measured values is greater than the predetermined value is ignored.

In both cases, the errors in measurements can occur when the measured system noise and interference fall. Through the above-described conditions to a large extent the impact of interference can be eliminated.

3. DESCRIPTION OF THE ALGORITHM

Declaring variables: This section describes the absolute all variables that will be used in the program executed by the microprocessor

Determination of inputs for measurement: In this part of the program to determine which pins on the microprocessor will be used to obtain a refund quote sensors and which will be used for transmission of already processed information. Besides the type of conclusion here determines what kind will be the input signal - analog or digital. In our case the input signal to be analog.

Starting serial communication: The relationship between the microprocessor and the next device that will process the measured data is done via the serial interface. This step configures the speed of transmission of data between the microprocessor and the next device.

Calibration of the ADC - Sets the maximum value that will be applied on ADC

System testing: Condition in which the program is implemented consistently, unless interrupted power. Power microprocessor. Interruption of power. Supply the microprocessor establishes end of the program.

Recording of measured values from sensors in buffer: instantaneous measured values are stored in the local memory of the microprocessor.

Comparison of measured values: In this part of the program is compared to the value of the instantaneous measured value from the sensor, and the previous measured value, if the new measured value is greater than the previous value and the new measured value is greater than the maximum

permissible value measured set in defining the variables, the last measured value is stored in the microprocessor. If the above condition is not fulfilled, the last measured value is ignored.

Clock – 1: By this timer is achieved through a particular point in time (eg 1s) measured and filtered off value (eg 1s) sensors to provide the next device for further processing. When the value is accepted by the next device, it is deleted from the memory of the microprocessor.

4. CONCLUSION

Developed Algorithm to calculate the maximum value of the low-frequency magnetic field using microprocessor and magnetic sensors makes it possible to calculate precisely the intensity of the magnetic field in 16 points. By using this algorithm achieves a reduction of measurement error caused by external noises come into the system.

Acknowledgment

The research in this paper is supported by contract No.142ПД0002-7.

References

[1] D. Dimitrov, Medical systems for influence of electromagnetic fields on human, education book, TU-Sofia, 2007.

[2] W. Y. Riadh, Electromagnetic Fields and Radiation (Human Bioeffects and Safety)", Marcel Dekker Inc. Canada, 2001, ISBN 0-8247-0877-3.

[3] V. Nikolov,. System for measurement of magnetic induction of low frequency magnetic field Proc. 9 Int. Conf. CEMA14. 16-18 Oct. 2014, Sofia, Bulgaria, p.

[4] Stefanov N., Power Supply, Technika, Sofia, 2002

[5] Microchip-спецификация на PIC18F452

[6] Stamboliev I., Medical equipment, Technika, Sofia, 1989

SYSTEM FOR MEASUREMENT OF MAGNETIC INDUCTION OF LOW FREQUENCY MAGNETIC FIELD

Vladimir Nikolov

Faculty of Telecommunication, TU-Sofia
Author Affiliation: Bulgarian
Postal address: Bulgaria, Sofia, Post Code 1000, boulevard "Kliment Ohridski" 8
T. +359 965 2278; F. +359 965 2278; E. v_nikolov@tu-sofia.bg.

Abstract

In this article is considered the construction of an apparatus for measuring the low-frequency magnetic fields in the range 0,1 Hz to 100 Hz. The construction of an apparatus for measuring the low-frequency magnetic fields in the range 0,1 Hz to 100 Hz is considered in this article. This instrument is capable of measuring low frequency magnetic fields used in many procedures in physiotherapy.

1. INTRODUCTION

During the past few decades, the advances in the theory and technology of modern electronics have led to improvements in medical diagnostic and therapeutic methods. As a result, bioelectric and biomagnetic phenomena have become increasingly important. Today it is not possible to imagine a hospital without electrocardiography and electroencephalography. The development of microelectronics has made the respective equipment portable and has increased its diagnostic power. Implantable cardiac pacemakers have made it possible for millions of people to return to normal life. The development of superconducting technology has provided the means to detect the weak biomagnetic fields induced by bioelectric currents. The latest advances in the measurement of electric currents flowing through a single ion channel of the cell membrane with the patch clamp have opened up completely new applications for bioelectromagnetism. With the patch clamp, bioelectromagnetism can also be applied to molecular biology, e.g. in developing new pharmaceuticals. These examples illustrate that bioelectromagnetism is a vital part of our everyday life. Modern bio-medical diagnostic technique involves two main groups of measuring instruments: ones for measuring bioelectric, biomagnetic, etc. signals and imaging systems. Registration systems are non-invasive bio-signals - with sensors and electrodes attached to the surface of the body in the form of implants, needle electrodes or chemical sensors.

The effect has been discovered in 1879 by Edwin Hall. There is a voltage between two sides of the plate (semiconductor) when it is placed in a magnetic field. Voltage Uhall depends linearly on the magnetic induction field B (unit tesla T or gauss G, by 1G = 0,1mT). This relationship is one of the great advantages of the Hall sensors, as it allows accurate measurements over a wide range of constant magnetic field through U_{hall}. The magnitude of U_{hall} is the sensitivity of the Hall element. Moreover, the expression of voltage U_{hall} is in force perpendicular to the magnetic field sensor and its value decreases when the field is at an perpendicular angle.

The output voltage of the Hall element is too small (amended by tens mV change in the magnetic field of 1mT), which is why their use alone is rare. An additional amplifier should be putted in the semiconductor in the case of measurement magnetic induction with small value. The positive supply voltage VCC has stabilized since REG, to reduce the impact of changes on its output voltage of the sensor. The transistor, which is NMOS in some ICs, is not mandatory. It is placed to provide enough current output. Due to the single power supply voltage output voltage is equal to 0,5 VCC where the semiconductor is out of magnetic field. This part is always one of the great sides of the hull of IC that is appropriately marked. The exact location of the sensor and the active thickness representing the distance between him and the marked side is given in the catalogs. The linear dependence of the magnetic induction B of Vout is valid only in a given part of its range, which. It corresponds to the minimum and maximum output voltage, which is shown in Fig. 1

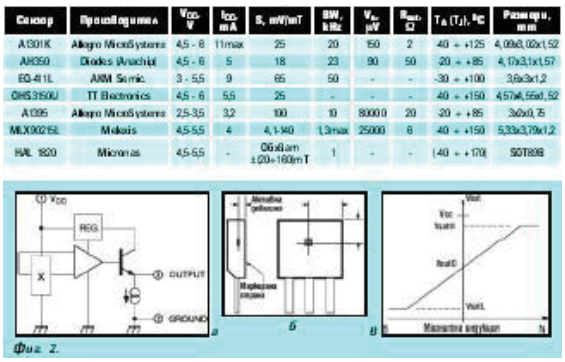

Fig. 1

These voltages are usually given as parameters for the IC. The most important parameter is the sensitivity. It allows us to calculate the maximum value of magnetic induction B B - to the graph of Fig. 2 for this south pole is BS = (VoutO - VsatL)/S and north pole BS = (VsatH - VoutO)/S, and usually both are equal and one is referred to as positive and the other as negative. For many applications it is essential that VoutO depends on temperature, which introduces an error in the measurement of C. Therefore, in most of the catalogs there is a graphics VoutO (t°). A note must be made that the voltage often increases in one direction of the magnetic field and decreases in the other. The temperature should be taken in account in the process of measurement of magnetic induction.

For our case we will be unable to apply the elements of Hall, because of the magnetic field, which measures a variable rather than a constant.

2. DESIGN OF A MAGNETIC INDUCTION MEASUREMENT SYSTEM

A small coil can be used as semiconductor for measurement of magnetic induction of low frequency magnetic field. The coil is made of dielectric on which reel is wound a copper wire with a thickness of 0,2 mm The coil is placed in a special housing with dimensions 15 mm X 80 mm. It has a cylindrical shape and is easy to use by the physician. The coil is a small, because the magnetic field measured at fixed points in space. The measurement coil is connected to the electronic unit of the described system. The connection between the probe and the meter is through a coaxial cable. It necessarily requires the use of shielded cable because noises is quite possible. The cable length is chosen as a compromise. On one hand the cable has to be as short as possible to reduce the noises and on the other, the medic should work normally and comfortably.

ADC

Analog-to-digital converter converts the digital signals. The resolution of the ADC is a 1024 levels. When this value of the quantization is achieved a high sensitivity of the system for measuring the magnetic field.

Power

Power of the device is external constant power supply 5v and 12 v.

Power consumption is consistent with the scheme, and used items are consistent with the medical device requirements. The selected transformer meets the requirement for continuous insulation between the primary and secondary coil capable 4KV.

3. MICROPROCESSOR CONTROL

Since we have 16 piece Sensor, it has to be controlled by a microcontroller. The sensor's outputs are connected to ADC. The microprocessor provides management of connection of different sensor's output to the ADC. Resulting from the ADC digital signal is sent to the microprocessor.

A specially developed algorithm calculates the value of the magnetic induction in the 16 points where the sensors are located.

The principle of action described below diagram 2.

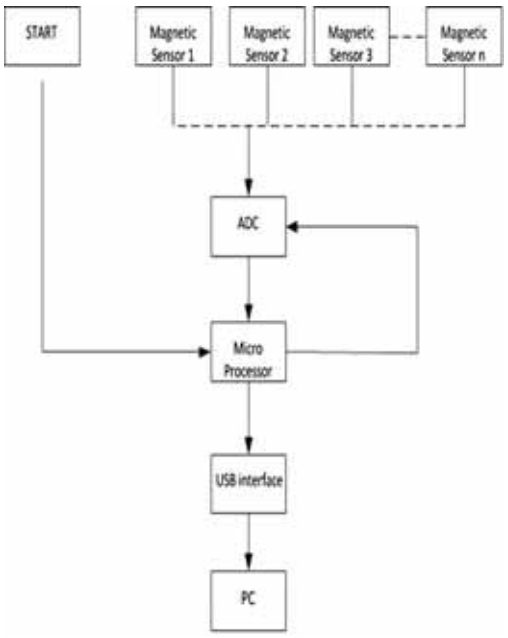

Fig. 2

The measured value of the magnetic field is supplied to the personal computer.

The PC processes the measured values of the magnetic induction and present them graphically.

4. ALGORITHM FOR GRADUATION OF SYSTEM FOR MEASUREMENT OF MAGNETIC INDUCTION

The adjustment of the measurement system can be provided using permanent magnetic field and low frequency magnetic field. The value of magnetic induction of permanent magnetic field should be the same as the amplitude of magnetic induction of low frequency magnetic field. The resulting value, which is measured, can be programmed in the memory of the microprocessor.

Table 1

Voltage	small range, mT	wide range, mT
1	0,5	10
	1	20
5	1,5	30

Based on this table is built and graduation curve (Fig.3) by the method of least squares

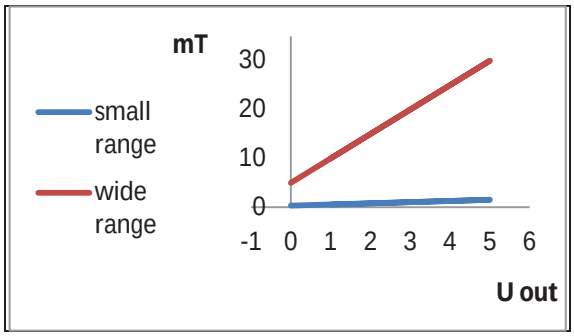

Fig. 3

5. CONCLUSION

The following processes are described in the paper. Inventions device for measuring low frequency magnetic field is consistent with the requirement for electrical safety. Power supply unit is used which has a power transformer, for galvanic separation of the device from grid

Using microprocessor allows for further upgrade of the system for measuring the low-frequency magnetic field.

The advantage of the invention device to Hall sensor that is able to measure low-frequency magnetic fields.

Acknowledgment:

The research in this paper is supported by contract No.142ПД0002-7.

References

[1] D. Dimitrov, Medical systems for influence of electromagnetic fields on human, education book, TU-Sofia, 2007.

[2] Stamboliev I., Medical equipment, Technika, Sofia, 1989.

[3] Valkov S., "Impulse Technology", Technika, Sofia, 2002

[4] Microchip-спецификация на PIC18F452

[5] Stefanov N., Power Supply, Technika, Sofia, 2002

EVALUATION OF A MAGNETIC 3D MEASUREMENT SYSTEM FOR APPLICATION IN COMPUTER ASSISTED SURGERY COMPARED TO ESTABLISHED OPTICAL TRACKING SYSTEMS

Mende, Matthias; Gerz, Erwin; Roth, Hubert

Universität Siegen
Postbox, D-57068 Siegen
T.+49 271 740 4176; F.+49 271 740 4382; E.matthias.mende@uni-siegen.de

Abstract

3D measurement systems are essential components for applications in computer assisted surgery to permanently acquire the spatial position of surgical instruments with regard to the patient's anatomy. The accuracy of these systems is of crucial importance. Unfortunately manufacturers only provide guaranteed error limits and only in very few cases error distributions in measurement volumes. This lack of information prevents the use of those systems in several applications.

In this work a tailor made experimental setup to solve this problem introduced by [1] was adapted for magnetic trackers to evaluate the accuracy of markers with a cheap and flexible environment to produce sufficiently precise and reproducible data to generate calibration maps for the requested measurement volume. Objects of different size and material have been introduced into the measurement volume to identify backlash on the detected positions and to check if a basic calibration based on the gathered information is possible.

1. INTRODUCTION

Some surgical tasks require precise feedback from trackers inside the human body, especially if this feedback is the only one the surgeon will get. This feedback gets really crucial if it is also used to control manipulators as it is done in the EU funded project Stiff-Flop (STIFFness controllable Flexible and Learn-able Manipulator for surgical OPerations, http://www.stiff-flop.eu). This project aims at the design of a flexible and stiffness controllable octopus-like robot that can go through narrow openings and manipulate soft organs. Controlling such a hyper-redundant system faces a lot of issues like distributed sensing (tactile as well as position), cognitive development and a reliable feedback. Possible surgical 3D tracking systems are available on the market; unfortunately it is not possible to compare them directly in terms of accuracy because manufacturers only provide guaranteed error limits under special conditions and in different measurement volumes. This initial situation made it necessary to find a platform that enables the user to find the best solution for his special application.

2. SPECIFICATIONS

The requirements for such a system are set by a number of factors. First of all the measurement system shall guarantee sufficient precise results; a resolution better than 5µm is intended. Along with this demand comes the necessity of reproducibility. In addition the system has to be flexible enough to handle different kinds of tracking systems available on the market and to deliver comparable results. Last but not least the system has to be affordable and handy to use.

3. THE SETUP

All these points are fulfilled by the system introduced by [1]. The authors developed a tailor made experimental setup to meet all those requirements for Optical 3D measurement systems. It evaluates the accuracy of marker based localization systems and displays the results in an intuitively understandable way. The basis here is a LEGO® brick base plate which has been fixed on a rigid aluminium board and calibrated by a high precision coordinate measuring machine afterwards. This approach seems appropriate, because the LEGO® system provides well usable equipment with high precision; the official production tolerance declared by the manufacturer is 2 µm.

The existing system had to be modified a little bit to get it running with the magnetic measurement system (NDI Aurora V2), because the aluminium plate prevented the system from working at all. The sen-

sors were detected at a minimum distance to the board of about 10 cm. Therefore a new LEGO® plate was mounted on an acrylic polymer board. The surrounding area was freed from any kind of conductive material, only the mounting of the field generator (medical steel) is kept because it belongs to the equipment provided by the manufacturer. The setup is shown in figure 6.

The position and orientation of markers at defined positions in workspace have been recorded relative to a fixed marker, which is used to eliminate possible vibrations of the mounting device holding the field generator and to monitor that no other external influence disturbed the measurement. This has been done one hundred times for each position and a median filter was applied in order to reduce noise and point out deviations from the original position.

As a first step these results were compared to optical tracking systems (Axios Cambar B2, NDI Polaris). The second step was the introduction of objects of different size and material into the measurement volume to identify backlash on the detected positions and to check if a basic calibration based on the gathered information is possible. All experimental arrangements have been examined several times to check and prove the reproducibility of the results.

The software is implemented in LabView and split into three major parts: One LabView program to establish a connection to the various tracking systems (including data conversion if necessary), one to record positioning data of markers and trackers and a third one to evaluate the recorded data and display the results in an intuitively understandable format. The whole system is designed in a modular way to guarantee extendibility without the danger of incompatibility between existing versions.

The software package is able to determine, compare and evaluate the Fiducial Localization Error (FLE, distance between actual and measured position of a single marker), Fiducial Registration Error (FRE, root-mean-square error in fiducial alignment between image space and physical space) and the Target Registration Error (TRE, similar to FRE, but for a tool centre point not located in the median point). Details about these error definitions can be found in [2]. For this investigation only the FRE is considered, because the small size and the shape of the sensor make it unnecessary to place it far away from the tool centre point of the device that is going to be monitored.

4. ACCURACY

The aurora tracking system offers two different measurement volumes: a smaller "cube" and a slightly bigger "dome" volume. The manufacturer provides error limits for both volumes, divided into "Position accuracy", "Position Precision" and "Position Trueness". The tracking mode has to be selected before start of tracking. At this point it is not clear if the decisive factor for those limits is the tracking mode or the position of the tracked object. In addition the error limits given by the manufacturer are based on [5] and not showing the accuracy of a single measurement but the mean of a "large number" – the amount is not specified.

According to [5] "Trueness" refers to the closeness of agreement between the arithmetic mean of a large number of test results and the true or accepted reference value, whereas "Precision" refers to the closeness of agreement between test results.

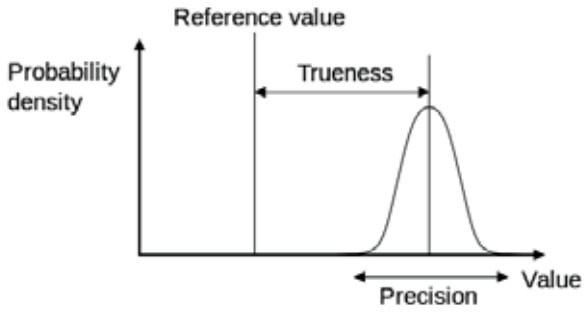

Fig. 1. Definition of "Trueness" and "Precision". Image is taken from [5]

The first experimental setup will have a look at the range of a single measurement and the impact of switching the measurement volume. Unfortunately we are only able to get information about the precision, not the trueness of the system, because the base frame is inside the field generator and cannot be accessed from outside.

Six defined positions were measured once in cube and once in dome mode. For each parameter set repeated measurements were conducted and the values were appended to achieve a total of 1000 values. This also proves the reproducibility of the measurement. An example of a single position measurement can be seen in figure 2.

The figure shows 1000 measurements of a point located at a position near the edge of the cube volume and about 350mm (z direction) away from the field generator. Figure 3 shows a histogram of the spatial deviation shown in figure 2:

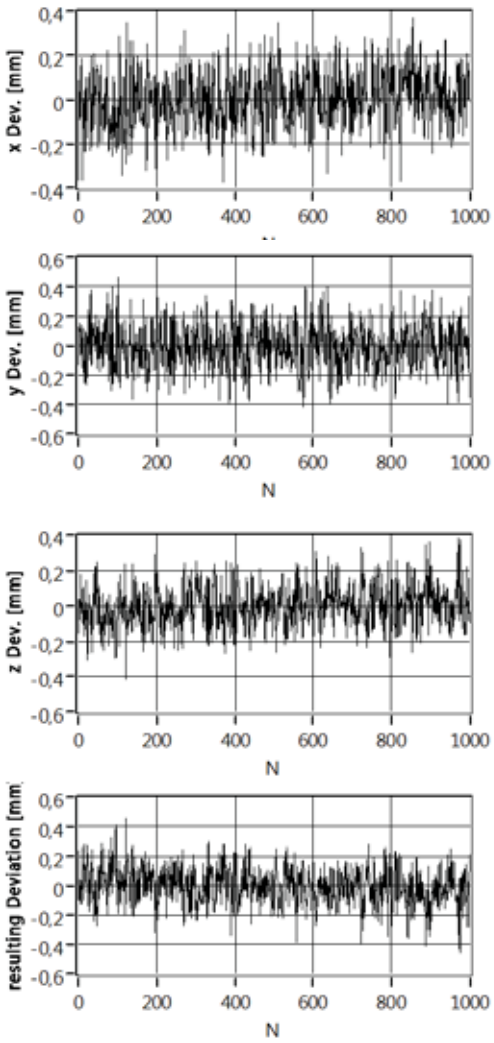

Fig. 2. Measured values in x, y and z direction and resulting deviation in space

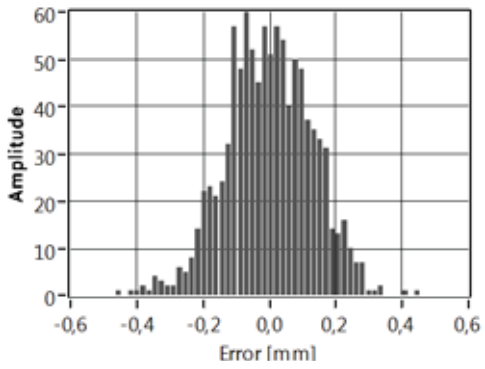

Fig. 3. Histogram of measurement series

The identified standard deviation for this example was 0.1289 mm.

The results of this experiment are diverse: First of all we can say that the standard deviation gets bigger at an increasing distance to the centre of the field generator in z direction as well as in x and y. Surprisingly the precision for sensors in the cube volume gets better if the operation mode is switched to "dome volume". This behaviour could not be illuminated at this stage of the current research work.

Another interesting point to look at would be the trueness of the measurement for different positions in workspace. Unfortunately an absolute comparison for single markers is not possible because the internal base frame of the field generator cannot be accessed from outside. The only way to get an idea of attainable trueness is to match known positions on the reference board to positions detected by the tracking system. In our case this point cloud matching is done based on an algorithm developed by [4]. The negative aspect of this procedure is the minimization of the errors at all measured positions – it is not possible to detect offsets of the whole point cloud.

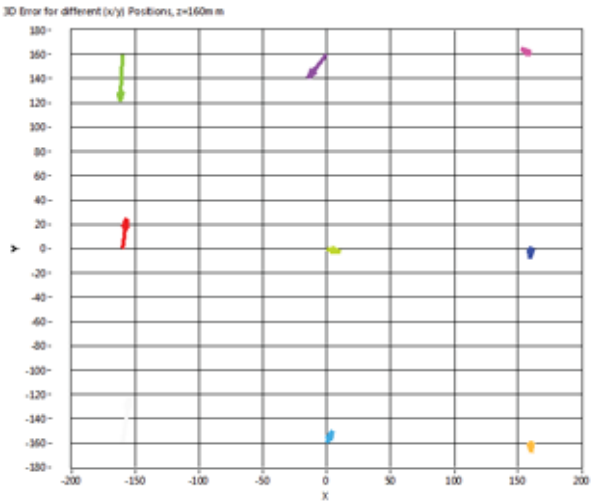

Fig. 4. 3D Error on a plane in cube volume, distance to field generator z=160mm. The vectors show the direction of the deviation and have been scaled by 2000. Unit is [mm]

The absolute deviations for an example plane (z=160 mm) after the matching can be found in figure 4. The vectors have been scaled by 2000 to make them visible.

The size of the absolute error in space is shown in figure 5.

5. RELIABILITY

The reliability of a tracking system is mainly determined by its robustness to external influences. Fortunately a magnetic tracker is not influenced by occlusion or changing lights as optical trackers are, but there might be other perturbations like external electro-magnetic fields or electrically conductive material nearby or inside the measurement volume.

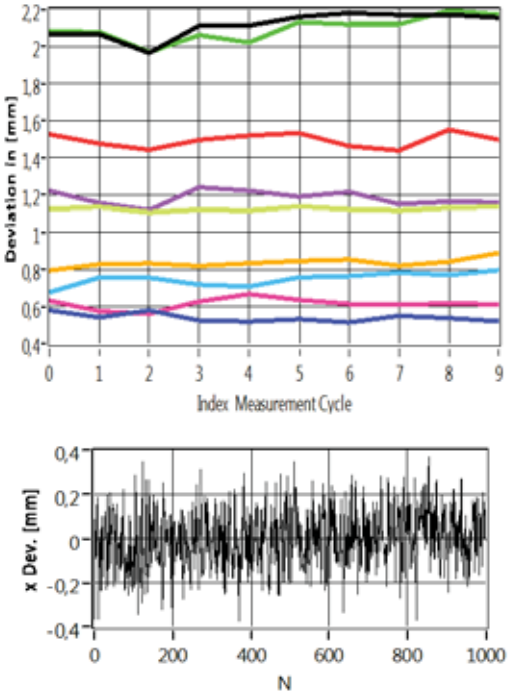

Fig. 5. Absolute deviation of all nine locations shown in Fig. 4. Unit is [mm]

To gain insights we tried to influence the system by objects of different size and material, starting with a huge brass tube in a distance of 400mm in y-direction to the centre of the cube volume (Figure 6). After 500 measurements the object had been moved to a distance of 300mm. Additional 500 measurements have been taken.

Fig. 6. Test with brass tube

The results can be seen in figure 7: All detected sensor positions moved into different directions, some of them up to 24 mm. Surprising was also the behaviour on the z-Axis (Figure 8): Deviations of up to 9mm were possible, although the tube still stood outside the measurement volume.

A possible explanation of this behaviour would be the generation of eddy currents in the electrically conductive material, disturbing the electromagnetic field of the generator.

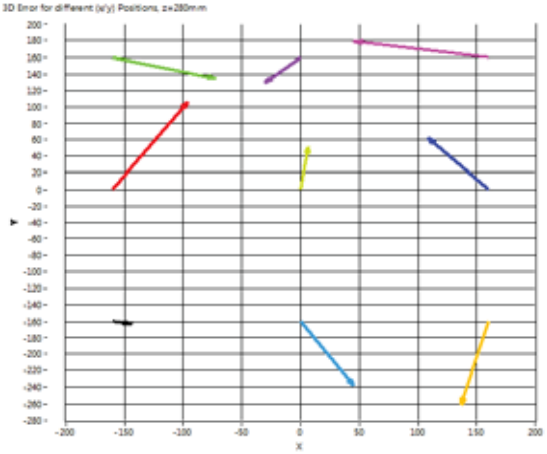

Fig. 7. Deviation of nine detected sensor positions in cube volume after placing a huge brass object beside the setup. Vectors have been scaled by 2000 to make them visible. Unit is [mm]

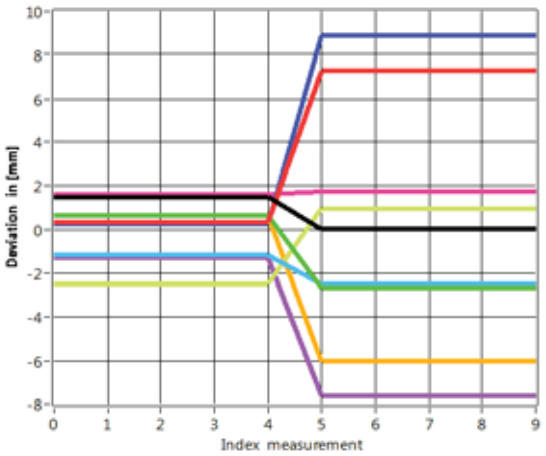

Fig. 8. Deviation in z-direction for the above shown sensor positions. After 500 measurement cycles the object has been moved closer. Unit is [mm]

The results and the possible explanation were verified by removing the tube and placing a small conductor loop inside the cube volume (diameter about 280mm, two coils). The results were not directly comparable because of the size and the position of the objects, but it was noticeable that also the loop had quite some impact on the accuracy. The expected effect of a "bundled" or "compressed" electromagnetic field in the centre of the cube volume is visible in figure 9 and figure 10 below. The first 500 measurements were made without the coil, the next 500 with it.

Quite unexpected was the result for the dimension of the deviation in space: Eight of nine sensors reported more accurate after inserting the coil.

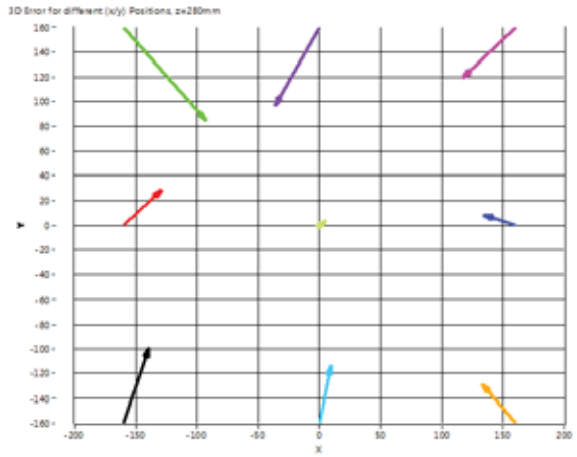

Fig. 9. Deviation of detected sensor positions in cube volume after placing an electrically conductive coil in the centre of the dome volume. Vectors have been scaled by 2000 to make them visible. Unit is [mm]

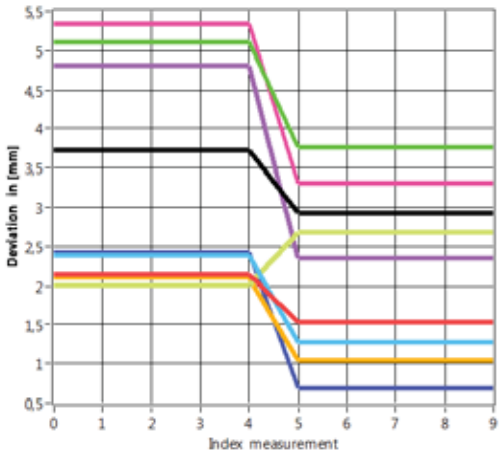

Fig. 10. Spatial deviation for the above shown sensor positions. Unit is [mm]

7. CONCLUSION

The magnetic system has demonstrated unexpected stability in the periphery of electromagnetic disturbances like connecting smartphones within the workspace. On the other hand we were able to identify critical situations when electrically conducting material was placed near the measurement volume. In some cases absolute and relative values showed quite unexpected results that need further investigation.

The desired goal to create a calibration algorithm for a magnetic tracker could not be achieved at this stage of work, because in our envisaged application we will not be able to refrain completely from electrically conductive material and the influence of those materials in range of the field generator is not neglectable und quite unpredictable. Although optical tracking systems suffer from other ambient conditions like illumination, higher distance to the measured object and target registration errors because of bigger locator geometries, they seem to be more suitable for high precision tasks in unknown environments. Another advantage is the bigger measurement volume of many optical systems. The big advantage of the magnetic tracking system is the small geometry of the sensors and the possibility to use the markers in an isolated space if the hull is made of non-conductive material.

References

[1] Sahm,S.; Kerstein, Th.; Scarpin, D.; Roth, H.; Wahrburg, J; "Evaluation of Optical 3D Measurement Systems for Application in Computer Assisted Surgery", tm-Technisches Messen, November 2013, pp. 379-387

[2] Fitzpatrick, J. M.; West, J. B.; Maurer, C. R., "Predicting Error in Rigid-Body Point-Based Registration", IEEE Transactions on medical imaging 17 (1998), October, No.5, pp. 694-702

[3] Lugez, E.; Pichora, D.R.; Akl S.G.; Ellis R.E.: "Evaluation of a six-DOF electromagnetic tracker", Proceedings Computer Assisted Orthopaedic Surgery (2014). In press

[4] Horn, B.K.P.; "Closed-form solution of absolute orientation using unit quaternions", Journal of the Optical Society of America A, Vol. 4, page 629, April 1987

[5] DIN ISO 5725-1:1994, (E) „Accuracy (Trueness and Precision) of Measurement Methods and Results"

EVALUATION STUDY OF UNDERWATER LASER COMMUNICATION SYSTEM IN SHATT AL – HILLA – IRAQ

Jassim Mohammed Jassim

Babylon University - College of Science for Women, Iraq

Abstract

In this research, an analytical study of laser communication in water of shatt Al - Hilla using laser source at different wavelengths (407nm, 473nm, 532nm, 632nm and 810nm) transport through samples of water have different turbidity (clear , low turbid and high turbid). Blue laser light was employed as the carrier signal for the reason that it could proceed under water with lowest Absorption coefficient (3.0 cm^{-1}), maximum transmission distance (78m) and Minimum distortion in signal, from the another laser lights.

1. INTRODUCTION

The beam attenuation coefficient, α(λ) is a measure of the light loss from the combined effects of scattering and absorption over a unit length of travel in an attenuating medium. The unit for α(λ)is cm^{-1}. The beam attenuation coefficient, *α(λ)*, is a measure of the decay of the unscattered light and may be described by the Beer–Lambert law as [1].

$$P_r = P_T \exp^{-\alpha R} ------1$$

where, p_r is Initial beam radiant power, p_T is Measured beam radiant power, and R is the water path length An easy way to remember the relationship among these properties is to recall that a(λ) + b(λ) = α(λ). The absorption coefficient, a(λ) is a measure of the conversion of radiant energy to heat and chemical energy[2]. It is numerically equal to the fraction of energy absorbed from a light beam per unit of distance traveled in an absorbing medium, therefore α(λ) can be expressed in terms of the transmittance as[3].

$$\alpha(\lambda) = \frac{1}{R} \ln \frac{1}{T(\lambda)} -----2$$

where T (λ) is the transmitted of under water ,beam is defined by *α(λ)* varies with depth under water temperature due to the non-homogeneous nature of water. Light scattering changes the direction of photon transport, “dispersing” them as they penetrate a sample, without changing their wavelength[4].The scattering coefficient, b(λ), is equal to the fraction of energy dispersed from a light beam per unit of distance traveled in a scattering medium, in cm^{-1}.In distill water, the scattering phenomenon is negligible. Therefore, the attenuation coefficient is equal to the absorption coefficient

(a(λ) = α(λ)).

2. BASICS THEORY

Point to point laser communication can be characterized by equation (3)[5].

$$P_r = P_T \frac{A_{rec}}{(\theta * R)^2} \exp^{(-\alpha R)} -------3$$

Where θ is the beam divergence of laser. The SNR (signal to nose ratio) for PIN photodetector receiver in optical communication is given by [6].

$$SNR = \frac{(RP_r)^2 R_L}{4kT\Delta f} ----4$$

where *K:* Boatman's constant, *T* is the temperature in Kelvin, Δf is the spectral frequency, R_L is the loading resistor and R the spectra responsively of detector. The communication quality of the system is determined by BER (bit error rate) [7].

$$BER = \frac{\exp^{(-SNR/2)}}{(2\pi SNR)^{0.5}} ----5$$

3. SYSTEM DESCRIPTION

Our optical transceiver system is consisting semiconductor laser diode emitting at 473 nm with drive the semiconductor laser modulation signals, so that issuing a series of laser pulses of light modulation by the sound and photodiode receiver to restored back optical signal to electrical signals. To simulate the underwater communication in the lab, a PVC

water cell of the diameter is 3Cm and path length is 100Cm ,the end of this cell is covered by two filter have high transmittance of laser beam is fabricated.. The provision for creating the turbulence is also kept using a electrical water motor, show as in figure (1).

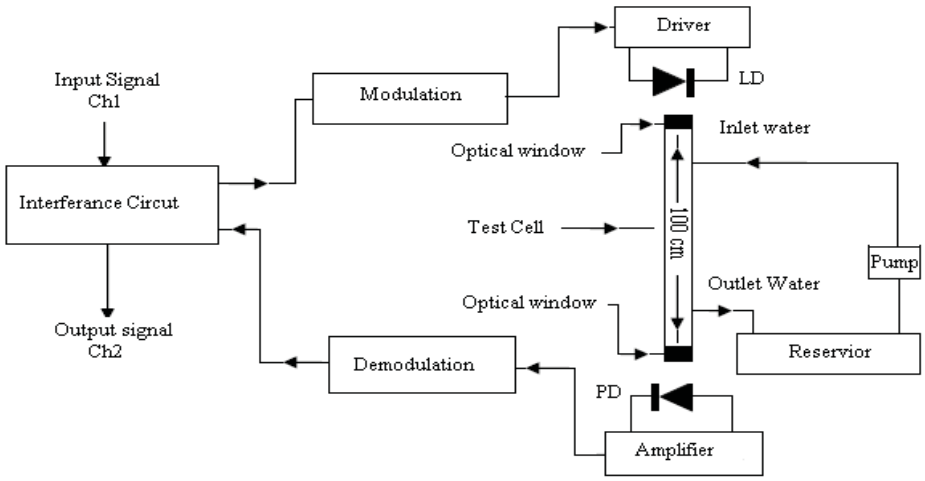

Fig. 1. Schematic diagram of overall system

4. RESULTS AND DESICCATION

4.1. Water Attenuation Measurements

Samples of water shatt Al-Hilla, Iraq placed under laser radiation (fig. 2). In this study diode laser with (407nm, 473 nm, 532 nm, 632 nm and 810 nm) wavelengths were used, with regard to result of this study the amount of light attenuation coefficient for three samples of water shatt Al–Hilla at different wavelengths calculated (Table 1). For the calculating the amount of light attenuation coefficient calculated by the formula.

$$\alpha = -\frac{\ln \frac{I}{I_0}}{X}$$

Where α is the absorption coefficient, X is the length of the cell, I_0 is the diode laser power, and I is the power diode laser power after the cell. It is found that the absorption coefficient varies with turbidity of water and has an value values (3.4×10^{-4} – 4.0×10^{-4} cm^{-1}) especially in blue-green region. So the blue-green laser (the wavelength is about 473 ~ 532*nm*) is typically laser it using in communication under this water. The blue-green laser has the minimum energy fading and can propagate from several tens of meters to in the water. Table (1) so insulator the effective the Contaminates in the water, the absorption coefficient it increased with increased the contaminates and also more effective on the beam propagation.

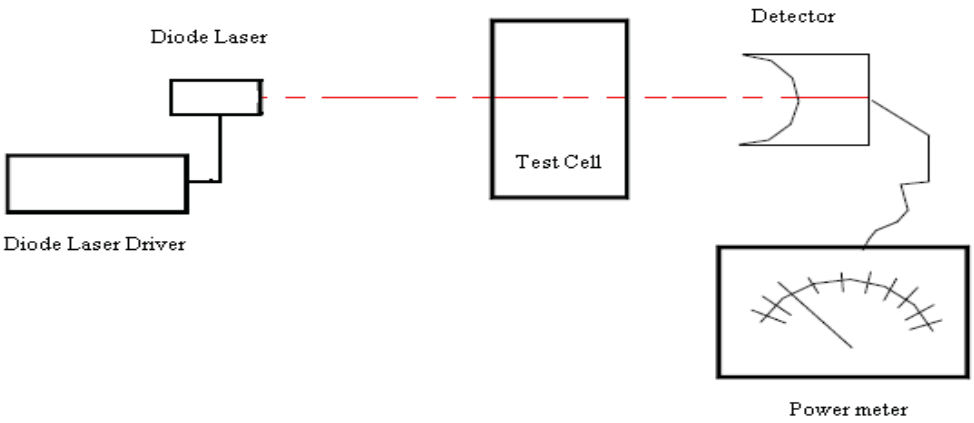

Fig. 2. Schematic set up for measuring absorption coefficient

Table 1. The absorption Coefficient for three types Water in Range (407-810 nm)

Water type	Absorption coefficient (10^{-4}) cm^{-1} λ=407nm	Absorption coefficient (10^{-4}) cm^{-1} λ=473nm	Absorption coefficient (10^{-4}) cm^{-1} λ=532nm	Absorption coefficient (10^{-4}) cm^{-1} λ=632nm	Absorption coefficient (10^{-4}) cm^{-1} λ=808nm
Clear	3.4	3.0	4.09	20.0	100.0
Light Turbid	4.6	3.6	5.4	24.2	108.3
High Turbid	26.0	25	27.8	40.6	165

4.2. Energy distribution Measurements

In this study used the same Schematic set up for measuring absorption coefficient except replace the power meter by the CCD camera .The important factor in propagation of the Gaussian beam (Fig. 3a) laser diode behavior investigation is received Energy of CCD. Obviously, there were (Fig. 3b, Fig. 3c and Fig. 3d), the energy of laser light has different distribution related to the turbidity of water. Fig. 4 shows the variation of light spot center position in the direction vertical (Yc) and direction horizontal (Xc) to the center of CCD Camera over time. The length of the vertical and horizontal lines indicates the maximum and minimum amplitude of the instantaneous deviation of light spots from the steady position. The position of light spots are the variation between maximum and minimum amplitude because the and flow rate of water.

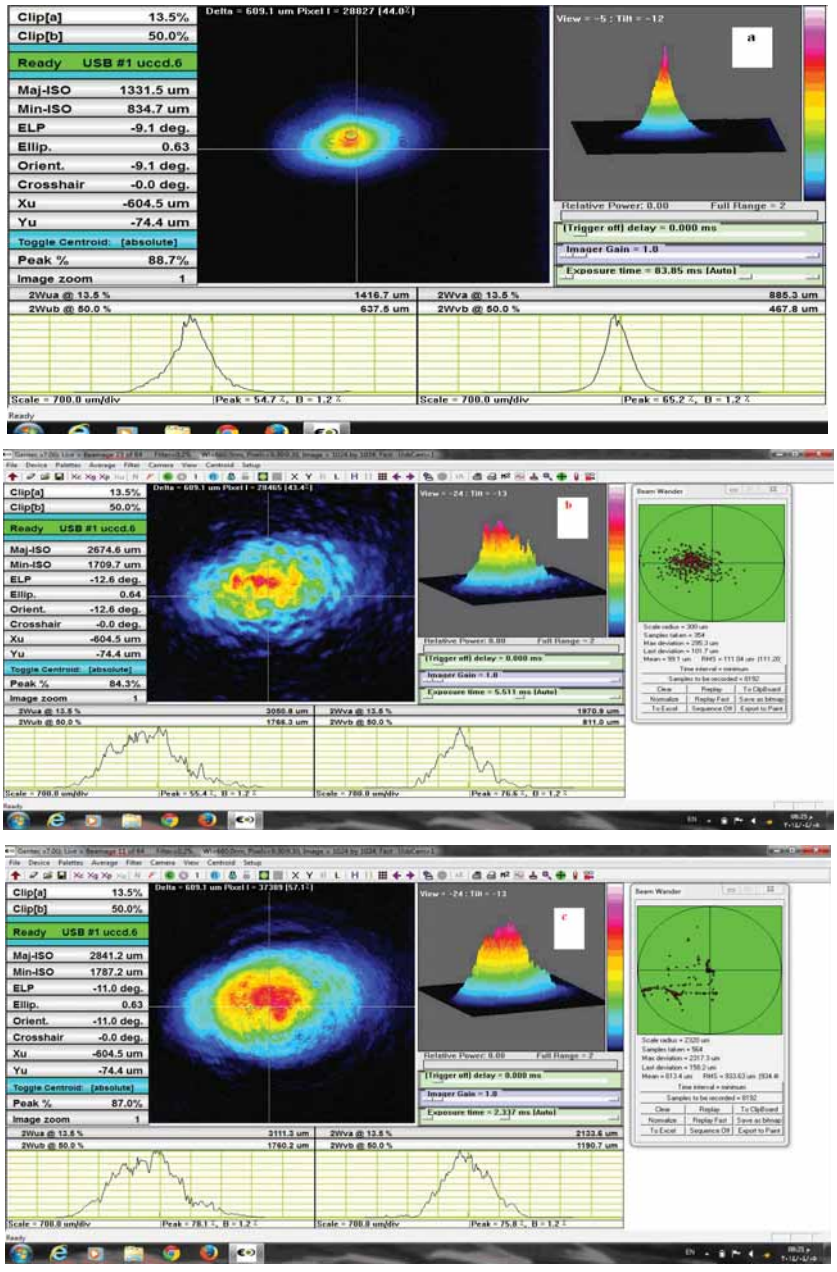

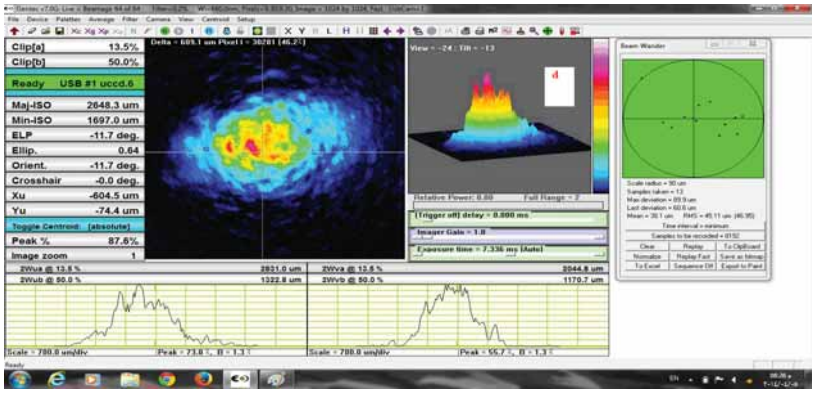

Fig. 3. Energy distribution for laser light (407 nm) through different samples of water at constant flow rate (a- without any effected b- Clear , c-light turbid and d-high turbid)

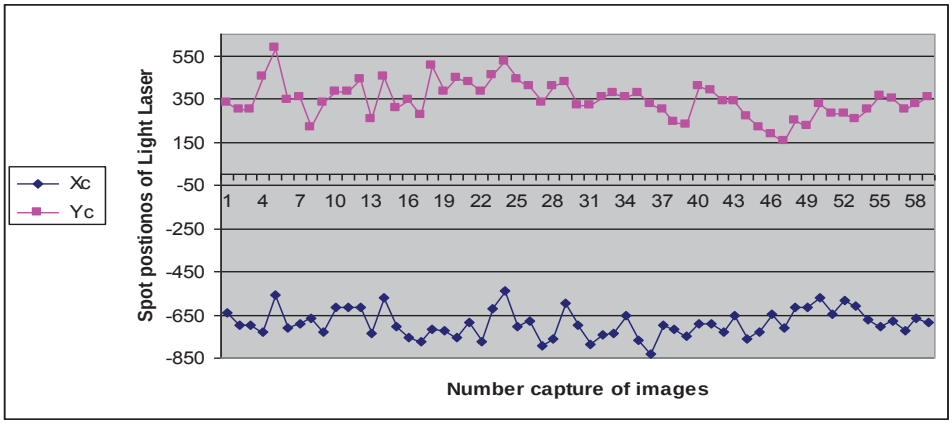

Fig. 4. Variation of Laser light-spot position on receiving CCD Camera

4.3. Long Light-Path Measurements

The relation between transmission distance for clear water and different wavelengths of incident laser light (Fig. 5), the red and infrared light wavelength had a little penetration, so low transmission distance about (2-10 m) and the Blue and Green light wavelength had the most penetration, so high transmission distance about (50-76 m). It's obvious that in Blue light wavelength the transmittance distance change related to the turbidity of water (Fig. 6), at the first sample the transmittance distance about (76 m) and at the last samples the transmittance distance about (10 m).

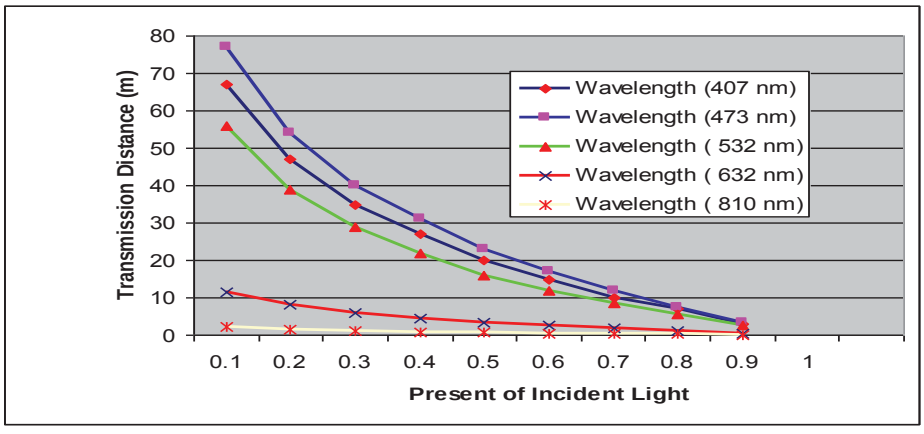

Fig. 5. The transmission Distance for Clear Water at different wavelength of Incident light

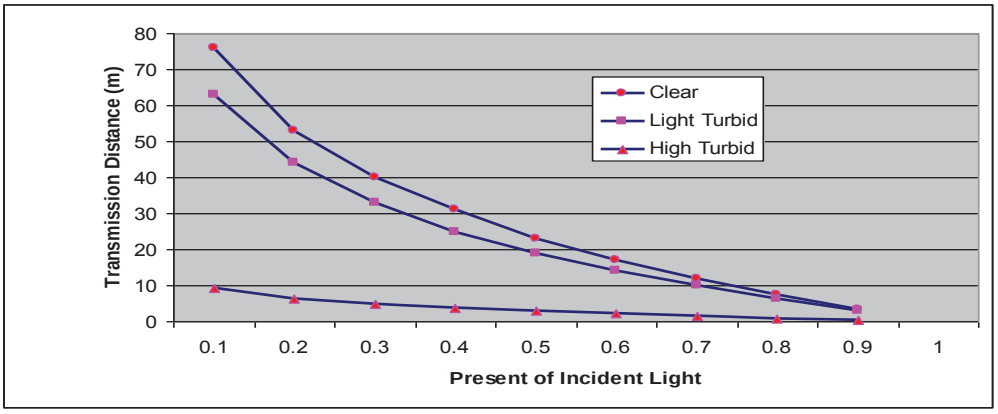

Fig. 6. The transmission distance varies with incident Blue Laser light (473 nm) for three samples of water

4.4. Distortion in optical signal measurements

Fig. 7 (a ,b, c, and d) show the transmitted signal (Ch1) and received signal (Ch2) through the water shatt Al –Hilla at different turbidity and flow rate. Observably that the broadening and attenuation on the input pulse (squire wave), it take different shapes dependent on the flow rate of water and different amplitude values dependent on the turbidity of water. Both broadening and attenuation case limitation on the optical transmission bandwidth and transmission distance.

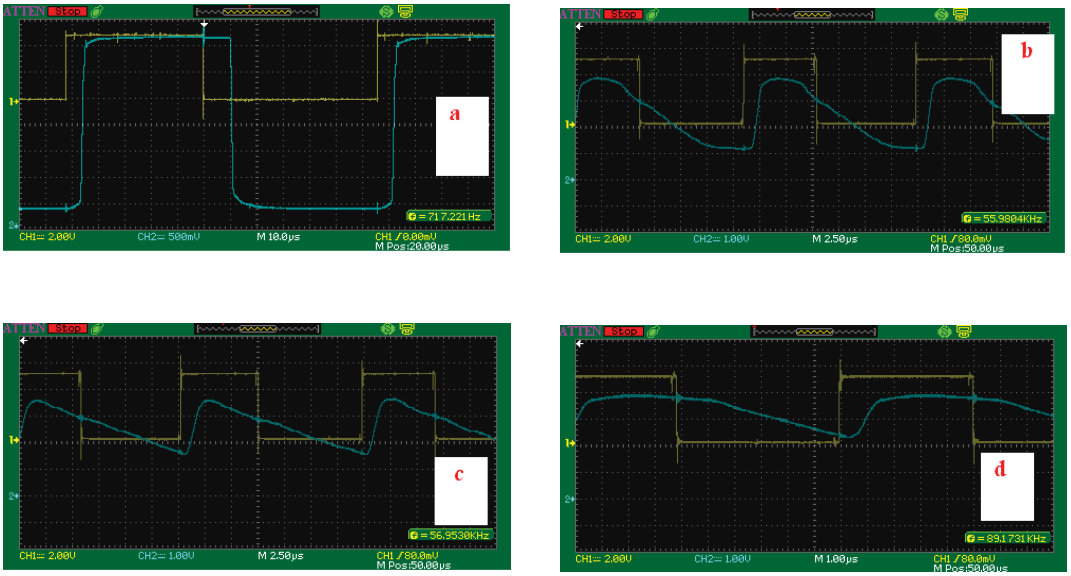

5. CONSOLATIONS

1. The laser beams with different wavelengths experience different transmission distance .the wavelength has strong influence on transmission distance in water.

2. Any increase in turbid of water causes a decrease in the amount of water transmission which leads to decrease in intensity peak and received power values.

3. Laser light-spot position it variation over the time with turbidity and flow rate of water

4. The turbidity and flow rate of water case distortion on optical sign

References

[1] B. woodward, 2008, "Underwater speech communications with a modulated laser", Appl. Phys. B 91, 189–194.

[2] W. Scott Pegau, Deric Gray, and J. Ronald V. Zaneveld, 1977, "Absorption and attenuation of visible and near-infrared light in water: dependence on temperature and salinity" APPLIED OPTICS, Vol. 36, No. 24.

[3] F. D. Kashani (C.A.), M. Reza Hedayati Rad and E. Kazemian , 2013 " Analyzing the Propagation Behavior of a Gaussian Laser Beam through Seawater and Comparing with Atmosphere" Iranian Journal of Electrical & Electronic Engineering, Vol. 9, No. 4.

[4] Ziad T. Al Dahan 1, Samar Y. Al Dabagh 2 and Asmahan Assad, 2013, "Design and Implementation of Under Water Optical Communication System" International Journal of Application or Innovation in Engineering & Management (IJAIEM)" Volume 2, Issue 6.

[5] Vikrant, Anjesh Kumar, Dr. R.S. Jha, 2012, "Comparison of Underwater Laser Communication System with Underwater Acoustic Sensor Network" International Journal of Scientific & Engineering Research, Volume 3, Issue 10.

[6] Mohammed F. Mohammed, Dina J. Matti, 2011, Analytical Study of Water Purity Using Low Power He:Ne Laser" Nahrain University, College of Engineering Journal (NUCEJ) Vol.14 No.1.

[7] M. Torabi Azad, H. Hosseini, M. R. Afzali and Moz. Emtyazjoo, 2011, "Physics of Light in the North Coasts of Persian Gulf (Bushehr province) during Winter Season" J. Phys. Educ. Vol. 5, No. 3.

ACTIVE SHAPE MODELS WITH 2D PROFILES FOR STRESS/ANXIETY RECOGNITION FROM FACE IMAGES

Martin Penev, Agata Manolova, Ognian Boumbarov

Radiocommunications and Videotechnologies Department
Faculty of Telecommunications, Technical University of Sofia
8 Kliment Ohridski Blvd., 1000 Sofia, Bulgaria
{martin, amanolova, olb}@tu-sofia.bg

Abstract

The facial expression is a visible manifestation of the emotional state, cognitive activity, intention, personality, and mental health of a person. In this paper we use an approach to distinguish between different emotions from images in particular the unhappiness related to anxiety and stress. The approach is based on Active Shape Model (ASM) with 2D profile for extracting important facial points (coordinates of edges of the mouth, eyes, eyebrows, etc.). Further the feature vectors are formed by concatenating the landmarks data from the proposed method and use the data as an input to kernel Support Vector Machine (SVM) classifier. The experimental results using Cohn-Kanade Extended Facial Expression Database show high recognition rate. 2D profile ASM significantly speeds up the fitting process comparing with 1D profile ASM by averagely over 40%.

1. INTRODUCTION

Face plays significant role in social communication. This is a 'window' to human personality, emotions and thoughts. The face we look at is a mix of both physical characteristics and emotive expressions. According to the psychological research, nonverbal part is the most informative channel in social communication. Verbal part contributes about 7% of the message, vocal – 34% and facial expression -55% [1, 2]. Facial expression recognition is a considerably challenging field to generate an intelligent system that is able to identify and understand human emotions for various vital purposes, e.g. security, society, entertainment, health care, human-computer interaction, industrial and personal robotics, surveillance and transportation. By using of the information that the face carrys, facial expressions can play an important role wherever humans interact with machines. Automatic recognition of facial expressions can act as a component of intelligent and adaptive human-machine interfaces. It is expected that introducing affective dimension can significantly enhance the users' interaction experience also can make that interaction more efficient. In general, the intelligent computer with the emotion recognition system can be used to improve the daily lives of people.

People with depression may feel sad, anxious, helpless, worthless or hopeless. They stop caring about things they used to enjoy, such as hobbies. Often they feel a loss of energy, and they may be incapable of concentrating on anything. Irregular sleep patterns and loss of appetite also indicate depression. Long-term effects of depression include chronic fatigue because of loss of energy and irregular sleep patterns. This, combined with a weakened immune system, can lead to a susceptibility to physical illness. Those with depression might also suffer chronic aches and pains. Depression also affects attention and memory. People who suffer from depression could find themselves forgetful and unable to concentrate, which can have a negative impact on their life. A history of depression may be associated with an increased risk of stroke [4]. A large body of evidence suggests that depression is associated with an increased risk of many chronic diseases, including hypertension [5, 6], diabetes [7], and particularly coronary heart disease [8]. There is also a great chance that depression and overweight will co-occur [9]. Results have shown that people with major depression who are recovering from strokes or heart attacks have a more difficult time making health care choices. They also find it more difficult to follow their doctor's instructions and to cope with the challenges their illness presents.

So for an intelligent medical system being able to recognize that the patient suffers from anxiety/depression is of essence.

The rest of the paper is organized as follows: In the next section we present a brief overview of ASM with 2D profile for extracting important facial points.

In Section 3 we present the classification approach – kernel SVM. In Section 4 we will illustrate the experimental results for the classification of the processed data using the proposed method. Finally section 5 will conclude the paper.

2. ACTIVE SHAPE MODEL WITH 2D PROFILE

Very important for the success of an automatic facial expression detector is the face alignment/ registration algorithm and the visual features derived from it. As expressions can be subtle, high accuracy is desired for the various facial features, enhancing the ability of a classifier to detect the facial expression correctly. To facilitate this, the ASMs have been widely used as they provide dense registration accuracy (i.e. 60-70 points on the face). ASM is a powerful statistical tool that has been used for the segmentation of a wide range of objects, including facial features [10].

ASMs are based on the combination of a Point Distribution Model (PDM) plus a set of local image texture models. The PDM describes the shape variability of the template and the texture models describe the image variability around each of its points. In order to correctly model the shape of human faces, it is first represented by a set of landmarks. Each landmark describes a particular part of the face such as the tip of nose and the eye pupils as shown in Figure 1. In order to build a model that is flexible enough to cover the most typical variations of facial shapes, a sufficiently large training set has to be used. The landmarks are manually labelled for each training image to generate a set of training shapes. An object shape is represented by a set of labelled points or landmarks. The number of landmarks should be large enough to show the overall shape. Our landmarking scheme uses 68 model points.

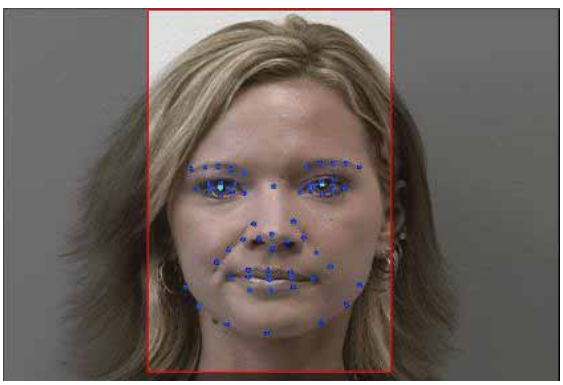

Fig. 1. The landmarks labelled on a facial image

The coordinates of all landmarks for each image are stored as a vector, called a shape, in the form $\mathbf{x} = (x_1, y_1, ..., x_N, y_N)^T$, where x_i and y_i are the coordinates of the *i*-th landmark and *N* is the number of landmarks used. The shapes in the training set are aligned with each other using Generalized Procrustes Analysis (GPA) which scales, rotates and translates each training shape so that the corresponding landmarks in the various images of the training set are as close as possible [11]. An example is illustrated in Figure 2.

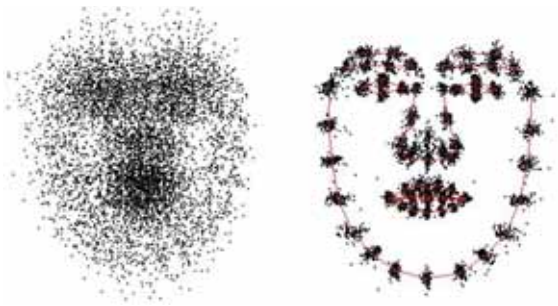

Fig. 2. Training set before and after alignment

The PDM is constructed by applying Principal Component Analysis (PCA) to the set of shapes in the training set. PCA is computed on these shapes and the eigenvalues of the covariance matrix contributing to 97% of the variation are sorted and used to store their corresponding eigenvectors in a matrix P. The mean shape is the mean of the aligned training shapes (which in our case are manually landmarked faces). The mean of the *N* training shapes is calculated as follows:

$$\bar{x} = 1/N \sum_{i=1}^{N} x_i \,, \tag{1}$$

where x_i is the *i*-th shape in the set of the *N* training images.

By subtracting the mean shape calculated above from each training shape, the covariance matrix of the deviations from the mean is calculated as follows:

$$S_s = 1/N \sum_{i=1}^{N} (x_i - \bar{x})(x_i - \bar{x})^T \tag{2}$$

The eigenvectors and eigenvalues of the covariance matrix are subsequently obtained by using the equation:

$$S_s \mathbf{v}_k = \lambda_k \mathbf{v}_k \,, \tag{3}$$

where $\mathbf{v}_k$ and λ_k are, respectively, the *k*-th eigenvector and eigenvalue of S_s. Any shape in the trai-

ning set can be approximated by the mean shape and a weighted sum of *t* eigenvectors. This is mathematically represented as:

$$x = \bar{x} + P\mathbf{b}, \quad (4)$$

where $P = (\mathbf{v}_1, \mathbf{v}_2, ..., \mathbf{v}_t)$ is a matrix whose columns are the *t* eigenvectors corresponding to the first *t* largest eigenvalues, and $\mathbf{b} = (b_1, b_2, ..., b_t)^T$ is a vector of weights applied to the eigenvectors. These weights (b_k) are the model parameters which control the shape generated by the PDM; thus, new facial shapes can be generated by varying these parameters. At the same time, these parameters are constrained in order for the model shape to be consistent with those in the training set. Since most of the population lies within three standard deviations of the mean, the model parameters are chosen to lie within the range given by:

$$-3\sqrt{\lambda_k} \le b_k \le 3\sqrt{\lambda_k} \quad (5)$$

where λ_k is the eigenvalue that corresponds to the *k*-th eigenvector of the *t* eigenvectors.

The next stage involves profiling to generate statistical models of the grey level intensities of the region around each landmark to build a subspace that spans the variations of the exemplar training images. The classical ASM employs 1D profile, which is generated by sampling grey-level intensities of *m* pixels centered at each landmark. The direction of the profile is chosen to be along a line orthogonal to the shape boundary at each landmark. The local grey-level gradient pattern is then utilized for searching a new position of each landmark along a line centered at the landmark. The model shape is iteratively changed for its better fit to the target face in the image. The classical ASM performs well if the landmarks of the initial model shape are placed close to their targets. However, the initial model shape could be placed only roughly whereby the landmarks often get placed away from their targets. Thus resulting in long search lines and consequently making the target search computationally expensive. It could also distract the landmarks by local structures in the image. In order to overcome the above drawbacks of the classical ASM, a multi-resolution approach of ASM, known as multi-resolution ASM (MRASM), is proposed in [12]. In this scheme, an ASM is first applied to a coarse image to roughly place the model shape near the target object, and then applied to finer images to refine the shape fitting. An image pyramid containing a set of images with different resolutions is used in order to build the LGGM for multiple image resolutions. For each level of the image pyramid, the corresponding LGGM is utilized for searching a new position of each landmark. Unlike the classical ASM, the multi-resolution approach requires only short search lines; thus reducing the risk of distraction of the landmarks by local structures in the image, and decreasing the computational complexity [12]. However, the 1D profile used in the classical ASM has a quite obvious shortcoming: every model point can only search its optimal location along its normal to the boundary and consequently, the search can converge to a local minimum and produces poor fitting results. In order to extend its flexibility, 2D profile ASM is proposed by Pei, J. [13]. Instead of sampling a single vector of gradients just along the profile normal in 1D profile ASM, an additional vector of gradients along the profile tangential is further used in 2D profile ASM. By sampling two vectors of gradients along these two directions, two sequential feature sets g_i^1 and g_i^2 can be obtained. The optimization process of each single model point can be realized by searching for the optimum along two directions in turn.

3. SUPPORT VECTOR MACHINES FOR EXPRESSION CLASSIFICATION

SVM is very popular and powerful method for binary and multi-class classification as well as for regression problems. For two class separation, SVM applies a maximum margin manner that estimates the optimal separating hyper plane. In our investigation we used the LibSVM library (http://www.csie.ntu.edu.tw/~cjlin/libsvm/) and Matlab functions. In general SVMs can only solve binary classification problems. For multi-class classification, LibSVM computes decision surfaces for all class pairs (one-against-one technique) and then find the correct class by a voting mechanism.

Let us given sample and label pairs $(x^{(i)}, y^{(i)})$, where $x^{(i)} \in R^m$, $y^{(i)} \in \{-1;1\}$ and $i = 1,...,K$. Here, for class "1" and for class "2", $y^{(i)} = 1$ and $y^{(i)} = -1$, respectively. We also define a feature map - $\phi : R^m \to \mathrm{H}$, where H denotes Hilbert space. The kernel implicitly performs the dot product calculations between mapped points: $k(x, y) = \langle \phi(x), \phi(y) \rangle_{\mathrm{H}}$. Now, the SVM can be formulated as following optimization problem:

$$\min_{\mathrm{w},b,\xi} \frac{1}{2}\mathrm{w}^T\mathrm{w} + C\sum_{i=1}^{K}\xi_i, \quad (6)$$

$$\text{s.t. } y^{(i)}(\mathrm{w}^{\mathrm{T}}\phi(x^{(i)}) + b) \geq 1 = \xi_i, \ \xi_i \geq 0, \quad (7)$$

where $\xi_i (i = 1,\ldots,K)$ are slack variables which measure the degree of misclassification of their associated training data points with respect to the current decision boundary and margin.

In our experiments, we applied kernel SVM classifier with the pure distance substitution linear kernel (k^{lin}) and the Gaussian radial basis kernel (k^{rbf}). The values of the penalty error *C* and the parameter for the Gaussian radial basis kernel are logarithmically varying along a suitable grid and only the best recognition rates are presented in the next section.

4. EXPERIMENTAL RESULTS

In our experiments we used the extended Cohn-Kanade (CK+) database [3], which contains 593 sequences from 123 subjects. From these, 118 subjects are annotated with 7 universal emotions: anger, contempt, disgust, fear, happy, sad and surprise (Table 1). The corresponding labels are used as the "ground truth" data.

Table 1. Distribution of emotion labels for 118 subjects from CK+ database

Emotion	Number images
Anger	45
Contempt	18
Disgust	59
Fear	25
Happy	69
Sad	28
Surprise	83

The dense facial landmarking annotation that we use allows us to achieve excellent fitting accuracy. We use 68 landmark points which are dense enough and optimally placed to not only perform accurate annotation based on the underlying facial geometry of typical human faces but to also model varied facial expressions. Initialization of an ASM is vital to ensuring high fitting accuracy. This initialization is usually provided by the bounding box around a face that is returned by a face detector. However, face detectors, such as Viola-Jones [14], are prone to errors that result in scale and translation effects in the bounding box. We use OpenCV's face detection implementation which performs well only for frontal faces without in-plane rotation. The 2D profile extension of ASM that we used made the landmark extraction process less sensitive to model initialization errors. Examples from the dataset with the proposed algorithm are illustrated in Figure 3.

Fig. 3. Examples for ASM with 2D profile

We trained a multi-class SVM using leave-one-subject-out cross validation method in which all images of the test subject were excluded from the training data. The conducted results of the classification accuracy are shown in Table 2. Our goal is to correctly classify the negative emotions related to stress and anxiety: fear, sadness, anger and contempt.

Table 2. Emotion classification confusion matrix for CK+ database using the proposed method

%	Anger	contempt	fear	sad	all others
Anger	80,22	6,67	0,00	2,22	10,89
Contempt	16,67	73,78	5,56	0,00	4,00
Fear	4,00	4,00	76,00	4,00	12,00
Sad	10,29	0,00	0,00	82,14	7,57
all others	8,89	1,20	0,00	10,11	79,80

5. CONCLUSION

In this paper we proposed a method for automatic facial expression classification in the context of stress/anxiety recognition task. The system is able to detect a human face from still image, extract feature vectors (the coordinates of specific important facial key-points) and then classify expression presented in the face using trained SVM. From the

conducted experiments on CK+ database, the classification rate vary between 76% and 82,14%. The system is capable to distinguish between the negative emotions "angry", "sad", "fear" and "contempt" expressions and all the rest.

The facial landmark information is very efficient for facial expression recognition provided that details of coordinates' changes are determined precisely. The current system can be extended by texture based algorithms to improve performance.

Acknowledgments

This paper was supported by Contract № 142ПД0028-07 of Technical University-Sofia, Research Sector. Research project: «Algorithms for image segmentation of face components» - 2014.

References

[1] S. Li, A. Jain, *Handbook of Face Recognition*, 2nd ed. Springer, 2011.

[2] G. Donato, M.S. Bartlett, J.C. Hager, P. Ekman, T.J. Sejnowski, "Classifying Facial Actions", *IEEE Trans. Pattern Analysis and Machine Intelligence*, Vol. 21, No. 10, pp. 974-989, 1999

[3] T. Kanade, J.F. Cohn, and Y. Tian, "Comprehensive Database for Facial Expression Analysis", *Proc. 4th IEEE Int.Conf. on Automatic Face and Gesture Recognition*, pp. 46–53, 2000

[4] Jia-Yi Dong,Yong-Hong Zhang, Jian Tong; Li-Qiang Qin, Depression and Risk of Stroke: A Meta-Analysis of Prospective Studies, Stroke 1 January 2012: 32-37.

[5] Jonas BS, Franks P, Ingram DD. Are symptoms of anxiety and depression risk factors for hypertension? Longitudinal evidence from the National Health and Nutrition Examination Survey I Epidemiologic Follow-up Study. Arch Fam Med. 1997; 6: 43–49.

[6] Davidson K, Jonas BS, Dixon KE, Markovitz JH. Do depression symptoms predict early hypertension incidence in young adults in the CARDIA study? Coronary Artery Risk Development in Young Adults. Arch Intern Med. 2000;160: 1495–1500.

[7] Mezuk B, Eaton WW, Albrecht S, Golden SH. Depression and type 2 diabetes over the lifespan: A meta-analysis. Diabetes Care. 2008;31: 2383–2390.

[8] Nicholson A, Kuper H, Hemingway H. Depression as an aetiologic and prognostic factor in coronary heart disease: A meta-analysis of 6362 events among 146 538 participants in 54 observational studies. Eur Heart J. 2006; 27:2763–2774.

[9] Albert J, Myles S Faitha, Kelly C Allisona, Depression and obesity, *Biological Psychiatry*, Volume 54, Issue 3, 1 August 2003, Pages 330–337.

[10] Lanitis, C.J. Taylor, and T.F. Cootes, "Automatic Interpretation and Coding of Face Images Using Flexible Models", *IEEE Trans. Pattern Analysis and Machine Intelligence*, vol. 19, no. 7, pp. 743-756, July 1997.

[11] J. C. Gower, "Generalized Procrustes Analysis," *Psychometrika*, vol. 40, no. 1, pp. 33-51, March 1975.

[12] T. F. Cootes, C. J. Taylor, A. Lanitis, "Active Shape Models: Evaluation of a Multi-Resolution Method for Improving Image Search," in *Proc. 5th British Mach. Vision Conf.*, York, 1994, pp. 327-336.

[13] Pei, J. I. A. "2D Statistical Models." (2010).

[14] Viola, P., Michael Jones, J.: Robust real-time object detection. In: *Second International Workshop on Statistical and Computational Theories of Vision-Modeling Learning, Computing, and Sampling* (2001)

SYSTEM FOR TOUCHLESS INTERACTION WITH MEDICAL IMAGES IN SURGERY USING LEAP MOTION

Agata Manolova

Radiocommunications and Videotechnologies Department
Faculty of Telecommunications, Technical University of Sofia
8 Kliment Ohridski Blvd., 1000 Sofia, Bulgaria
amanolova@tu-sofia.bg

Abstract

In the operating room surgeons need to have access to pre- and intra-operative images such as computer tomography (CT), magnetic resonance imagery (MRI), x-ray images and fluoroscopy along with various procedure-specific imaging applications. This visual data supports diagnostics and planning and provide virtual "insight" into the body of the patient during surgery. Although surgeons rely on capture, browsing and manipulation of these images they are constrained by typical interaction mechanisms such as keyboard and mouse. At the heart of this constraint is the need to maintain a strict boundary between the sterile and non sterile environment. In this paper we present a new system based on combining the Leap Motion gesture recognition controller and medical imaging toolkit for touchless visualization and browsing for medical image data.

1. INTRODUCTION

During recent years, doctors and particularly surgeons have become increasingly reliant on a range of digital imaging systems for navigation, reference, diagnosis and documentation. The need to interact with images in the operating room offers one particular challenge arising from the need to maintain boundaries between sterile and non-sterile environment. The usual input devices such as keyboard, mouse and touch screen surfaces are reliant on physical contact. Such contact-based interaction introduces the possibility for contamination to be transferred between the sterile and non-sterile objects in the operating room. This constraint creates difficulties for surgical staff who are scrubbed up and are dependent upon others to manipulate images on their behalf. This can create inefficiencies, which in turn can entail potential medical complications. Additionally, it can interfere with the surgeon's interpretive and analytic use of the images [1, 2]. To get around this constraint, the surgeons have developed several strategies for interacting with images, though they are often not ideal; for example, surgeons commonly request other members of the surgical team to manipulate images under their instruction. But this is not without complications: team members are not always available. Issuing instructions, though fine for relatively discrete and simple image-interaction requests, can be cumbersome and time consuming. More significant, indirect manipulation is not conducive to the more analytic and interpretive tasks performed by surgeons using medical images. The way they interact with, browse, and selectively manipulate them is closely bound up with their clinical knowledge and clinical interpretation. So in these cases the surgeon tries to manipulate the controls by him/her self by pulling their surgical gown over their hands and moving the mouse through the gown. Such practices are not risk free. For non-invasive procedures, such practice can be justified due to the clinical benefits it brings in terms of time savings and direct control of the images. For more invasive procedures, such practice is less appropriate and could be potentially dangerous for the patient [3].

The challenge is to design a system that will be more or less effortless and will overcome some of the drawbacks related to the touchless technology like the inherent *live mic* [4] and lack of haptic feedback [5], where manipulations made are harder to be finely tuned. This is because there is nothing for the user to hold, feel, or grasp and the movement of the user's hands has no momentum of a held object. Thus, the accuracy of the user in touchless interaction systems is entirely dependent on the agility of their limbs.

The rest of the paper is organized as follows: In the next section we present a brief overview of existing systems for touchless interaction in surgical settings. In Section 3 we present the developed system in details. In Section 4 we will evaluate the performance of the system. Finally section 5 will conclude the paper.

2. BRIEF OVERVIEW OF EXISTING SYSTEMS

Giving surgeons direct control over image manipulation and navigation while maintaining sterility within the operating theatre is a key goal, one that has captured the imagination of research groups and commercial entities worldwide during the last couple of years.

Graetzel et al. [6] developed an early example of touchless medical imaging system that let surgeons control standard mouse functions (such as cursor movement and clicking) through camera-tracked hand gestures. Shortly afterward, more sophisticated air-based gestures were used for surgical-imaging technology in the form of Wachs et al.'s [7]. These initial systems paved an important path, and, more recently, the number of systems and research efforts considering touchless control of medical images for surgical settings has grown significantly by including more bespoke gesture-based control (such as for navigation, zooming, and rotation) [8, 9, 10]. One enabler of this growth is the Kinect sensor and software development kit [11].

The Kinect sensor is based on a laser and an infrared (IR) camera. The laser projects a known pattern onto the scene. The depth of each point in the scene is estimated by analyzing the way the pattern deforms when viewed from the Kinect's IR camera. The software development kit allows computing the position of the "skeleton," a stickman representation of the human controller.

A leading example involves the system used for multiple kinds of surgery at Guy's and St Thomas' hospital in London [12] in which a Kinect helps navigate a predefined stack of MRI or CT images is illustrated on Figure 1. This system uses simple constrained gesture vocabulary to move forward or backward through the images and engage and disengage from the system.

Fig. 1. Kinect-based touchless medical imaging system [12]

One of the main conclusion that one can make after doing a survey of the available systems of this kind is that a limited number of gestures yields benefits in terms of ease of use and the learning and adaptive ability of the user. By using a constrained gesture vocabulary can have also some reliability benefits: such as enabling use of reliably distinctive gestures while avoiding the problem where gestures in a vocabulary share common kinaesthetic components, possibly leading to system misinterpretation.

3. GESTURE RECOGNITION SYSTEM

The proposed system contains a Leap Motion gesture controller and an open-source interface for visualization of medical data. Based on research and gathered information through literature review and conversations with surgeons and medical practitioners at the St. George University Hospital in Plovdiv, Bulgaria, a conceptual model can be set up. This model of the proposed system is an outline for the current research conducted in this project (see the acknowledgments). The conceptual model is illustrated on Figure 2.

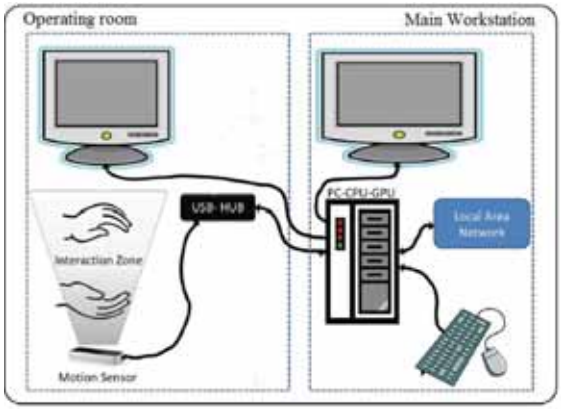

Fig. 2. Schematic diagram of the custom image workstation for the touchless interface in the operating room

3.1. Leap motion gesture controller

The Leap Motion controller, the main device used for this conceptual model, is a type of touchless interaction device owned and manufactured by Leap Motion Inc. (https://www.leapmotion.com/). It offers an open library for gesture recognition. The Leap can detect a user's hands, fingers, and finger-like objects (pen or pointer) in its inverted square pyramid field of view. The field of view has an effective range of 25 to 600 mm measuring from the top of the device. The Leap is designed so that it sits in front of the user's computer screen. Interaction is

done by making gestures with the hands fingers, or finger-like objects. The Leap can recognize three aspects of hand input. The first aspect is the ability to recognize hands, fingers, and finger-like tools and provide software interfaces to get information on each of these input types. The second aspect is the recognition of gestures, such as circles, key taps, and screen taps. The last aspect is the recognition of motions of the hands, fingers, and finger-like tools such as scaling, translation, and rotation.

3.2. Medical Imaging Toolkit (MITO)

As mentioned above the system needs an appropriate viewer for visualization of the medical image data. For the first test of the system we have chosen the Medical Imaging Toolkit (MITO) (http://ihealthlab.icar.cnr.it/index.php/projects/9-mito.html). MITO is able to let the user interact with the DICOM images using gestures and have volume navigation in surgery. MITO is an open source software released under the terms of the GNU General Public License. However, this interface requires the user to select an image using mouse and keyboard before the gesture interaction can take place. After this selection, the user is able to interact with the image. The user can measure distances, change the contrast, do translations, rotate and zoom. Normally during a surgery, the surgeon has to ask the assistant to perform these tasks.

4. EVALUATION OF THE SYSTEM

Preliminary usability testing was carried out for accessing all kinds of supported DICOM images, simulating typical laparoscopic surgery situations. During this phase, the positions of all system's components were calibrated and adjusted to facilitate working with the system. After trying different positions, we chose the final location of the Leap controller, taking into account the fact that the interaction space of the controller allowed the operator to move his/her hands in an ergonomic way in order to avoid fatigue during the gestures. Different light conditions were tested to verify whether the controller performance was affected. Different Leap Motion control settings were tested for a smooth and stable interaction, and the proposed system was set at 42 fps with a processing time of 23.2 ms; the interaction height was set as automatic. The touchless application for the Leap Motion controller was set in advanced mode. This proposed system recognized gestures that emulated touching a vertical virtual touch surface in the air (in the interaction zone above the sensor). When the operator pointed one or two fingers towards the screen, the system drew a cursor on the screen so that the operator could point items or buttons in the imaging software, and when the operator moved the finger farther towards the screen, the pointed item was selected (similar to a mouse click). The functions that required two points of control (modification of scale, zoom, or rotation) could be controlled with two fingers of one hand, or one finger of each of the two hands. By the use of this hand gesture, the operator is able to navigate through the windows, zooming in and out, manipulate the different images and slices, and use imaging tools such as the adjustment of image contrast or brightness, image enhancements, and measurement. It was possible to move and rotate the 3D simulation model from the MITO toolbox (Figure 3).

Fig. 3. Touchless manipulation of 3D simulation model from MITO toolbox"

The combined system performed very well, and it was found to be very useful in controlling the system without touching anything and maintaining the

surgical environment. The habituation period for the user should not very long; it may depend on how the user is accustomed to other multipoint input devices such as touchscreens.

In surgery settings, it is recommended that the user spend several training sessions (4-6 sessions of 30 min each), assuming that he/she had a previous knowledge about the usage of the software with the standard input devices (mouse, touchpad, and touchscreen). With a little training by the user, without a doubt, it is easier and faster than changing sterile gloves or having an assistant outside the sterile environment.

During our experiments we have also considered using the MS Kinect sensor for this system. The Kinect uses a horizontal tracking approach and needs a minimal working distance in approximately 1.2 m. In contrast, the Leap Motion tracks in much smaller interaction zone. The interaction zone of the MS Kinect is larger (approximately 18 m^3) than that of the Leap Motion (approximately 0.23 m^3). So the Leap requires much smaller operating space.

5. CONCLUSIONS

The goal of this study is not simply to demonstrate the feasibility of touchless control in the operating room. During the initial steps of the development of the system important design challenges have arisen. They range from choosing the appropriate gesture vocabulary for the surgeon to finding the appropriate combination of input modalities and specific sensing mechanisms. These choices can play important role in the development of the systems but must be addressed further, especially when the system will be used in real-world clinical settings. These are the first step to develop an autonomous system for touchless interaction the operating room capable of servicing the needs of any medical practitioner required to work in sterile environment.

It will be challenging to consider the fatigue due to prolonged use of the touchless system that could affect its use, as well as other physical features of surgical practice.

Acknowledgments

This paper was supported by Contract № 141ПР0011-07 of Technical University-Sofia, Research Sector. Research project: «System for recognition and visualization with gesture control» - 2014.

References

[1] H. M. Mentis, K. O'Hara, A. Sellen, R. Trivedi, "Interaction Proxemics and Image Use in Neurosurgery", *Proceedings of the SIGCHI Conference on Human Factors in Computing Systems*, 2012, pp. 927-936.

[2] K. O'Hara, G. Gonzalez, A. Sellen, G. Penney, A. Varnavas, H. Mentis, A. Criminisi, R. Corish, M. Rouncefield, N. Dastur, T. Carrell, "Touchless Interaction in Surgery", *Communications of the ACM*, Vol. 57 No. 1, 2014, pp. 70-77.

[3] R. Johnson, K. O'Hara, A. Sellen, C. Cousins, A. Criminisi, "Exploring the potential for touchless interaction in image-guided interventional radiology", *Proceedings of the SIGCHI Conference on Human Factors in Computing Systems*, Vancouver, Canada, May 7–12, ACM Press, New York, 2011.

[4] D. Norman, "Opportunities and Challenges for Touch and Gesture-Based Systems. The Next Touch Evolution. Advancing the Consumer Experience in Other Realms: Tasks and Tough Environments". *Society for Information Display conference*, Vancouver, Canada, 9th March 2014.

[5] O'Hara, Kenton & Harper, Richard & Mentis, Helena & Sellen, Abigail & Taylor, Alex, "On the naturalness of touchless - putting the "interaction" back into NUI". Microsoft Research, Cambridge, UK. *ACM Transactions On Computer Human Interaction*, 2012.

[6] C. Graetzel,T. Fong, S. Grange, C. Baur, "A non-contact mouse for surgeon-computer interaction". *Technology and Health Care* 12, 3 (2004), pp. 245–257.

[7] J. Wachs, H. Stern, Y. Edan, M. Gillam, C. Feied, M. Smith, J. Handler, "Real-time hand-gesture interface for browsing medical images". *International Journal of Intelligent Computing in Medical Sciences & Image Processing* 2, 1 (June 2008), pp. 15–25.

[8] L. Ebert, G. Hatch, G. Ampanozi, M. Thali, S. Ross, "Invisible touch: Control of a DICOM viewer with finger gestures using the Kinect depth camera". *Journal of Forensic Radiology and Imaging* 1,1 (Jan. 2013), pp.10-14.

[9] L. Gallo, A.P. Placitelli, M. Ciampi, "Controller-free exploration of medical image data: Experiencing the Kinect", In *Proceedings of the 24th International Symposium on Computer-Based Medical Systems* (Bristol, England, June 27–30). IEEE Press, 2011, pp. 1–6.

[10] G. Ruppert, P. Amorim, T. Moares, J. Silva, "Touchless gesture user interface for 3D visualization using Kinect platform and open-source frameworks", In *Proceedings of the Fifth International Conference on Advanced Research in Virtual and Rapid Prototyping* (Leiria, Portugal, Sept. 28–Oct. 1), 2011, pp. 215–219.

[11] Microsoft Corp. Communicate with computers naturally: Kinect for Windows; http://www.microsoft.com/en-us/kinectforwindows/develop/downloads-docs.aspx

[12] C. MacGregor, "Kinect imaging lets surgeons keep their focus", *New Scientist*, Magazine issue 2865, 17 May 2012.

THE IMPACT OF THE ELECTROMAGNETIC FIELD RADIATIONS FROM THE GADGETS TO THE USERS

Darko Brodić, Čedomir A. Maluckov

University of Belgrade, Technical Faculty in Bor
Vojske Jugoslavije 12, 19210 Bor, Serbia
e-mail: dbrodic@tf.bor.ac.rs

Ivo R. Draganov, Agata H. Manolova

Laboratory of Audio and Video Technologies
Radiocommunications and Videotechnologies Dept.
Faculty of Telecommunications, Technical University of Sofia
8 Kliment Ohridski Blvd., 1756 Sofia, Bulgaria

Abstract

The paper considers the impact of the magnetic field from the gadgets to its users. Accordingly, the impact of the magnetic field characterized by the low frequencies (up to 300 Hz) has been examined. The experiment consists of the electromagnetic field (EMF) measurement in the adjacent neighborhood of the gadgets. The measured data are presented and discussed as well. Therefore, they are compared with the critical values suggested by the Serbian Ministry of Environment, Mining and Spatial Planning. It is shown that some of them get a very strong EMF. Hence, it is recommended to be used with caution.

1. INTRODUCTION

The increasing growth of the gadgets use is world widespread. The gadgets typically include cell phones (recently touchscreen models) and tablets. Hence, the raised concern because they might cause detectable impairment of the health of the exposed individual is evident [1]. It is based on the effect of the non-ionized electromagnetic radiation characterized by the low frequency up to 300 Hz. In this frequency region, the non-ionized radiation is the implication of the home and office appliances.

Recently, some scientists have recognized the occurrence of hypersensitivity to electromagnetic radiation stems from a common exposure, such as gadgets, wireless systems, computer systems and electrical appliances in the home or the office [2]. Similarly, World Health Organization (WHO) has reported that the electromagnetic hypersensitivity symptoms which are commonly experienced include dermatological symptoms as well as neurasthenic and vegetative symptoms [1]. Some symptoms of electromagnetic hypersensitivity are shortness of breath, arrhythmia, fatigue and nausea, memory and concentration problems, headache, blurred eyesight, limb pains, muscle stiffness, burning sensations, etc [3], [4]. In ref. [5], the authors address the problem of the cell phones use by the young adolescent. Furthermore, some researcher put to the test the cell phone use and its negative consequences to the user's health [6], [7]. Still, there are no tests made on the tablet computers.

According to the safety rules of the Serbian Ministry of Occupational Safety and Environmental Protection [8], the limit level of the magnetic induction for the EMF (up to 800 Hz) is $2/f$, where f represents the low level frequency. In this way, the referent limit level is defined as the critical level of the radiation above which the environmental conditions can be unsafe for humans. Hence, the referent limit level is up to 0.04 μT for the office appliances (f = 50 Hz). Consequently, the Serbian Ministery of Occupational Safety and Environmental protection brought the Law on the non-ionized radiation protection [9], which determines the risk conditions and protection measures in the critical situations.

In this paper, we addressed the problem of the EMR received from the gadgets. Furthermore, the measurement of the EMR is carried out. Then, the risk assessment of the low frequent magnetic induction from gadgets to the humans according to the Law is discussed. At the end, the conclusions are made as well as the future research work direction.

2. METHODS

The methods of the work consist of the EMF measurement of the gadgets. In the first experiment the tablet is tested. We propose 6 measurement points around the tablet. Figure 1 illustrates the measurement points.

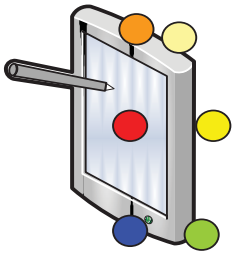

Measurement at the top of the tablet (P1)
Measurement in the front of the tablet (P2)
Measurement at the bottom of the tablet (P3)
Measurement at the top of the tablet from back (P4)
Measurement from the back of the tablet (P5)
Measurement at the bottom of the tablet from back (P6)

Fig. 1. EMF measurement points in the neighborhood of the tablets

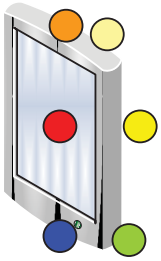

Measurement at the top of the cel phone (P1)
Measurement in the front of the cell phone (P2)
Measurement at the bottom of the cell phone (P3)
Measurement at the top of the cel phone from back (P4)
Measurement from the back of the cell phone (P5)
Measurement at the bottom of the cell phone from back (P6)

Fig. 2. EMF measurement points in the neighborhood of the cell phones (touch-screen model)

In the second experiment thetouchscreenn cell phone is tested. Similarly, 6 measurement points around the cell phone are proposed. Figure 2 illustrates these points.

3. EXPERIMENTS

The measurements were performed in the office where the influence of the magnetic field is negligible, i.e. it is lower than 0.01 μT. EMF measurement was performed by Lutron EMF 828 device. It is shown in Figure 3.

Fig. 3. Lutron EMF 828 measurement unit

It measures the magnetic induction from 0.01 μT to 2 mT, which frequency range is between 30 and 300 Hz. The EMF 828 has three measurement extents: 20 μT, 200 μT and 2000 μT. The precision of the measurement heavily depends on the measurement extent. Consequently, it is of the order 0.01 μT for the measurement extent of 20 μT, 0.1 μT for 200 μT and 1 μT for 2000 μT, respectively. Lutron EMF 828 measures all three components of the magnetic induction, i.e. *x*, *y* and *z*. Hence, the total intensity of EMF is determined as follows:

$$\square = \sqrt{(\square_x^{\square} + \square_y^{\square} + \square_{\square}^{\square})} \, . \qquad (1)$$

4. RESULTS AND DISCUSSION

The results of the first experiment show that EMF appears at all six measurement points. Table 1 shows the EMF measured values at all six points around the tablets.

There exists the opinion that the tablet is free of EMF. However, it is not a valid. It is true that the tablet has no hard disk, CD-ROM or similar parts. Nevertheless, it has the central processing unit and graphics card. Furthermore, the tablet battery charger has a negligible EMF.

Figure 4 and 5 shows measured EMF components and the total value, respectively.

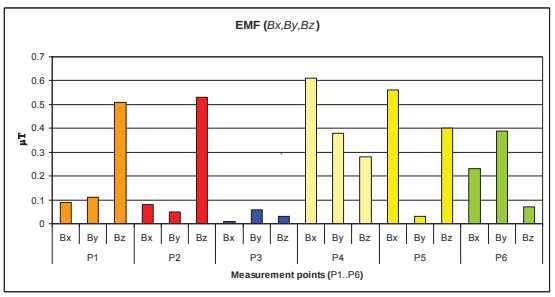

Fig. 4. EMF components at measured points (P1..P6) for tablets

Table 1. EMF measurement for the tablets (at all 6 points)

Position	P1				P2				P3			
EMF	B_x	B_y	B_z	B	B_x	B_y	B_z	B	B_x	B_y	B_z	B
typical	0.09	0.11	0.51	0.53	0.08	0.05	0.53	0.54	0.01	0.06	0.03	0.07
Position	P4				P5				P6			
EMF	B_x	B_y	B_z	B	B_x	B_y	B_z	B	B_x	B_y	B_z	B
typical	0.61	0.38	0.28	0.77	0.56	0.03	0.40	0.69	0.23	0.39	0.07	0.46

Table 2. EMF measurement for the cell phones (att all 6 points)

Position	P1				P2				P3			
EMF	B_x	B_y	B_z	B	B_x	B_y	B_z	B	B_x	B_y	B_z	B
calls off	0.00	0.00	0.01	0.01	0.00	0.00	0.02	0.02	0.00	0.00	0.01	0.01
calls on	0.01	0.03	0.08	0.09	0.00	0.06	0.03	0.07	0.00	0.04	0.04	0.06

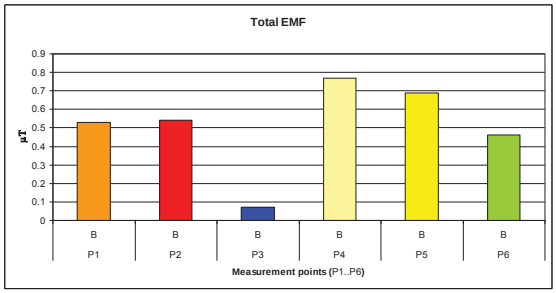

Fig. 5. Total EMF at measured points (P1..P6) for tablets

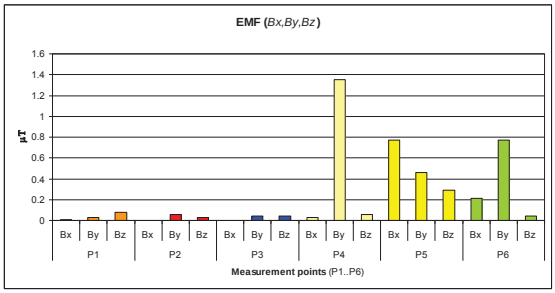

Fig. 6. EMF components at measured points (P1..P6) for cell phones

The tablet is characterized with the total intensity of the magnetic induction between B 0.07 and 0.77. The back of the device represents the more critical EMF position leading to maximum B of 0.77. Although, the EMF is considerably lower than in the laptop neighborhood [10], it still exists. It has to be noticed that according to the Law, the security level of the EMR is below 0.04 μT [8]. Hence, the caution during tablet use is necessary.

Likewise, the consequences of the second experiment show that EMF appears only in some measurement points. Furthermore, the second experiment is enlarged by measuring EMF for the cell phones during receiving calls. Table 2 shows the EMF at all six positions in the cell phones neighborhood during the calls off and on.

We have to point out that the EMF measurement is made exclusively for the low frequencies case. It means that the cell phones are not tested on the high frequencies EMF. Furthermore, it can be noted that the cell phones do not emit EMR when there is no calls. During the phone rings, EMR is significantly increased. Figure 6 shows measured EMF components.

Figure 7 shows total EMF.

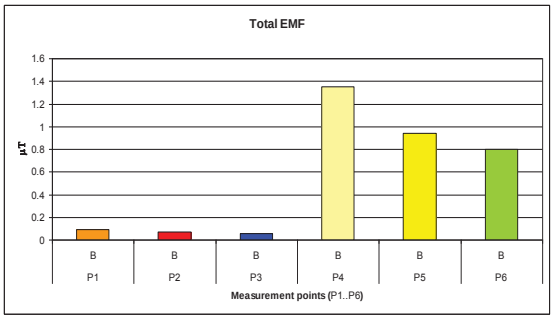

Fig. 7. Total EMF at measured points (P1..P6) for cell phones

From the above figures it is clear that EMF radiation appeared at the front side of the cell phone is noticeably lower than on its back side. It is a consequence of the EMF radiation protection that is put on the front side of the cell phones. Still, during the phone calls the emitted EMF radiation is slightly higher than the referent limit level proposed by the Law. Hence, it is recommended to be used with caution, especially by children or pregnant woman.

4. CONCLUSION

The paper addresses the problem related to the EMF radiation, which exists in the neighborhood of the

gadgets like tablets and the cell phones. The measurements of EMF characterized by the low level frequencies are carried out by Lutron EMF 828 device. The obtained results show the critical levels of the EMF, which are sometimes above the law limits [8]. Consequently, they pointed out the gadget positions where the EMF radiation is vital. This information can be exploited for their safe use.

Future research work will extend to the EMF measurements of the portable and stationary computer office appliances such as: laptop, desktop computers, printers, scanners, and so on.

Acknowledgments

This work was supported by the Ministry of Education, Science and Technological Development of the Republic of Serbia (Project III43011 and TR33037) and Contract № 141ПР0011-07 of Technical University-Sofia, Research Sector. Research project: «System for recognition and visualization with gesture control» - 2014.

References

[1] World Health Organization (WHO), *Extremely Low Frequency Fields*, Environmental Health Criteria Monograph No. 238.

[2] Hallberg O., Oberfeld G., ,"Letter to the editor: will we all become electrosensitive?," Electromagnetic, Biology and Medicine, vol.25, no.3, 2006, pp.189-191.

[3] Lonn S., Ahlbom A., Hall P., Feychting M., "Mobile phone use and the risk of acoustic neuroma, Epidemiology," vol.15, 2004, pp.653-659.

[4] Nordström G., *The Invisible Disease - The Dangers of Environmental Illnesses caused by Electromagnetic Fields and Chemical Emissions*, O'Books, Hants and New York, 2004.

[5] Abramson M. J, Benke G. P., Dimitriadis C., Inyang I. O., Sim M. R., Wolfe R. S., Croft R.J., "Mobile telephone use is associated with changes in cognitive function in young adolescents, Bioelectromagnetics," vol.30, no.8, 2009, pp.678-686.

[6] Agarwal A., Deepinder F., Sharma R. K., Ranga G., Li J., "Effect of cell phone usage on semen analysis in men attending infertility clinic, Fertility and Sterility," vol.89, no.1, 2008, pp.124-128.

[7] Ahlbom A., Feychting M., Green A., Kheifets L., Savitz D. A., Swerdlow A. J., "Epidemiologic evidence on mobile phones and tumour risk: a review," Epidemiology, vol.20, no.5, 2009, pp.639-652.

[8] Safety Rules, Possed by the the Ministry of Occupational Safety and Environment Protection (in Serbian), *Pravilnik o granicama izlaganja nejonizujućim zračenjima, Službeni glasnik Republike Srbije 36/09*, 2009.

[9] Low on the Non-Ionized Radiation Protection, Brought by the Ministery of Occupational Safety and Environment Protection (in Serbian), *Zakon o zaštiti od nejonizujućeg zračenja*, 2009.

[10] Bellieni C. V., Pinto I., Bogi A., Zoppetti N., Andreuccetti D., Buonocore G., "Exposure to Electromagnetic Fields From Laptop Use of "Laptop" Computers," Archives of Environmental & Occupational Health, vol. 67, no. 1, 2012, pp. 31-36.

DETECTION OF RENAL CYSTS BASED ON COMPLEX SEGMENTATION OF CT IMAGES

Veska M. Georgieva

Faculty of Telecommunications, Technical University of Sofia, Bulgaria
1000 Sofia, "Kl. Ohridsky" str.8
T. (+359 2) 965-3293; E-mail: vesg@tu-sofia.bg

Antonia D. Nankova

Faculty of German Engineering Education and Industrial Management, Technical University of Sofia, Bulgaria
1000 Sofia, "Kl. Ohridsky" str.8
E-mail: antonianankova@gmail.com

Abstract

In the paper is presented an approach for detection of renal cysts. It consist of preprocessing and complex segmentation method of Computed Tomography (CT) images. This method is a combination of 2 basic methods for image segmentation such as color based K-mean clustering, following of split & merge algorithm. As preprocessing stage can be used choosing a region of interest (ROI), grayscale conversion or filtration.

Some experimental results are presented, obtained by computer simulation in the MATLAB environment. Implementation results are given to demonstrate the visual quality in the perspective of clinical diagnosis and the right treatment decisions.

1. INTRODUCTION

A renal cyst is a small oval or round thin-walled sac with watery fluid insides. A cyst may grow in any part of the kidneys, such as renal cortex, renal medulla, renal parenchyma, etc.

Two broad categories of renal cyst exist [1]:

- Simple cyst;

These cysts are spherical in shape and filled with fluid. They are very commonly found (up to 27% of people older than 50 have asymptomatic simple cysts) very low risk of being or becoming cancerous.

- Complex cyst;

These cysts are often irregularly shaped and contain both a thick outer wall and thick septa, they are often calcified, and they often receive their own blood supply. They are an irregularly shaped cyst that is suspicious for cancer.

Monitoring of renal function by standard measurements, follow-up of patients with Autosomal Dominant Polycystic Kidney Disease (ADPKD) is based on radiologic investigations that are performed with ultrasounds, computerized tomography (CT), or magnetic resonance imaging (MR), with the aim of evaluating renal cyst morphology and volume and estimating the amount of residual renal parenchyma. [1].

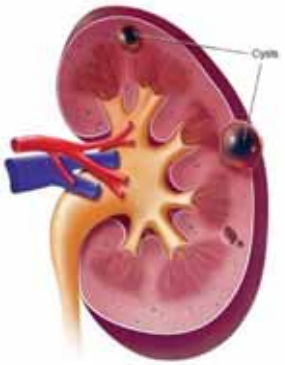

Fig. 1. Kidney with cysts

In our investigations we use CT images. CT has the advantages of widespread availability, more rapid examination time in comparison with MR imaging, and lower cost than MR imaging. Three kidney tissue classes were characterized on CT images: Cysts, parenchyma, and intermediate volume. [2].

Segmentation is a classical method in image processing. The goal of segmentation is to simplify and to change the representation of an image into something that is easier to analyze. Image segmentation is typically used to locate objects and their boundaries (lines, curves, etc.) in medical images. There are some publications based only on basic methods of segmentation for detection of kidney cysts [3, 4].

We propose to use a complex segmentation method, based on combination of color based K-mean clustering, following of split & merge algorithm with the goal to obtain more information and better defined boundaries of the cysts. As preprocessing stage can be performed choosing a region of interest (ROI), gray scale conversion or filtration to reduce the effect of noise on the acquired images.

The paper is arranged as follows: In Section 2 is described the main algorithm of processing; in Section 3 are presented some experimental results, obtained by computer simulation and their interpretation; in Section 4- the Conclusion.

2. COMPLEX SEGMENTATION OF CT IMAGES

In the paper is proposed to use of combination of two basic image segmentations techniques in order to effectively solve a medical image segmentation problem for a problem domain. As first stage is applied clustering. Clustering technique classifies the pixels with the same characteristics into one cluster, thus forming different clusters according to coherence, between the pixels in a cluster. Clustering analysis assigns a set of observations into subsets called as cluster so that the observations in the same cluster are similar in some sense. We have selected the L*a*b* color space which is a perceptually uniform orthogonal Cartesian coordinate system. The differences between two pixels in L*a* b* color space is the same with the sense of the human eyes visual system and this color space enables doctors to quantify these visual differences. Color-Based Segmentation using K-mean clustering segments colors in an automated fashion using the L*a*b* color space and K-means clustering method. K-means clustering treats each object as having a location in space. It finds partitions such that objects within each cluster are as close to each other as possible. K-means requires that the number of clusters to be partitioned should be specified and also a distance metric to quantify how close two objects are to each other [5]. Fig.2 presents the basic flow diagram for the computation procedure by this stage.

By the next stage of processing is used as basic image this cluster, which obtains the most information about the investigated object. For this stage of processing is used the Split and merge segmentation techniques. A region is split, for example, into four sub regions until a given uniformity condition is achieved for the (sub)regions. For gray-level images, this condition can be that the variance of the gray-levels within a region is smaller than a given threshold value *T.* When this condition for a region is not met, this region is further split up.

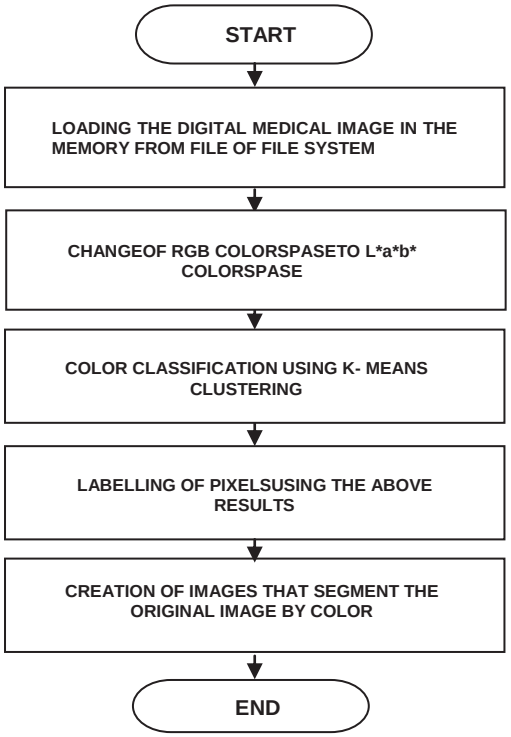

Fig. 2. Block diagram of Color-Based Segmentation using K-mean Clustering

Figure 3 illustrates an example [6]. There R indicates the entire image. Each node correspondsto a (sub)region, whereby in this example only region R4 was further divided up.If the image is divided up only into regions, adjoining regions will be similar inthe final division. These will be merged together in a following step according tothe given condition of uniformity in order to attain uniform regions of maximalsize.The predicate of homogeneity for a region R is based on two criteria:

1. The average gray level of the region R is lower than a threshold.
2. The variance of the gray levels in the region R is greater than a threshold.

This approach tends to be computationally intensive.

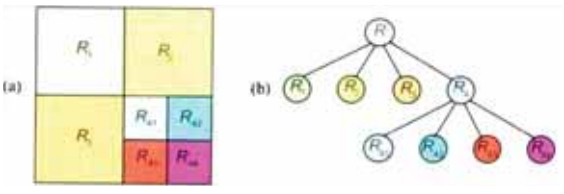

Fig. 3. Illustration of Split & Merge Algorithm:
a) a splited image; b) the corresponded quadtree

In preprocessing stage, which can be applied before the segmentation we propose to be used some standard techniques such as choosing a region of interest (ROI), grayscale conversion or filtration to reduce the effect of noise on the acquired images. They are not obligatory for all images. It is dependent on the specific quality of the image and medical information of the objects, which are investigated.

3. EXPERIMENTAL RESULTS

The formulated stages of processing are realized by computer simulation in MATLAB 7.14 environment by using IMAGE PROCESSING TOOLBOX [7]. The experiments are implemented by using of special graphic user interface, which is created for that purpose [8].

In analysis are used 10CT images from kidney in coronal and 10 CT images in axial planes with size 533x370 pixels in png file format. For processing they are converted in bmp format. Some results from simulation, which illustrate the working of proposed algorithm, are presented in the next figures below.

In Fig. 4 is shown the original CT abdominal image in axial plane with kidney cysts.

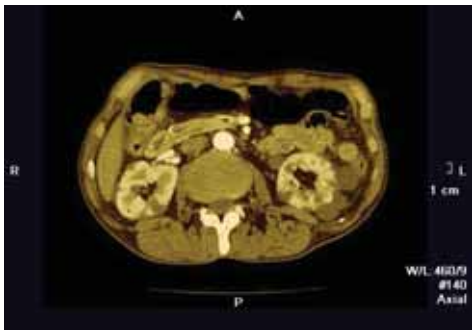

Fig. 4. Original CT image with kidney cysts

In Fig.6 ispresentedcluster 1 of CT image.

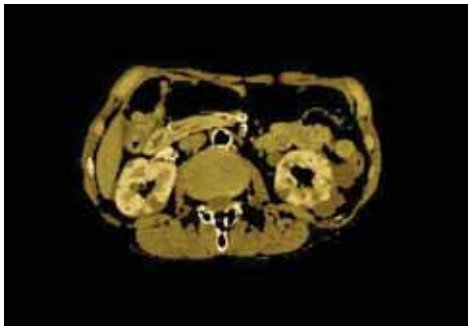

Fig. 5. Cluster 1 of CT image with kidney cysts

The gray scale color conversation of cluster 1 is shown in Fig. 6. It is needed for next step of complex segmentation, based on split and merge algorithm.

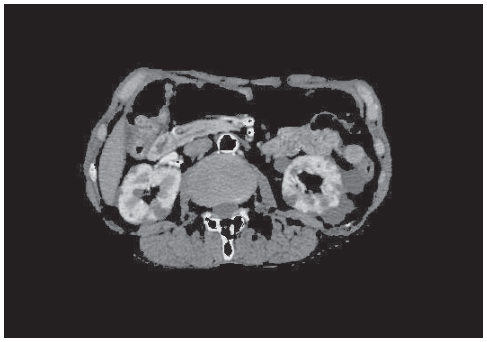

Fig. 6. Grayscale modification of Cluster 1

In Fig. 7 are presented the selected ROI image of Cluster 1. This image of is of size 121x113 pixels from right kidney.

Fig. 7. ROI image of Cluster 1, presented right kidney

In Fig. 8 are presented the same ROI image and its modification, obtained by split & merge algorithm. The value of standard deviation by split and merge algorithm is defined in the case of more gray in the ROI image in grayscale. In this case are visible more details of contours of renal cysts.

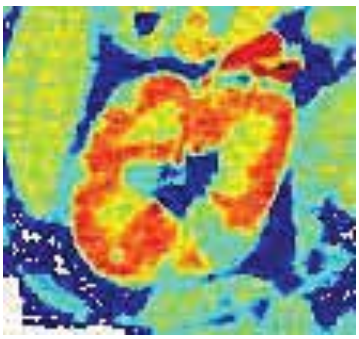

Fig. 8. Modification of ROI image of Cluster 1, obtained by split & merge algorithm

The advantages of results, obtained by the proposed method can be compared to results obtained by

complex segmentation based on color segmentation, using K-mean clustering and region growing algorithm.

In Fig. 9 is presented the modification of ROI image of Cluster 1, obtained by region growing algorithm. The best result is obtained for the value 0.12 of the parameter threshold by region growing algorithm.

Fig. 9. Modification of ROI image of Cluster 1, obtained by region growing algorithm

4. CONCLUSION

In the paper is presented an approach for detection of renal cysts, based on complex segmentation in CT images. The obtained results give detailed information about detected cysts in axial as in coronal plane of CT images.

The proposed method can be used to locate specific objects and their boundaries. It can be used also in real time to provide important anatomical information in medical images to physicians and specialist upon which can be made more precise diagnoses of different diseases. It can be used also in monitoring the disease progression.

The results by segmentation of sequences of CT images can be used for future application in 3D visualization.

Our future work will be concentrated in measurement of some statistical parameters, which are necessary for classification and analysis by renal cysts.

References

[1] G. Eknoyan, "A Clinical View of Simple and Complex Renal Cysts", Journal of the American Society of Nephrology, vol. 20 no. 9 pp.1874-1876, 2009

[2] N. Mekhaldi, M. Benyettou, "Detection of renal cysts by a method of CVM Classification", Annals. Computer Science Series, vol.11, pp.67-71, 2013

[3] Jicksy Susan Jose, R. Sivakami, N. Uma Maheswari, R. Venkatesh, "An Efficient Diagnosis of Kidney Images Using Association Rules", International Journal of Computer Technology and Electronics Engineering (IJCTEE), ISSN 2249-6343, vol.2, pp.14-20, 2013

[4] Chapman, L. Guay-Woodford, J. Granrham, et al, "Renal structure in early autosomal-dominant polycystic kidney disease (ADPKD)", The Consortium for Radiologic Imaging Studies of Polycystic Kidney Disease (CRISP) Cohort. Kidney Int 64:1035–1045, 2003

[5] W. Pratt, "Digital Image Processing", John Wiley & Sons Inc., 2001.

[6] Koschan, Mo. Abidi, Digital color image processing, John Wiley & Sons, Inc., Hoboken, New Jersey, 2008

[7] MATLAB User's Guide. Accessed at: www.mathwork.com

[8] V. Georgieva, A. Nankova, "GUI for Complex Segmentation of Medical Images", Proceedings of CEMA'14, Sofia, Bulgaria, 2014, accepted.

GUI FOR COMPLEX SEGMENTATION OF MEDICAL IMAGES

Veska M. Georgieva

Faculty of Telecommunications, Technical University of Sofia, Bulgaria
1000 Sofia, "Kl. Ohridsky" str.8
T. (+359 2) 965-3293; E-mail: vesg@tu-sofia.bg

Antonia D. Nankova

Faculty of German Engineering Education and Industrial Management, Technical University of Sofia, Bulgaria
1000 Sofia, "Kl. Ohridsky" str.8
E-mail: antonianankova@gmail.com

Abstract

In the paper is presented software for complex segmentation and preprocessing of medical images and its graphic user interface (GUI). It works in the MATLAB environment and uses IMAGE TOOLBOXES defined functions. Three basic methods for image segmentation such as region- growing, split & merge and color based K-mean clustering algorithms are used, regarding to process different medical modalities of the images. The GUI proposes also an interactive option to make some preprocessing such as choosing a region of interest (ROI) in the processed image, grayscale conversion and filtration.

The proposed GUI can be applied to real medical images attempt to make diagnostic more precise. The presented GUI is suitable also to engineering education for studying of this processing.

1. INTRODUCTION

The medical images provide important anatomical information to physicians and specialist upon which can be made diagnoses [1]. Segmentation is a classical problem in image processing; it can be described as the process of partitioning an image into a set of non-overlapping homogeneous regions. The goal of segmentation is to simplify and to change the representation of an image into something that is easier to analyze. Image segmentation is typically used to locate objects as organs and tumors and their boundaries (lines, curves, etc.) in medical images. This is a process of assigning a label to every pixel in an image such that pixels with the same label share certain visual characteristics.Region growing is one of the simplest approaches to image segmentation; neigh boring pixels of similar amplitude are grouped together to form a segmented region. However, in practice, constraints, some of which are reasonably complex, must be placed on the growth pattern to achieve acceptable results [2].Split and merge segmentation techniques are based on a quad tree data representation whereby a square image segment is broken (split) into four quadrants if the original image segment is no uniform in attribute. If four neighboring squares are found to be uniform, they are replaced (merge) by a single square composed of the four adjacent squares [3]. This approach tends to be computationally intensive. Color-Based Segmentation using K-mean clustering segments colors in an automated fashion using the L*a*b* color space and K-means clustering method. The L*a*b* color space (also known as CIELAB or CIE L*a*b*) enables quantifying of visual differences in colors and clustering is a way to separate groups of objects. K-means clustering treats each object as having a location in space. It finds partitions such that objects within each cluster are as close to each other as possible, and as far from objects in other clusters as possible [4].

The proposed program is created in MATLAB 7.14 environment by using IMAGE PROCESSING TOOLBOX.

The graphic user interface consists of checkboxes, buttons, edit boxes, pop-up controls, which make it easy to use. Users enter or choose input data in a single form, because input information changes and visualizations are easier and faster in this way. The processed images can be saved on the disk and so can be used to another processing or its visualization.

The paper is arranged as follows: In Section 2 is described the GUI; in Section 3 are presented the tasks carried out from the main program some ex-

perimental results, obtained by computer simulation and their interpretation; in Section 4 - the Conclusion.

2. THE GUI FOR COMPLEX SEGMENTATION OF MEDICAL IMAGES

The GUI for region segmentation of medical images is shown on Fig.1. It is divided in several areas, where the user applies different settings, concerning image preprocessing, segmentation techniques and theirs parameters and areas for universal application.

The area "Input Image Path" is for entering an image file name with an image file extension. The user can navigate among the folders in the work folder and choose image by using "Browse" button and view the image by using "View Image" button. There is a separate area for "Image preprocessing", shown in Fig. 2. The segmentation technique can be selected in area "Image segmentation", shown in Fig. 3.

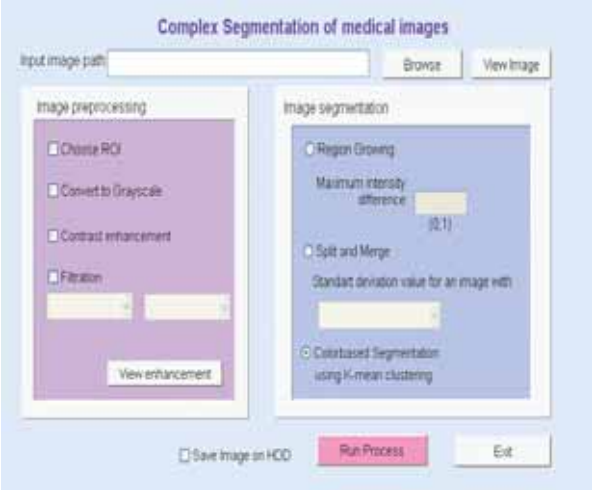

Fig. 1. GUI for complex segmentation of medical images

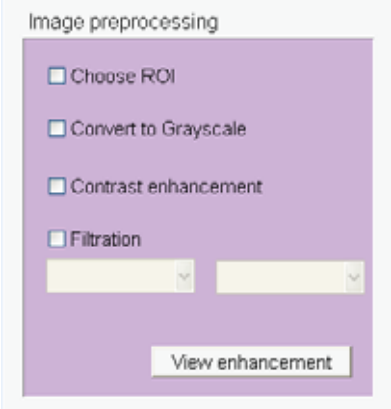

Fig. 2. Area "Image preprocessing"

In the first area the user can choose between four possibilities: Choose ROI(Region of interest); Convert to grayscale; Contrast enhancement; Filtration.There are different methods of filtration that can be used. On the left pop-up menu are listed filtration-methods for both truecolor and grayscale images: average; Gaussian; motion; unsharp; homomorph. On the right pop-up menu there are methods for filtration only of grayscale images. After choosing the preferred preprocessing variations the user can see the results by pressing the button "View enhancement".

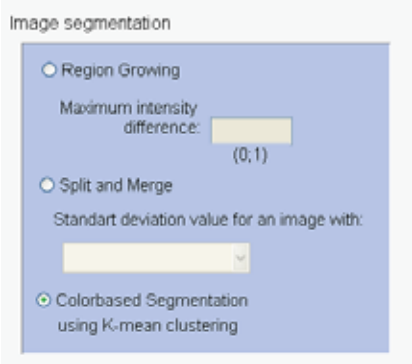

Fig. 3. Area "Image segmentation"

In the second area the user can select between three different segmentation techniques: region-growing, split and merge and color-based algorithms. The important parameters of these methods are maximum intensity difference (threshold) with values between 0 and 1. It can be input manually. Another parameter is a standard deviation. It is specific for the split and merge algorithm.

"Save Image on HDD" is checked to save results in image files in 'jpg' format. After choosing all input information the procedure of processing begins, when the user clicks on button "Run Process". Then the final result is shown – original image, and processed images. When button "Exit" is pressed the program can be closed.

3. TASKS CARRIED OUT FROM THE MAIN PROGRAM

The basic algorithm that works behind is shown in Fig. 4.

By acting of component from GUI can be implemented a callback-function from the main program. Every graphic component can be treated to object. Every object can be referred to handle. The objects referred a complex of attributes, which can be ma-

nipulated from the software. The multifarious attributes can be leaved for using in MATLAB environment, such as "Enabled", "Value", "Visible", "On", "Off" etc. [5]. Every attribute can be enabling in the presence of corresponding handle or reference to the object. Every graphic component can be reiterated to a cycle of events for the MATLAB environment by initialization of the graphic application. It submits addresses of the callback-functions, associated to a given event, which are important. By its identification can be called out a corresponding callback-function. One of the important tasks that the main program has is input data validation. The execution is canceled if an error concerned with wrong information occurs. Another essential purpose of the main program is presenting the input information in appropriate data structures. It is necessary for the next steps in the processing strategy, in this step the processing is made with appropriate input data. Wrong information prevents segmentation from carrying out or may lead to wrong output.

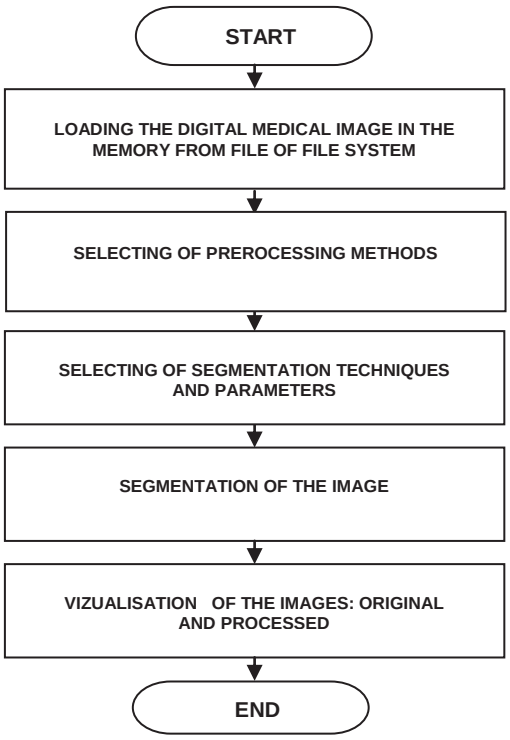

Fig. 4. Block diagram of the algorithm

Some results from simulation, which illustrate the working of the program, are presented in the next figures below. In Fig. 5 is shown the original colorful CT oncology image of size 600x390 pixels from left kidney cancer.

In Fig. 6 is presented the original image after speckle noise reduction, made on the base of homomorph filtration.

Fig. 5. Original CT image

Fig. 6. CT image after filtration

In Fig. 7 are presented the selected CT ROI image of size 203x312 pixels from kidney with cancer and its modifications, obtained by region growing algorithm. The best result is obtained for the value 0.15 of the parameter threshold by region growing algorithm.

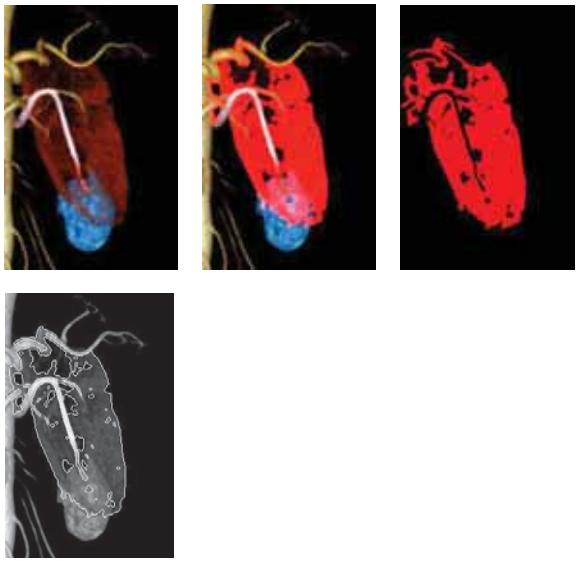

Fig. 7. CT ROI image and its modifications by region growing

In Fig. 8 are presented the same CT ROI image and its modifications, obtained by split & merge algorithm. The value of standard deviation by split and merge algorithm is defined in the case of more gray in the ROI image in grayscale.

In Fig. 9 are presented the same CT ROI image and its modifications, obtained by color-based segmentation using K-mean clustering algorithm.

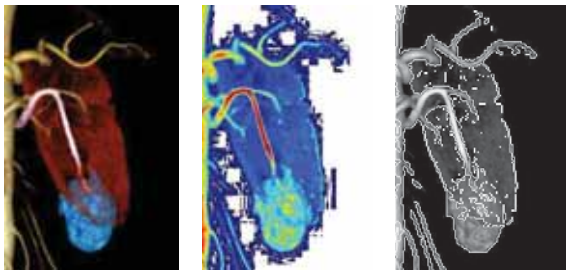

Fig. 8. CT ROI image and its modifications by split & merge

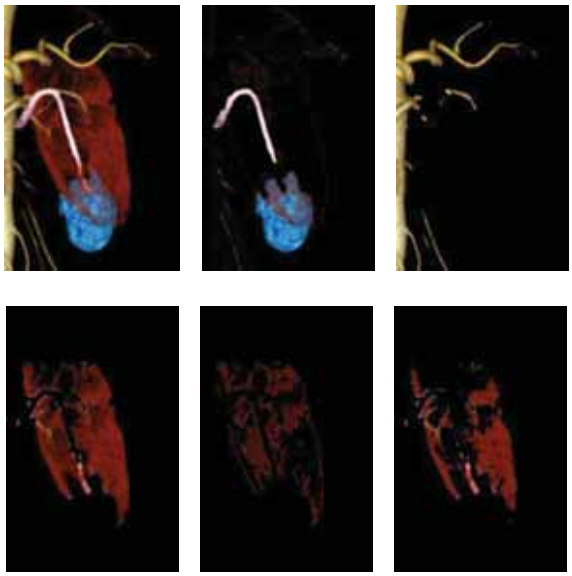

Fig. 9. CT ROI image and its modifications obtained by color-based segmentation using K-mean clustering

4. CONCLUSION

In the paper is presented a GUI for preprocessing and complex segmentation of medical images. It uses MATLAB defined function and works in MATLAB 7.14 environment. The processing can be used to locate objects as organs and tumors and their boundaries by using of region growing, split and merge, color-based segmentation using K-mean clustering algorithms. The GUI can be used in engineering education for studying those processes. It can be used also in real time to provide important anatomical information in medical images to physicians and specialist upon which can be made diagnoses of different diseases. The results by segmentation of sequences of CT images can be used for future application in 3D visualization.

From the simulation-images can be make a comparison between the different kinds of segmentation algorithms in the GUI. By the region growing algorithm it is obvious that the kidney can be extracted in a different color or by a contour but in grayscale. The second shown segmentation (split & merge) works only with grayscale images and converts firstly the image in grayscale, than after segmenting the image paints it in different colors depending on the region. Finally the kidney can be extracted by a contour, but results in this phase are usually not as good as those after using the region growing algorithm. The third color-based segmentation using K-mean clustering can be made only for true color images. The result images are presented in more different segments of the original image by separation of the colors in three clusters and two nuances of one of the clusters. That brings more information about the kidney itself, the vascular and more important about the tumor formation.

References

[1] M. Smith, A. Docef, "Transforms in telemedicine applications", Kluwer Academic Publishers, 1999.

[2] Sheng-Chih-Yang, Chuin-Mu Wang, Yi-Nung Chung, Giu-Cheng Hsu, San-Kan Lee, Pau-Choo Chung and Chein-1 Chang "A Computer Aided System for Mass Detection and Classification in Digitized Mammograms", Biomedical Engineering-Applications, Basis and Communications, vol. 17, No.5, pp. 215-228, 2005.

[3] W. Pratt, "Digital Image Processing", John Wiley & Sons Inc., 2001.

[4] Nankova, Master Thesis on "Farben basierte Segmentierung von medizinischen Bild reihen folgen durch K-Mittelwert Clustering"("Color-based segmentation of medical image sequences by K-mean clustering"), 2014

[5] MATLAB User's Guide. Accessed at: www.mathwork.com

INFRARED TEMPERATURE CONTROL DURING MAGNET THERAPY

Kalin Dimitrov, Atanas Dimitrov, Tsvetan Mitsev

Technical University of Sofia
8, Kl. Ohridski, blvd. Sofia, Bulgaria
T.+35929653145; F.+35929653145; E.kld@tu-sofia.bg.

Abstract

In this paper we have considered a practical research of skin surface temperature change during physiotherapy with low frequency magnetic field. In order to measure the temperature, we have used a thermo graphic camera. The research has been conducted during magneto therapy of a hand in clinical conditions.

1. INTRODUCTION

Optical technologies, and those with infrared light in particular, are becoming more and more commonplace in our lives. As well as in the commonly used optical fibers for transmitting information, the infrared light is also used for indirect temperature measurement. Of essential interest is the compiling and processing of information for temperature fields in the human body [1-9].

The infrared rays which emit from a surface form an image defined a thermograph. Localized increases in the temperature of tissue can be caused by abnormalities which can resemble hot spots or inhomogeneous areas in the thermogpraph. This image has been applied in the investigation of various clinical problems and its reliability and convenience have been proven. Thus, it includes changes of temperature in the regions affected by physiotherapy, and the measurements of temperature may be applicable as an adjunctive physiologic test when the patients' response to treatment is assessed and documented.

Special video cameras which do not have the option of being affixed to a segment of the body, are at the basis of infra red systems. This study aims to assess the applicability of infra red thermography for the evaluation of local physiologic responses in the cases of patients undergoing magneto therapy.

As a safe physiatrist method applied in the treatment of various diseases (articular, intraabdominal, intracranial), magneto therapy has a long history.

This type of therapy, being an alternative physical therapy agent, provides beneficial effects because it has the ability of penetrating deeply in the tissue during the repair process.

The action's mechanism depends on the flow of electrical charges which cause a net flow of ionic current necessary for activities related to the restoration of basic cells and this is believed to result in reproducible healing effects by cell cytoprotection and growth factor synthesis stimulation.

Due to modern devices, it is possible to generate various frequencies, modulations, impulse shapes and duration of exposure.

The frequencies applied are between 1 and 100 Hz, while the magnetic flux density is up to 20 mT. The established physical mechanisms for the interaction of pulsed magnetic fields with living matter are three: magnetic induction, magnetomechanical effects and electronic interactions which is

believed to be responsible for the vasodilatation, analgesie, anti-inflammatory, anti-edematous and spasmolytic activity, as well as for the acceleration of healing.

2. EXPERIMENT

The experiment was conducted within the physiotherapy department of Diagnostic-Consultative Centre 5 – Sofia. Thirty infrared pictures were produced during therapy with two toroidal magnets, of the hand of a sixty-five-year-old volunteer patient (fig. 1 - fig. 3). The pictures were produced at thirty-second intervals. The adjustments of the magneto therapy procedure are the following: magnetic induction 20 mT, square pulses with frequency 10Hz and duty cycle 0,4. The thermography was obtained using infrared thermography device FLIR E40.

All examinations were performed in a sitting position in a quiet room at a constant room temperature following an acclimatization period of 20 min keep-

ing the hands free of any contact to the rest of the body or other objects. All temperature images were archived using internal SD memory card. For the final analysis, the temperature values were determined and given in degrees Celsius (°C). The temperature and perfusion measurements were processed electronically using the device related software from FLIR.

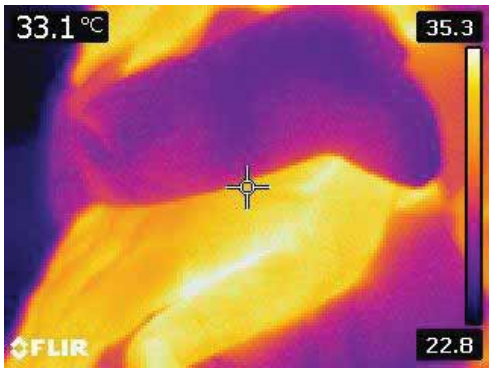

Fig.1. Infrared image with measurement of the region of interest

Fig. 2. The same image as the one in fig. 1 but in visible light

Fig. 3. Infrared image with the measurement of coil temperature

For the emissivity of human skin is taken a constant value 0.98 for the wavelength range of 2–14 um. Recordings were made with a rate of one image per 30 s for a period of 15 minutes. The temperature drift due to the heating of the IR detector was corrected by periodic self-calibration.

3. RESULTS

The results are presented in the following table

No	1	2	3	4
T, °C	33.1	33.2	33.1	33.2

5	6	7	8	9
33.3	33.8	33.2	33.7	33.4

10	11	12	13	14
33.3	33.5	33.3	32.9	33.4

15	16	17	18	19
32.7	33.3	33.4	33.1	32.7

20	21	22	23	24
32.7	33.2	33.2	32.9	32.9

25	26	27	28	29
32.8	32.6	33,2	33,1	32,7

30	31
33,5	33,3

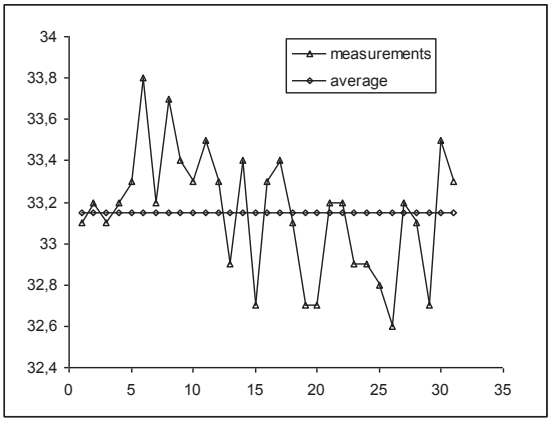

Fig. 4. Graphical representation of results (x-axis – number of measurement, y-axis – temperature in Celsius)

The average and variation are respectively 33,15 and 0,09.

4. CONCLUSIONS

No tendency of temperature change in the selected region has been detected. Fluctuations have been observed in both increasing and decreasing directions. It can be stated that they are due to involuntary twitching of the patient and measurement method error. As a next step is envisioned the broad-

ening of the research to a greater number of patients and wider regions of interest.

References

[1] C. Wu, K. Yu, H. Chuang, M. Huang, T. Chen, C. Chen, "The Application of Infrared Thermography in the Assessment of Patients with Coccygodynia before and after Manual Therapy Combined with Diathermy", Journal of Manipulative and Physiological Therapeutics Thermography for Coccygodynia, 2009, pp.287-293

[2] O. Schlager, M. Gschwandtner, K. Herberg, T. Frohner, M. Schillinger, R. Koppensteiner, W. Mlekusch, "Correlation of infrared thermography and skin perfusion in Raynaud patients and in healthy controls", Microvascular Research, 80, Elsevier, 2010, pp. 54–57.

[3] G. Schaefera, M. Závišekb, T. Nakashimac, "Thermography based breast cancer analysis using statistical features and fuzzy classification", Pattern Recognition, 47, Elsevier, 2009, pp.1133--1137

[4] D. Giansanti, "Improving spatial resolution in skin-contact thermography: Comparison between a spline based and linear interpolation", Elsevier, Medical Engineering & Physics, 30, 2008, pp.733–738

[5] D. Rodrigues-Bigaton, A. Filho, A. de Souza Costa, A. Packer, E. de Castro, "Accuracy and Reliability of Infrared Thermography in the Diagnosis of Arthralgia in Women with Temporomandibular Disorder", Infrared Thermography and Arthralgia, 2013, pp.253-258

[6] T. Borchartt, A. Concia, R. Limab, R. Resminia, A. Sanchez, "Breast thermography from an image processing viewpoint: A survey", Elsevier, Signal Processing, 93, 2013, pp.2785–2803.

[7] B. Lahiri, S. Bagavathiappan, T. Jayakumar, J. Philip, "Medical applications of infrared thermography: A review", Infrared Physics & Technology, 55, 2012, pp. 221–235

[8] N. Ludwig, D. Formenti, M. Gargano, G. Alberti, "Skin temperature evaluation by infrared thermography: Comparison of image analysis methods", Infrared Physics & Technology, 62, 2014, pp.1–6.

[9] O. Faust, U. Acharya, E. Ng, T. Hong, W. Yu, "Application of infrared thermography in computer aided diagnosis", Infrared Physics & Technology, 66, 2014, pp.160–175.

[10] T. Yambe, A. Inoue, K. Sekinea, Y. Shiraishi, M. Watanabe, T. Yamaguchi, M. Shibata, M. Maruyama, S. Konno, S. Nitta, "Effect of the alternative magnetic stimulation on peripheral circulation for regenerative medicine", Biomedicine & Pharmacotherapy, 59, 2005, pp. S174-S176

[11] K. Sweeney, M. Merrick, C. Ingersoll, J. Swez, "Therapeutic Magnets Do Not Affect Tissue Temperatures", Journal of Athletic Training, 36(1), 2001, pp.27–31.

[12] J. Lin, Electromagnetic Fields in Biological Systems, CRC Press, 2011.

[13] E. Kanata, A. Alpb, M. Yurtkuranba, "Magnetotherapy in hand osteoarthritis: Apilot trial", Complementary Therapies in Medicine, 21, Elsevier, 2013, pp.603—608

Acknowledgment

The research in this paper is supported by grant DDVU 02/74-7.

STUDIES OF SOUNDPROOFING CHARACTERISTICS OF SANDWICH PANEL WITH HONEYCOMB CORE AND ELASTIC POROUS ABSORBER

Tsvetan Nedkov

Department of Telecommunications,
Technical University - Sofia, Kliment Ohridski 8, Sofia
ceco@decibel.bg

Abstract

In this paper, some experimental data on soundproofing characteristic of triple sandwich partitions combined between ceramic bricks with holes with honeycomb core, elastic porous absorber and heavy weighted gypsum fiberboard is presented. The honeycomb core is widely used in automotive and aerospace industry in a variety of applications to reduce noise and vibrations and to improve sound quality. On the other hand gypsum fiber boards and porous absorbers are widely used in building constructions and the examination of the properties of combination between these tree type of cores will be useful.

Keywords: soundproofing, sandwich panel, honeycomb, porous absorber

1. INTRODUCTION

Sound insulation between two rooms is very important problem and there is a lot of well known methods for solving it. However, with the development of new materials and construction methods the interest of lighter, thicker and more efficient constructions grows.

Over the years, a great deal of research has been carried out in identifying the transmission loss (TL) characteristics of different panel constructions. Unique approaches to achieving high TL within mass limitations include a design developed by Watters and Kurtze [1], the “shear wall”, and the “coincidence wall” developed by Warnaka [2]. These designs are based on understanding of coincidence effects in the interaction of the incident sound field with the vibration response of the panel. Moore and Lyon [3] developed analytical model for calculating TL of sandwich panel with orthotropic honeycomb core. Dimino, Vitiello and Aliabadi [4] developed analytical model in transportation vehicles to predict sound transmission trough infinite sized triple panel partition placed in a rigid baffle. They also developed a numerical procedure to evaluate the transmission characteristics of finite partitions due to an incident diffuse field. The method is based on FEM/Rayleigh methodology and utilizes numerically calculated sound transmission loss of flat multipanel partitions and box like cavities with idealized boundary conditions.

Ballagh [5] developed a low frequency model for triple partitions that can predict the transmission loss relatively well up to about 250 Hz.

It is interesting to compare a double panel and triple panel system where the overall width and mass of the system is constrained. Ballagh [5] examine the behavior of double and triple partitions with same summarized mass and air cavity. The results are shown in Figure 1 where it can be seen that although the triple panel system has superior performance at higher frequencies, its performance at low frequencies is markedly inferior.

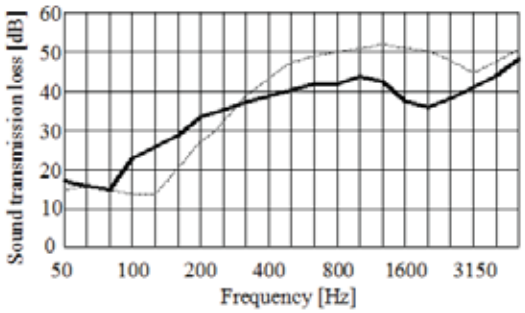

Fig. 1. Transmission loss comparison between:
double partition ——;
triple partition ▬▬

For residential buildings the most common sound sources are speech, sound generated from TV and small home music systems.

To achieve satisfactory levels of transmission loss of partitions and to receive unintelligible speech the

frequency region of interest is between 400 and 5000 Hz. Sound waves striking such a panel are predominantly transmitted by travelling bending waves and the damping of banding waves reduces the transmission of intelligible speech trough the panel by interfering with the normal propagation of the sound radiating waves. The damping of bending waves is more effective than the damping of other vibrations with the result that by placing the critical frequency for bending waves at or near the upper end of the bass region, all frequencies above this region are effectively cut off. Cutting off all of the speech frequencies above bass essentially prevents transmission of intelligible speech trough the panel.

In this document is presented comparison of transmission loss between two types of sandwich partitions: first consist of heavy and light face sheets and elastic core; second consist of heavy and light face sheets and addition honeycomb structure placed in the center between two elastic layers. In both cases, face sheets and elastic cores are with same thickness and densities. This comparison validate that the introduction of additional layer with high bending stiffness and relatively small density has the potential to improve transmission loss of related structure in the desired frequency range.

2. ACOUSTIC MODELING OF TRIPLE PANELS

For modelling triple wall panels it is satisfactory to divide the frequency region into a low frequency region where a lumped parameter model is satisfactory, a mid frequency region where wave motion in the porous elastic absorbing layers is important, and a high frequency region where structural coupling between panels is important.

At low frequencies, where sound waves have very large wavelengths, it is found that it is the bulk properties of materials such as their mass are most significant.

The components in the wall can be regarded as masses or springs coupled. This is the classical lumped parameter model. Panels are described with their masses per unit area (surface mass) and filled air gaps with porous elastic absorber are modelled as springs. In its simplest form a triple panel wall would be represented by 3 masses connected by two springs (Fig. 2).

A simplified system of three masses attached to each other by springs with rigidity k_1 and k_2, eq. (1) can be defined, and this can be solved to give the natural frequencies of the system:

$$\begin{aligned}&[m_1 m_2 m_3]\left(\omega^2\right)^2 - [k_1 m_3 (m_1 + m_2) + \\ &k_2 m_1 (m_2 + m_3)]\left(\omega^2\right) + \\ &[k_1 k_2 (m_1 + m_2 + m_3)] = 0\end{aligned} \tag{1}$$

With $k_1 = \dfrac{\rho c^2}{d_1}$ and $k_2 = \dfrac{\rho c^2}{d_2}$, where d_1 and d_2 are the thickness of the elastic layers and ω is a resonance frequency.

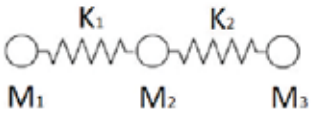

Fig. 2. Mechanical scheme of coupled triple panel

For the case of sound insulation of a structure (consisting of tree or more panels), the transfer function of interest is the ratio of the incident sound pressure to the velocity of the radiating panel.

Rindel [6] gives the transmission loss as:

$$R = 10\log\left(\frac{\langle \rho_s^2 \rangle}{4(\rho c^2)\langle v_r^2 \rangle}\right) \tag{2}$$

and it can be seen that it is ratio of incident pressure $<\rho_s>$ to velocity $<v_s>$ of the radiating panel that is important.

By using standard Fourier transform methods the transfer function can be derived.

The sound transmission coefficient (τ) is defined as the square of the absolute value of the ratio of the transmitted to incident pressures:

$$\tau = \left| p_t / p_i \right|^2, \tag{3}$$

Where for anti symmetric panels:

$$\frac{p_i}{p_t} = \frac{(1 + \bar{z}'/2z_a)(1 + \tilde{z}'/2z_a) - \alpha_2\alpha_5}{(\bar{z}'/2z_a) - (\tilde{z}'/2z_a)} \tag{4}$$

In eq.(4) $\bar{z}'$ and $\tilde{z}'$ are impedances of symmetric and anti symmetric motions in the panel, z_a is the modified acoustic impedance of the acoustic field:

$$z_a = \rho_a c_a / \cos\theta \tag{5}$$

Where $\cos\theta$ is angle of incidence of sound wave, ρ_a is the density of the air and c_a is the speed of sound in air.

In eq. (4) α_2 and α_5 are ratios of operators that appear as coefficients in the equations of Dym, Ventres and Lang [7].

The transmission coefficient is a function of the angle of incidence of the sound waves. To account for this distribution, an averaged form of the transmission coefficient is used. Conventionally this averaged form of equation is:

$$\bar{\tau} = \int_0^{\theta_{lim}} \tau \sin\theta\cos\theta d\theta \Big/ \int_0^{\theta_{lim}} \sin\theta\cos\theta d\theta, \quad (6)$$

where $\bar{\tau}$ being known as the field incidence averaged transmission coefficient. The limiting angle θ_{lim} is taken as equal to 78°, based on field and laboratory measurements. Finally, the field incidence averaged TL is:

$$TL = 10\log_{10}\left|1/\bar{\tau}\right| \quad (7)$$

In the observed triple partition, the middle panel is selected to be fabricated from recycled paper honeycomb structure laminated on both sides with elastic porous polyurethane foam. Such materials have different stiffness modules in planes perpendicular and parallel to the direction of the cells, and can be characterized as orthotropic with nine independent stiffness constants.

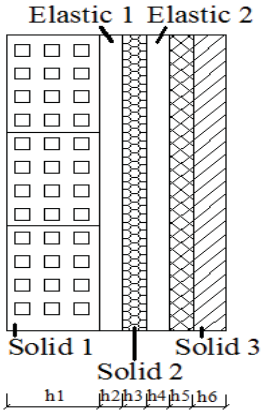

Fig. 3. Section of observed triple partition:
Solid 1 – ceramic brick with holes; Solid 2 – honeycomb structure; Solid 3 – laminated gypsum fiber board and gypsum board; Elastic 1 and 2 – PU elastic absorber

The honeycomb panel TL behaviour is conveniently explained in terms of coincidence effects associated with motions in the panel that are either symmetric or anti-symmetric in character. The decomposition into symmetric and anti-symmetric motions is exact for symmetric panel constructions with identical face sheets and a homogeneous core material.

When the wave speed for either motion in the honeycomb panel exceeds the sound speed, then a matching condition occurs between that motion in the panel and the incident acoustic wave that results in increased transmission trough the panel. For symmetric panel motions, these occur due to a double wall resonance and at higher frequencies where the motion is controlled by bending deformation in the face sheets. For anti symmetric panel motions panel motions, three regions exist with bending deformation of the entire panel cross section: the controlling factor at low frequencies; the core shear stiffness controls in the mid frequency transition region; and bending deformation in the face sheets is the limiting behavior at high frequencies. The wave speed for anti symmetric motions increases monotonically with frequency trough the three regions. Where coincidence first occurs is importantly dependent on the shear stiffness in the core. If the stiffness is too large, coincidence can easily be shifted to occur below the mid-frequency region at lower frequencies with the TL adversely decreased over the useful frequency range.

In Table 1 are given physical properties of the examined material:

Table 1. Physical properties of solid materials in observed triple partition

Type of material	Density	E Modulus	Coeff. of Poisson	Coeff. of internal loss
---	*kg./m³*	*GPa*	*v*	*η*
Ceramic brick with holes	655	6,85	0,12	0,013
Gypsum fiber board	1130	3,9	0,3	0,012
Gypsum board	680	2,1	0,24	0,01
Honey comb structure	28	4.0	0.21	0.03
PU elastic absorber	150	0,7	0,35	0,15

The calculation of TL where done with software INSUL taking into account all the parameters described in Table 1.

3. EXPERIMENTAL PART

For the experiment was built a soundproofed chamber with test opening with dimensions of 185 x 132 cm and volume of 9.96 m^3. The receiving room is with volume of 265 m^3. The sound reduction index Rw of the partitions of the chamber, build from two layers of concrete bricks with air gap between them, filled with mineral wool is 65 dB. Tested specimen is separated from the other partition elements with a 10 mm rubber stripe. In the source chamber is placed a dodecahedron sound source connected with a generator of "pink noise". One microphone is placed in the source chamber, connected with a sound level meter and frequency analyzer. In the source, room at distance 100 cm from the specimen is placed a condenser microphone, connected with a sound level meter and a frequency analyzer. The generated sound pressure in the source room is SPL = 94 dB.

As the smallest dimension of tested partition is 135 cm the results for frequencies with length of wave below half of this dimension (below 500 Hz) are considered to invalid.

4. RESULTS

As obvious from Fig. 4 there is a significant difference between theoretical calculations and experimental results.

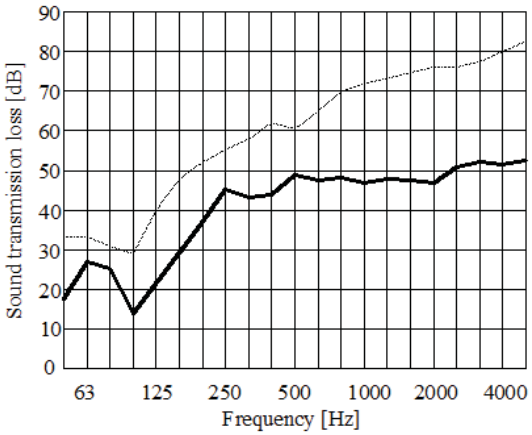

Fig. 4. Comparison of calculated and measured TL of triple panel: measured TL ▬; calculated TL —

Resonance frequency is determined well, but the sound pressure level varies in range of 5 dB for low frequencies to up to 25 dB for high frequencies. Coincidence region from is quite short compared with the measured. It can be take into account that the flanking paths determine the continuous horizontal part of transmission loss curve for measured results. It's benefit that the start of coincidence region is from 250 Hz and is well subscribed until 500 Hz after that the amplitude of bending waves is reduced.

On Fig. 5 is presented comparison of TL between triple partition with middle solid of honeycomb, triple partition with middle solid of gypsum fiber board and double partition where middle solid is removed.

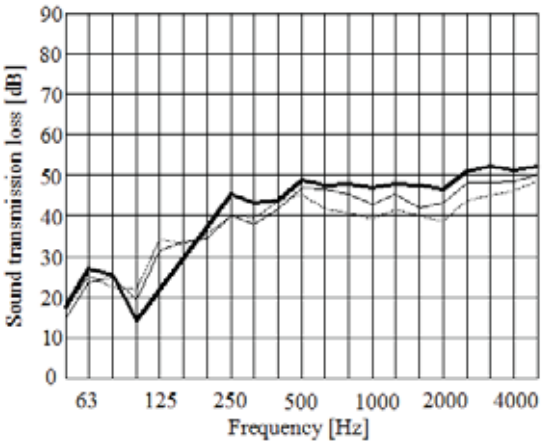

Fig. 5. Comparison of TL between: triple partition with honeycomb: ▬; triple partition with gypsum fiber board:——; double partition with removed middle solid layer: ·····

5. CONCLUSION

For triple anti symmetric partitions the usage of middle orthotropic honeycomb solid panel benefit TL behaviour. In comparison with heavy solid middle layer from gypsum fiber board TL is improved up to 7 dB and the coincidence region is with smaller amplitude of bending waves.

This phenomenon is provided by different bending stiffness in directions and highest internal loss of honeycomb structure. When partitions are used for blocking intelligible speech with frequency range of interest from 400 to 4000 Hz the application of honeycomb structure is beneficial. Theoretical model for prediction is poor presented so for future work will be useful to be developed model for predicting TL of triple anti symmetric partitions with orthotropic middle solid layer.

6. APPENDIX AND ACKNOWLEDGMENTS

This paper was supported by Technical University - Sofia inner program to support PhD research projects under Contract 145 PD0017-07: "Development of algorithms to study the acoustical characteristics of covering materials for recording studios and concert halls".

References

[1] B. G. Watters and G. Kurtze, "*New Wall Design for High Transmission Loss or High Damping*", J. Acoust. Soc. Am. 31, 739-748, 1959.

[2] G. Warnaka, US Patent No. 3, 422, 921, "*Sound Attenuating Wall for Blocking Transmission of Intelligible Speech"*, 1969.

[3] J. A. Moore and R. H. Lyon, "*Sound Transmission loss characteristics of Sandwich Panel Constructions*", J. Acoust. Soc. Am. 89, 777-791, 1991.

[4] I. Dimino, P. Vitiello, F. Aliabadi, "*Sound Transmission Trough Triple Panel Partitions*", Recent Patents in Mechanical Engineering, 200-215, 2010.

[5] K. H. Ballagh, "*Sound Transmission trough Triple Panel Walls - Low Frequency Model,* XXIst Biennial Conference of the Acoustical Society of New Zealand, 2012.

[6] J. H. Rindel, "*Sound Radiation from Building Structures and Acoustical Properties of Thick Plates*", XXIst BCOM-MET-SAVOIR Course CSTB, 1995.

[7] ISO EN 140-1 – 1997, "*Acoustics. Measurements of sound insulation in buildings and of building elements. Part 1: Requirements for laboratories"*.

DEVELOPMENT OF SOUND SOURCE LOCALIZATION MODULE BASED ON MEMS TECHNOLOGY

V. Hristov

Department of Telecommunications,
Technical University - Sofia, Kliment Ohridski 8, Sofia
hristov.viktor@gmail.com

Abstract

Sound source localization is a wide spear method for finding direction from where the sound waves come from a sound source to a listener. If the listener is a person, the human hearing system do this sound source localization very precise, but in cases when the listener is an automatic system for example a mobile robot, a surveillance system, a videoconference system, etc., this sound source localization is not so easy to do. Usually the realization of an automatic sound source localization system is based on microphone arrays as hardware and on some developed methods and algorithms as software for processing sound signals from each of the microphones in microphone array, leading to angle determination of sound source direction of arrival to the place of microphone array.

The goal of this article is to develop an appropriate sound source localization module working as a microphone array based on MEMS technology.

Keywords: *Sound Source Localization Module, MEMs Technology, Development, Signal processing*

1. INTRODUCTION

Since the invention of the telephone systems, sound signals become an essential part of acoustic and speech processing. Traditionally, sound signals are recorded with the use of only one microphone, but this was with some limitations. To preserve the sound fidelity, spatial realism and increase the processing flexibility with multiple sources, microphone arrays were invented [1].

A microphone array consist of a number of acoustic sensors positioned on the proper distance between each other in a way that spatial information can be captured [2]. As a result, the array outputs contain signal of interest, noise, interference and also propagation information that is represented by the acoustic impulse response from the radiating sources to the microphones.

The most popular methods used in microphone arrays are for sound source localization. They can be defined in three main groups: dependent from time of arrival, fixed beamforming and adaptive (hybrid) beamforming using correlation functions [3].

Beamforming is spatial filtering based on microphone characteristics and microphone array configuration. It can be classified in two groups: fixed (classical) and adaptive (hybrid) depending of the input data [3].

There are two scenarios dependent of the distance from source to the microphone: far-field and near-field. Depending of the place, were experiment was done it could be open space, without any reflections and in closed space, also called multipath propagation, because each reflection from the wall or object can be treated as a separate source [4].

Micro-electromechanical systems (MEMS) is a new technology allow to realize the sound localization module as micro miniature device and as a programmable system changing microphone array configuration. This process technology used to create a tiny integrated devices or systems that combine mechanical and electrical components [5].

In the beginning of this article are mentioned main existing sound localization methods are their possibilities to implement in microphone arrays devices. The MEMS technology is also briefly presented to define it ability for development of a microphone array using MEMS microphones [6]. The steps of sound source localization module development applying MEMS microphones are described carefully in the next parts of this article and after that are presented some results of developments: sound source localization module functional schema, simulation of some possible configurations (number

of MEMS microphones, space structure of microphones placement in microphone array, etc.) of microphone arrays in developed sound source localization module and some important characteristics of the developed sound source localization module.

The target of this experiment is to develop an appropriate sound source localization module working as a microphone array based on MEMS technology.

2. BLOCK DIAGRAM OF THE DEVELOPED SOUND SOURCE LOCALIZATION MODULE

On Fig. 1 is shown block diagram of the constructed and investigated device. It consists n-microphones from MEMS type from which will be received audio signals.

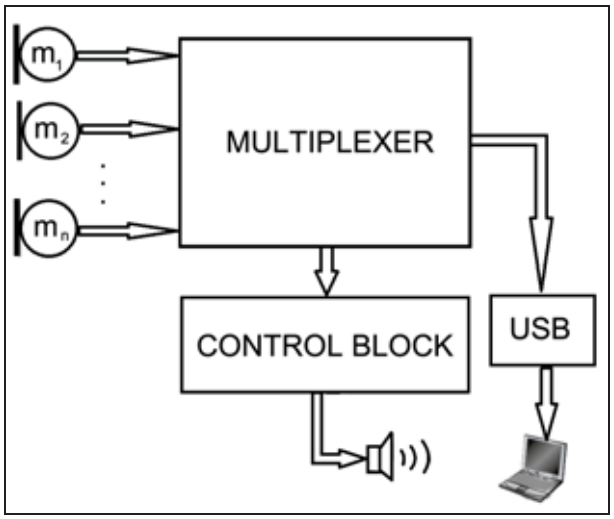

Fig.1. Block diagram of SSL module

Then they were processed in multiplexor block where the signals are converted to a standard data stream. After that received output can be amplified and heard using a control block and speaker. The other output option is to be visualized following the USB interface and proper computer software.

3. DEVELOPMENT OF THE PRINCIPLE SCHEME OF THE SOUND SOURCE LOCALIZATION MODULE

For realization the sound source localization module is used equipment from ST Microelectronics producer. On Fig. 2 is shown all used components that is need for realization – MEMS microphones, multiplexor, control block, software and computer or laptop.

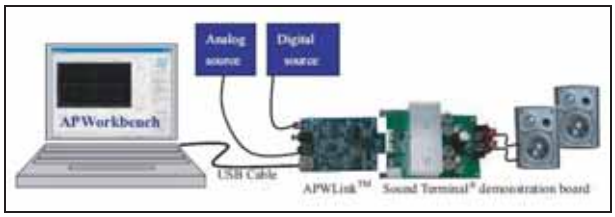

Fig. 2. Block diagram

On Fig. 3 is shown multiplexer block diagram. Analog signal which was received from MEMS Microphone 1-6, will be digitalized in PDM interface. After that it is possible mixing and filter applying and all calculations will be done from scalable microphone processor. Finally the signal can be recorded or played back depending of the used outcome.

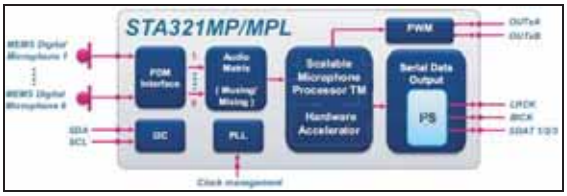

Fig. 3. Multiplexer block diagram

3.1. Used components

For project implementation are used MEMS microphones MP34DB01, board components STEVAL-MKI126V2, MKI129V2 and CCA035V1 and of STMicroelectronics.

3.1.1. MEMS microphone choice

The MP34DB01 (Fig. 4) is an ultra-compact, low-power, omnidirectional, digital MEMS microphone built with a capacitive sensing element.

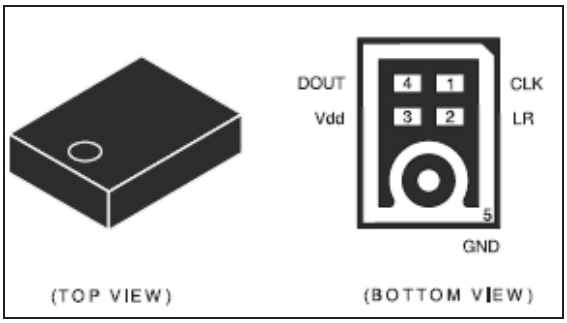

Fig. 4. MP34DB01 microphone

The IC interface is with stereo operation capability is manufactured using a CMOS process that allows to design a dedicated circuit able to provide a digital signal externally in PDM format. The MP34DB01

has an acoustic overload point of 120 dBSPL with a best on the market 62.6 dB [8].

3.1.2. Multiplexor development

The STEVAL-MKI126V2 system evaluation board (Fig. 5) can connect up to six microphones using the sockets provided or through a dedicated six microphone array.

Fig. 5. STEVAL-MKI126V2

The main purpose of the STEVAL-MKI126V2 is to convert the PDM signals provided by the microphones into the more common I2S and PWM signals. The I2S signal is routed both on general and interface connectors, while the suitably-filtered PWM signals provide an analog interface.

Mounted on the STEVAL-MKI126V2 are two MP34DB01 microphones and an STA321MPL processor [9].

3.1.3. Control block

The control block is CCA035V1 demonstration board (Fig. 6) implements an APWLink designed as a USB interface board to control ST Sound Terminal® demonstration boards [10].

In addition, in order to provide controlling signals to external Sound Terminal® demonstration boards, analog/digital audio inputs are also provided within APWLink.

Fig. 6. Control block CCA035V1

3.1.4. Microphone adapters

Microphone adapters are small circular PCBs with a single soldered MEMS microphone. Used board STEVAL-MKI129V2 (Fig. 7) is with mounted digital microphone - MP34DB01 [11].

Fig. 7. Microphone adapter MKI129V2

3.2. Used program products

For visualization of the sound signals is used APWorkbench software suite (Fig. 8).

Fig. 8. APWorkbench software

It provides a comprehensive environment for the customer to explore, evaluate and configure devices within ST's product portfolio for audio applications, including stereo and multi-channel amplifiers, DSP and digital MEMS microphones. The tool rep-

resents a unique solution enabling the user to conveniently evaluate, configure and tune advanced audio IPs embedded in ST's Sound Terminal® products.

Custom controls and a user-friendly graphical interface expose the complexity of today's audio devices in a simple and intuitive manner, guiding the novice through the basic configuration steps and providing acoustic expertise to tune the devices for optimal performance.

4. SOFTWARE SYSTEM FOR EXPERIMENT WITH MEMS MICROPHONE ARRAYS

Starting software is used the option STSmartVoice Demo Kit (Fig. 9). Selection of the USB port APWLink interface (1) starts communication between software and module. This will be used for realtime manipulation of the audio input. There is another option - "USB digital voice recorder" which provides ability to save audio in digital format. This will be used fot storing and audio probes and after that invetisgation of the sound source localization using different techniques.

Fig. 9. Module choice

Before applying the configuration (Fig. 9) it can be selected the number of used microphones (2 – 6). There are two onboard MEMS microphones and there is an option up to four – using the digital microphone interface. In further investigation different type of microphone arrays can be constructed and applied.

Fig. 10. Microphone selection

On Fig. 11 is shown the application of filter. There is a choise between LoPass, HiPass, LoShelf, HiShelf Notch, AllPass filters. Optional can be fine-tunned all coefficients.

Fig. 11. Apply filters

Optional can be imported filter (Fig. 12) from Math Lab using the Fdatool.

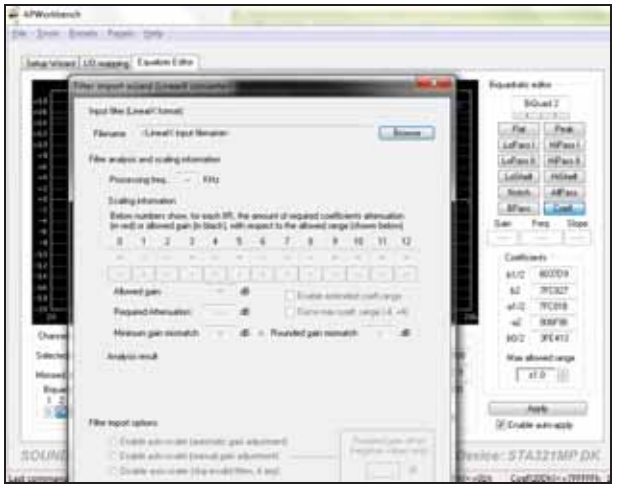

Fig. 12. Filter import

Beamforming of the microphone arrays allows to use summantion of the signal (Fig. 13). The signal's amplitude can be configured before application of the filter.

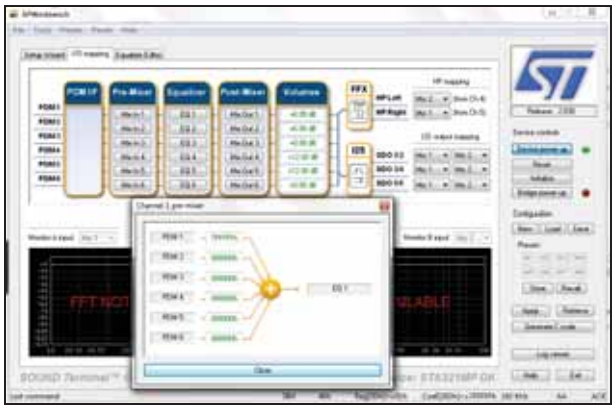

Fig. 13. Beamforming of the microphone array

This is analog of the block diagram shown on Fig. 14 for filter-and-sum beamforming technique. Each filter coefficient ω_n can be set separately in hexadecimal values.

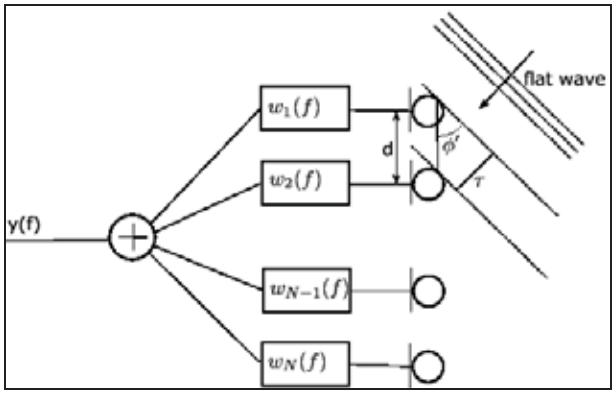

Fig. 14. Filter-and-sum algorithm blocks diagram

The input signal (considered to be coming from a distant source and flat) arrives to each microphone from an angle φ' at a different time instant. The signals from the different microphones are passed through a filter ω_n, independent for each microphone (1 through N), which accounts for an amplitude and time delay.

$$y(f) = \sum_{n=1}^{N} w_n(f) x_n(f) \qquad (1)$$

The output signal y(f) is the sum of all signals from MEMS microphones $M_1 \ldots\ldots M_N$.

This type beamforming technique was selected for the implementation of the meetings systems because it agrees with all desire characteristics. Furthermore, its simplicity allows for a fast implementation, normally under real-time, that allows it to eventually be used in a real-time system.

5. CONCLUSION

This article was presented developed hardware and software system for Sound Source Localization using beamforming technique. It was described MEMS technology which was used to construct the module.

There are used line microphone array modules and in future investigation will continue with assembling and constructing other different types. There are described all interfaces, which can be used for the connection with computer. It was presented the software that can manage and exanimate the different configurations of modules attached.

In future using the same microphones with different position to investigate their ability to Sound Source Localization using beamforming technology.

Acknowledgment

This paper was supported by Technical University – Sofia inner program to support PhD research projects under Contract 142 PD 0018-07: "Development of methods and tools to locate audio sources in information and communication networks".

References

[1] *J. Benesty, and J. Chen, Study and Design of Different Microphone Arrays, 2013.*

[2] *Muller, R.S., Howe, R.T., Senturia, S.D., Smith, R.L., and White, R.M, Microsensors, IEEE Press, New York, 1991.*

[3] *Yong Rui and Dinei Florencio, "New direct approaches to robust sound source localization", January, 2004.*

[4] *Iain McCowan, Microphone Array, April 2001.*

[5] *Banesty, Jacob, Chen, Jingdong, Huang, Yiteng, Microphone Array Signal Processing, 2008.*

[6] *Trimmer, W.S., Micromechanics and MEMS: Classic and Seminal Paper to 1990, New York, NY, 1997*

[7] *An Introduction to MEMS, Prime Faraday Technology Watch, 2002*

[8] http://www.st.com,*MP34DB01 datasheet*

[9] http://www.st.com,*Steval-MKI126v2 datasheet*

[10] http://www.st.com,*CCA035V1 datasheet*

[11] http://www.st.com,*Steval-MKI129V2 datasheet*

KEY CHALLENGES FOR BIOMEDICAL ENGINEERING CONCERNING LIFELONG LEARNING PROGRAMMES ON APPLICATION OF INFORMATION TECHNOLOGIES IN MEDICINE

Dimitar Dimitrov

Technical University of Sofia
8, Kliment Ohridski str. 1000 Sofia, Bulgaria
T.+359 2 965 2278, E. dcd@tu-sofia.bg

Abstract

The objective of the present paper is to enhance the competitiveness of biomedical engineering as important part of Information Engineering education within Europe, especially in relation with actual global technical challenges. As first step in the described investigation It's necessary to be identified and defined the global technical challenges in the process of application of information engineering technologies in medicine. Then, as second step and as basic goal of present investigation, it's necessary to be provided interpretation of technical challenges as basic challenges in the process of biomedical engineering education for a long time. In result the main modules for this education can be:

– Communication environments for transfer of medical information as wireless systems, cable systems, GSM-systems, Internet, satellite systems, etc. Compatibility of different communication systems in a global system for telemedicine. – Interactive medical systems for permanent observation at home of people with health problems. – Computer systems for save and protection of medical information in the cases of cyber crime – Computer restoration of medical diagnostic signals carried in different communication environment in the case of interference of physical overlay of noise from external sources. The basic requirements about final professional skills of graduated students in above mentioned engineering area are done as conclusion.

1. INTRODUCTION

Information and communication technologies are about to make a massive move into medical practice, not only in selected areas of 'high-tech' medicine, but throughout the field. The past few years have seen rapid advances in communication and information technology (C&IT), and the pervasion of the worldwide web into everyday life has important implications for education. The application of information technologies is important not only in modern medical practice (telemedicine), but in engineering and medical education, also. Most engineering and medical universities provide extensive computer networks for their students, and these are increasingly becoming a central component of the learning and teaching environment. Such advances bring new opportunities and challenges to education, and are having an impact on the way that we teach and on the way that students learn, and on the very design and delivery of the curriculum. The plethora of information available on the web is overwhelming, and both students and staff need to be taught how to manage it effectively. In the process of lifelong education must be develop clear strategies to address the issues raised by these technologies, also. In this paper there is a short description how universities are rising to this challenge, look at some of the ways in which communication and information technology can be used to enhance the learning and teaching environment, and discuss the potential impact of future developments of education, first of all lifelong education on biomedical engineering. On Fig. 1 can be seen one typical organisation of system for telemedicine. On Fig. 2 can be seen one typical application of INTERNET for transfer of medical information as it's communication environment, also.

2. KEY CHALLENGES FOR BIOMEDICAL ENGINEERING

2.1. Compatibility of different communication environment and interactive medical systems

On Fig. 1 can be seen different communication environment as wireless systems, cable systems, GSM-systems, Internet, satellite systems, etc. which are used in telemedicine. Therefore one preliminary detailed introducing with these communication systems is one of the basic challenges and requirement in the process of preparing curriculum for livelong biomedical engineering education. Stu-

dents should be introduced also with methods for obtaining of compatibility between different communication environment in systems for telemedicine. As can be seen on Fig.2 students should have good skills on INERNET network and its application for transfer of medical information and as one user friendly Interactive environment in medical systems for permanent observation at home of people with health problems. This is an other challenge in the process of preparing curriculum for livelong biomedical engineering education.

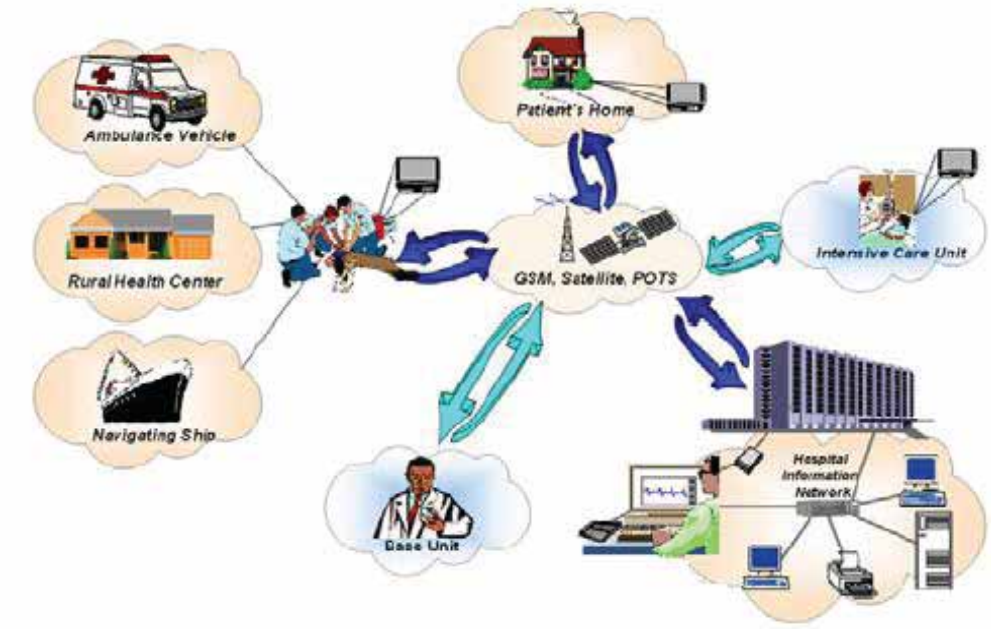

Fig. 1. Communication system for telemedicine

.

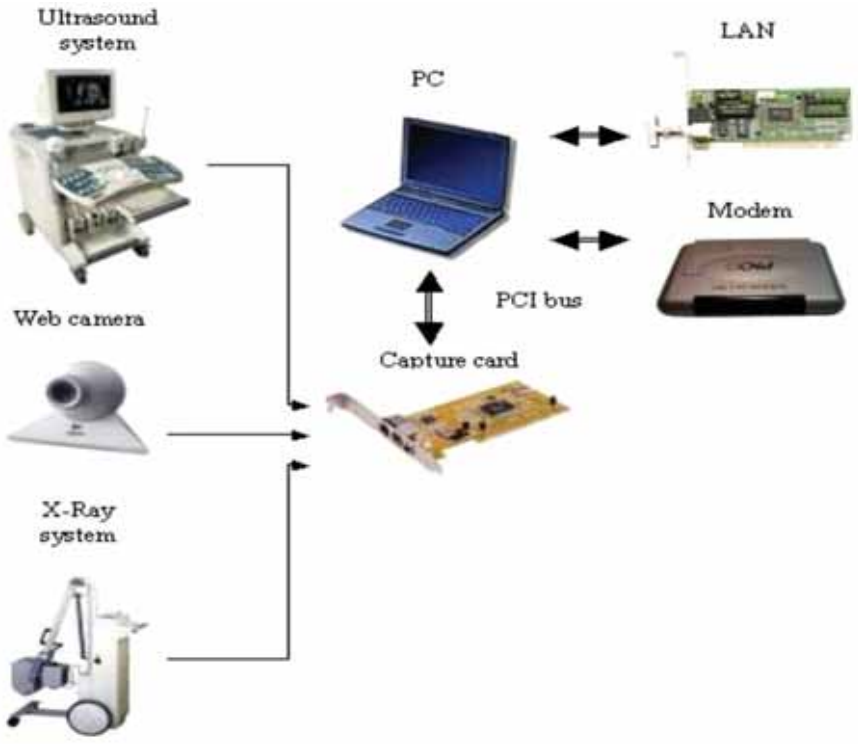

Fig. 2. Application of INTERNT for transfer of medical information

2.2. Risk and protection of Medical Information Systems

Several problems are described in the present paragraph as important challenges in the process of preparing curriculum for livelong biomedical engineering education.

These problems are mutually connected and should be described together.

So, medical data confidentiality is an essential demand for each kind of data processing and information handling in medicine nowadays. The delivery of healthcare to patients increasingly relies on Medical Information Systems (MedIS). These systems rely on modern information technology (IT) to electronically collect, process, distribute, display, and store patient data. Telemedicine is one of the very important scientific area which developed a lot last decades with the new technologies. There are many health networks FTTH „fibre to the home", which includes not only many hospitals, but many patients also (Fig. 3).

Fig. 3. Centre of a health network „fibre to the home"

These new information and communication technologies in medicine create new problems. MedIS, like other IT-systems, are vulnerable to malware attacks. Data protection, confidentiality and computer security are basic requirements for the appropriate introduction and use of information and communication technologies in health care. The basic technical challenge is the openness of modern data processing and communication systems. There is virtually no paper on medical data processing that doesn't mention the need of data protection. But with new technologies the situation becomes even worse, as they change the way medical data have to be protected. The paper identifies some of the main problem domains.

2.2.1. Potential Vilnerabilities

Systems become vulnerable to malicious logic when they are placed in an environment that allows an attacker access. The most invulnerable MedIS would have proprietary software, running only one dedicated application, isolated from other systems, afforded perfect physical access control, developed in a malware-sterile factory, requiring no service. Every deviation from this impossible hypothetical system results in the risks and vulnerabilities outlined in this section. [1,2]

✓ *Physical Access to Medical Information Systems*

A knowledgeable attacker with physical access to a system including media access, e.g., floppy disk or CD-ROM drives, may be able to infect it with malware. Highly mobile systems increase the difficulty of controlling physical access to them. This increases the likelihood of unauthorized use and modification.

✓ *Connectivity*

Vulnerabilities appear when MedIS come into contact with the outside world. This may happen via direct serial port connection, modem, or network connections.

✓ *Stand-Alone Systems*

Stand-alone systems without media access (i.e., no floppy drives, CD-ROM drives, nor net-work) are at the least risk of attack. They remain vulnerable to:

- Infected service tools used on-site;
- Malicious or inappropriate actions by service technicians;
- Malicious or inappropriate actions by vendors or suppliers during manufacture;
- Malicious or inappropriate actions by users.

✓ *Media Access*

In the past media was the predominant means of interconnecting IT systems with each other. Malware-infected media can cause infection of systems that access it. So infected media was a common vector for attacking systems with malicious logic.[11] Though still an issue, infected media is losing importance as MedIS is increasingly becoming electronically interconnected. [10]

✓ *Networked Systems*

Networked devices are increasingly replacing standalone systems to improve workflow and reduce

administrative costs.[2] They share the above risks (Fig. 4). In addition, they also are subject to wider ranges of malicious logic that can traverse the network from one machine to the next and therefore, are vulnerable to:

- Internal forms of malicious logic, which can also be propagated from one system to another, e.g., worms
- External forms of malicious logic that operate from outside of the MedIS, e.g., malware-induced DoS.

Fig. 4. Network accessible for vulnerabilities

Malware propagates between interconnected MedIS using the same technical mechanisms intended for normal communication. Networked systems may require specific services, e.g., http, ftp, SSL, and others, and correlated pre assigned ports, depending on the intended use.

Attackers typically desire to affect the greatest number of systems they can, so most frame their service-related attacks on the most common implementations of a service. The more of these services are on a system, the more likely that system will be affected by a successful attack. Likewise, the greater the interconnectivity of devices, the more opportunity an attacker may have to gain access.

The more potential attackers, the greater the risk. Devices connected directly to the Internet have the greatest risk. It is not the kinds of vulnerabilities that change, but the potential number of attackers that increases.

- ✓ *Software Related Vulnerabilities*
- ✓ *MedIS Using Common Software –*

Malware attacks often attack commonly used platforms because they are easy to find, weak-nesses are known, and they have the highest impact. General purpose systems, which are based on common standards and protocols, are therefore more vulnerable than specialized systems. Despite the increased risk, the healthcare enterprise has benefited greatly from using common software platforms.

- ✓ *Device-Specific Application Software*

The software intended to accomplish the dedicated task of a specific type or model of medical equipment can be termed device-specific. It likely will be written to take advantage of common protocols and to operate with a standard operating system such as Unix or Windows, but is specific and functional only with particular MedIS. Such device-specific software is not general-purpose and, as compared to other application software – like office applications for word processing or spreadsheets – is distributed in narrow communities under strict licensing and version controls.

- ✓ *Shared Use Systems*

MedIS installed onto a shared use general purpose IT system remains vulnerable to all of the relevant media and network access threats of a dedicated system. In addition, it becomes vulnerable to all the subsequent malware infections of the host system. The MedIS vulnerability further increases when the host system also includes E-mail, enables Internet access, or offers services such as FTP, NFS, and RPC. The shared use system cannot make as many changes because the sys-tem must support the needs of all the different uses. [3,4,6]

The first and most important use of a computer in a clinic or a physicians practice is the management of the patient data. The electronic patient record (or computer-based patient record–CPR) serves several purposes: billing the patient, legal documentation, quality control. The doctor has to archive the data for several years and has to transmit some of the data to a health insurance company for billing. Technical means should ensure that the patient record is disclosed only to authorized persons or institutions, according to the 'need to know' principle, and that the integrity of the data is protected. Defence.

2.2.2. Against Malicious Logic for MedIS

The definition of administrative and technical measures should be started with an intended use risk and threat analysis, so that resources are utilized where most beneficial. It should consider the following points.

- ✓ *System Integrity Assurance*

Integrity assurance can prevent or at least detect modification of the software installed in the system.

Unintended or unexpected software changes might be due to the introduction of malware anywhere in the design, manufacturing, installation, and service process. We will discuss some technical approaches to assuring integrity of the system in the following sections. [1,7,8,9]

✓ *Hardware Protection*

Hardware can be used to raise the level of assurance that software has not been changed in an unauthorized way, for example, Read Only Memory (ROM) and key-locked cabinets.

✓ *Checksum Calculation*

Checksums can be computed and compared to assure that a file is not modified. A check-sum is a value calculated from the content of a file that gives the system ability to check its integrity before use. Possible implementations range from a simple parity bit check, as typically used when transmitting data over a serial line, to a 128-bit hash created when using the MD-5 algorithm. In principle, all methods share the common properties of ease in computing and low probability that correct matches between computed and expected values occur with changed data. However, the ease in computing, in terms of CPU load, varies widely with techniques, as does the probability of detecting problems.

✓ *Digital Signatures*

Digital signatures are an extension of checksums. When a checksum is digitally signed, the probability that the original file has been changed by an unauthorized user or process can be further minimized.

✓ *System Profiles*

System profiles are sophisticated check summing systems that go beyond a simple list of checksums. They verify complete directory structures, e.g., including verification of file attributes, presence or absence of files, and many other characteristics of the entire combination of files present. System profiles often employ digitally signed databases and may incorporate file system checks that bypass normal operating system facilities in order to detect the more sophisticated checksum aware malicious logic.

✓ *Manufacturing Scan*

Using virus detection software, with up-to-date virus signature files, at appropriate stages of the manufacturing process is another way to assure system integrity. A scan by an off-the-shelf virus detection tool could assure the delivery of malware free products and updates.[5] This does not prevent a subsequent infection.

2.3. Defensive System Design

Many attack paths utilize flaws that result from common software development errors that do not introduce problems during normal operation. The most common such mistake is called the "buffer overflow" error already exploited by many malicious attacks. It permits a malicious code to overflow the allocated buffer and take control of the system. The design methodology used by the engineering staff should help to avoid, detect, and eliminate these flaws. Specific tools and techniques should be used by engineering staff, several of which are discussed within this section.

✓ *Developmental Tools*

There are development tools and methodologies that can analyze systems to detect and help eliminate flaws. Some of them are formal evaluation methods, such as those found in the Common Criteria (ISO/IEC 15408), as well as code analysis, requirements analysis, and design analysis tools.

✓ *Programming Language*

Some programming languages, such as Java and C#, incorporate security features that provide protection against some forms of malware attack. There are also support library and compiler features for some languages, such as C and C++, which can be used to reduce vulnerability to some forms of attack.

✓ *OS and Hardware Services*

Some operating systems and hardware provide security features such as execute protection bits, privilege rings, etc. Applications should run with the lowest privilege practical.

✓ *Network Service Restrictions*

Many MedIS systems are based upon common computer platforms that incorporate many network features such as logical ports and a suite of available network services. Remove or close all unnecessary features, ports, and services to eliminate potential malware attack points. For example, e-mail or web access facilities should be deliberately removed from MedIS that have no need for these services. Their absence may be noticeable to the users who are accustomed to generic computer

platforms but it should be understood as normal and desirable to increase IT security.

✓ *Security-focused Engineering Services*

Software audits and inspections by independent personnel, including peer reviews and soft-ware walkthrough sessions, can further reduce inadvertent errors. These techniques are commonly used for detection of functional flaws. Their scope should be expanded to include vulnerability reduction.

✓ *Host Virus Checkers*

Virus checkers or virus scanning software is well known as a class of application software that searches hard drives, disks, etc. Unfortunately this software i only for viruses which arre known by that software. Virus checkers typically consist of an executable application (scan engine) and a data file of virus patterns containing the information required by the scan engine to detect known viruses. After detecting a virus the virus checker performs a pre-configured action e.g., making an entry in a log-file, spawning a pop-up window with a warning text, performing an automated at-tempt to repair the infected file. Virus scanners have significant drawbacks when used with MedIS. Some common impacts when using virus scanners with MedIS include the following:

– Medical images, e.g., x-rays, can be damaged because the virus scanner consumes too much system resources
– Medical image files can be damaged because the virus scanner attempts to fix what it falsely identified as a virus
– Virus scanning software set to detect system behavior abnormalities can falsely identify medical software as having malicious behavior and shut down the medical software
– Pop-up windows from virus scanners can obscure medical images and medically necessary alerts

✓ *Specifics and Restrictions for Medical Information Systems*

Healthcare-specific regulatory and technological requirements further influence the choice of countermeasures used in MedIS as compared to those that might be used with standard of-fice IT:

– MedIS must operate safely and effectively. Protection mechanisms must not interfere with the intended medical use of the equipment.
– When there is a failure, MedIS usually "fails open," leaving the system usable. Non-medical IT equipment usually shuts down upon failure, e.g. Automatic Teller Machines go out-of-service in the event of a problem.

2.2.3. Defenses Against Malicious Logic for MedIS Users

✓ *Behavioral/Administrative Defenses*

In addition to the protective measures described above, organizations should consider the following additional processes and technologies:

– Risk analysis and mitigation planning.
– Restrict physical access to MedIS whenever possible by physically hiding MedIS, closing doors, locking keyboards etc.
– Review all connections of MedIS to other equipment and networks for necessity and reduce such connections to the absolute minimum. Properly configured routers by trained IT staff can deliver a high level of security.
– Wireless communications must receive special attention. For example improperly configured devices could inadvertently connect to an adjacent but unknown network.

✓ *Defence in Depth*

The Defence in Depth concept realizes that protecting the security of an enterprise is best achieved by duplicating controls at multiple locations. A healthcare facility should establish a multi-layered defence against the risks and consequences of malware and other MedIS threats. It is helpful to provide defences at different layers. In this way, if an attacker gets through one network security measure, there are additional security measures to help thwart the attack.

3. CONCLUSION

A single standardized solution to the issues raised by malicious logic cannot be offered in this paper. Instead, in Sections 2 and 3, a basic set of reasonable technical measures for users has been described. Depending on the local situation each measure by itself may help healthcare providers using MedIS to increase the level of protection against the threats imposed by malicious logic. Some of these measures require in-depth analysis of the impact to safe intended use of the MedIS and thus should be the joint responsibilities of the

MedIS users. Most defences are well-established common IT tools and may be properly configured by the healthcare provider. The best approach is defence in depth. Users must take special care when defining and configuring their local security concept to avoid implementing measures that weaken the inherent security level of their MedIS.

References

[1] Jordanova L., Tz. Dimitrova. Investigation on Noise Characteristic of Cable Channel for Telemedicine, electronics and Engeneering (Lithuania), ISSN 1392-1215, 2009, No 4(92), pp. 103-106

[2] Tz, Dimitrova, Medical Data risk exposure, 4th International Conference CEMA09, Sofia, October, 08-10,2009, pp. 32-35

[3] L. Cranor, P. Guduru, and M. Arjula, User interfaces for privacy agents. ACM Transactions on Computer Human Interaction, 12(2):135–178, 2006.

[4] R. de Paula and et. al. Two experiences designing for effective security. In SOUPS '05: Proceedings of the second symposium on Usable privacy and security, New York, NY, USA, 2005. ACM.

[5] R. Dhamija, J. Tygar, and M. Hearst. Why phishing works. In Proceedings of the SIGCHI Conference on Human Factors in Computing Systems, 2006.

[6] J. S. Downs, M. B. Holbrook, and L. F. Cranor, Decision strategies and susceptibility to phishing. In SOUPS '06: Proceedings of the second symposium on Usable privacy and security, New York, NY, USA, 2006. ACM.

[7] Michael Pluscauskas, Security of health information debate. Internet forum healthnet.calvin.dgbt.doc.ca, Jan 18, 1994

[8] Working paper: Project No.:8353Z, Contract No.:

DAAB07-94-C-H601, Taxonomy of Threats and Security Services for Information Systems, Gulachenski and Cost, (MITRE, 1994)

[9] D. Tz. Dimitrov, Iproving the Perfrmance of Program Package for 3D Simulation of Low Frequency Magnetic Field in Medical Therapy, Journal "Electronics and Electrical Engineering", Litvania, ISSN 1392-9631, 2007, No.1(73), p.69-72

[10] D. Dimitrov, An Investigation on Influence of Electromagnetic Field of GSM Apparatuses on the Human Body, The Mediterranean Journal of Electronics and Communication, Vol.2, No.4, 2006, p.141-147

[11] D. Dimitrov, Visualization of a Low Frequency Magnetic Field, generated by Girdle Coil in Magnetotherapy, Journal "Electronics and Electrical Engineering", Litvania, ISSN 1392-1215, 2007, -No.6(78), p.57-60

Acknowledgements

The research in this paper is supported by project: Strategic Alignment of Electrical and Information Engineering in European Higher Education Institutions (SALEIE)

Reference number: 527877-LLP-1-2012-1-UK-ERASMUS-ENW

SOME BASIC CHALLENGES FOR COURSES ON MEDICAL SYSTEMS FOR THERAPY IN BIOMEDICAL ENGINEERING CURRICULUM IN THE PROCESS OF LIFELONG LEARNING

Atanas Dimitrov

Technical University of Sofia
8, Kliment Ohridski blvd, 1000, Sofia

Abstract

It's well known that the engineering education on health issues (bioengineering) is one interdisciplinary education. Principally the challenges for medical systems for therapy are a big part of challenges for engineering education on these systems, also. As result, a new methodology for presentation of courses on medical systems for therapy can be created and implemented in bioengineering education in the process of lifelong learning. The courses on medical systems for therapy can include new modules as: computer simulation and investigation of movements of ions in live tissues under influence of external electromagnetic fields in a long frequency band; computer visualization of these movements of ions in 3D; investigation on "internal" electromagnetic signals in live tissues as "reply" of influence of external electromagnetic signals; new interpretation of connection between parameters of movement of ions in live tissues and parameters of "internal" electromagnetic signals; formalization of live tissues as system in theoretical investigations; new explication of some reasons for result of therapy in connection with "internal" electromagnetic signals, etc. On the base of above mentioned investigations, some recommendations for the processes of actualization of bioengineering's curriculums and especially actualization of courses on medical systems for therapy, including new methodology are done at the end of paper.

1. INTRODUCTION

Exposure to electromagnetic fields is not a new phenomenon. However, during the 20th century, environmental exposure to man-made electromagnetic fields has been steadily increasing as growing electricity demand, ever-advancing technologies and changes in social behaviour have created more and more artificial sources. Everyone is exposed to a complex mix of weak electric and magnetic fields, both at home and at work, from the generation and transmission of electricity, domestic appliances and industrial equipment, to telecommunications and broadcasting. Tiny electrical currents exist in the human body due to the chemical reactions that occur as part of the normal bodily functions, even in the absence of external electric fields. For example, nerves relay signals by transmitting electric impulses. Most biochemical reactions from digestion to brain activities go along with the rearrangement of charged particles. Even the heart is electrically active - an activity that your doctor can trace with the help of an electrocardiogram.

2. BASIC CHALLENGES FOR COURSES ON MEDICAL SYSTEMS FOR THERAPY IN BIOMEDICAL ENGINEERING CURRICULUM

Most often systems for low frequency electrical field and systems for low frequency magnetic field are used in physiotherapy. Usually the application of these systems is user friendly and allow to be obtained good effect of therapy. Therefore there is not only permanent engineering development of systems for medical therapy by using of electromagnetic field, but development of medical methods for application of these systems in the cases of more and more disease. Because of that the courses "Medical Systems for Therapy" in biomedical engineering curriculum are one of the basic courses. These courses are very important in the process of lifelong learning also because of permanent development of these systems.

Usually there is only one macro description of phenomena of influence of electromagnetic field on live tissues in the engineering courses on medical systems for therapy by using of electromagnetic field. Often there is not description of connection between parameters of external electromagnetic field and biological phenomena in live tissues under influence of electromagnetic field. Only final effect of therapy is mentioned as result of this influence.

The presentations of lectures are only on the base of engineering skills of students, but not connected with preliminary skills on biology. It's a big disadvantage because these courses are on one interdisciplinary scientific area. In result students have not enough knowledge on connection between parameters of external electromagnetic field, biological phenomena in live tissues and final effect of therapy. This is one restriction when future engineers go to the design and optimization of systems for medical therapy. Often the descriptions of influences of low frequency electrical and magnetic field on the human body in the courses on systems for medical therapy are the next [1,2]: "Low-frequency electric fields influence the human body just as they influence any other material made up of charged particles. When electric fields act on conductive materials, they influence the distribution of electric charges at their surface. They cause current to flow through the body to the ground". Or "Low-frequency magnetic fields induce circulating currents within the human body. The strength of these currents depends on the intensity of the outside magnetic field. If sufficiently large, these currents could cause stimulation of nerves and muscles or affect other biological processes".

Or"Biological effects are measurable responses to a stimulus or to a change in the environment"t.[3]Or "It is not disputed that electromagnetic fields above certain levels can trigger biological effects. and influence people's well being"[4]. Some members of the public have attributed a diffuse collection of symptoms to low levels of exposure to electromagnetic fields at home. Reported symptoms include headaches, anxiety, suicide and depression, nausea, fatigue and loss of libido. To date, scientific evidence does not support a link between these symptoms and exposure to electromagnetic fields. Finally some keypoints[5] are determined in the courses on medical systems for therapy using electromagnetic field:

- A wide range of environmental influences causes biological effects.
- At low frequencies, external electric and magnetic fields induce small circulating currents within the body. In virtually all ordinary environments, the levels of induced currents inside the body are too small to produce obvious effects.
- The main effect of radiofrequency electromagnetic fields is heating of body tissues.
- Despite extensive research, to date there is no evidence to conclude that exposure to low level electromagnetic fields is harmful to human health.

It's clear that in the courses on medical systems for therapy it's necessary to be used new methodology. It would be on the description of some processes in live tissues as result of influence of external electromagnetic field. It should be engineering presentation, but it should be on the base of structure and properties of live tissues. In other site this engineering course should be the base for future investigation and design of real medical systems for therapy. Therefore the above mentioned description of processes in live tissues under influence of external electromagnetic field is not appropriate for engineering education. This description is are too yeasty. The described phenomena are not presented as result of movement of ions in live tissues under influence of external electromagnetic field. There is not any mathematical description of processes, which is compulsory for one engineering course.

3. AN ACTUAL PRESENTATION FOR THE COURSES OF BIOENGINEERING ON PROCESSES IN LIVE TISSUES IN THE CASE OF INFLUENCE OF EXTERNAL LOW FREQUENCY ELECTROMAGNETIC FIELD

Often encounter cases where low-frequency electromagnetic field affects the ions in various linear environments including living tissue, also. Always there is a movement of ions because of influence of electromagnetic field. In other site the motion of charged particles (ions) in the volume of research can be seen as electromagnetic signals with a determined space-time configuration in the system. These signals can be seen, also as a reaction of the system. In this sense, the low frequency electric and/or magnetic signals that trigger these movements of charged particles can be considered respectively as formal influence of electric and/or magnetic signals on the system. This part of the physical environment in which there is a a movement of charged particles under the influence of external electric and/or magnetic signals can be viewed as a system. Generally in this case there is a spatial and temporal effects of low frequency electric and/or magnetic signals on the system (especially living tissue).

It's possible to speak about a process of space-time processing of low frequency electric and / or magnetic signals as far as the external impacts on the system cause the system's reaction and the space-time configuration of the "external" low-frequency electric and / or magnetic signals do not coincide with the space-time configuration of the signals considered as system response.. The equations (1), (2) and (3) are known in the references [6,7,8] for the case of disposition of electrical charges $Q(t)$ with linear distribution $q(x)$ on axis X, trajectory of movement $X(t)$ and velocity $V(t)$ of electrical charges. It's possible to be used these equations for obtaining of parameters of system's reaction, respectively, current density $\left|\vec{\delta}(t)\right|$ and current $i(t)$ through surface s in alive tissues and spectral function $\dot{S}_i(\omega)$ of this current.

$$\left|\vec{\delta}(t)\right| = \frac{dQ(t)}{dt} = \frac{d}{dt}\int_0^{X(t)} qdx = q\frac{dX(t)}{dt} = qV(t) \qquad (1)$$

$$i(t) = \int_{(s)} \vec{\delta}(t)d\vec{s} \qquad (2)$$

$$\dot{S}_i(\omega) = qs\int_0^{\infty} \frac{dX(t)}{dt} e^{-j\omega t} dt \qquad (3)$$

Therefore, the determining of components of the velocity $\vec{V}$ of the movement of ions on the three axes X, Y, Z is the first step in the process of determining the response of the system, i.e. determining of the parameters of the "internal" signals. Because of that, the determination of the components of velocity $\vec{V}$ of the movement of ions on the three axes X, Y, Z is an important result in the paper as one result of method for visualization of movement of ions by the action of external low frequency electromagnetic signals. This method and the obtained results would be important for medical therapy.

3.1. Presentation of mathematical model as base of the lecture

The mutual disposition of both independent vectors of electrical intensity $\vec{E}(x,y,z,t)$ and magnetic induction $\vec{B}(x,y,z,t)$ in the case of simultaneously influence of low frequency electrical and magnetic field on the ions can be seen on Fig. 1.

It's assumed that the origin of coordinate system is at the point in which is situated the charged particle. This point can be any point in space, in which act both signals. Below without reducing community of investigations is assumed that the location of the axes of the three dimensional coordinate system is chosen so, that the vector of the magnetic induction $\vec{B}(x,y,z,t)$ coincides with the axis Z. The components of vector of electrical intensity $\vec{E}(x,y,z,t)$ on the axis X, Y, Z of coordinate system are E_x, E_y, E_z. The vector differential equation (4) of movement of ion can be done taking in account Fig. 1.

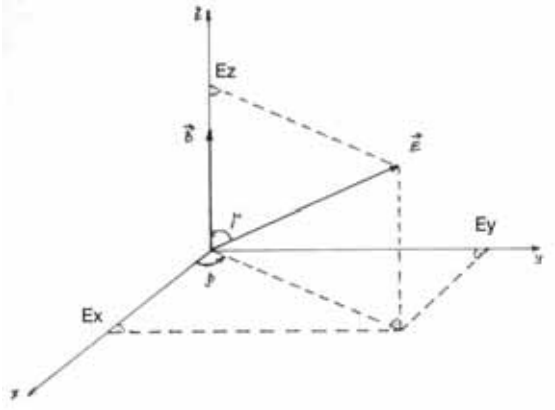

Fig. 1. The mutual disposition of both independent vectors of electrical intensity $\vec{E}(x,y,z,t)$ and magnetic induction $\vec{B}(x,y,z,t)$

$$m\frac{d^2\vec{r}(t)}{dt^2} = q\vec{E}(x,y,z,t) + q[\frac{d\vec{r}(t)}{dt} x\vec{B}(x,y,z,t)] \qquad (4)$$

Where:

m is the masse of ion?
q is the electrical charge of ion;
$\vec{r}$ is tangential trajectory's vector of ion's movement;

3.2. Presentation of Experimental Investigations and Discussion at the end of lecture

It is known that sodium ions Na^+ have a considerable percentage of the composition of living tissue. Therefore the further results are on investigations on movement of sodium ions Na^+ because the effect of different low frequency "external" signals on ions. Therefore, the movements of sodium ions Na^+ under influence of "external" signals with certain parameters are described in the article as examples. Some results of visualization of movement of ions, which have been obtained by computer's methods for solution of differential equation (4) using MATLAB for instance. As example can be presented a simple phenomena in the case of sim-

ultaneously influence on the ions of both simple sinusoidal magnetic signal and permanent electrical field (very often used process of magneto-therapy with ionoforesis) The terms of the influence of "external" signals on magnetic ions are defined by the expression (5).

$$\vec{E}(x,u,z,t) = const \wedge \vec{B}(t) = \vec{B}_m \cos\omega_3 t \wedge \\ \wedge \vec{B}(x,y,z) = const \wedge \omega_3 = const \wedge \beta = 45^\circ \wedge \gamma = 45^\circ \quad (5)$$

Where:

B_m is the amplitude of magnetic induction in any points of homogenous sinusoidal magnetic field;

ω_3 is the frequency of the simple magnetic signal

Below the system of differential equations (6) is a modification of differential equation (4) taking in account expression (5).The solutions of system differential equations (6) can be seen on Fig.3. The dimensions for the trajectory of movement of ions are $[m.10^{-1}]$ and the dimension for the velocity of ions is $[m.s^{-1}]$.

$$m\frac{d^2x(t)}{dt^2} = q[E\sin\gamma\cos\beta + \frac{dy(t)}{dt}B_m\cos\omega_3 t]$$

$$m\frac{d^2y(t)}{dt^2} = q[E\sin\gamma\sin\beta + \frac{dx(t)}{dt}B_m\cos\omega_3 t] \quad (6)$$

$$m\frac{d^2z(t)}{dt^2} = qE\cos\gamma$$

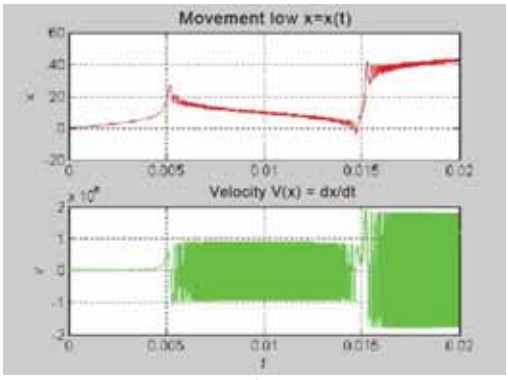

a)

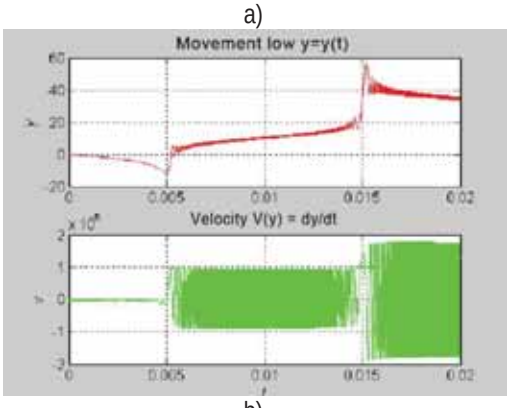

b)

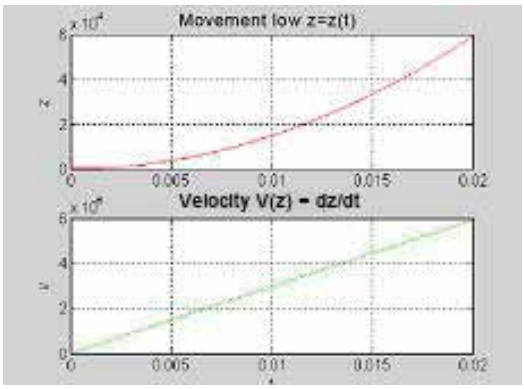

c)

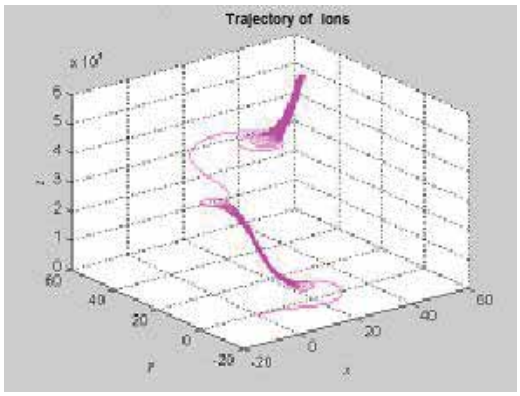

d)

Fig. 2. The solutions of system differential equations (6)

The components of velocity and trajectory of movement of ions on the axis X, Y, Z can be seen on fig. 2a, 2b and 2c.

The second step of presentation of processes in live tissue can be on the base connection between velocities of ions on the axis X, Y, Z (fig. 3a, 3b and 3c) and current density $\left|\vec{\delta}(t)\right|$ and current $i(t)$ through surface s in alive tissues according to equations (1) and (2). It would be one basic and detailed description of the processes in live tissue.

The trajectory of movement of ions can be seen on fig. 3d. This visualisation of trajectory of ions in live tissue is very important because:

- it's connected with movement of determined kind of ions in the case of determined conditions according to equations (5) and (6);
- one optimisation of this trajectory can be obtained by optimisation of parameters of external electromagnetic field. It's important for physician for obtaining of more good and more fast effect of therapy. It's important also for engineer in the process of design of systems for therapy.

On the base of above discussion it would be easy to explain for students the process of magneto-therapy with ionoforesis (Fig. 3), as example for one engineering interpretation in the course on medical systems for therapy.

Fig. 3. Visualisation of process of magneto-therapy with ionoforesis

On the base of discussion and in relation to equations (1) and (2) can be obtained the next important conclusion. The forms of the components of the "internal" signals (reaction of the system) along the three axes X, Y and Z are the same as the shape of the components of the velocity of the ions along the respective axes.. Therefore, the solution of the differential equations (6) practically defines the reaction of system (living tissue).Thus, the description of the process of space-temporal processing of low frequency electric and magnetic signals in linear environments (especially in living tissue) can be obtained solving the system differential equations for the movement of ions.

4. CONCLUSION

A new engineering method for education in the process of lifelong learning about influence of external low frequency electromagnetic signals on alive tissues is described in the article. The external electromagnetic signals are described as influence on one linear system (alive tissues) and the reaction of this system is described through "internal" low frequency electromagnetic signals. According to the equations (1), (2), (3) the reaction("internal" low frequency electromagnetic signals) of system (alive tissues) depends to the velocity of movement of ions under influence of external low frequency electromagnetic field. It's the base for presentation and engineering explanation of process of therapy.

References

[1] http://www.utwente.nl/en/education/master/programmes/biomedical engineering/?gclid=CPzp5sfdjcECFcISwwodkKkArA

[2] http://www.bme.umich.edu/index.php

[3] http://www.bme.jhu.edu/

[4] http://www.bu.edu/bme/

[5] http://www.embs.org/about-biomedical-engineering

[6] D. Dimitrov, N.Ralev, Signals and System for Electrosleep, Electronics and Electrical Engineering, ISSN-1392-1215, No.5(93),2009, pp.95-98,

[7] V. C. A. Ferrarof and C. Plumpton, An Introduction to Magneto-Fluid Mechanics, 2nd edition, Oxford University Press,p.330,2006.

[8] B. O. Lehnert, Dynamics of Charged Particles, North-Holland , p.520,2004

Acknowledgements

The research in this paper is supported by project: Strategic Alignment of Electrical and Information Engineering in European Higher Education Institutions (SALEIE)

Reference number: 527877-LLP-1-2012-1-UK-ERASMUS-ENW

ON INTERPOLATION METHODS OF LOW FREQUENCY MAGNETIC FIELD IN SYSTEMS FOR MAGNETOTHERAPY

B. Kudrin

St. Petersburg State University, Faculty of Math. & Mech., bogdan.kudrin@gmail.com

I. P. Soloviev

St. Petersburg State University, Math. & Mech. Faculty, i.soloviev@spbu.ru

Abstract

In this work we apply methods of 3-dimensional linear interpolation, one-dimensional quadratic Lagrange interpolation and cubic spline to interpolate electromagnetic induction values in 3D. For a given 3-dimensional lattice (base points) values are obtained by calculation in accordance with a mathematical model. Then for a new set of points we obtain electromagnetic induction values both interpolation and calculation. Numerical results show that interpolation algorithms reduce run time considerably without loss of accuracy.

1. INTRODUCTION

At the moment there are many types of magnetotherapy devices that are successfully used in medicine. In most cases, in practice the required space configuration of the magnetic field is created by means of one or more air coils (without core) which are appropriately arranged in the space. Because of that there is a linear relationship between the magnetic flux density of the excited magnetic field and current in the coils. It is assumed that the environment in which the space-time configuration of the magnetic field is seen is linear. The result is the superposition of the fields of the individual coils that forms a more complex time-spaced magnetic field. We suppose that the environment around the coils is homogeneous and the relative magnetic permeability is constant.

In this work we apply numerical algorithms to interpolate low frequency magnetic field obtained in a magnetotherapy device that was designed and constructed in Sofia Technical University and used in clinical practice.

The solution of the problem of the modelling and visualization in 3D of electromagnetic field generated by this apparatus is given in articles [1,3,4]. The obtained data allows a physician to study the graphical representation of the magnetic induction field. By changing the position of coils, distance between them and the current intensity the physician can select an appropriate regime to achieve the best results for minimal treatment time.

For this model the algorithm of calculation of electromagnetic induction in nodes of a base 3-dimensional lattice was designed and implemented. The obtained results are saved in an array having size [nx3], where n – the number of nodes. Any element of the array contains coordinate values of electromagnetic induction vector. When visualizing results, the value of the module defines the color selection – the more value the more saturation of the color.

In this model the superposition principle is used and the magnetic induction in a point is the sum of the induction values generated by all the coils, and in every coil – by all its contours. Hence this algorithm is time-consuming. In this connection in [5] a method of 3-dimensional linear interpolation was implemented. Base values were obtained by calculations described and implemented in [1,3,4]. Such an approach resulted in performance increasing without loss of accuracy.

Here we use values obtained by calculations as base ones. These values are in nodes of 3-dimensional lattice and form interpolation nodes. Then we present the results of application of 3 interpolation methods using the nodes: a) 3-dimensional linear interpolation, b) one-dimensional quadratic Lagrange interpolation and c) coordinate-wise cubic spline. Numerical experiments show that any of methods reduces the run-time and does not lead to a loss of accuracy.

2. MATHEMATICAL MODELS

2.1. 3-dimensional linear interpolation (3D l)

Select a cube of the base lattice. All its vertices contain values of electromagnetic induction obtained by calculation. We select the center of the cube as interpolation point. This scheme is shown on Fig. 1. The interpolation nodes are 8 nearest nodes of the base lattice: $\{(x_i, y_j, z_k)\}$, i,j,k={0,1}.

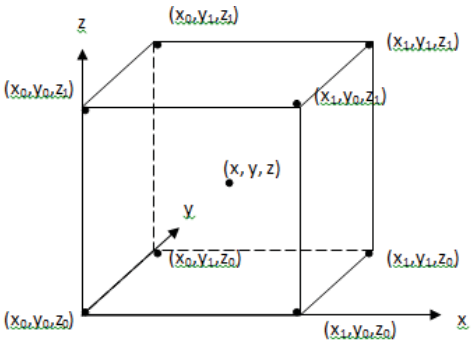

Fig. 1. Base nodes and the interpolation point for 3-dimensional linear interpolation

Consider Lagrange interpolation polynomial

$$l_{nmp}(x,y,z) = \prod_{i=0,i\neq n}^{1}\prod_{j=0,j\neq m}^{1}\prod_{k=0,k\neq p}^{1}\frac{(x-x_i)(y-y_j)(z-z_k)}{(x_n-x_i)(y_m-y_j)(z_p-z_k)}. \quad (1)$$

It follows that

$$l_{nmp}(x_i, y_j, z_k) = 0, i \neq n \vee j \neq m \vee k \neq p$$

$$l_{nmp}(x_n, y_m, z_p) = 1.$$

The interpolation polynomial has the form

$$L(x,y,z) = \sum_{n=0}^{1}\sum_{m=0}^{1}\sum_{p=0}^{1} f_{nmp}\cdot l_{nmp}(x,y,z), \quad (2)$$

where f_{nmp} – the vector of values obtained by the calculation in the point (x_n,y_m,z_p).

Hence we use linear interpolation that takes into account contribution of all the 8 interpolation nodes. It should be noted that in (2) we use such a form for brevity, because this formula is applied for every coordinate of f_{nmp} by turns.

2.2. One-dimensional quadratic Lagrange interpolation (1D l)

The method of one-dimensional quadratic Lagrange interpolation is applied – the interpolation point and the nodes are on the same line.

In this case the interpolation point is also the center of the cube. We use 3 nodes of the base lattice so that the nodes and the interpolation point belong to the same diagonal.

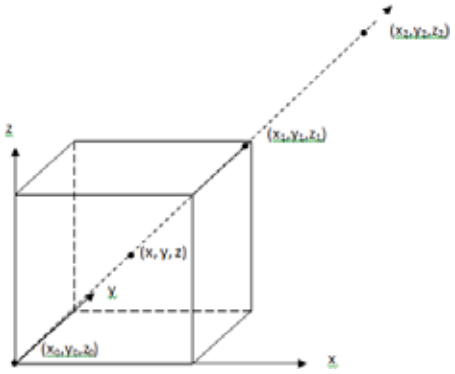

Fig. 2. Base nodes and interpolation point for one-dimensional Lagrange interpolation

The base polynomial has the form

$$l_n(x,y,z) = \prod_{n=0,n\neq i}^{2}\frac{\sqrt{(x-x_i)^2+(y-y_i)^2+(z-z_i)^2}}{\sqrt{(x_n-x_i)^2+(y_n-y_i)^2+(z_n-z_i)^2}} \quad (3)$$

and satisfies the conditions

$$l_n(x_i, y_i, z_i) = 0, i \neq n$$

$$l_i(x_i, y_i, z_i) = 1.$$

The interpolation polynomial is represented as

$$L(x,y,z) = \sum_{n=0}^{2} f_n \cdot l_n(x,y,z), \quad (4)$$

where где f_n is the value in the base node (x_n,y_n,z_n).

As in the previous case (4) means that the interpolation is performed by coordinate-wise.

2.3. Cubic spline

Let a function *f(x)* be defined on a segment [*a*,*b*]. Consider a partition of the segment $[x_i, x_{i+1}]$, where $x_0 = a, x_n = b, i = 0,...n-1$. A function *S*(*x*) is

said to be cubic spline for *f*(*x*) if it satisfies the conditions:

1. on every element of the partition *S(x)* is the polynomial with power not greater than 3;
2. the first and the second derivatives of *S(x)* are continuous on [*a*,*b*];
3. $f(x_i) = S(x_i), i = 0,..n$;
4. $S''(a) = S''(b) = 0$.

As it is known [2], the function *S(x)* is defined by the conditions uniquely.

The polynomial *S(x)* on the segment *[a,b]* is constructed by the following way:on every element of the partition $[x_i, x_{i+1}]$ we write interpolation polynomial in the form

$$S_i(x) =$$

$$a_i + b_i(x - x_i) + \frac{c_i}{2}(x - x_i)^2 + \frac{d_i}{6}(x - x_i)^3.$$

By writing the above conditions we obtain a system to find the coefficients a_i, b_i, c_i, d_i.

The coefficients are obtained by sweep method applied to the matrix of the system.

One can obtain a complexity estimation for the described algorithm [2]. Let *n* be the common number of points and *k* be the number of point where we know values of the function. Time complexity of sweep method for 3-diagonal matrix is *O*(*n*). Time complexity of the interpolation in every from *n-k* points is *O*(*k*). So time complexity of the algorithm is *O*(*n*)+(*n-k*) *O*(*k*). If *k* depends on *n* linearly, then time complexity is $O(n^2)$. If k is a constant we obtain *O*(*k*).

The method of cubic spline is used coordinate-wise,i.e coordinates of magnetic induction vectors. Supposing that parameters of parallelepiped bounding the area where electromagnetic induction is calculated are *l* (length), *m* (width), and *h* (height), the asymptotic estimation for time complexity is *O*(*lmh*).

3. RESULTS OF EXPERIMENTS FOR 3-DIMENSIONAL LINEAR AND ONE-DIMENSIONAL QUADRATIC INTERPOLATION

We analyzed run-time for programs implementing the algorithms by the following way. For a given base lattice electromagnetic induction vectors are calculated in the nodes. The interpolation is performed in the centers of cubes of the lattice. The number of nodes in the base lattice (n) is comparably with the number of interpolation points (n/8), that allows us to compare run-times of calculation and interpolation objectively.

To estimate miscalculation we find norms (module maxima) of two 3-dimensional arrays: obtained by calculation (B) and by linear interpolation (L) and square one (S). The interpolation coefficients are defined as L/B and S/B. The table 1 shows that miscalculation is not greater than 8 % for linear interpolation and not greater than 12% for quadratic one. As 3-dimensional linear interpolation (3d I) uses 8 nodes, it has the greater accuracy than quadratic one. In experiments we considered the area 600x500x232 mm. In the table the number of base nodes is given depending on the step by every dimension.

Table 1. Comparing run-times of algorithms

Lattice size		Run time(sec)			Interpolation coefficient	
n	step(mm)	Base algorithm	3d I	1d I	3d I (L/B)	1d I n (S/B)
70000	10	6	1	<1	0.92	1.03
200000	7	17	2	1	0.93	1.10
550000	5	49	8	5	0.96	1.10
2550000	3	228	38	25	0.97	1.12

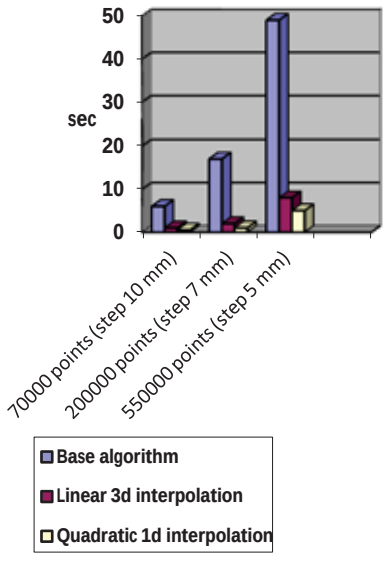

Fig. 3. Diagram of the algorithms run times

4. RESULTS OF INTERPOLATION BY CUBIC SPLINE

In experiments we used the data obtained by calculation in the points of integer lattice with size 100x100x100 (module1). Then we constructed sets of initial data for interpolation as all the points of the base lattice with coordinates: a) by module 2; b) by module 4; c) by module 8 and d) by module 16. Interpolation by cubic spline method was performed in the inter lattice points by module 1. The results were compared with given data. In the table run times (in sec) of the methods are given.

Config.	a	b	c	d
Run time	6.912	4.896	4.541	4.356

The following figure shows the initial magnetic field (obtained by calculation) and results of visualization for configurations a), b), c), d). The most reliable results were obtained for configurations a) and b), i.e. for interpolation nodes being on the distance not greater than 4 in the integer lattice.

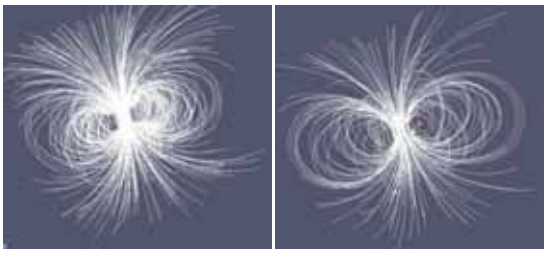

Initial data a

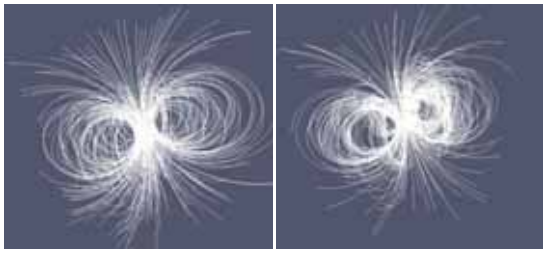

b c

d

5. CONCLUSION

The interpolation of electromagnetic field in magnetotherapy devices is very important because it reduces runtime considerably. The results of experiments show that all the described interpolation methods give reliable results.

Acknowledgements

The work was partially supported by the grant RFBR 13-01-00782.

References

[1] N. Ampilova, D. Dimitrov, B. Kudrin. Mathematical modeling of low frequency magnetic field in systems for magnetotherapy. Proc. 8 Int. Conf. CEMA13, 17-19 Oct. 2013, Sofia, Bulgaria. p. 48-51.

[2] V. O. Ashkenazi. Spline-surfaces. Theory and calculating algorithms. Tver, Izd. Tverskogo Gos.Univ., 2003.

[3] B. Kudrin, A. Dimitrov. An algorithm for visualization of low-frequency magnetic signals in systems for magnetotherapy. Proc. 8 Int. Conf. CEMA13. 17-19 Oct. 2013, Sofia, Bulgaria, p. 31-35.

[4] B. Kudrin, A. Dimitrov. Computer visualization of low frequency magnetic signals in systems for magnetotherapy with variable parameters. Proc. 8 Int. Conf. CEMA13. 17-19 Oct. 2013, Sofia, Bulgaria, p. 36-39.

[5] B. Kudrin. On interpolation of electro-magnetic field in magnetotherapy devices.Proc.conf. "Herzen readings – 2014", St.Petersburg, Russia, April 2014, p. 210-212.(in Russian)

[6] Samarsky, A. Gulin. Numerical methods, M.Nauka, 1989. (in Russian)